

KLAIPĒDA UNIVERSITY

Edvinas TIŠKUS

ADVANCEMENTS IN ECOLOGICAL MONITORING  
THROUGH UNMANNED AERIAL VEHICLE  
AND SATELLITE DATA: STUDIES IN WATER CLARITY,  
COASTAL MANAGEMENT,  
AND VEGETATION DYNAMICS

DOCTORAL DISSERTATION

NATURAL SCIENCES,  
ECOLOGY AND ENVIRONMENTAL SCIENCES (N 012)

Klaipėda, 2024

The doctoral dissertation was prepared in the period 2019 – 2024 at Klaipėda University, based on the conferment a doctorate right which was granted for Klaipėda University by the order of the Minister of Education, Science and Sport (Republic of Lithuania) No. V-160, signed on 22 February 2019.

### **Academic Advisor**

Dr. Diana VAIČIŪTĖ (Klaipėda University, Natural Sciences, Ecology and Environmental Sciences – N 012).

The doctoral dissertation is defended at the Board of Klaipėda University in Ecology and Environmental Sciences:

### **Chairman**

Dr. Andrius ŠIAULYS (Klaipėda University, Natural Sciences, Ecology and Environmental Sciences – N 012);

### **Members:**

Dr. habil. Paweł TEREFENKO (University of Szczecin, Poland, Natural Sciences, Physical geography – N 006);

Prof. dr. Evaldas VAIČIUKYNAS (Kaunas University of Technology, Technological Sciences, Informatics Engineering – T 007);

Dr. Ele VAHTMÄE (University of Tartu, Estonia, Natural Sciences, Ecology and Environmental Sciences – N 012);

Dr. Natalja ČERKASOVA (Klaipėda University, Natural Sciences, Ecology and Environmental Sciences – N 012).

The dissertation will be defended in a public meeting of the Board in Ecology and Environmental Sciences, Klaipėda University, Marine Research Institute Conference Hall at 1 p. m. on 13 June, 2024.

Address: Universiteto av. 17, LT-92294, Klaipėda, Lithuania.

The doctoral dissertation was sent out on 13 May, 2024.

The doctoral dissertation is available for review at the Library of the Klaipėda University.

KLAIPĖDOS UNIVERSITETAS

Edvinas TIŠKUS

EKOLOGINĖS STEBĖSENOS TOBULINIMAS  
NAUDOJANT BEPILOČIŲ ORLAIVIŲ IR PALLYDOVŲ  
DUOMENIS: VANDENS SKAIDRUMO, PAKRANČIŲ  
VALDYMO IR AUGMENIJOS KAITOS TYRIMAI

DAKTARO DISERTACIJA

GAMTOS MOKSLAI,  
EKOLOGIJA IR APLINKOTYRA (N 012)

Klaipėda, 2024

Disertacija rengta 2019–2024 metais Klaipėdos universitete pagal Klaipėdos universitetui Lietuvos Respublikos švietimo, mokslo ir sporto ministro 2019 m. vasario 22 d. įsakymu Nr. V-160 suteiktą Ekologijos ir aplinkotyros mokslo krypties doktorantūros teisę.

### **Vadovas**

dr. Diana VAIČIŪTĖ (Klaipėdos universitetas, gamtos mokslai, ekologija ir aplinkotyra – N 012).

Daktaro disertacija ginama Klaipėdos universiteto Ekologijos ir aplinkotyros mokslo krypties taryboje:

### **Pirmininkas**

dr. Andrius ŠIAULYS (Klaipėdos universitetas, gamtos mokslai, ekologija ir aplinkotyra – N 012);

### **Nariai:**

habil. dr. Paweł TEREFENKO (Ščecino universitetas, Lenkija, gamtos mokslai, fizinė geografija – N 006);

prof. dr. Evaldas VAIČIUKYNAS (Kauno technologijos universitetas, technologijos mokslai, informatikos inžinerija – T 007);

dr. Ele VAHTMÄE (Tartu universitetas, Estija, gamtos mokslai, ekologija ir aplinkotyra – N 012);

dr. Natalja ČERKASOVA (Klaipėdos universitetas, gamtos mokslai, ekologija ir aplinkotyra – N 012).

Daktaro disertacija bus ginama viešame Ekologijos ir aplinkotyros mokslo krypties tarybos posėdyje 2024 m. birželio 13 d. 13 val. Klaipėdos universiteto Jūros tyrimų instituto konferencijų salėje.

Adresas: Universiteto al. 17, LT-92294, Klaipėda, Lietuva.

Daktaro disertacija išsiųsta 2024 m. gegužės 13 d.

Disertaciją galima peržiūrėti Klaipėdos universiteto bibliotekoje.

# Abstract

This dissertation advances the use of Unmanned Aerial Vehicles (UAVs) and satellite imagery in environmental monitoring, specifically targeting eutrophication indicators and bathing water quality within aquatic and coastal ecosystems. Through a cumulative series of studies, innovative approaches integrating UAV remote sensing, deep learning techniques, and the quasi-analytical algorithm for precise water quality assessments and vegetation mapping were developed and validated. This work addresses gaps in the current capabilities for ecological observation and management, with advancements in both methodology and application.

The research establishes a comprehensive framework for UAV surveys, illustrating the effectiveness of combining diverse sensor technologies and analytical methods for detailed vegetation analysis. This framework supports efforts in biodiversity conservation, ecosystem structure analysis, and monitoring phenological and stress-related changes in vegetation, guiding environmental scientists and resource managers in the adoption of UAV technology across various ecosystems.

In the assessment of changes in aquatic vegetation, particularly reed beds, the study highlights the utility of the normalized difference water index derived from Sentinel-2/MSI data and Yen binary thresholding, validated through UAV imagery. This approach is found reliable in detecting mowing-induced changes in reed beds, with enhanced accuracy for areas larger than 0.1 ha.

Furthermore, the quasi-analytical algorithm for estimating Secchi depth from multispectral UAV imagery was tested, identifying Hedley's sun glint correction method as the most precise. The research emphasizes the algorithm's adaptability and the impact of environmental factors, such as CDOM concentration and solar zenith angle, on the accuracy of Secchi depth measurements, underscoring the potential of UAV technology in providing scalable and efficient water quality assessments across extensive areas.

Lastly, the study explores the performance of the U-Net model in segmenting beach wrack from UAV imagery, indicating that "RGB" data combinations yield the most accurate beach wrack detections. Contrary to expectations, the addition of multispectral and elevation data did not significantly improve segmentation accuracy, suggesting the importance of selecting appropriate data combinations based on specific site characteristics to optimize model performance across varied coastal landscapes.

Collectively, these studies represent a significant advancement in the application of UAV and satellite technologies for environmental monitoring, offering methodologies and insights for the comprehensive assessment of aquatic and coastal ecosystem health. This integrated approach not only enhances current monitoring practices but also establishes a new standard for precision and efficiency in environmental science research.

## Keywords

Remote sensing, unmanned aerial vehicle, Secchi depth, beach wrack, helophytes.

# Reziumė

Šioje disertacijoje aptariamas bepiločių orlaivių ir palydovinių vaizdų naudojimas aplinkos, tiksliau, eutrofikacijos rodiklių bei maudyklų vandens kokybės ir pakrančių ekosistemose stebėsenai. Atlikus tyrimus sukurti ir patvirtinti nauji metodai, apimantys bepiločių orlaivių nuotolinį stebėjimą, gilaus mokymosi metodus ir kvazianalitinį algoritmą, skirti tiksliai vertinti vandens kokybę ir sudaryti augmenijos žemėlapius. Šiame darbe didelis dėmesys skiriamas spręsti dabartinių ekologinio stebėjimo ir valdymo galiomybių trūkumo problemas tobulinant metodiką ir pritaikymą.

Tyrimo metu sukurta išsami bepiločių orlaivių pritaikymo sistema, parodanti, kaip veiksmingai derinti įvairias jutiklių technologijas ir analitinius metodus siekiant atlikti išsamią augalijos analizę. Ši sistema padeda stebėti biologinę įvairovę, analizuoti ekosistemų struktūrą, fenologinius ir su stresu susijusius augalijos pokyčius, taip pat padeda aplinkos mokslininkams ir išteklių valdytojams pritaikyti bepiločių orlaivių technologijas įvairiose ekosistemose.

Vertinant vandens augalijos, tai yra, nendrių sąžalynų, pokyčius tyrime pabrėžiama normalizuoto vandens skirtumo indekso, gauto iš Sentinel-2/MSI duomenų, ir Yen dvinarinio slenksčio, patikrinto naudojant bepiločių orlaivių vaizdus, nauda. Ištirta, kad šis metodas yra patikimas nustatant pokyčius nendrių sąžalynuose, kurių plotai didesni nei 0,1 ha, atlikus šienavimą.

Be to, atliktas Secchi gylio vertinimas naudojant daugiaspektrinius bepiločių orlaivių vaizdus ir kvazianalitinį algoritmą nustatyta, kad Hedley'io saulės atspindžio korekcijos metodas yra tinkamiausias norint gauti tikslesnius rezultatus. Tyrime pabrėžiamas ne tik algoritmo pritaikymas ir aplinkos veiksnių, tokių kaip spalvotų ištirpusių organinių medžiagų koncentracija ir saulės zenito kampas, įtaka Secchi gylio matavimų tikslumui, bet ir bepiločių orlaivių technologijos potencialas atliekant veiksmingus vandens kokybės vertinimus didelėse teritorijose.

Tyrime nagrinėjamas U-Net modelio efektyvumas segmentuojant paplūdimio sąnašas iš bepiločių orlaivių vaizdų. Tyrimo metu išsiaiškinta, kad „RGB“ duomenų deriniai padeda tiksliausiai aptikti paplūdimio sąnašas. Priešingai, nei tikėtasi, pridėjus daugiaspektrinius ir aukščio duomenis segmentavimo tikslumas nepadidėjo, todėl norint optimizuoti modelio veikimą įvairiose pakrantėse, svarbu parinkti tinkamų duomenų derinius, atsižvelgiant į konkrečias vietovės charakteristikas.

Apibendrinant šiuos tyrimus galima teigti, kad jie daro reikšmingą pažangą taikant bepiločių orlaivių ir palydovų technologijas aplinkos stebėsenai. Tyrimuose pateiktos metodikos ir įžvalgos, skirtos išsamiam vertinti vandens ir pakrančių ekosistemų būklę. Šie integruoti metodai ne tik pagerina dabartinę stebėsenos praktiką, bet ir nustato naujus tikslumo ir efektyvumo standartus aplinkos mokslų tyrimuose.

## Reikšmingi žodžiai

Nuotolinis stebėjimas, bepilotis orlaivis, Secchi gylis, paplūdimio sąnašos, helofitai.

---

# Contents

ABSTRACT	5
REZIUMË	6
LIST OF ORIGINAL PUBLICATIONS	9
LIST OF ADDITIONAL PUBLICATIONS	9
AUTHOR'S CONTRIBUTIONS	10
ABBREVIATIONS	11
1. INTRODUCTION	13
1.1. Aim and objectives	17
1.2. The novelty of the study	18
1.3. Scientific and applied significance of the results	18
1.3.1. Scientific significance	18
1.3.2. Applied significance	19
1.4. Scientific approval	20
2. MATERIALS AND METHODS	21
2.1. Study sites	21
2.2. Data collection	23
2.2.1. Unmanned aerial vehicles data acquisition techniques	24
2.2.2. Remote sensing and Earth observation data	27
2.2.3. Field sampling	27
2.3. Image processing	29
2.4. Statistical methods and validation	34
3. RESULTS AND DISCUSSION	37
3.1. General guidance for vegetation monitoring using UAV	37

3.1.1 Species composition: highlighting biodiversity	38
3.1.2 Ecosystem structure: measuring biomass, volume, and stand complexity	39
3.1.3 Plant status: phenology and plant stress	39
3.1.4 Ecosystem dynamics: disturbances and regeneration	40
3.2. UAV and satellite analysis of reed bed dynamics in Plateliai Lake	40
3.2.1 Effectiveness of automatic workflow and satellite image analysis	40
3.2.2 Analysis of reed bed area changes and mowing impact	44
3.2.3 Implications for water body management and reed bed density recovery	45
3.3. Enhanced water clarity assessment via unmanned aerial vehicle imagery	46
3.3.1 Choice for sun glint correction	46
3.3.2 Quasi-Analytical Algorithm-derived Secchi depth compared to in situ measurements	48
3.3.3 Influence of Water Constituents for Quasi-Analytical Algorithm Secchi Depth Values	49
3.4 Unmanned aerial vehicle based beach wrack quantification	51
3.4.1 Performance evaluation across data combinations and classes	51
3.4.2. Quantitative analysis of beach wrack heights and areas	54
3.5. Results and discussion synthesis	56
4. RECOMMENDATIONS	59
5. CONCLUSIONS	61
6. ACKNOWLEDGEMENTS	63
7. REFERENCES	65
8. SUMMARY IN LITHUANIAN	81
ĮVADAS	81
Tyrimo tikslas ir pagrindiniai uždaviniai	83
Darbo naujumas	84
Rezultatų mokslinė ir praktinė reikšmė	85
METODAI	86
Tyrimų vietos	86
Duomenų rinkimas	86
Vaizdų apdorojimas	88
Statistiniai metodai ir validacija	89
REZULTATAI IR APTARIMAS	90
Bendrosios rekomendacijos dėl augalijos stebėsenos naudojant bepilotės skraidykles	90
Nendrių sąžalynų dinamikos analizė iš bepiločių orlaivių ir palydovų vaizdų Platelių ežere	92
Automatinės darbo eigos ir palydovinių vaizdų analizės veiksmingumas	92
Poveikis vandens telkinių valdymui ir nendrių sąžalynų tankio atsistatymui	93
Vandens skaidrumo vertinimas naudojant bepiločio orlaivio vaizdus	94
Bepiločiu orlaiviu atliekamas paplūdimio makrodumplių sąnašų kiekybinis vertinimas	95
IŠVADOS	96
CURRICULUM VITAE	98
PUBLICATIONS	99



## LIST OF ORIGINAL PUBLICATIONS

The material of this study was presented in 4 original publications, published in peer-reviewed scientific journals:

- I. Müllerová, J., Gago, X., Bučas, M., Company, J., Estrany, J., Fortesa, J., Manfreda, S., Michez, A., Mokroš, M., Paulus, G., **Tiškus, E.**, Tsiafouli, M.A., Kent, R., 2021. Characterizing vegetation complexity with unmanned aerial systems (UAS) – A framework and synthesis. *Ecological Indicators* 131, 108156. <https://doi.org/10.1016/j.ecolind.2021.108156>
- II. **Tiškus, E.**, Vaičiūtė, D., Bučas, M., Gintauskas, J., 2023. Evaluation of common reed (*Phragmites australis*) bed changes in the context of management using earth observation and automatic threshold. *European Journal of Remote Sensing* 56, 2161070. <https://doi.org/10.1080/22797254.2022.2161070>
- III. **Tiškus, E.**, Bučas, M., Vaičiūtė, D., Gintauskas, J., Babrauskienė, I., 2023. An Evaluation of Sun-Glint Correction Methods for UAV-Derived Secchi Depth Estimations in Inland Water Bodies. *Drones* 7, 546. <https://doi.org/10.3390/drones7090546>
- IV. **Tiškus, E.**, Bučas, M., Gintauskas, J., Kataržytė, M., Vaičiūtė, D., 2023a. U-Net Performance for Beach Wrack Segmentation: Effects of UAV Camera Bands, Height Measurements, and Spectral Indices. *Drones* 7, 670. <https://doi.org/10.3390/drones7110670>

## LIST OF ADDITIONAL PUBLICATIONS

- V. Bučas, M., Lesutienė, J., Nika, N., Skersonas, A., Ivanauskas, E., Srėbaliėnė, G., **Tiškus, E.**, Gintauskas, J., Šaškov, A., Martin, G., 2022. Juvenile Fish Associated With Pondweed and Charophyte Habitat in the Curonian Lagoon. *Front. Mar. Sci.* 9, 862925. <https://doi.org/10.3389/fmars.2022.862925>
- VI. Free, G., Bresciani, M., Pinardi, M., Giardino, C., Alikas, K., Kangro, K., Rõõm, E.-I., Vaičiūtė, D., Bučas, M., **Tiškus, E.**, Hommersom, A., Laanen, M., Peters, S., 2021. Detecting Climate Driven Changes in Chlorophyll-a Using High Frequency Monitoring: The Impact of the 2019 European Heatwave in Three Contrasting Aquatic Systems. *Sensors* 21, 6242. <https://doi.org/10.3390/s21186242>
- VII. Vaičiūtė, D., Bučas, M., Bresciani, M., Dabulevičienė, T., Gintauskas, J., Mėžinė, J., **Tiškus, E.**, Umgieser, G., Morkūnas, J., De Santi, F., Bartoli, M., 2021. Hot moments and hotspots of cyanobacteria hyperblooms in the Curonian Lagoon (SE Baltic Sea) revealed via remote sensing-based retro-

spective analysis. *Science of The Total Environment* 769, 145053. <https://doi.org/10.1016/j.scitotenv.2021.145053>

Published papers are reprinted with permission of the publishers.

## **AUTHOR'S CONTRIBUTIONS**

- I. First E.T.: conceptualization, methodology, investigation, resources, data curation, writing—original draft, visualization.
- II. Second E.T.: conceptualization, methodology, software, validation, formal analysis, investigation, resources, data curation, writing—original draft, writing—review and editing, visualization, supervision.
- III. Third E.T.: conceptualization, methodology, software, validation, formal analysis, investigation, resources, data curation, writing—original draft, writing—review and editing, visualization, supervision.
- IV. Fourth E.T.: conceptualization, methodology, software, validation, formal analysis, investigation, resources, data curation, writing—original draft, writing—review and editing, visualization, supervision.

## ABBREVIATIONS

Abbreviation	Explanation
<b>AOI</b>	Area of interest
<b>AUC</b>	Area Under Curve (statistical term)
<b>BW</b>	Beach wrack
<b>CDOM</b>	Coloured Dissolved Organic Matter
<b>Chl-a</b>	Chlorophyll-a
<b>IoU</b>	Intersection over union
<b>MAE</b>	Mean Absolute Error
<b>MAPD</b>	Mean Absolute Percentage Deviation
<b>MSFD</b>	Marine Strategy Framework Directive
<b>NDAVI</b>	Normalized Difference Adjusted Vegetation Index
<b>NDRE</b>	Normalized Difference Red Edge Index
<b>NDVI</b>	Normalized Difference Vegetation Index
<b>NDWI</b>	Normalized Difference Water Index
<b>NIR</b>	Near-Infrared
<b>QAA</b>	Quasi-analytical Algorithm
<b>RGB</b>	Red green blue
<b>RMSE</b>	Root Mean Square Errors
<b>Rrs</b>	remote sensing reflectance
<b>S2/MSI</b>	Sentinel-2/MSI (Multispectral Instrument)
<b>SD</b>	Secchi Depth
<b>UAV</b>	Unmanned aerial vehicle
<b>WAVI</b>	Water Adjusted Vegetation Index
<b>WFD</b>	Water Framework Directive



# 1

---

## INTRODUCTION

Water bodies including the majority of the lakes, the Baltic Sea and its coastal region are greatly impacted by eutrophication and under continuous observation to assess water quality and ecosystem health (Murray et al., 2019), supported by international frameworks such as the Water Framework Directive (WFD), the Marine Strategy Framework Directive (MSFD), Habitat Directive and the Helsinki Convention. These directives focus on sustainable water use, prevention of degradation, and marine ecosystem conservation (Chemin et al., 2004; Dassenakis et al., 2011). In the assessment of Baltic marine environmental health based on these international policies, two critical parameters are emphasized for monitoring and evaluation of eutrophication: transparency of water column and distribution of macrophytes. Another important aspect of monitoring the Baltic Sea's coastal environment, in line with the Bathing Water Directive and Lithuanian hygiene standards, involves the regular assessment and classification of bathing water quality and beach wrack (BW), which plays a role in understanding the ecological status and human health implications of coastal waters (European Parliament, 2006).

Water transparency is primarily measured using Secchi depth (SD), which is labor-intensive and subject to observer bias, as noted by Jiang (2012) and Yu et al. (2014). This method provides only point-level measurements, which may not accurately represent larger areas (Pham et al., 2020; Stock, 2015). The WFD mandates monitoring

## 1. Introduction

of all inland waters larger than 0.5 km<sup>2</sup>, a challenging goal that requires innovative monitoring methods (Dworak et al., 2005). For example, in Estonia, approximately 80 waterbodies exceeding 0.5 km<sup>2</sup> of area are subject to monitoring, yet in 2014, only about 40% were annually monitored (Alikas et al., 2015). In Sweden, the monitoring task is even harder with over 7200 lakes, where only lakes larger than 1 km<sup>2</sup> were included in the latest WFD status classification due to practical and financial constraints. This limitation was criticized, and plans are in place to include all lakes in future reports. Considering the vast number of lakes, this imposes a significant financial challenge when relying solely on traditional monitoring methods.

In Europe, the sampling procedures for assessing macrophyte abundance under the WFD are diverse but most countries utilize transect-based sampling, a method where point (from squares or sections) observations are made along set lines across a water body, covering different depth zones (Poikane et al., 2018). The coverage of macrophytes is estimated using a 4–9 point scale or percentage coverage scale and each country has developed specific reference values to assess ecological status. Traditional *in situ* measurements are mainly destructive and are constrained by their labor-intensive nature and limited accessibility, especially in aquatic environments. The monitoring frequency of macrophyte populations in European lakes varies from annual (Søndergaard et al., 2013) to once in 6 years (the reporting cycle under the WFD), indicating the lack of an annual time-series of monitoring in most water bodies during six-year cycles. Under the Habitat Directive in the Natura 2000 areas, the monitoring of macrophyte habitats (characterized by species such as *Phragmites*, *Zostera*, *Potamogeton*, and *Chara*) in coastal lagoons, rivers and lakes is important for the assessment of their conservation status (European Commission, 2013).

While the monitoring approach effectively captures data on various macrophyte species, BW, an important indicator in coastal ecosystems, remains less emphasized in current monitoring practices. Integrating BW monitoring within the existing framework could provide a more holistic understanding of coastal ecosystem health under the Bathing Water Directive (Directive 2006/7/EC). Furthermore, BW often harbors fecal indicator bacteria and potentially pathogenic microorganisms, including *Vibrio* species, which pose health risks in coastal environments and necessitate consideration in monitoring protocols (Kalvaitienė et al., 2023, and references therein). Coastal monitoring, which incorporates BW as a key component, faces challenges in its detection and quantification due to its variable distribution and the limitations of traditional mapping methods. BW monitoring methods, often labor-intensive and reliant on manual field surveys, are prone to human error. This indicated a need for improved methodologies in comprehensive coastal health assessment, as exemplified by some countries integrating BW monitoring within their coastal management frameworks, adapting to their unique conditions (Schlacher et al., 2008; Woelfel et al., 2021; Busotti et al., 2022).

## 1. Introduction

In Lithuania, water transparency and macrophyte monitoring are integral to assessing lake and coastal water ecological conditions, which methods are approved by the Lithuanian Ministry of Environment (Lithuanian Republic Ministry of Environment, 2013) and currently cover around 80 lakes every 6 years in Lithuania, as well all freshwater habitats larger than 50 ha, as required by WFD (Broeck et al., 2015). Water transparency is categorized into five classes, from ‘very good’ to ‘very bad’, with specific thresholds of good ecological status: in lakes, ‘good’ exceeds 1.3 m, while in coastal waters, it exceeds 5.0 m. In inland and transitional waters, the macrophyte assessment method employs transect-based sampling, using the Braun-Blanquet or percentage scale to evaluate the coverage of macrophyte species primarily during July and August. The same approach is used for macrophyte habitat monitoring under the Habitat Directive. For instance, in the Curonian Lagoon, the area of the red-listed species *Nymphioides peltata* is crucial for its habitat assessment, especially using orthophotos (Bučas et al., 2023). This approach could also be suitable for monitoring large-scale habitat changes (Sinkevičienė et al., 2017) that are challenging to evaluate through traditional methods (transect surveys). Furthermore, monitoring of BW is often inconsistently managed by local beach authorities by visual evaluation on whether the BW is spreading (Republic of Lithuania, Ministry of Environment, 2007), leading to potentially unaddressed environmental issues, for example, large accumulations of BW.

Techniques utilizing platforms such as satellites provide valuable insights into the spatial and temporal variations in water quality (Chen et al., 2007; Strong and Elliott, 2017). Remote sensing data, varying in spatial and spectral resolution, include Earth observation data from satellites such as the Sentinel-2 multispectral instrument (S2/MSI). The S2/MSI satellite is notable for its high spatial resolution data with a ground sampling distance of up to 10 m and frequent revisit times (around 1 image per 3 days), aiding in a range of environmental monitoring tasks (Drusch et al., 2012). Additionally, S2/MSI offers a range of spectral bands (12 total), particularly in the visible and near-infrared portions of the spectrum, that are critical for detecting water quality constituents. Studies utilizing S2/MSI imagery have contributed significantly to detailed ecological assessments (Ghirardi et al., 2022). By unifying satellite data, researchers can obtain extensive aquatic environmental information, offering a holistic overview of environmental conditions. Satellites reveal details on aquatic plant distribution, water temperature, turbidity, and other pivotal indicators of aquatic ecosystem health (McCullough et al., 2012). Remote sensing, enhanced with machine learning models, has advanced environmental monitoring by offering broader coverage and cost-effectiveness. Recent advancements in aquatic monitoring and management are predominantly driven by the integration of remote sensing and machine learning, yet these innovations also come with their own set of limitations. Integrating satellite data, especially with advanced techniques like deep learning models, poses challenges in data acquisition and processing. The performance of machine learning models can

## 1. Introduction

vary widely, requiring accurate optimization and standardization for broad applicability and reliability. Moreover, the process of integrating satellite data to monitor coastal environments or characterize vegetation complexity underscores the need for sophisticated computational methods that can manage large datasets without compromising accuracy. Additionally, factors such as meteorological conditions (strong winds, rain, snow, etc.) and solar positioning can affect data accuracy, limiting the methods' applicability (Dugdale et al., 2019). The financial implications of acquiring and maintaining advanced satellite technologies can also be prohibitive, especially in resource-limited regions (Sibanda et al., 2021).

Further advancements in remote sensing have also led to the development of methods for Unmanned Aerial Vehicle (UAV) use in similar research topics, such as those equipped with the multispectral camera (e.g., Micasense Rededge), offering even higher spatial resolution imagery (ground sampling distance of 2 cm per pixel) than Earth observation satellites for detailed environmental studies (Deng et al., 2018; Knoth et al., 2013), and capacity to capture spectral details in visible, near-infrared and red-edge bands for precise vegetation and water quality analysis. By unifying drone and satellite data, researchers can obtain both very high-resolution and extensive aquatic environmental information, thus yielding a holistic overview of environmental conditions. These methodologies allow for the monitoring of large areas in a timely and cost-efficient manner, acquiring high-resolution data on diverse parameters (Hilton et al., 1984). UAVs deliver precise imagery and insights into water quality (Lally et al., 2019) and are crucial for analyzing aquatic zones, including lakes, rivers, wetlands, and coastal regions (Dronova et al., 2021). Equipped with multispectral cameras, drones can capture detailed images of underwater habitats, aiding in the identification and mapping of macrophytes and other essential aquatic terrains (Zhang et al., 2016). They also assess water quality parameters such as clarity and monitoring issues like eutrophication. Recent studies employing UAVs have enhanced our understanding of vegetation complexity in ecosystems worldwide (Alvarez-Vanhard et al., 2020; Gonzalez et al., 2016; Jiménez López and Mulero-Pázmány, 2019). Improved water quality monitoring has also advanced notably, with sensor and communication technology enabling rapid detection of hydrological changes and early warning systems for events such as harmful algal blooms (Glasgow et al., 2004). Integrating UAV data can improve aquatic environmental understanding and refine conservation and management tactics (Paneque-Gálvez et al., 2014; Ruwaimana et al., 2018). However, the accuracy and efficiency of UAV-derived measurements can also be compromised by environmental variables like cloud cover, water turbidity, sun angle, and the dynamic nature of the subjects under study. The complexity of ecosystems adds difficulty in data classification and feature delineation, such as reed beds (Kislik et al., 2018). UAV-based multispectral sensors provide spatial data across different environments, but capturing high-quality data in environments like underwater



## 1. Introduction

habitats remains challenging (Zhang et al., 2016). Despite advancements, comprehensive integration and standardization of UAV technologies for aquatic environmental monitoring are still developing.

Remote sensing innovations are vital for the conservation and sustainable management of water bodies and their vast resources, allowing for the development of efficient monitoring workflows that are transferable across different coastal environments (Tomaseello et al., 2022). These methods offer efficient, large-scale monitoring capabilities, especially for submerged aquatic vegetation management, but they require specific corrections and analysis methods to be effective (Rowan & Kalacska, 2023). Deep learning applications in remote sensing show promise in detecting water pollution outbreaks, highlighting a significant step forward in environmental monitoring (Kwon et al., 2018; Sagan et al., 2020). The integration of cross-mission data merging and deep learning in automating continuous water quality monitoring represents a significant improvement in management strategies, especially in sensitive environments (Chang et al., 2017). However, challenges remain in this field, where addressing technical limitations and refining these tools is essential for optimizing their application in environmental conservation.

### 1.1. Aim and objectives

The overall aim of this doctoral dissertation is to evaluate and enhance the capabilities of UAVs and satellites in assessing eutrophication and bathing water quality within aquatic and coastal ecosystems.

Four main objectives of this thesis are framed around the following research aims, which address critical gaps in current environmental monitoring practices:

1. Based on a comprehensive synthesis of UAV applications in vegetation studies to identify common vegetation parameters that shape workflows guiding the design of UAV surveys, to establish an integrated framework for mapping essential aspects of biodiversity and ecosystem functioning. (Paper I)
2. To investigate the applicability of satellite data in detecting mowing-induced changes in aquatic vegetation, such as reed beds, and assess how these detections can contribute to the development of strategic management interventions. (Paper II)
3. To evaluate the effectiveness of UAVs equipped with multispectral cameras in estimating Secchi depth using the Quasi-Analytical Algorithm in inland water bodies. (Paper III)
4. To test whether the use of UAVs with multispectral camera for U-Net models can be applied in coastal monitoring, especially for beach wrack detection and monitoring across a range of beach types, each exhibiting unique geomorphological features. (Paper IV)

### 1.2. The novelty of the study

The proposed study addresses the current gap in understanding the use of remote sensing data, specifically from UAVs and Earth observation satellites, for monitoring aquatic environments in Lithuania. However, the suggested method workflows could be applied in other locations, assuming similar environmental conditions. The novelty of this dissertation lies in its approach to utilizing the capabilities of UAVs for ecological and environmental monitoring leveraging techniques like deep learning and automated workflows. An important aspect of the study's novelty is the extensive volume of image data collected from diverse geographical locations, utilizing advanced multispectral camera technology together with a conventional RGB camera, which significantly enhances the depth and accuracy of analysis. While individual studies have explored UAV applications in environmental science, this work provides assessment across diverse domains — ranging from water quality evaluation to vegetation change and complexity mapping. By evaluating the QAA in the context of Secchi depth determination and integrating U-Net convolutional neural network models for BW segmentation, this research introduces a simpler, cost-effective methodology previously untested in these domains, significantly reducing the time and resources required for traditional SD and BW in situ measurements. Moreover, the unique focus on mowing-induced changes in reed bed areas, especially for sizable patches, fills a significant knowledge gap in management using remote sensing. The last component is the synthesis of UAV-based ecosystem complexity studies, aiming to create a universally applicable framework for vegetation analysis. This study consolidates multiple research approaches and sets forth best practices and workflows, aiming to standardize and optimize future UAV-driven ecological studies.

### 1.3. Scientific and applied significance of the results

#### 1.3.1. Scientific significance

The research presented in this dissertation exemplifies the intricacies of aquatic ecosystems within the Baltic region, enhancing our understanding of surface water quality through the innovative use of UAVs and satellite remote sensing technologies. By integrating these technologies, this study offers novel insights into the spatial and temporal dynamics of water transparency and aquatic vegetation changes. It underlines the critical role of detailed, high-resolution data in capturing the subtle complexities of small and shallow water bodies, areas that have previously been challenging to monitor accurately.

## 1. Introduction

The study expands the scientific discourse on remote sensing methodologies by validating the effectiveness of the Quasi-analytical algorithm (QAA, Lee et al., 2015) specifically tailored for UAV applications. This advancement underscores the algorithm's enhanced precision in assessing water transparency, a vital parameter in water quality studies.

In addressing the ecological concerns associated with aquatic vegetation, this study provides a deeper understanding of reed beds growth patterns and distribution shifts, particularly in response to anthropogenic interventions such as mowing. The scientific contribution of this work also lies in its examination of automatic thresholding algorithms, which have shown to be effective in delineating between different types of aquatic and coastal vegetation. While beach wrack distribution is not a direct indicator of water quality, the research establishes its significance in coastal ecosystem health assessments, offering a methodological improvement in its monitoring.

Moreover, the study furthers scientific knowledge by demonstrating the capability of the U-Net convolutional neural network to enhance the classification accuracy of drone imagery. This finding is a testament to the growing synergy between AI and environmental science, creating the way for more sophisticated analytical tools in remote sensing research.

### 1.3.2. Applied significance

The developed methods for water quality assessment can be used by environmental managers and policymakers to monitor and make informed decision, leading to more effective and sustainable management strategies. The findings related to the regrowth of common reed areas post-mowing can inform management interventions for controlling this vegetation. Additionally, the demonstrated success of UAV multi-spectral imaging in measuring water transparency offers a cost-effective and efficient method for large-scale water quality monitoring, which can be particularly useful in regions where in situ measurements are challenging or resource-intensive. Lastly, the ability to map and quantify beach wrack using drone imagery and machine learning can aid in beach management, potentially informing clean-up operations, microplastic pollution mitigation, and even resource recovery for uses such as fertilization. All these applications have the potential to contribute to the conservation and improved health of our aquatic ecosystems.

## 1. Introduction

### 1.4. Scientific approval

1. COST HARMONIOUS (poster, 2019 11 06 Portugal) – *Mapping of aquatic vegetation habitats and water bird distribution using unmanned aerial vehicle*
2. EOMORES workshop (poster, 2020 01 23 Netherlands) – *Mapping of aquatic vegetation habitat distribution using remote sensing*
3. Jūros ir krantų tyrimai (poster, 2020 Lithuania) – *Makrofitų išteklių pokyčių vertinimas pasitelkiant palydovinius duomenis*
4. Marine Research Institute seminar (oral, 2021 04 08 Lithuania). *Remote sensing methods for aquatic vegetation monitoring in Lake Plateliai and other ecological monitoring using drones*
5. Jūros ir krantų tyrimai (poster, 2021 10 21 Lithuania) – *Paplūdimių dumblių sankaupų erdvinio paplitimo tyrimai panaudojant bepilotės skraidykles*
6. MRI Thursday seminar (oral, 2022 04 28 Lithuania). *Spatial distribution and coverage of beach wrack using drone imagery*
7. Living Planet Symposium: (poster, 2022 05 23-27, Germany, Bonn) *Beach and shallow sea wrack spatial distribution detection using unmanned aerial vehicles*
8. Fourth ICES PICES Early Career Scientist Conference – (poster, 2022 07 17 – 21, Canada, Newfoundland) *Beach and shallow sea wrack spatial distribution detection using unmanned aerial vehicles*
9. Jūros ir krantų tyrimai (oral, 2023 04 19 – 04 21 Lithuania) – *Drono vaizdai išmetamų pakrantėje dumblių sankaupų įvertinimui*

# 2

---

## MATERIALS AND METHODS

### 2.1. Study sites

The research was carried out across three distinct aquatic environments in Lithuania: Plateliai Lake, four coastal beaches, and 42 Lithuanian lakes and reservoirs. Each site was selected for its specific features, contributing to the overall study objectives (Figure 1).

Plateliai Lake (Paper II) was chosen as the test site for detecting macrophytes using Sentinel-2 satellite imagery, with UAV images serving as validation. The lake was chosen for its well-studied macrophyte community and its management strategy of lake water quality maintenance, which provided a useful test environment for evaluating the accuracy of the macrophyte detection method. Covering 1,200 ha, Plateliai Lake has an average depth of 10.5 m and reaches a maximum depth of 49.1 m, is classified as an oligo-mesotrophic lake (with  $2.4 \pm 1.8 \mu\text{g}$  chlorophyll-a l<sup>-1</sup> in the period 2001–2010) that is located in the western part of Lithuania and is part of the Žemaitija National Park. The common reed beds are unevenly distributed along the coastline of the lake, with a higher concentration found in the eastern part (Sinkevičienė et al., 2005). From 2017 to 2019, the Žemaitija National Park directory performed mowing operations in seven areas within the littoral zone of the lake. For this study, eight areas of interest (AOIs) were selected, seven aligning with mowing areas and one serving as a reference point where mowing was not performed (Figure 1). The first seven AOIs

## 2. Materials and methods

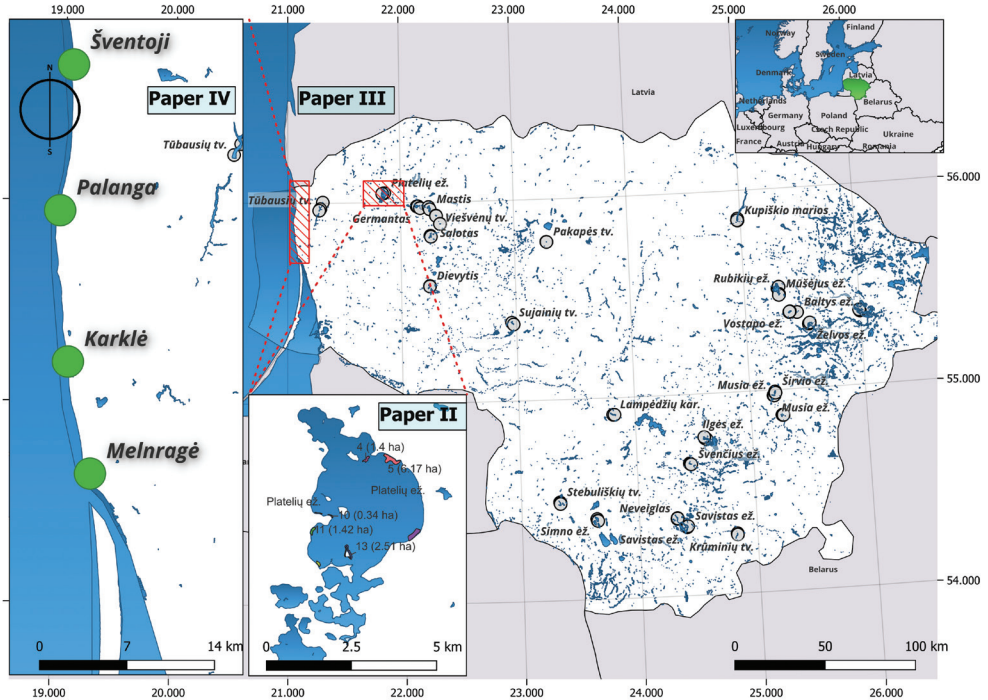


Figure 1. Locations of study sites in Lithuania. Plateliai Lake, utilized for macrophyte detection and mowing zone evaluation; four coastal beaches — Melnragė, Karklė, Palanga, and Šventoji—for beach wrack studies; and the 42 lakes and reservoirs chosen for SD assessment using UAV multispectral imaging.

were numbered based on the technical specification document of the reed mowing (Technical specification of Plateliai Lake reed mowing, 2017). These AOIs, covering a combined area of 18 ha (1.5% of the total lake area), were primarily inhabited by common reeds with small stands of lakeshore bulrushes (*Schoenoplectus lacustris*) in some areas.

A set of lakes and reservoirs in Lithuania (Paper III) were selected to measure SD using a UAV multispectral camera. The water bodies were chosen for their diversity in size, surrounding vegetation and proportion of optically active in-water components – turbidity, chlorophyll-a (Chl-a) and colored dissolved organic matter (CDOM), which provided a representative amount of the diverse aquatic environments in Lithuania.

Coastal Beaches (Paper IV) with the set of four areas of interest (AOIs) along the continental Lithuanian coastline selected for monitoring BW from April 2021 to May 2022. These AOIs included Melnragė, Karklė, Palanga, and Šventoji Beaches. Each

## 2. Materials and methods

site presents distinct features such as proximity to urban areas, shipping and tourism activities, and the presence of coastal features such as dunes. For example, Melnragė is located near The Port of Klaipėda, which is heavily used for shipping and is also close to Klaipėda – the largest city in the western Lithuanian region, with a connection to the Curonian Lagoon via a port. Karklė beach is characterized by the presence of boulders, which support the growth of algae, and is located in a more rural area, surrounded by forest (Jarmalavičius et al., 2011). Palanga Beach is a popular tourist destination during the summer season and is cleaned regularly by the municipality, which removes larger trash from the sand and BW. Šventoji is a small fishery port, with the widest sandy beach of all AOIs, measuring around 107 m, as well as an outflow of River Šventoji. Dunes are present in all of the studied AOIs and the AOI of Karklė also has clay cliffs. The total length of beach in the study area was approximately 39 km and the entire coast is exposed to the Baltic Sea.

The BW along the Lithuanian Baltic coast is primarily composed of perennial red algae, predominantly *Furcellaria lumbricalis* and *Vertebrata fucoides*, which account for 85% of the overall BW biomass. In comparison, filamentous green algae, *Cladophora glomerata* and *C. rupestris*, and brown algae, primarily *Fucus vesiculosus* and *Sphacelaria arctica*, make up 14% and 1% of the BW biomass, respectively (Kalvaitienė et al., 2023). Red algae species are widespread on rocky substrates at depths ranging from 3 to 16 m. In contrast, filamentous green algae are densely populated on stones in more shallow (< 6 m) waters. *Sphacelaria arctica*, a filamentous brown algae species, typically occupies harder substrates at greater depths (> 9 m). Overgrowths of the genera *Pylaiella* and *Ectocarpus* are observed on both natural and artificial substrates, such as boulders and piers, within a depth range of 1 to 5 m (Bučas et al., 2009). Notably, *Fucus vesiculosus* populations have not been detected on the hard-bottom environments of the south-eastern Baltic Sea coast, implying potential transportation from other, more sheltered coastal regions.

### 2.2. Data collection

A comprehensive remote sensing approach was employed through the integration of *in situ* measurements, UAV imagery, and satellite data, where *in situ* measurements provided ground truth validation, UAVs captured high-resolution spatial details, and satellites offered extensive temporal coverage. Some data acquisition or processing steps are similar among studies II through IV (Figure 2). More details are provided in specific sections within each published paper, which extend beyond data acquisition, data processing and analysis. This approach not only enhanced the spatial and temporal resolution of the environmental assessments but also increased the validity of the findings, as detailed in the individual papers.

## 2. Materials and methods

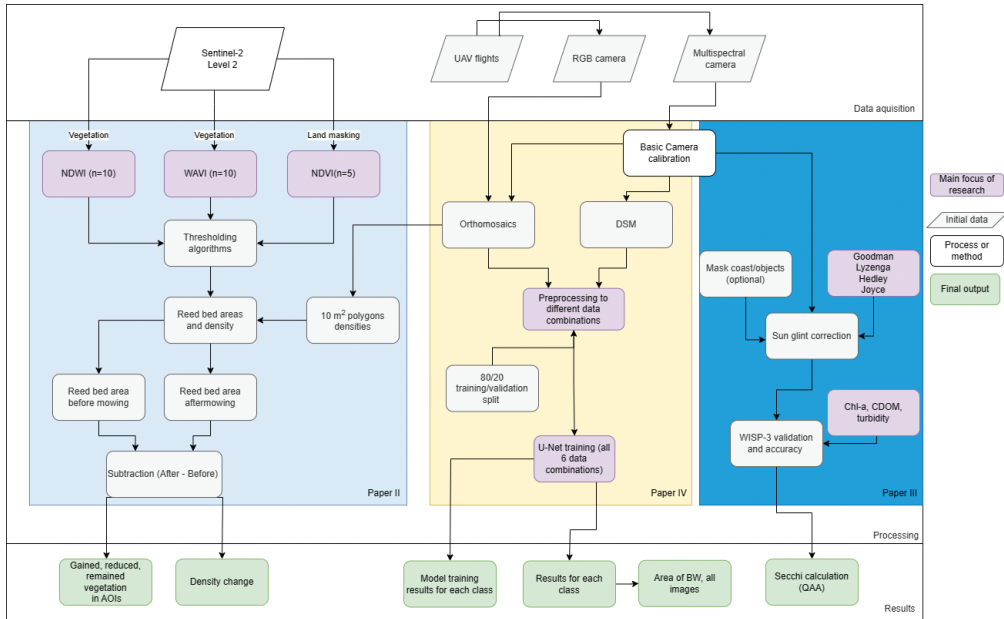


Figure 2. Simplified workflow of studies (for Papers II-IV).

### 2.2.1. Unmanned aerial vehicles data acquisition techniques

The methodological framework of the first study (Paper I) is based on a group of scientists, created during the European Cooperation in Science and Technology (COST) Action, Harmonization of UAS techniques for agricultural and natural ecosystems monitoring (HARMONIOUS) project (Action CA16219, 2017). Within the Vegetation Monitoring working group meeting, experts based on their best practices identified common parameters that were tested in UAV vegetation studies. The objective was to summarize insights on how UAVs have been previously deployed in ecological research, focusing on the heterogeneity of vegetation, survey methodologies, and data processing techniques (Figure 3). To support the methodology further, a review of existing literature was undertaken, utilizing the Scopus database as the primary resource. This review process was structured to cover studies applicable to each of the identified parameters.

In the rest of the three studies (II–IV), UAVs paired with high-resolution cameras were employed to capture images, which served to validate mapped data and enhance the understanding of the target environments. The primary objective of the image analysis, while exhibiting underlying similarities in the methodological application of UAVs across the studies, is distinguished by the selection of different UAV and



## 2. Materials and methods

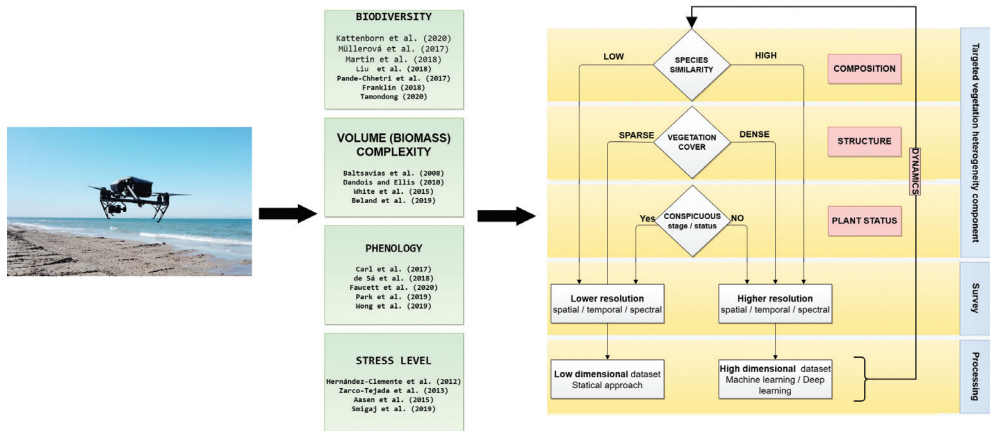


Figure 3. Graphical summary of reviewed parameters and processes (reprinted from Paper I).

camera models, flight protocols — including the altitude of flights, frequency of image captures, and image overlap, adhering to optimal weather conditions: wind gusts below 10 m/s, absence of precipitation, and temperatures exceeding 0°C, as colder temperatures might reduce battery longevity and thus flight duration. Different studies also employed varied software tools, however, all mosaicking software in the back end used the structure from motion algorithm, resulting in the production of orthophotos. Flight planning was done using the PIX4Dcapture app, maintaining a consistent flight altitude of 40–60 m with a 75% overlap between images. An additional transect was integrated into the flight plan, aiming to decrease distortions in the core area of the mosaics.

In the reed bed changes study (Paper II), UAV images were captured using a DJI Phantom 4 multi-rotor UAV with a 20-megapixel RGB camera (Table 1). The flight height was set at 40 m, with a 75% overlap between images to generate detailed orthophotos (ground sampling distance 2 cm). The images were used to validate reed beds mapped from Sentinel-2/MSI data (see section 2.2.2.). Ground control points (GCPs) were used to georeference orthophotos, thereby achieving more accurate results.

For the SD (Paper III) analysis, a DJI Inspire 2 multirotor UAV with a RedEdge-MX camera was used, which had five spectral bands: Blue (475 nm ± 16 nm), Green (560 nm ± 13 nm), Red (668 nm ± 8 nm), Red edge (717 nm ± 6 nm), and Near-infrared (842 nm ± 28 nm). Each band has a resolution of 1.2 megapixels and offers a 47.2° horizontal and 34.4° vertical field of view. The UAV images were acquired at an altitude of 60 m using a function that captured images every 3 seconds, allowing for a ground sampling distance of around 3 cm.

## 2. Materials and methods

*Table 1.* Drone images for validation with corresponding reed-cutting areas derived from S2 images.

Sentinel-2/MSI	UAV dates and AOI	Mowing status
2016 May 10	-	Land masking
2016 Jun 19	-	Before mowing
2016 Aug 28	-	Before mowing
2017 May 5	-	Land masking
2017 Jul 14	-	Before mowing
2017 Aug 31	-	After mowing
2018 May 10	-	Land masking
2018 Jul 17	2018 Jul 10 (AOI:5, reference); 18(AOI:4,5); 19(AOI:1, 10, 11)	Before mowing
2018 Sep 20	-	After mowing
2019 Apr 23	-	Land masking
2019 Jul 12	-	Before mowing
2019 Aug 26	2019 Aug 12(AOI: 10, 11, reference); 20(AOI:5, 9)	After mowing
2020 Apr 20	-	Land masking
2020 Jul 18	-	No mowing
2020 Sep 1	-	No mowing
2020 Sep 6	-	No mowing

For the BW study (Paper IV), the flights were planned roughly every 10 days at AOIs with BW presence. If conditions were unsuitable, flights were rescheduled to the closest favorable day, preferably soon after sunrise (between 6 am and 10 am local time) to mitigate sunlight reflections on water and to ensure minimal human presence on the beaches, aligning with European regulations (EU 2019/947 and 2019/945, 2022) which restrict flight over crowds. The multispectral camera yielded images with a ground sampling distance of roughly 3.5 cm/pixel. In contrast, RGB camera images had a resolution of about 1.5 cm/pixel. Mosaics varied from 0.20 to 1.7 km of beach length, depending on the BW size. For U-Net modeling, 29 multispectral images were assembled into mosaics and subsequently segmented into 163 tiles, each measuring 5000 x 5000 pixels. Of 75 total flight missions, the multispectral count included 7 in Melnragė, 4 in Karklė, 3 in Palanga, and 15 in Šventoji, while the remainder employed RGB imaging used solely for digital elevation models (see 2.2.3).

Both Zenmuse X5S and RedEdge-MX camera selections were due to their ability to generate image mosaics and digital surface models as well as digital terrain models, crucial for calculating BW heights. The produced mosaics were georeferenced to a Lithuanian orthophoto map of 0.5 m spatial precision using QGIS (QGIS.org, 2022). During each georeferencing instance, a minimum of three ground control points, representing static objects, ideally located at the UAV orthophoto's corners, were identified.

## 2. Materials and methods

### 2.2.2. Remote sensing and Earth observation data

Satellite data used in this study were sourced from the Sentinel-2A and Sentinel-2B satellites (S2/MSI). The S2/MSI delivers data with varying spatial resolutions across its 12 bands at 10 m (red 664 nm, green 559 nm, blue 492 nm, NIR 832 nm), 20 m (vegetation red edge 704, 740, 782 nm, narrow NIR 864 nm, SWIR 1613, 2202 nm) and 60 m (coastal aerosol 442 nm, water vapor 945 nm, cirrus 1373 nm) depending on bands used. In the spectral dimension, it spans from 440 nm to 2202 nm. For the area under observation, the Plateliai Lake, the S2/MSI satellites provide a revisit time of every three days, ensuring frequent data acquisition for robust analysis.

In total, sixteen S2/MSI images were utilized in the reed bed mowing evaluation study. These images were strategically chosen to align with the commencement of the reed mowing period, specifically, between the 20th of July and the 10th of September.

An essential aspect of the data selection process was to ensure minimal cloud coverage, as clouds and their shadows can significantly impact the data quality. For most areas of interest (AOIs), these criteria were satisfactorily met, except for two cases. In AOI 5, the image corresponding to the mowing date (6th September 2020) contained cloud shadows, prompting the use of an earlier image from the 1st of September 2020. Similarly, the image from the 19th of June 2016 had a cloud shadow obscuring half of AOI 13. However, since no cloud-free images were available during the relevant period, the image was used, excluding AOI 13 from the analysis. Such considerations underscore the practical challenges in satellite remote sensing and the adaptive strategies required to maintain data quality (Turner et al., 2015).

A significant portion of the Sentinel-2/MSI products used in the study had already undergone processing to Level-2A data. This level of processing includes atmospheric correction by the Sen2Cor processor, which is crucial to derive accurate surface reflectance values. The Sen2Cor processor transforms top-of-atmosphere Level-1C images into atmospherically corrected Level-2A surface reflectance images, along with maps and quality indicators. Processed data is freely available for download on the Copernicus Open Access Hub, a dedicated platform that hosts Earth observation datasets. However, for images before September 2017, Level-2A data were not readily available. To fill this gap, the Sen2Cor processor was applied to Level-1C images using SNAP software (version 8), ensuring a consistent level of data processing across all used datasets.

### 2.2.3. Field sampling

Field measures for the SD study (Paper III) were concurrently executed to the UAV imaging. Measurements of SD were taken using a 20 cm white Secchi disk, a globally recognized tool for determining water transparency in diverse aquatic environments

## 2. Materials and methods

(Lin et al., 2022; Stephens et al., 2015). This study was executed from May to September from 2021 to 2022.

Alongside SD, water samples were collected for further analysis of Coloured Dissolved Organic Matter (CDOM), Chlorophyll-a (Chl-a), and turbidity. A dataset consisting of 43 paired *in situ* SD measurements and UAV images was assembled for subsequent analysis.

The process of quantifying Chl-a concentration involved filtering water samples through glass fiber GF/F filters with a nominal pore size of 0.7  $\mu\text{m}$ , followed by extraction into 90% acetone. The concentration of photosynthetic pigments was then determined spectrophotometrically, and estimated via the trichromatic method (Jeffrey and Humphrey, 1975, Parsons et al., 1984). CDOM concentration was measured in water samples filtered through 0.22  $\mu\text{m}$  membrane filters prior to spectrophotometric analysis. The CDOM absorption coefficient at 440 nm ( $g_{440}$ ) was determined following the methodology detailed by Kirk (2010). A SHIMADZU UV-2600 spectrophotometer was used to analyze both Chl-a and CDOM.

Turbidity, an important factor influencing water clarity, was quantified using a turbidity meter (Eutech Instruments TN-100, Landsmeer, The Netherlands), which provided readings in nephelometric turbidity units. The device is equipped with a near-infrared light-emitting diode at 850 nm and measures light scatter at a 90° angle, in compliance with the International Standard Organisation (ISO) 7027. Using this integrated approach to field sampling, which combines both optical and chemical assessment, was crucial for validating the data of the studied water bodies.

In the field, remote sensing reflectance ( $R_{rs}$ ) was obtained within the spectral range of 400–800 nm. This was achieved by conducting simultaneous measurements of downwelling irradiance, upwelling radiance, and downwelling radiance, employing the WISP-3 spectroradiometer (Hommersom et al., 2012). The relationship between these parameters is given by equation 1.

$$R_{rs} = \frac{L_u - \rho L_d}{E_d} . \quad (\text{eq. 1})$$

In this equation,  $L_u$  denotes the upwelling radiance,  $L_d$  signifies the downwelling radiance, and  $E_d$  represents the downwelling irradiance. The term  $\rho$  stands for a water surface reflectance factor, set to a value of 0.028 in this study (Hommersom et al., 2012).

After these measurements, they were utilized to validate the corresponding wavelengths derived from UAV observations of water surface reflectance (see statistics 2.3.4). Given that the WISP-3 spectroradiometer is a hyper-spectrometer, it captures data across a broad range of narrowly spaced wavelengths. However, only the central

## 2. Materials and methods

wavelengths corresponding to the Rededge MX camera were considered in this study, excluding the NIR band. The wavelengths used were 475 nm, 560 nm, 668 nm, and 717 nm.

In addition to the aforementioned field measurements, *in situ* sampling was also conducted for the assessment of BW heights (Paper IV). This process involved a series of 16 field missions, carried out concurrently with UAV flights at AOIs. During these missions, the height of BW deposits was measured using a plastic ruler, ensuring minimal disturbance to the underlying sand layer. Measurements were taken at approximately every 10 m along a transect line that spanned the entire width of the BW deposit. This transect line (Figure 4) included three key sampling points: the start of the BW deposit (closest to the water), a middle point and the end of the BW deposit (furthest from the water).

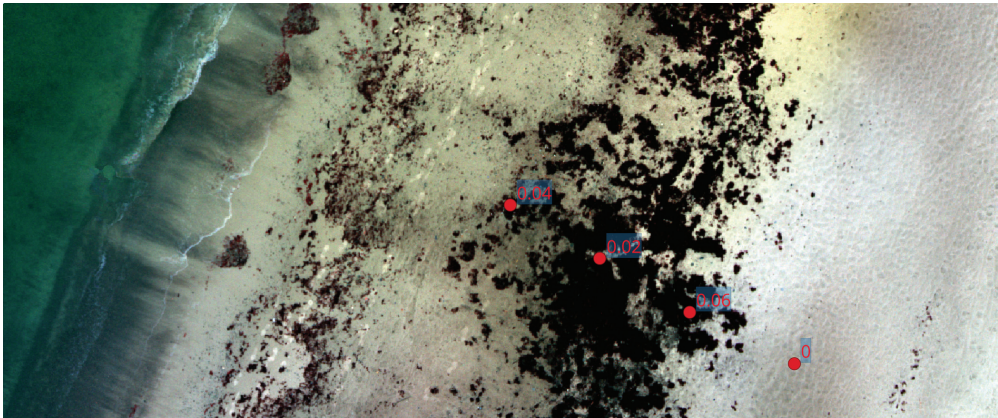


Figure 4. Measured points along selected beach wrack (BW) transect. Close to water, in the middle, at the edge of the BW and at one point in the sand for reference.

A total of 177 measurement points were recorded across the four study sites, both within the areas of BW deposits and in reference areas without BW, where only coordinates were measured and height considered as 0 cm. These *in situ* height measurements were essential for validating the UAV-derived estimates of BW heights.

### 2.3. Image processing

The reed beds (Paper II) were manually delineated from the UAV orthophotos and reed density in percentages was evaluated visually using 10 m<sup>2</sup> polygons, matching the resampled S2/MSI pixel size. The shoreline boundary was defined using a lake polygon map obtained from the Lithuanian geoportal database, with islands such as

## 2. Materials and methods

Pilies, Veršio, Briedsalė, Pliksalė, and Gaidsalė removed. Moreover, a 10 m buffer zone was established from the shoreline towards the lake to prevent the misidentification of trees as reeds. To ensure consistent spatial resolution across all bands for ease of analysis, all S2/MSI images were resampled to a final spatial resolution of 10 m. This process aligns the data to a uniform grid, which simplifies subsequent image processing and analysis steps.

The most important test in this study was the application of binary classification methods for indices to classify and evaluate the changes in reed bed areas using Earth observation data. The primary indices used for the classification were the Water Adjusted Vegetation Index (WAVI, eq. 1) and the Normalized Difference Water Index (NDWI, eq. 2). These indices were automatically classified into water and reeds using seven binary thresholding algorithms, selected out of sixteen available algorithms in Fiji software (Schindelin et al., 2012). The thresholding algorithms employed include Otsu (Otsu, 1979), Yen (Yen et al., 1995), RenyiEntropy (Kapur et al., 1985), Triangle (Zack et al., 1977), Mean, and Iso (Ridler and Calvard, 1978). The thresholding algorithms were grouped based on the information exploited from the image histogram as per the classification by Sezgin & Sankur (2004): Otsu, Mean, and Iso are defined as clustering thresholding algorithms, Yen and RenyiEntropy as entropy thresholding algorithms, and Triangle as a geometric thresholding algorithm.

$$\text{WAVI} = (1 + L) \frac{RrsNIR - RrsBlue}{RrsNIR + RrsBlue + L} \quad (\text{eq. 2})$$

$$\text{NDWI} = \frac{RrsGreen - RrsNIR}{RrsGreen + RrsNIR} \quad (\text{eq. 3})$$

In the SD estimation study (Paper III), the Quasi-Analytical Algorithm (QAA) developed by Lee et al. (2015) was tested. This semi-analytical method stands out for its capability to estimate SD without the need for recalibration with *in situ* data, a significant advancement over traditional empirical approaches. The QAA is based on a mechanistic model that comprehensively accounts for light attenuation, scattering, and reflection within the water column, as well as the specific properties of the Secchi disk. Central to this algorithm is the total absorption coefficient ( $a$ ) and the total backscattering coefficient ( $b_b$ ), from which the diffuse attenuation coefficient ( $K_d$ ) is derived (eq. 4). This coefficient,  $K_d$ , is integral to the SD calculation formula, involving the minimum value of  $K_d$  selected from blue, green, and red bands, and the minimum above-surface  $R_{rs}$  of the band with the lowest  $K_d$  value. The QAA method (eq. 5), therefore, offers a robust and adaptable framework for monitoring SD across diverse aquatic environments, enhancing the utility of imagery in water clarity assess-

## 2. Materials and methods

ments. The approach's precision is further refined by accounting for the solar zenith angle, computed using the Python library *pytz* (Bishop, 2002), and by selecting the appropriate reference wavelength based on the specific characteristics of the observed water body.

$$K_T\_K_d = \frac{1.04*(1+5.4u)^{0.5}}{1/\left(1-\frac{\sin(\theta)^2}{Rl^2}\right)^{0.5}} \quad (\text{eq. 4})$$

$$SD = \frac{1}{kt_{kd}*minKd} \ln\left(\frac{0.14-minRrs}{0.013}\right) \quad (\text{eq. 5})$$

Before implementing the QAA for SD calculations, a comprehensive preprocessing of UAV images was essential to ensure data accuracy. This process began with image masking and sun glint correction (Figure 5). Initially, four water bodies were excluded from the analysis due to factors like excessive cloud glint, proximity to the shore, and the presence of emerged macrophytes, which could affect reflectance measurements. For instance, in the case of Krūminiu Reservoir, the survey conducted late in the day resulted in shadows covering half the area; the unshaded portion was isolated for analysis using binary thresholding (Walt et. al., 2014). After these exclusions, 39 water bodies remained for the study. Key to this preprocessing step was the application of the NDWI, calculated to differentiate between water and non-water pixels. This index was further processed using the Yen thresholding method to mask non-water pixels as NaN values, an approach that was also applied to the NIR band for identifying and masking areas affected by sun glint. In cases where water waves generated significant sun glint, correction algorithms developed by Hedley et al. (2005), Goodman et al. (2008), Lyzenga et al. (2006), and Joyce (2005) were tested. These algorithms consider water surface reflectance as a linear combination of water reflectance and sun glint reflectance, with models using examples on image parts where pixels are unaffected by sun glint. The applied method varied based on NIR values, with adjustments made for the different spectral bands.

## 2. Materials and methods

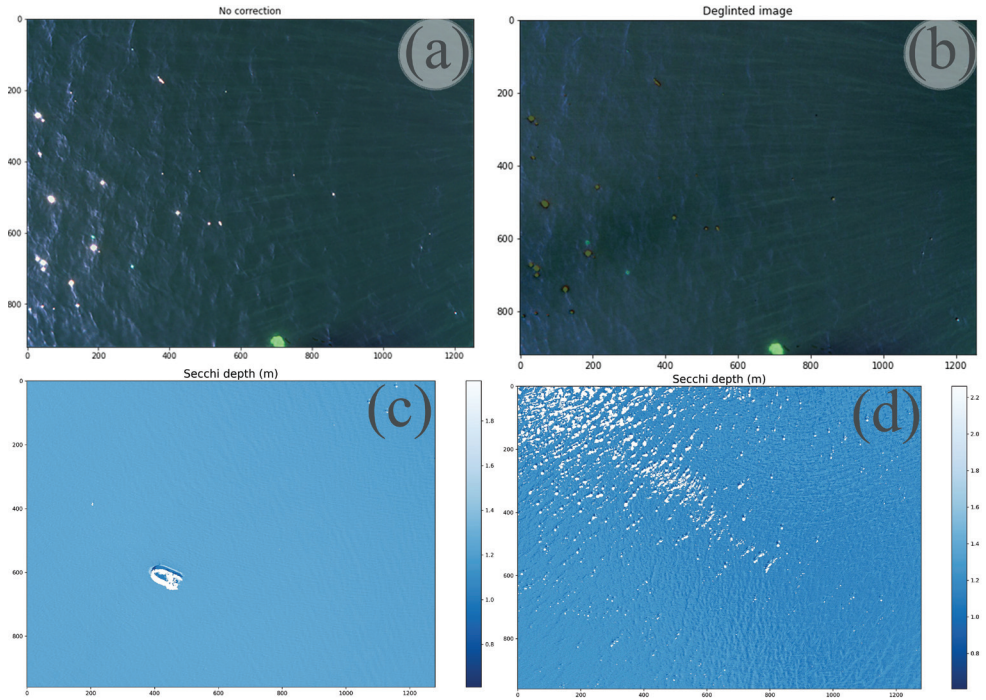


*Figure 5.* (a) RGB image before the sun glint correction; (b) deglinted RGB image using Hedley’s method; (c) boat removed from normalized difference water index using Yen’s threshold, and recalculated to SD; (d) threshold removed sun glint area from NDWI image, recalculated to Secchi depth (reprinted from Paper II).

The data processing for U-Net model training (Paper IV) was conducted on a computer equipped with computational resources of 32 GB RAM, Intel Core i7 8th gen CPU and NVIDIA GTX 1070 GPU. To manage memory constraints typical in deep learning, high-resolution UAV imagery was segmented into smaller tiles of  $256 \times 256$  pixels, preserving the visibility of objects of interest. From the 163 tiles generated, 17 were selected via expert judgment for the training set, ensuring representation of each acquisition date and AOI. Six different multispectral data combinations, including RGB bands, RGB with heights, and various spectral indices like Normalized Difference Vegetation Index (NDVI), NDWI, and Normalized Difference Red Edge Index (NDRE, eq. 5), were used to train the models, that were preprocessed using Python with GDAL 3.4.3 (GDAL/OGR contributors, 2022). These indices were chosen for their spectral sensitivities for BW identification: NDVI (Karlsen et al., 2018; Wang et al., 2021), NDWI (Marusig et al., 2020; Zhang et al., 2018), NDRE (Sharifi and Felegari, 2023). Data augmentation, involving random rotations and flips, was implemented on one dataset incorporating all spectral bands and heights to explore spatial location bias.



## 2. Materials and methods

$$\text{NDRE} = \frac{RrsNIR - RrRedEdge}{RrsNIR + RrsRedEdge} \quad (\text{eq. 6})$$

The UAV-based BW height estimation involved processing digital surface models and digital terrain models (DTM) using the Geospatial Data Abstraction Library (GDAL) to accurately determine the height of the BW deposits. The collection of this data was critical in enhancing the accuracy of UAV-based BW height estimations and in validating remote sensing methodologies applied in the study.

The U-Net architecture (Figure 6), originally introduced by Ronneberger et al. (2015), was adapted for this study, considering its effectiveness in handling smaller datasets and precision in complex image segmentation tasks. The architecture was modified for multispectral images with added layers, padding, and a dropout of 20% as a regularization technique (Srivastava et al., 2014). Model training utilized Python 3.9 and Keras 2.3.1 (Chollet, 2015), with TensorFlow 2.1.0 (Abadi et al., 2016) for custom operations. The training, set for 100 epochs, employed an early stopping mechanism to prevent overfitting, which was halting if no improvement occurred after 6 consecutive epochs. The loss function was a combination of Dice loss (Milletari et al., 2016) and focal loss (Lin et al., 2017), balancing class overlaps and focusing on poorly trained pixels.

The labeling facilitates the U-Net convolutional neural network model's differentiation of BW from other classes like sand or water. This process, crucial for evaluating the model's effectiveness in BW identification, involved using the "Labkit" plugin in ImageJ FIJI for supervised machine learning-assisted labeling, with manual review and corrections by experts. These labeled images were processed in ImageJ and exported as TIFF files. Masking focused on identifying BW accumulations, sometimes roughly in cases of small, dispersed BW. Multispectral images were composed into three-band TIFF images using green, blue, and near-infrared bands for visual labeling. Pixels in these images were categorized into five classes: 0 for BW, 1 for potential underwater beach wrack, 2 for water, 3 for sand (including pebbles and rocks), and 4 for other objects, with the background labeled as "other". Notably, the near-infrared band was instrumental in distinguishing between small rocks and BW, a task difficult in RGB images (Arzt et al., 2022).

The image segmentation workflow started with labeled TIFFs for pre-processed images. In the end the Smoothly-Blend-Image-Patches (Vooban, 2018) package was used to eliminate edge effects in patching images.

## 2. Materials and methods

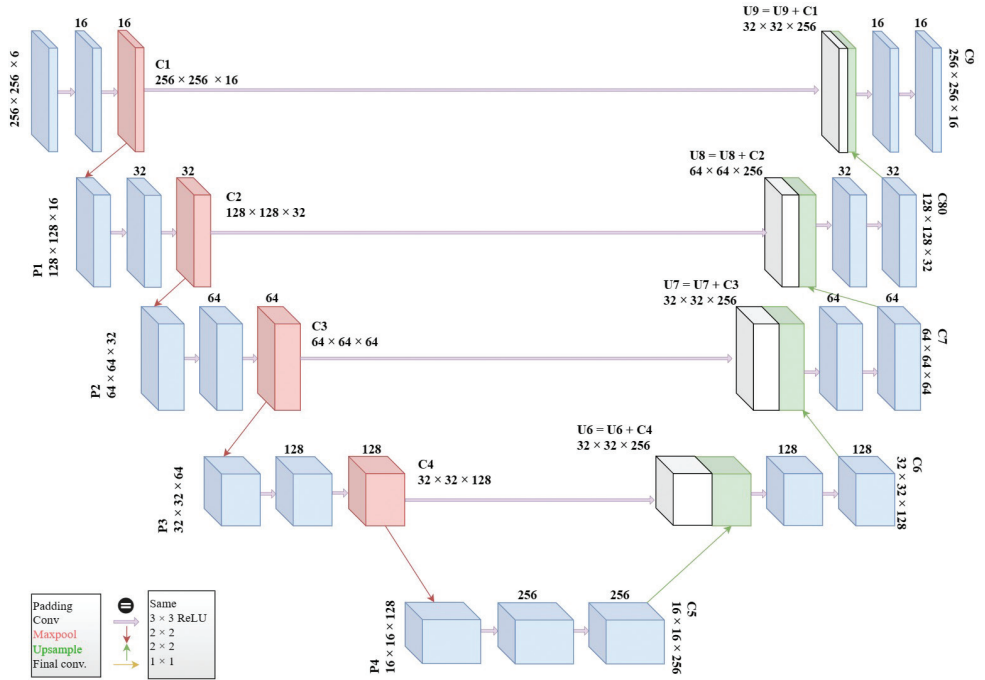


Figure 6. U-NET architecture used (modified from Ronneberger et al., 2015)

### 2.4. Statistical methods and validation

The statistical approach applied involves a combination of traditional statistical methods and spatial image segmentation and classification techniques (Paper II and III).

The most suitable index along with a threshold was selected after post validation with 12 UAV orthophotos (see 2.2.1. UAV Techniques, Table 1). Polygons of 10 m<sup>2</sup> from orthophotos were classified as vegetation or water, and compared to overlapping pixels of reed beds derived from satellite data. The accuracy of the satellite-derived reed beds was assessed using a confusion matrix (Ting, 2017), with the Area Under the Curve (AUC; Egan, 1975) alongside sensitivity and specificity calculated to ascertain the most accurate approach for reed bed area mapping utilizing satellite imagery. Thresholding algorithms, used for the masking of water and leaving aquatic vegetation, achieving a sensitivity and specificity value equal to or higher than 0.5 were deemed suitable, indicating a correct classification for 50% of the data. After the rejection of unsuitable thresholding algorithms, the t-test with the post hoc Bonferroni correction was applied to ascertain differences among the mean AUC values of different thresholding algorithms based on indices (WAVI or NDWI).

## 2. Materials and methods

Further validation was carried out on the thresholding algorithm's reliability at certain vegetation density using the confusion matrix of the best performing Sentinel-2/MSI index with the thresholding algorithm. Dunnett's post hoc test was utilized to compare the mean AUC of the group (each vegetation density) to a control group (AUC value of 0.5), representing poor discrimination between classes (Mandrekar, 2010).

Lastly, the estimated density values of reed beds in AOIs were retrieved from Sentinel-2/MSI data using WAVI, and validated with the density visually determined in percentages from UAV orthophotos. A linear regression was derived from WAVI values, averaged over each density class of vegetation, which was then utilized to convert WAVI values to extrapolate density values.

The investigation of SD accuracy (Paper III) leveraged generalized additive models to explore the relationships between the discrepancies in modeled and *in situ* SD values against a specified set of independent variables: CDOM, Chl-a, turbidity, and solar zenith angle. Generalized additive models were selected due to their adeptness at modeling nonlinear associations while accommodating interactions among predictors. The significance and relative importance of the independent variables were defined through F and p-values, with a p-value below 0.05 denoting a statistically significant relationship. The analysis was executed utilizing the R programming language, employing the mgcv package (Wood, 2023) library for statistical parameter estimation and the ggplot2 (Wickham, 2016) library for data visualization.

The accuracy of these methods, as well as for reflectance validation, was evaluated using bias, while the root-mean-square deviation (RMSD) was used as an indicator of the QAA model's precision, and the Pearson's correlation coefficient ( $r$ ) described the relationship strength between the model's output and the real data values.

In evaluating the model's performance of BW (Paper IV), during its training phase, the data was divided into two subsets: 80% was allocated for training and 20% for validation, a standard approach to prevent overfitting and assess the model's generalization capacity. This division ensured that the model had a sufficiently large dataset for learning essential features, while also providing a distinct data set for performance evaluation. A separate validation set encompassing all tiles was utilized to test the model's generalization to new data. The model's performance was evaluated using several metrics: precision, recall, F1 score, and Intersection over Union (IoU). Precision is the ratio of correctly predicted positive values to the total predicted positives, while recall is the fraction of correctly predicted positive values to the total actual positive values. The F1 score merges precision and recall providing a balanced performance metric. IoU, also known as the Jaccard Index, goes beyond pixel accuracy to evaluate the resemblance between predicted and ground truth labels. The effectiveness of the chosen models was assessed on test data by comparing the IoU metric across different AOIs and classes. While no single IoU threshold is universally applicable, a threshold of 0.5 is typically employed for accurate segmentation. In

## 2. Materials and methods

this study, IoU values above 0.7 were deemed high, those between 0.5 and 0.7 were considered moderate, and values below 0.5 were categorized as low.

To our knowledge, only two studies (by Pan et al., 2021 and Karstens et al., 2022) have previously been conducted in the context of UAVs monitoring BW. These studies employed object-based image analysis and achieved a high producer accuracy of over 80% in classification. In contrast, this research primarily used the IoU metric, which is considered superior, particularly when used alongside other measures like the F1 score. The IoU metric is more reliable because it considers the entire area, unlike methods that use random samples of points or polygons, as suggested by Müller (2022). However, a significant drawback is that the labeling process for metrics that encompass an entire image is time-consuming, particularly for large datasets like the 29 mosaiced orthophotos in their study, but after the initial training, the U-Net model can be applied to new images, instead of labeling the entire image, the results can be adjusted and used as labels for further training rounds, thereby reducing labeling time and progressively enhancing the model's accuracy and generalizability.

Dunn's test was used for post-hoc pairwise comparisons of IoU between AOIs, with p-values adjusted using the Bonferroni correction to account for multiple comparisons. A one-way ANOVA test was conducted to compare averages. All statistical analyses were performed using numpy (Harris et al., 2020), scipy (Virtanen et al., 2020), statsmodels (Seabold and Perktold, 2010), and sklearn (Pedregosa et al., 2011) Python packages, with a significance level set at 0.05.

Lastly, *in situ* measured heights were compared with heights derived from UAV data using Pearson's correlation coefficient. The precision of these measurements was further quantified through Root Mean Square Errors (RMSE) and Mean Absolute Error (MAE) across separate AOIs.

Mean Absolute Percentage Deviation (MAPD) and RMSD are two measures of accuracy used to compare forecasting errors of different models for a particular dataset. RMSD is scale-dependent and always non-negative, with a value of 0 indicating a perfect fit to the data. MAPD, on the other hand, is a commonly used metric to measure the forecasting accuracy of a model, calculated as the average absolute percent difference between the actual and the forecasted values.

# 3

---

## RESULTS AND DISCUSSION

Each of the studies collectively contributes to a more comprehensive understanding of surface water quality assessment using remote sensing technologies. The first study (Paper I) gives a background on parameters and workflows used with UAVs in vegetation monitoring. The second study (Paper II) demonstrates how remote sensing can be used to track changes in aquatic vegetation, specifically common reed beds. This is important as the presence and health of such vegetation are key indicators of water quality, particularly in terms of nutrient levels. The third study (Paper III) complements this by using remote sensing to monitor water transparency, another critical water quality parameter, across a range of lakes with different trophic statuses. Finally, the fourth study (Paper IV) expands the scope of this approach to the coastal environment, using remote sensing to map the distribution and coverage of BW, an often overlooked aspect of the marine ecosystem that can impact water quality. Together, these studies highlight the potential of integrating remote sensing data with traditional field methods to enhance our capacity to monitor and manage water quality across diverse aquatic environments.

### **3.1. General guidance for vegetation monitoring using UAV**

The authors present a synthesized set of recommendations for applying UAVs in vegetation studies, addressing various ecological aspects. The Paper emphasizes the

### 3. Results and discussion

importance of selecting appropriate UAV technologies and methodologies tailored to four specific research objectives and vegetation characteristics. For species composition (see 3.1.1.), it suggests employing high spectral resolution and advanced image processing techniques to distinguish closely related species. In assessing ecosystem structure (see 3.1.2.), the use of LiDAR and high-resolution photogrammetric sensors is recommended to accurately gauge stand volume and complexity. The study highlights the utility of hyperspectral and thermal imagery in evaluating plant status (see 3.1.3.), particularly for tracking phenology and stress levels. For ecosystem dynamics (see 3.1.4.), such as disturbances and regeneration, the Paper advises on the strategic use of temporal resolution and frequent UAV surveys, focusing on change detection over time. The four parameters are linked to the abiotic factors influencing vegetation heterogeneity, involving suitable survey designs and data processing strategies (Tmušić et al., 2020). These recommendations are derived from a comprehensive analysis of existing literature, encompassing a range of ecological studies and applications, and aim to guide researchers in optimizing UAV use for diverse ecological assessments. The integration of these insights led to the development of an interactive workflow graph, accessible on the COST Harmonious website (see <https://www.costharmonious.eu/characterizing-vegetation-complexity-with-uas>), providing a versatile and simple tool for choosing the right research methods, especially for beginners with UAVs. This graph encapsulates the decision-making process in UAV vegetation surveys, emphasizing the importance of aligning research objectives and ecosystem characteristics with the appropriate UAV survey resolution across spatial, temporal, and spectral dimensions.

This research and its framework are beneficial for environmental scientists, ecologists, and natural resource managers who are engaged in the monitoring and management of vegetation, its quality, and ecosystem dynamics using remote sensing technologies, particularly UAVs. By synthesizing advanced UAV data acquisition techniques and integrating them with traditional field methods, the findings offer a methodology for comprehensive assessment of ecological parameters across diverse environments, from terrestrial ecosystems to aquatic and coastal areas. The insights from this review have been important in refining research methodologies in this thesis, notably in the analysis of macrophyte changes in Lake Plateliai (Paper II) where the suggestion was made for sparse vegetation cover UAV research, by choosing passive sensor together and high image overlap, and in mapping BW mosaics (Paper IV) with the same parameters.

#### 3.1.1 Species composition: highlighting biodiversity

Species composition in vegetation, influenced by spatio-temporal heterogeneity, varies across biogeographical zones and biomes (Lambers and Oliveira, 2019; Pug-

### 3. Results and discussion

naire and Valladares, 1999). UAV applications in this domain have demonstrated effectiveness in habitat mapping and monitoring for conservation, with methodological choices driven by targeted species or vegetation characteristics (Müllerová, 2019). Differentiation of species, particularly those with low spectral and structural divergence, necessitates varying levels of data resolution and complex algorithmic approaches (Müllerová et al., 2017a; Tamondong et al., 2020). The integration of shape, texture, and contextual information enhances species identification precision, especially when employing low-cost RGB cameras (Franklin, 2018; Gini et al., 2014; Pande-Chhetri et al., 2017). Object-based image analysis effectively mitigates the issues of ultra-high spatial resolution, though it requires careful selection of spatial resolution to manage spectral, morphological, and variability of proximity characteristics (Yuba et al., 2021). For complex vegetation, a combination of higher spectral/spatial/temporal resolution data, multiple data sources, 3D information, and advanced algorithms, including machine and deep learning, is crucial (Kattenborn et al., 2020; Liu et al., 2018; Martin et al., 2018; Michez et al., 2013).

#### 3.1.2 Ecosystem structure: measuring biomass, volume, and stand complexity

Ecosystem structure, a key driver of resource variability, requires detailed information on canopy structure, gaps, and spatial aggregation (Bagaram et al., 2018; Getzin et al., 2012; Kent et al., 2015). Most UAV studies primarily focus on forests, employing 3D data from various sensors to analyze stand complexity and quantify biomass (Cunliffe et al., 2016; Meneses et al., 2018; Swetnam et al., 2018). The use of LiDAR sensors is pivotal for generating digital terrain models and assessing structural layers, particularly in dense stands (Aguilar et al., 2019; Camarreta et al., 2020; Giannetti et al., 2018; Kašpar et al., 2021). Photogrammetric point clouds, derived through techniques like structure from motion, offer a lower-cost alternative for less dense stands, though they face challenges in dense or vertically complex canopies (Baltsavias et al., 2008; Dandois and Ellis, 2010; White et al., 2015; Westoby et al., 2012; Seifert et al., 2019). Combining data sources, such as adding spectral properties to LiDAR, and precise co-registration of different datasets, can enhance structural analysis (Lisein et al., 2013; Wallace et al., 2016).

#### 3.1.3 Plant status: phenology and plant stress

Plant status, encompassing phenological stages and physiological responses to stressors, benefits from the high spatial and temporal resolution of UAVs (D'Odorico et al., 2020; Zarco-Tejada et al., 2012). While extensive research exists in agricultural and forestry contexts, studies in species-rich natural ecosystems are limited (Banerjee

### 3. Results and discussion

et al., 2020; Zhang et al., 2017). Phenomena ranging from distinct spectral properties to more subtle indicators require sophisticated hyperspectral and thermal sensors coupled with complex modeling (Jones and Vaughan, 2010; Zarco-Tejada et al., 2012). Thermal imagery and leaf energy balance models are effective in early detection of stress, particularly in assessing drought and herbivory impacts (Gago et al., 2017; Smigaj et al., 2019; Zarco-Tejada et al., 2013). UAVs also enable detailed monitoring of phenological stages, offering the flexibility for timely data acquisition and high-resolution observation of individual plants (Carl et al., 2017; Müllerová et al., 2017b; Fawcett et al., 2021; Gago et al., 2020).

#### 3.1.4 Ecosystem dynamics: disturbances and regeneration

UAVs are instrumental in studying dynamic natural processes, particularly in aquatic plant composition, ecosystem structure, and plant status, by employing a change detection approach in repeated measurements (Berra et al., 2019; Fawcett et al., 2021; Park et al., 2019; Laslier et al., 2019; Michez et al., 2016). Their flexibility is crucial in responding to dramatic events like floods or significant water quality changes, thus facilitating immediate data collection while minimizing field survey risks (Novković et al., 2023). UAVs aid in understanding and early detection of disturbances within aquatic ecosystems, utilizing a range of sensors from sophisticated hyperspectral to consumer-grade cameras (Song & Park, 2020; de Castro et al., 2021; Chabot et al., 2017). The integration of UAV and satellite data can extend monitoring over larger areas, enhancing the assessment of outbreak patterns and guiding aquatic management strategies.

## 3.2. UAV and satellite analysis of reed bed dynamics in Plateliai Lake

The reed bed research applied seven distinct binary thresholding algorithms to classify the vegetation indices (NDWI and WAVI) and validated these results with high-resolution orthophotos from UAV surveys.

### 3.2.1 Effectiveness of automatic workflow and satellite image analysis

It is important to note that the utility of Earth observation data is constrained by the lack of high-resolution validation data. This limitation requires the use of supplementary methods for ground-truthing and enhancing the accuracy of interpretations made from satellite observations (Ozesmi and Bauer, 2002). Earth observation application along with other techniques, such as UAV-based surveys, can offset its resolution lim-



### 3. Results and discussion

itations. For instance, UAV data, with its higher resolution and flexibility, can serve as an effective validation tool for the macrophyte areas identified by Earth observation satellites, enhancing the overall accuracy of the vegetation analysis (Anderson and Gaston, 2013). Therefore, while acknowledging its limitations, the use of Earth observation data remains a useful approach in the context of long-term ecological monitoring and management strategies for aquatic environments.

The findings revealed that five thresholding algorithms, namely Triangle, Iso, Li, Mean for WAVI, and Triangle for NDWI, frequently misclassified water as a vegetated area in over half of the evaluated cases, indicating a specificity lower than 0.5 (Table 2). The remaining thresholding algorithms, for WAVI and NDWI – Otsu, RenyiEntropy, Yen and just for NDWI – Iso, Li, Mean, demonstrated a specificity rate higher than 0.5, accurately distinguishing water in more than 50% of the cases. However, four thresholding algorithms, Otsu, RenyiEntropy, Yen for WAVI, and Otsu for NDWI, exhibited a sensitivity lower than 0.5. Therefore, these algorithms were excluded from further analysis, narrowing the focus to five NDWI index thresholding algorithms: RenyiEntropy, Yen, Iso, Li, and Mean.

*Table 2.* Performance of reed bed classification using seven thresholding algorithms for WAVI (top) and NDWI (bottom). Performance was measured by mean ( $\pm$  standard deviation) area under the curve (AUC), sensitivity and specificity. The best performing threshold and index is marked with “\*” symbol.

Parameter	Otsu	Renyi Entropy	Yen	Triangle	Iso	Li	Mean
<b>WAVI</b>							
AUC all	0.67 $\pm$ 0.12	0.72 $\pm$ 0.14	0.70 $\pm$ 0.13	0.64 $\pm$ 0.19	0.59 $\pm$ 0.12	0.59 $\pm$ 0.13	0.65 $\pm$ 0.19
Sensitivity all	0.34 $\pm$ 0.23	0.45 $\pm$ 0.28	0.40 $\pm$ 0.25	0.95 $\pm$ 0.07	0.74 $\pm$ 0.35	0.77 $\pm$ 0.31	0.95 $\pm$ 0.07
Specificity all	1.00 $\pm$ 0.00	0.99 $\pm$ 0.02	0.99 $\pm$ 0.02	0.33 $\pm$ 0.43	0.45 $\pm$ 0.50	0.41 $\pm$ 0.51	0.34 $\pm$ 0.43
<b>NDWI</b>							
AUC all	0.71 $\pm$ 0.14	0.70 $\pm$ 0.14	0.76 $\pm$ 0.12*	0.75 $\pm$ 0.17	0.74 $\pm$ 0.17	0.73 $\pm$ 0.17	0.64 $\pm$ 0.16
Sensitivity all	0.42 $\pm$ 0.27	0.54 $\pm$ 0.29	0.53 $\pm$ 0.23	0.86 $\pm$ 0.19	0.83 $\pm$ 0.14	0.84 $\pm$ 0.13	0.70 $\pm$ 0.26
Specificity all	0.99 $\pm$ 0.02	0.97 $\pm$ 0.06	0.98 $\pm$ 0.06	0.43 $\pm$ 0.47	0.63 $\pm$ 0.42	0.65 $\pm$ 0.42	0.69 $\pm$ 0.44

Among these, the Yen thresholding algorithm for the NDWI index exhibited the highest AUC. Nevertheless, the Bonferroni post hoc correction revealed no statistically significant difference ( $p > 0.05$ ) when compared with the other thresholding

### 3. Results and discussion

algorithms. A marked difference was observed in the mean specificity of the Iso, Li, and Mean thresholding algorithms, which was about 30% lower than that achieved by RenyiEntropy and Yen. This discrepancy led to a considerable number of false positive values in one of the validation images (Figure 7, a). The mean AUC and specificity of RenyiEntropy were marginally lower than those of the Yen thresholding algorithm. Hence, the Yen thresholding algorithm was chosen as the final method for classifying vegetated areas and water. In contrast with the Li threshold, which showed an overestimation of reed beds in the open lake area, the Yen thresholding accurately depicted the distribution of reed beds without overestimation (Figure 7, b).

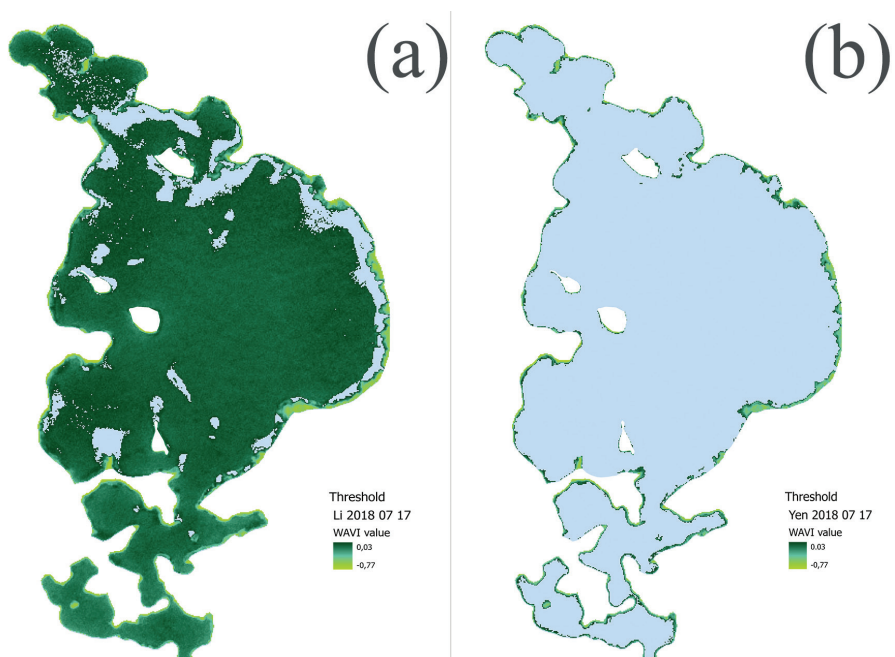


*Figure 7.* NDWI index (derived from Sentinel-2/MSI image acquired on 17 July 2018) with (a) Li threshold showing overestimation of reed beds in the open lake part, and (a) with Yen thresholding showing the distribution of reed beds with no overestimation (reprinted from Paper II).

Further analysis using the Dunnett post hoc test indicated higher AUC values for both high ( $df(43)=5.78$ ,  $p<0.05$ ) and medium ( $df(43)=4.30$ ,  $p<0.05$ ) vegetation densities compared to a baseline AUC value of 0.5 (i.e. no discrimination between classes), indicating the accuracy of 50-80 % and 31% for high and medium densities respectively. No significant differences were observed in low-density vegetation ( $df(43)=2.12$ ,  $p=0.1$ ) compared to the same baseline. The mean specificity for all vegetation densities was consistent and exceeded 0.97 (Figure 8). The mean sensi-

### 3. Results and discussion

tivity values for high and medium vegetation densities were reliable, being higher than 0.5. The sensitivity for low vegetation density was less than 0.5. Therefore, the delineation method used is recommended primarily for denser reed beds, potentially leading to a 15% underestimation.

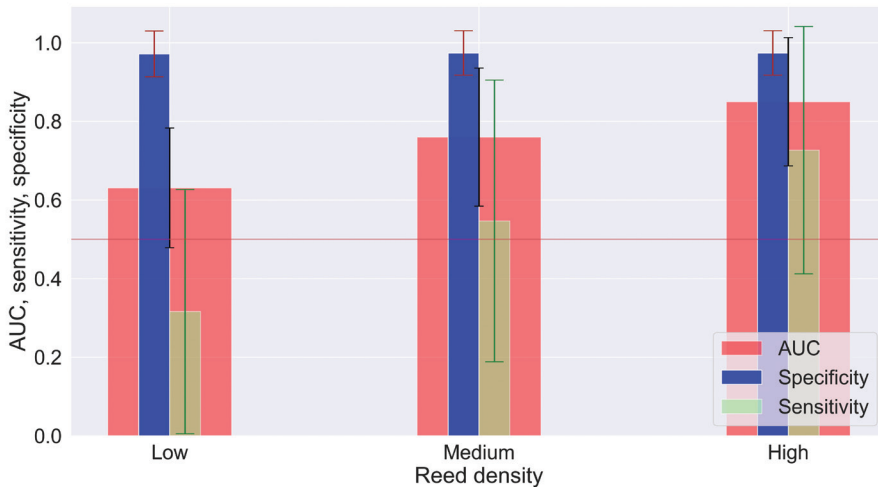


*Figure 8.* Mean area under the curve (AUC), sensitivity and specificity using Yen thresholding for NDWI, considering different densities of vegetation derived from the UAV data. The red line marks a value of 0.5 below which indicates random discrimination between classes (reprinted from Paper II).

When comparing vegetated regions identified in satellite imagery to those mapped using UAV orthophotos, a slight underestimation was noted. These minor discrepancies are likely attributable to the substantial difference in spatial resolution between the orthophotos, which are at 2 cm/pixel, and the S2/MSI with 10 m/pixel resolution (Bollas et al., 2021).

Another reason for the underestimation of vegetation area partly stemmed from including areas with low-density vegetation. To enhance the detection of vegetation, the incorporation of a short-wave infrared (SWIR) band is recommended (Oyama et al., 2015). The Modified Normalized Difference Water Index (MNDWI), incorporating SWIR, reportedly achieves better results than the NDWI (Xu, 2005) and outperforms the Sentinel-2 Water Index (SWI) in classification accuracy (Jiang et al., 2020). However, the SWIR band originally acquires data at 20 m resolution and, therefore needs resampling to 10 m resolution for consistency in the study of reeds, which may enhance misclassification.

### 3. Results and discussion

#### 3.2.2 Analysis of reed bed area changes and mowing impact

Significant decreases in vegetation area ( $\geq 0.1$  ha, which is equal to one S2/MSI pixel together with a buffer of surrounding pixels combined) were noted during mowing years (Figure 9). In the reference AOI, the reed bed area did not significantly change in 2016 and 2017, but the vegetated area showed a notable increase in the subsequent years of 2018, 2019, and 2020, exceeding 0.32 ha. During the reference years, the average reduced vegetation area was significantly lower ( $0.8 \pm 1.1\%$ ) compared to the years when mowing was performed ( $14.7 \pm 13.0\%$ ), with a statistically significant difference ( $df(35) = -6.3$ ,  $p < 0.01$ ). Additionally, the remaining vegetation was higher in the reference years ( $35.5 \pm 28.6\%$ ) than in the mowing years ( $18.3 \pm 11.6\%$ ), again showing a significant difference ( $df(35) = 3.46$ ,  $p < 0.01$ ). The impact of mowing on vegetation is observable from EO data, especially in areas larger than 0.1 ha, where reduced vegetative coverage is distinctly evident compared to non-mowed reference AOI (Figure 9). The years with mowing activities also exhibited a significantly greater reduction in vegetation.

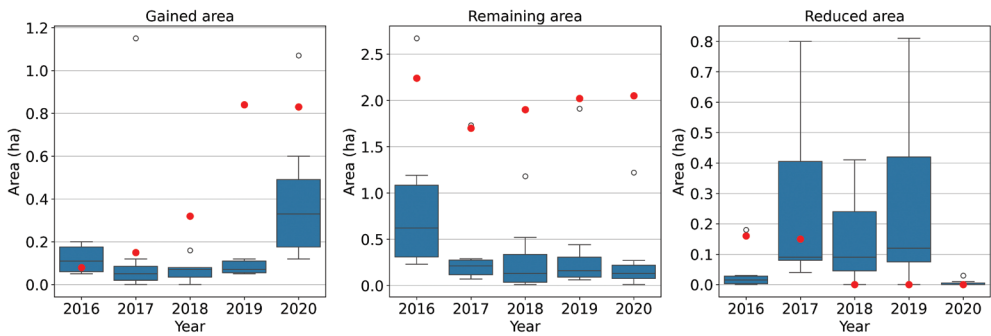


*Figure 9.* Boxplots of estimated reed bed areas (ha) in 8 AOIs derived from S2/MSI images after removal of water pixels determined by the Yen thresholding algorithm for NDWI: the estimated reed bed areas that were reduced, remained and gained during the study years (mowing years 2017–2019). Red dots represent the reference AOI that was not mowed, the central line inside each box represents the median, while the edges of the box indicate the 25th and 75th percentiles. Hollow points show the outliers (note the different scales for the area).

Continuous mowing is essential for sustained reed management, as highlighted by Ailstock et al. (2001), Asaeda et al. (2006), and Derr (2008). The 2017–2019 management program indicated a notable reduction in reed bed areas, implying successful nutrient removal, however, the regrowth of reed areas in 2020 necessitated repeated mowing due to eventual reed recovery, as observed in the post-mowing years. The average gained vegetation area of all AOIs was highly influenced by the year following the completion of mowing, 2020, in which the average vegetation gain of all AOIs

### 3. Results and discussion

was significantly higher ( $30.4 \pm 18.8\%$ ,  $0.69 \pm 0.74$  ha) compared to the preceding years:  $7.2 \pm 6.8\%$  in 2017,  $11.8 \pm 16.9\%$  in 2018, and  $10.7 \pm 12.5\%$  in 2019, with a significant statistical difference ( $df(21) = -5.2$ ,  $p < 0.01$ ). This is confirmed by Derr (2008) who notes that the reed regrowth rate can decrease by about 55% only with herbicide application after mowing.

#### 3.2.3 Implications for water body management and reed bed density recovery

WAVI was a reliable proxy for the reed density since the mean WAVI and emergent vegetation density, assessed from UAV data, strongly correlated ( $r_s = 0.99$ ,  $p < 0.05$ ). Using a derived linear regression function, WAVI values below 0.04 were considered as water with 0% vegetation and values over 0.22 as fully covered by reeds with 100% vegetation.

A significant difference in average change (Figure 10) was found in years 2016 with vegetation density being higher by  $36.2 \pm 19.2\%$ , lower in 2018 by  $17.9 \pm 11.3\%$  and higher again in 2019 by  $28.0 \pm 21.1\%$ ; however, significant ( $df(7) = 0.43$ ,  $p > 0.05$ ) change was not found in the first mowing year with an average of  $-1.8 \pm 26.4\%$  lower in the vegetation density, and the reference year 2020 lower on average by  $-12.0 \pm 35.1\%$  ( $df(7) = 0.2$ ,  $p > 0.05$ ).

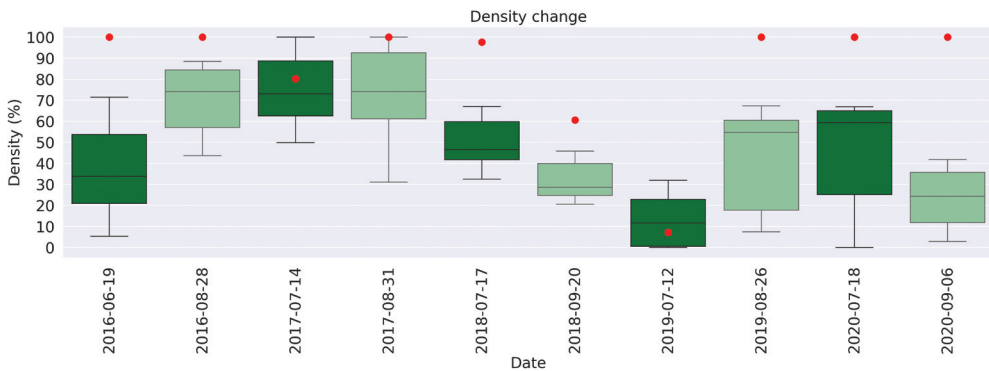


*Figure 10.* The relative reed density of 8 AOIs estimated from WAVI values retrieved from Sentinel-2/MSI images during 2016–2020 (mowing years 2017–2019). The beginning of vegetation season is indicated by dark green and the end of vegetation season – the light green color. Red dots show the density of reference AOI not included in the mean density.

The natural vegetation change seen from the reference year (2016), when mowing did not occur, shows that density increases naturally at the end of the vegetation

### 3. Results and discussion

season. This higher estimated vegetation density after mowing might be attributed to vegetation season, since the reeds reach their physiological maturity at the end of August (Villa et al., 2013). Interestingly, despite the lowest vegetation densities being recorded in 2018, which corresponded with the smallest vegetation areas, no significant relationship ( $r=0.05$ ,  $p>0.05$ ) was found between changes in the vegetated area and estimated vegetation densities.

The lack of correlation was consistent even when only considering AOIs with significant vegetation area loss or gain. This mismatch could be partially accounted due to one satellite image (2019 July 12) that was used for validation with UAV images, that had a low intra-class variance due to a cloud haze that was not fully corrected by Sen2Cor atmospheric correction (Gao & Li, 2012; Richter et al., 2011). This could have an influence on the final results of this image classification by used algorithms (Triangle, Iso, Mean, and Li) and also on density values that do not match area results, where area decreased but density increased. Therefore, as the gained vegetation area was significantly higher next year (2020) when mowing ended, this suggests that the reed bed areas recover over time and mowing will have to be repeated (Corti Meneses et al., 2018; Fogli et al., 2014; Rapp et al., 2012).

Remote sensing techniques offer a broader, more frequent perspective on lake ecosystems, complementing traditional macrophyte monitoring methods like those of the Environmental Protection Agency (EPA) Ireland and EPA Illinois. The approach used in this study is cost-effective and enables monitoring beyond just mowed areas. Timely satellite data aids in determining optimal mowing times, varying per lake management goals (Fogli et al., 2014). UAV data is gaining favor for validating satellite images due to its accuracy and wider coverage (Kattenborn et al., 2019). Conducted by mowing personnel or lake managers, UAV flights, coupled with structure from motion techniques, can precisely quantify above-ground biomass (Meneses et al., 2018). This multi-faceted approach, blending satellite and UAV data, enhances lake environment management.

### 3.3. Enhanced water clarity assessment via unmanned aerial vehicle imagery

Several sun-glint correction methods – Hedley, Goodman, Lyzenga, Joyce, and threshold-removed glint were applied to refine the estimation of Secchi depth (SD) from UAV multispectral imagery.

#### 3.3.1 Choice for sun glint correction

The application of sun glint correction methods in multispectral images yielded mixed results in terms of the RMSD and bias. The data revealed a consistent pattern across the

### 3. Results and discussion

green (560 nm), blue (475 nm), and red (668 nm) bands, with the green band consistently showing the peak mean value and the blue band indicating the lowest mean value. This spectral feature remained robust across all correction methods and in situ data.

Regarding multicollinearity, the green and red bands demonstrated the strongest correlation with a value of 0.97, followed by green and red edge at 0.96, and red and red edge at 0.95. The blue band also had strong multicollinearity with other bands, exhibiting correlation values of 0.97 with green, 0.94 with red, and 0.91 with red edge. These correlation metrics align well with the notion that factors such as a weak water surface signal and the rough texture of the water's surface can lead to both systematic and random inaccuracies in detecting the water surface, as noted by Wang et al. (2022). Furthermore, the association with the blue band was found to be the least stable, due to a higher susceptibility to scattering, a characteristic common to these wavelengths in aquatic settings, as described by Zaneveld et al. (2005), as CDOM primarily absorbs light within the ultraviolet and blue spectrum, it results in a diminished signal captured by sensors (Warren et al., 2019). Among the correction methods evaluated (Figure 11), Lyzenga showed the highest mean values across all bands, while Goodman showed the lowest. This contrasts with other studies, such as the one by Muslim et al. (2019), which indicated Lyzenga as the most accurate for mapping coral reefs. However, Goodman method showed the highest correlation for the green and red edge bands, with  $r$  values of 0.90 and 0.92, respectively, while having low  $r$  values for blue and red bands (0.32 and 0.71, respectively). This implies that environments with different amounts of water quality indicators (e.g. CDOM, chl-a, turbidity etc.) may influence the effectiveness of the correction methods.

Notably, the RMSD for Goodman ranged from 0.002 to 0.005, underscoring its effectiveness in applications where low reflectance intensity deviation is required. A comparable approach was utilized in a research by Muslim et al. (2019), which involved testing various techniques for correcting sun glint. They discovered that the Lyzenga method was the most precise. However, it is important to acknowledge that their study primarily aimed at mapping coral reefs, and the bottom was visible in much of their research area, potentially impacting their findings. On the other hand, Windle and Silsbe (2021) observed that the Hedley method had the best performance in terms of the highest correlation coefficient ( $r$ ) and the lowest RMSD. These results align closely with those from our study.

### 3. Results and discussion

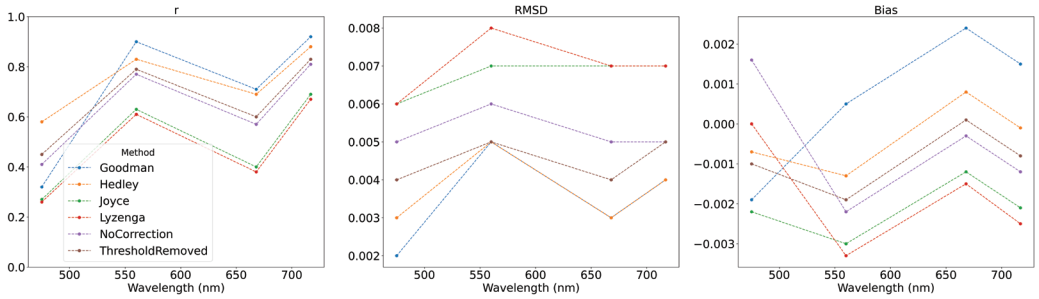


Figure 11. Reflectance compared by the mean correlation coefficient ( $r$ ), root-mean-square deviation (RMSD) and bias for each correction method to in situ measurements, across all available wavelengths. Both RMSD and bias were expressed in reflectance units sr-1 (reprinted from Paper III).

It is worth mentioning that applying glint correction to the entire image rather than just the binary thresholded area appeared to yield better results in terms of overall accuracy, suggesting that future research should consider a broader application of these methods.

Overall, the Goodman and Hedley sun glint correction methods demonstrated the best performance, with Goodman showing the highest correlation for the green and red edge bands and Hedley consistently performing well across all bands, suggesting their potential for further use in correcting sun glint in multispectral UAV image data.

#### 3.3.2 Quasi-Analytical Algorithm-derived Secchi depth compared to in situ measurements

The performance evaluation using the QAA model to retrieve SD revealed high correlation values across all sun glint correction methods when compared to in situ measurements. Specifically, the  $r$  values ranged from 0.74 for the threshold-removed glint method to 0.92 for the Hedley glint correction. RMSD values varied between 0.65 m and 1.05 m, and biases ranged from -0.78 to 0.58 m, indicating overall acceptable performance. The study noted similar trends in the accuracy for both when comparing band reflectances and SD values.

Among the methods, Hedley sun glint-corrected images (Figure 12) achieved the best RMSD measure of 0.65 m, with a slightly smaller  $r$  value of 0.91 compared to the Goodman method ( $r = 0.92$ , RMSD = 1.00 m). It's important to mention that the Goodman method underestimated most SD values.



### 3. Results and discussion

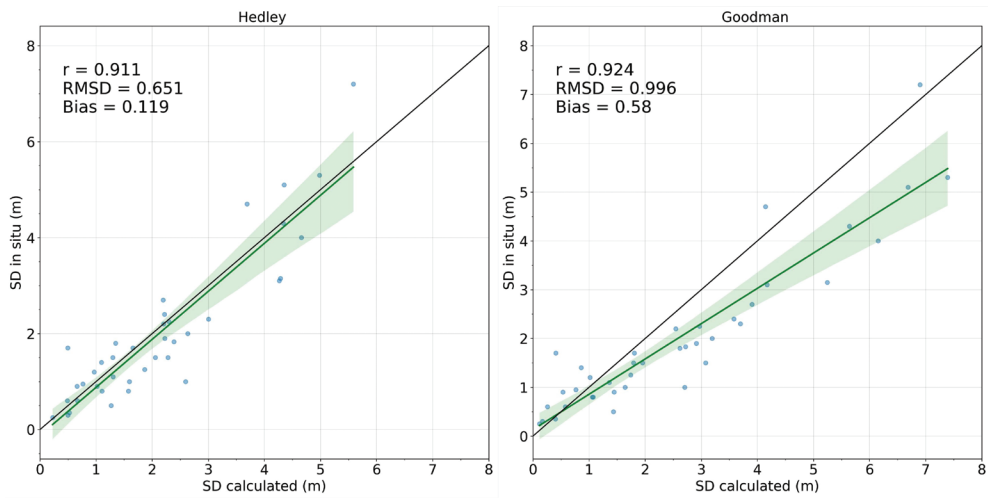


Figure 12. Scatter Plots with linear regression line and 95% degrees of freedom (green) of modeled and in situ SD. Best-fit line (1:1) (black) for each image dataset, using Hedley and Goodman methods.

Hedley and Goodman methods stood out as the most effective, albeit with specific limitations, where the Hedley method achieved the lowest RMSD (0.65 m) with an  $r$  of 0.91, while Goodman showed the highest  $r$  value of 0.92 but a higher RMSD (1.00 m). It was noticed that selecting the most appropriate sun glint correction method might require considering multiple metrics depending on the application. This combined analysis of the performance of various sun glint correction methods reveals that while some methods excel in certain metrics, they may not perform as well in others, therefore, informing future research to aim for improving the generalization of reflectance correction methods.

#### 3.3.3 Influence of Water Constituents for Quasi-Analytical Algorithm Secchi Depth Values

The average *in situ* SD of the lakes was measured to be about 1.91 m, with varying amounts of CDOM, Chl-a, and turbidity. The GAMs (Figure 13) explained around 38% of the variance in the SD measurements, where significant environmental factors were CDOM ( $F = 6.808$ ,  $p$ -value  $< 0.05$ ) and the sun zenith angle ( $F = 4.84$ ,  $p = 0.02$ ).

### 3. Results and discussion

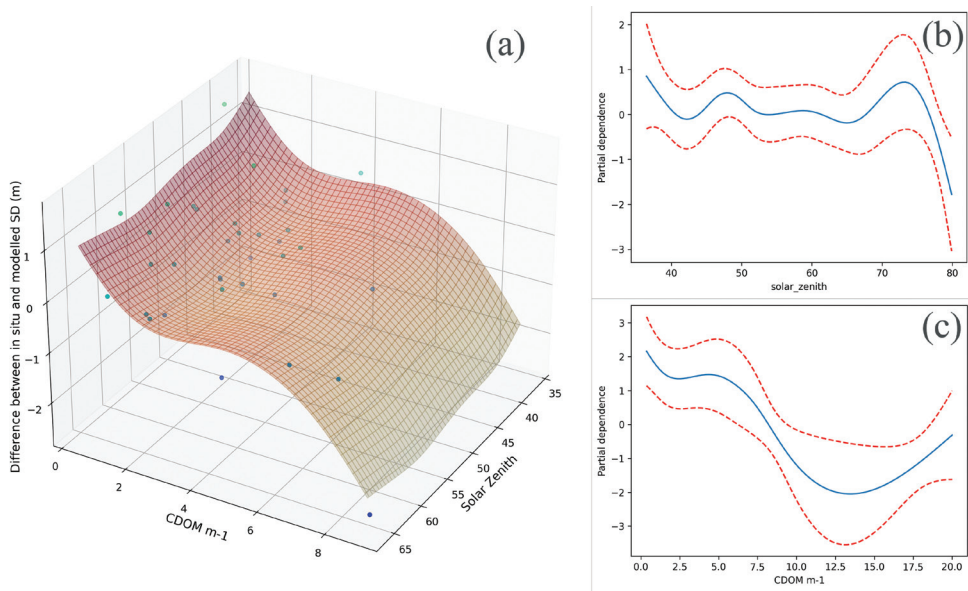


Figure 13. Interaction plot of solar zenith angle, CDOM and predicted difference plane between in situ and modeled SD (m). Partial dependence plots for parameters influencing SD significantly – CDOM  $m^{-1}$  and solar zenith angle (reprinted from Paper III).

Notably, Chl-a ( $F = 0.295$ ,  $p = 0.59$ ) values did not make a significant impact on the model. Additionally, high solar zenith angles, especially above 70 degrees, were found to reduce the accuracy of modeled SD, sometimes underestimating it by up to 1.5 m. This likely results from increased scattering and absorption of light at higher angles, which reduces the amount of light reaching the water surface, thus widening the gap between modeled and on-site SD measurements (Hashimoto et al., 2019). Therefore, this finding highlights the importance of advanced algorithms capable of accurately accounting for these complex environmental variables in SD predictions.

The correlation between *in situ* SD measurements and the estimated SD values from models might be attributed to how these models handle factors like CDOM and solar zenith angles, which are key to model accuracy. Since CDOM predominantly absorbs light in the ultraviolet (UV) and blue spectrum, leading to a reduced signal detected by sensors (Warren et al., 2019), this aligns with our finding where the blue band showed weaker correlations between *in situ* and UAV-derived reflectance measurements (Mamaghani and Salvaggio, 2019). It suggests that the methods developed by Goodman and Hedley might be more effective in addressing this issue, as evidenced by the Hedley method achieving the highest correlation coefficient ( $r$ ) and the Goodman method recording the lowest RMSD for blue band reflectance, thereby aligning more closely with *in situ* values.

#### 3.4 Unmanned aerial vehicle based beach wrack quantification

The study applied UAV camera bands, height measurements, and spectral indices for beach wrack segmentation using the U-Net convolutional neural network.

##### 3.4.1 Performance evaluation across data combinations and classes

In the study of the U-Net model's performance across various data combinations (5 bands and height, 5 bands, RGB and height, RGB, augmented and band ratio indices), the model exhibited its highest effectiveness when using the "band ratio indices" combination, particularly in the segmentation of BW. This was evidenced by an F1 score of 0.86 and an IoU of 0.75 (Figure 14). Such results underscore the model's proficiency in semantic segmentation tasks, especially when applied to high-resolution remote-sensing images collected by UAV. Despite this, it is noted that all combinations yielded relatively lower IoU scores for the potential BW class, indicating a variation in the model's performance across all classes (BW, potential BW, sand, water, other). The post hoc tests revealed that the differences in performance between various data combinations were not statistically significant, with p-values  $\geq 0.74$ . This suggests that the choice of data combination did not significantly impact the IoU scores. The IoU values for BW were moderately consistent across all data combinations, suggesting potential for generalizability and time-based transferability. This is due to the dataset including images from various seasons and weather conditions, as highlighted in studies by Lu (2016) and Bao et al. (2018), demonstrating UAVs' effectiveness in diverse beach mapping.

For BW segmentation on validation data (Figure 14), the combination utilizing "RGB" bands was found to be the most effective, achieving an IoU of 0.42, complemented by an F1 score of 0.54. For the potential BW segmentation, the combination of "5 bands and height" was the best, marking an IoU of 0.20 and an F1 score of 0.38. The "RGB" and "5 bands" combinations followed closely in performance.

The "RGB" combination emerged superior in both the water and sand classes, with IoUs of 0.64 and 0.70 respectively, and commendable F1 scores of 0.76 and 0.82. The other class had the highest IoU of 0.95 in the "RGB and height" combination.

### 3. Results and discussion

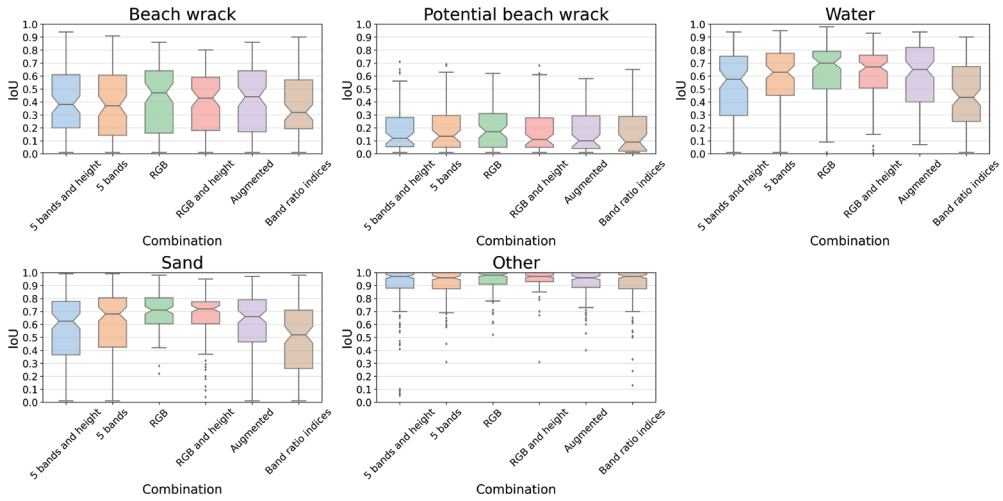


Figure 14. The boxplots present the IoU scores for the six different data combinations applied during the U-Net (CNN) model validation. The plots show the distribution of IoU scores for each segmentation class: BW, potential BW, water, sand, and other. The central line inside each box represents the median, while the edges of the box indicate the 25th and 75th percentiles. Outliers may be represented by individual points (reprinted from Paper IV).

An overview of the average performance of all data combinations indicated no significant difference, with the “RGB” combination recording the highest average metrics. The transferability of the model was confirmed through Dunn’s post hoc tests for IoU, which showed significant differences ( $p < 0.05$ ) across various AOIs, with Karklė demonstrating distinct performance compared to other AOIs (Figure 15). The moderate IoU values for BW across all data combinations underscore the model’s potential for generalization and transferability, despite the variability of season and weather conditions during the collection of the data. The results reaffirm the utility of UAVs in monitoring diverse beach characteristics effectively.

Transferring the model to a new AOI might be challenging, particularly in areas with less uniform surfaces. In Karklė (Figure 15, b), the inclusion of height data resulted in lower performance (BW IoU = 0.37), indicating a need for cautious application of height data, as also suggested by Pichon et al. (2016) and Gruszczyński et al. (2019). Improving height accuracy might be achieved by incorporating oblique images for better digital surface model calculations as mentioned by Taddia et al. (2019). The model’s transferability was evident in AOIs with relatively uniform surfaces, such as Šventoji, Melnragė, and Palanga, where the predictability of the substrate contributed to successful segmentation.

### 3. Results and discussion

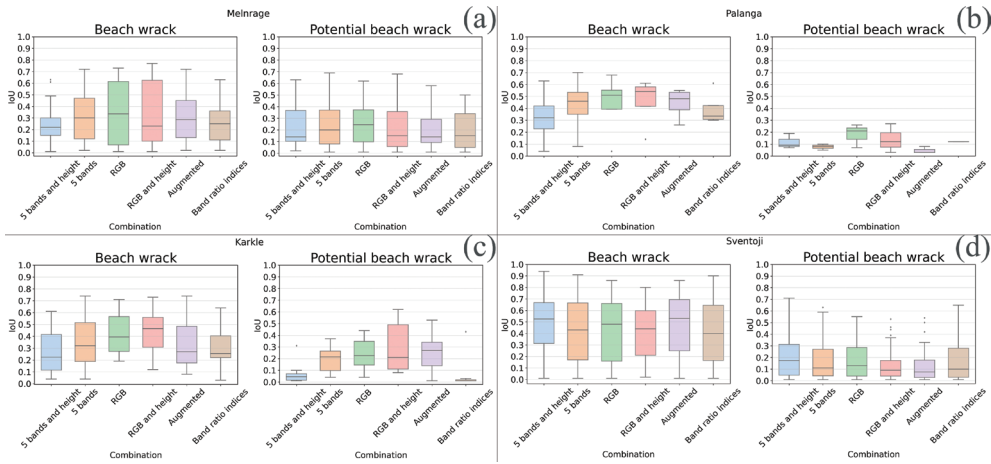


Figure 15. Boxplots for each AOI separately where (a) is Melnragè, (b) Palanga, (c) Karklè and (d) Šventoji. Each boxplot represents the results for all data combinations, and notches show a confidence interval around the median (reprinted from Paper IV).

Furthermore, the model’s consistency in performance with the augmented data (of 5 bands and height) combination indicates an absence of bias towards spatial localization, reinforcing its adaptability and transferability across diverse scenarios and object placements within the AOIs. The moderate accuracy and lower computational demands make the “RGB” data combination preferable for BW segmentation using the U-Net CNN.

The model faces specific challenges in detecting potential BW, largely due to the complex nature of aquatic environments and the behavior of light underwater. A key difficulty arises from the way water alters light absorption and reflection (Xue et al., 2016), rendering some remote sensing algorithms less effective due to optical complexities in water bodies, like varying depth, turbidity and waves. Additionally, sun glint can mask water-leaving radiance at high solar angles, introducing noise into image data, as noted by Gagliardini and Colón (2004). Factors like wave activity and sea surface roughness further complicate the optical properties of water, impacting remote sensing reflectance quality (Zhang et al., 2018). Enhancing potential BW segmentation might require additional preprocessing steps to correct for water depth (Nomura et al., 2018) and sun glint effects (I; Windle and Silsbe, 2021;). Efficient removal of potential BW is crucial to maintain the ecological balance, odor, and aesthetics of beaches. Missing potential BW deposits can lead to underestimation of BW accumulation on beaches, thereby impacting beach management strategies.

### 3. Results and discussion

#### 3.4.2. Quantitative analysis of beach wrack heights and areas

The study quantified labeled BW areas ranging from 236 m<sup>2</sup> to 11193 m<sup>2</sup>. In comparison, the U-Net model, utilizing the “RGB” data combination (Figure 16), derived the BW areas ranging from 9 m<sup>2</sup> to 3710 m<sup>2</sup>. The average labeled area was 1888 ± 2199 m<sup>2</sup>, corresponding to the U-Net derived area of 1218 ± 940 m<sup>2</sup>, indicating a generally linear relationship but with notable variance. In terms of the agreement between labeled and segmented areas, the “RGB” combination achieved the highest correlation coefficient ( $r = 0.87$ ), with the lowest errors (MAE of 562 and RMSE of 783).

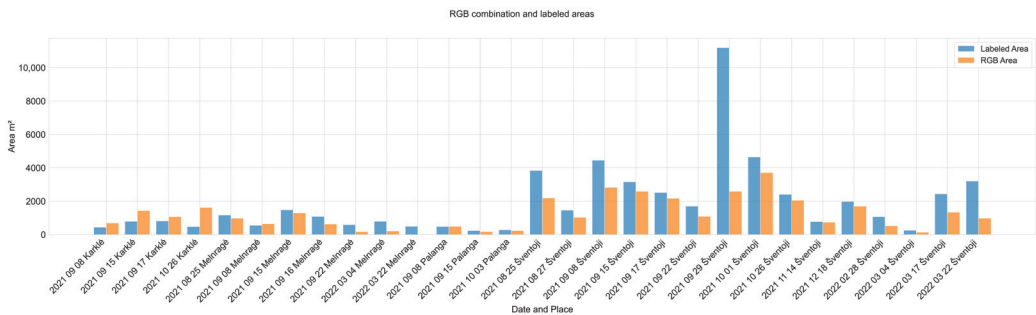


Figure 16. The areas of BW coverage in the investigated AOIs retrieved from UAV after the application of the U-Net model with the “RGB” combination and labeled BW areas (reprinted from Paper IV).

The correlation between modeled and *in situ* heights was 0.44, which was significant ( $p < 0.05$ ). However, the average calculated BW height from UAV was  $0.46 \pm 0.40$  m, which was a five-fold overestimation compared to *in situ* measured heights of  $0.09 \pm 0.11$  m, suggesting that heights acquired using the methods in this study should be used carefully. Nonetheless, for future research the accuracy of height could be improved by taking images with oblique angles in addition to nadir, increasing the information available for digital surface model calculations using structure from motion algorithms (Taddia et al., 2019).

Visual representations of all AOIs indicated that the model performed well in classifying most of the BW. Discrepancies in classification were noted in specific regions of Palanga and Melnragė, even though they were exceptions from the normal classification, rather than the rule. The visual outcomes for sand and water classes were most accurate, with only minor variations observed. For Karklė specifically (Figure 17, a), a clear visible advantage is seen when distinguishing BW from its surroundings using multispectral data, where piles of small pebbles (red circle in Figure 17, b) look similar in RGB, but with multispectral data, more specifically with NIR the BW can be easier delineated. In Melnragė and Šventoji, more misclassifications were seen in the water,

### 3. Results and discussion

where potential BW was being identified. In Šventoji images, wavy water conditions added complexity that lowered the detection of BW. However, in Melnragė, during calm water conditions, a large amount of sun glint was observable (red hue area in Figure 17, d), which was uneven throughout the territory as the clouds disrupted light differently.

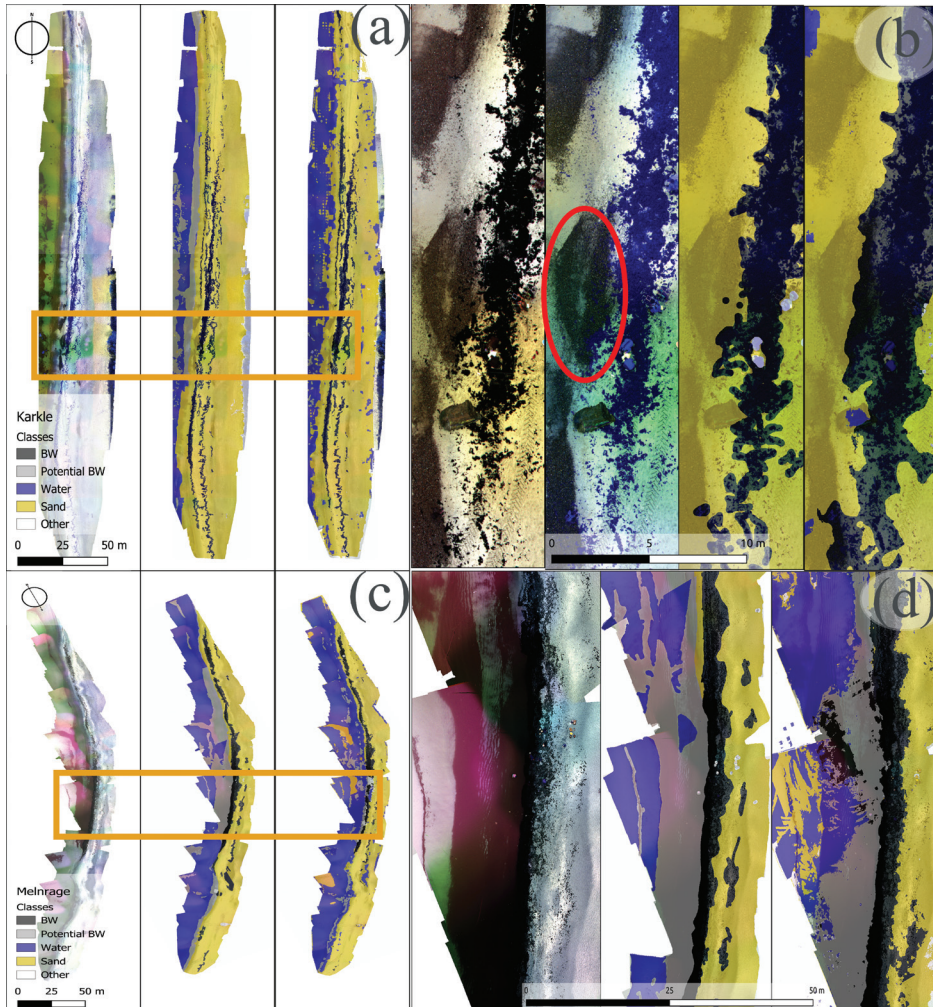


*Figure 17.* Examples of BW spatial distribution in AOIs of Karklė (a) and Melnragė (c) after UAV image processing with the U-Net model using the “RGB” combination, with NIR, green and blue combination on left, labeled in the center and modeled on the right. Additionally zoom in areas of the same images with RGB (left), NIR, green and blue combination (second from left), labeled BW (second from right), and modeled BW (right) maps are provided for (b) 17 September 2021 in Karklė, and same without NIR, green and blue for (d) 16 September 2021 in Melnragė. Zoomed in areas, shown in orange rectangles and red circle in (b) show the area where a larger amount of pebbles are located (reprinted from Paper IV).

### 3. Results and discussion

Classification of a single image tile requires only about 5 minutes, which is crucial for management tasks that demand a rapid assessment of whether the amount of BW should be removed. This strategy could significantly advance these coastal monitoring efforts for beach management applications, with the ability of cost-effective and efficient monitoring workflows that can adapt to various beach types, without relying on extensive computing resources.

Future directions for research should consider broadening the range of environmental conditions and selected beach morphologies, to solidify the model's transferability. Refining segmentation accuracy could also be achieved by integrating advanced data pre-processing techniques as sun glint removal and additional radiometric correction to mitigate variable water reflectance and a systematic evaluation of individual spectral bands' impact on the model's performance, enhancing interpretability and feature classification efficiency.

#### 3.5. Results and discussion synthesis

The suite of studies presented in this dissertation collectively demonstrates a novel approach to ecological monitoring, designed to address gaps in traditional monitoring methods (Figure 18). These gaps include limited spatial and temporal coverage, labour-intensive processes subject to observer bias, and the underutilization of modern technological advances in ecological assessments. By using Unmanned Aerial Vehicles (UAVs) and advanced remote sensing algorithms, this research offers substantial improvements in the precision, efficiency, and scalability of ecological monitoring. The first study establishes a framework for utilizing UAVs in ecological assessments, offering a methodology that resonates through the subsequent papers. This framework is essential in navigating the complexity of vegetation monitoring, emphasizing the selection of suitable UAV technologies and data processing strategies to address specific ecological parameters.

Building on this foundation, the second paper explores the dynamics of aquatic vegetation, using the Yen binary thresholding algorithm on the normalized difference water index to precisely delineate reed beds – an important aspect of water quality indicators. This methodological approach showcases the efficacy of combining UAV data with satellite imagery, providing an expanded toolkit for long-term monitoring and management of aquatic ecosystems.

In the third study, continuing using the first paper a methodological selection guide, the quasi-analytical algorithm (QAA) is shown as a tool for assessing water clarity, another key indicator of further water quality, in addition to macrophytes from the second paper. The use of sun glint correction methods, especially Hedley's, enhances the accuracy of Secchi depth estimations and illustrates the significant role that image





### 3. Results and discussion

scalable, precise, and adaptable framework. The integration of the U-Net model, the precision of the Yen thresholding for vegetation detection, and the effectiveness of the quasi-analytical algorithm for water clarity measurements demonstrate a harmonious integration of UAV technology with machine learning and image processing techniques. This comprehensive approach positions these methodologies to significantly enhance national monitoring programs, providing a replicable model for ecological research and resource management.

# 4

---

## Recommendations

### **Integration Across Domains (Paper I)**

UAVs have proven to be useful in environmental monitoring scenarios, therefore it is worth developing integrated monitoring systems that leverage UAVs for both water and land-based environmental vegetation assessments.

### **Supplement Satellite Imaging for Vegetation Monitoring (Paper II)**

Given that satellite imaging alone cannot provide a comprehensive view of vegetation monitoring, it should be used in tandem with *in situ* or UAV measurements. The Yen binary thresholding on the NDWI index method is effective, especially for reed beds with a density of  $\geq 50\%$ , where classification accuracy is from 50% to 85%.

### **Suggested use of Quasi-analytical algorithm (Paper III)**

Given that Hedley's method improved the accuracy for SD estimations the most, it is suggested to use it as a pre-processing step. The Quasi-analytical algorithm using a multispectral UAV camera is recommended for water bodies, where CDOM concentration is less than  $12 \text{ m}^{-1}$ , while performing the UAV data collection closer to noon, when the solar zenith angle is less than  $70^\circ$ .

## 4. Recommendations

### **Secchi depth practical measurements (Paper III)**

The Quasi-analytical algorithm can be integrated into lake monitoring workflows, potentially automating the processing of Secchi depth calculation for lakes over 5 hectares within 20 minutes. With around 6000 lakes in Lithuania, this approach could enhance national monitoring, improving the accuracy and coverage of environmental monitoring efforts.

### **Further Testing of Convolutional Neural Network Models for Beach Wrack Segmentation (Paper IV)**

The U-Net model has shown promising results in segmenting beach wrack. However, it may benefit from further fine-tuning, specifically if used in other areas, distinctive from this research (e.g. different water reflectance and morphological structures).

### **Inclusion of Height Data in U-Net Models (Paper IV)**

While height data did not significantly improve the model's performance, its potential should not be entirely dismissed. Future studies should consider the use of LiDAR-derived height data, and integrate it into the model.

### **Computational Resource Optimization (Paper IV)**

Given that the U-Net model could run without high-end computing resources it allows for wider application for quick BW area classification.

# 5

---

## Conclusions

1. Framework was established for unmanned aerial vehicle surveys, demonstrating how diverse data resolution, sensor integration, and advanced analytical techniques guide the mapping of four identified vegetation parameters, highlighting their effectiveness in biodiversity conservation, ecosystem structure analysis, phenology, and stress monitoring. This framework guides environmental scientists and resource managers, offering a comprehensive methodology for leveraging unmanned aerial vehicle remote sensing to monitor and manage vegetation across diverse environments.
2. The changes in reed bed, induced by mowing activities, were effectively detected using the Yen binary thresholding algorithm on normalized difference water index derived from the Sentinel-2/MSI data, offering a reliable approach for monitoring and managing reed bed dynamics in lakes like Plateliai. The significant detection accuracy was enhanced for denser (50 %) reed bed areas of  $\geq 0.1$  ha.
3. The potential of the quasi-analytical algorithm in estimating the Secchi depth was confirmed, with the benefit of its adaptability in analyzing data from multispectral unmanned aerial vehicle sensors. The accuracy of the Secchi depth measurements from unmanned aerial vehicle flights is significantly influenced by the sun glint correction methods used, of which the Hedley's method was

## 5. Conclusions

found to be the most accurate ( $r=0.91$ ), allowing the Secchi depth determination over extensive areas using the quasi-analytical algorithm.

4. The U-Net model utility in beach wrack segmentation, was particularly effective with the “RGB” data combination, indicating its potential for coastal monitoring applications. Performance varied across beaches with different geomorphological features (e.g., sandy or pebble beaches), suggesting the need for adaptation if transferring the model to new areas, by adding new images for retraining, that would fine-tune the model. Integrating the multispectral and elevation data did not significantly enhance segmentation accuracy compared to simpler “RGB” combination.

# 6

---

## Acknowledgements

I am grateful to the Marine Research Institute of Klaipėda University, where the enriching environment and cutting-edge resources provided an excellent foundation for my research endeavors, particularly within the remote sensing group. This thesis stands as a testament to the collaborative spirit and intellectual rigor that pervades this esteemed institution.

Foremost, I owe a debt of gratitude to my supervisor, Dr. Diana Vaičiūtė, and my advisor, Prof. Dr. Martynas Bucas. Their guidance was pivotal in shaping my academic journey; from involving me in significant projects to imparting the craft of academic writing, their influence has been immeasurable. Their patience, wisdom, and encouragement have been my guiding lights.

I wish to acknowledge the support and guidance of the PhD committee, especially Dr. Jurate Lesutienė and Prof. Habil. Dr. Sergej Olenin. Their insightful feedback and unwavering support have been instrumental in my development as a researcher. My heartfelt thanks go to my colleagues, the administrative staff Eglė Navickienė and Eglė Karimžanova, and fellow PhD students at the institute. Special mention is due to Jonas Gintauskas, Viktorija Sabaliauskaitė, Dr. Arūnas Balčiūnas, Greta Kalvaitienė, Dr. Marija Kataržytė, and Irma Babrauskienė, whose assistance in field research was invaluable.

## 6. Acknowledgements

On a personal note, my appreciation goes to my wife, Rūta Tiškuvienė, for her support, both emotionally and practically, in the visualizations and language correction of all my papers. Her love and belief in my work have been my cornerstone. Additionally, I am thankful for my friends and family, whose support and encouragement have been a constant source of strength throughout this journey.

Reflecting on this journey, it has been a once-in-a-lifetime opportunity to learn, grow, and evolve both professionally and personally. Despite the stress and challenges, the journey has been replete with satisfying and enlightening moments, marking significant milestones in my life and career. As I look to the future, I am hopeful for the opportunities to collaborate and continue contributing to the field, building on the valuable experiences and knowledge gained during my PhD studies.

Lastly, this research received partial funding from three projects. Their support not only facilitated the practical aspects of my research but also significantly contributed to the broader scientific community's understanding of our focus areas. I am profoundly grateful for their belief in my work and their contribution to the advancement of science:

- COST Action CA16219 “HARMONIOUS - Harmonization of UAS techniques for agricultural and natural ecosystems monitoring”
- ESMIC Interreg V-A Latvia-Lithuania Program project ESMIC “Assessment, Monitoring and Reduction of Plastic Pollutants in the Latvian-Lithuanian Coastal Zone through Innovative Measures and Awareness Raising” project (No. LLI-525).
- The field campaigns co-funded by the Environmental Protection Agency contract “Assessment of the water condition and its more efficient management of the remote monitoring data collection, processing, use and storage system, to ensure accurate results (NUOTOLIS)” (grant 28T-2021-64/SUT-21P-20).



# 7

---

## References

- Abadi, M., Agarwal, A., Barham, P., Brevdo, E., Chen, Z., Citro, C., Corrado, G.S., Davis, A., Dean, J., Devin, M., Ghemawat, S., Goodfellow, I., Harp, A., Irving, G., Isard, M., Jia, Y., Jozefowicz, R., Kaiser, L., Kudlur, M., Levenberg, J., Mane, D., Monga, R., Moore, S., Murray, D., Olah, C., Schuster, M., Shlens, J., Steiner, B., Sutskever, I., Talwar, K., Tucker, P., Vanhoucke, V., Vasudevan, V., Viegas, F., Vinyals, O., Warden, P., Wattenberg, M., Wicke, M., Yu, Y., Zheng, X., 2016. TensorFlow: Large-Scale Machine Learning on Heterogeneous Distributed Systems.
- Aguilar, F.J., Rivas, J.R., Nemmaoui, A., Peñalver, A., Aguilar, M.A., 2019. UAV-Based Digital Terrain Model Generation under Leaf-Off Conditions to Support Teak Plantations Inventories in Tropical Dry Forests. A Case of the Coastal Region of Ecuador. *Sensors* 19, 1934. <https://doi.org/10.3390/s19081934>
- Alikas, K., Kangro, K., Randoja, R., Philipson, P., Asuküll, E., Pisek, J., Reinart, A., 2015. Satellite-based products for monitoring optically complex inland waters in support of EU Water Framework Directive. *Int. J. Remote Sens.* 36, 4446–4468. <https://doi.org/10.1080/01431161.2015.1083630>
- Alvarez-Vanhard, E., Houet, T., Mony, C., Lecoq, L., Corpetti, T., 2020. Can UAVs fill the gap between in situ surveys and satellites for habitat mapping? *Remote Sens. Environ.* 243, 111780. <https://doi.org/10.1016/j.rse.2020.111780>

## 7. References

- Anderson, K., Gaston, K.J., 2013. Lightweight unmanned aerial vehicles will revolutionize spatial ecology. *Front. Ecol. Environ.* 11, 138–146. <https://doi.org/10.1890/120150>
- Arzt, M., Deschamps, J., Schmied, C., Pietzsch, T., Schmidt, D., Tomancak, P., Haase, R., Jug, F., 2022. LABKIT: Labeling and Segmentation Toolkit for Big Image Data. *Front. Comput. Sci.* 4.
- Bagaram, M.B., Giuliarelli, D., Chirici, G., Giannetti, F., Barbati, A., 2018. UAV Remote Sensing for Biodiversity Monitoring: Are Forest Canopy Gaps Good Covariates? *Remote Sens.* 10, 1397. <https://doi.org/10.3390/rs10091397>
- Baltsavias, E., Gruen, A., Eisenbeiss, H., Zhang, L., Waser, L.T., 2008. High-quality image matching and automated generation of 3D tree models. *Int. J. Remote Sens.* 29, 1243–1259. <https://doi.org/10.1080/01431160701736513>
- Banerjee, B.P., Raval, S., Cullen, P.J., 2020. UAV-hyperspectral imaging of spectrally complex environments. *Int. J. Remote Sens.* 41, 4136–4159. <https://doi.org/10.1080/01431161.2020.1714771>
- Berra, E.F., Gaulton, R., Barr, S., 2019. Assessing spring phenology of a temperate woodland: A multiscale comparison of ground, unmanned aerial vehicle and Landsat satellite observations. *Remote Sens. Environ.* 223, 229–242. <https://doi.org/10.1016/j.rse.2019.01.010>
- Bi, S., Wang, L., Li, Y., Zhang, Z., Wang, Z., Ding, X., Zhou, J., 2021. A Comprehensive Method for Water Environment Assessment considering Trends of Water Quality. *Adv. Civ. Eng.* 2021, e5548113. <https://doi.org/10.1155/2021/5548113>
- Bishop, 2002. pytz Python historical timezone library and database. URL <https://github.com/stub42/pytz> (accessed 2023-03-04).
- Bollas, N., Kokinou, E., Polychronos, V., 2021. Comparison of Sentinel-2 and UAV Multispectral Data for Use in Precision Agriculture: An Application from Northern Greece. *Drones* 5, 35. <https://doi.org/10.3390/drones5020035>
- Bucas, M., Daunys, D., Olenin, S., 2009. Recent distribution and stock assessment of the red alga *Furcellaria lumbricalis* on an exposed Baltic Sea coast: combined use of field survey and modelling methods. *Oceanologia* 51, 341–359.
- Bučas Martynas, Bagdonas, P., Morkūnas, J., Staponkus, R., Bagdanavičiūtė, I., Daunys, D., 2023. Natura 2000 tinklo vertybių, esančių Kuršių mariose, geros apsaugos būklės kriterijų ir apsaugos tikslų nustatymas (paslaugų sutartis nr. F4-83/SUT-23P-14).
- Bussotti, S., Guidetti, P., Rossi, F., 2022. *Posidonia oceanica* wrack beds as a fish habitat in the surf zone. *Estuar. Coast. Shelf Sci.* 272, 107882. <https://doi.org/10.1016/j.ecss.2022.107882>
- Camarretta, N., Harrison, P.A., Bailey, T., Potts, B., Lucieer, A., Davidson, N., Hunt, M., 2020. Monitoring forest structure to guide adaptive management of forest res-

## 7. References

- toration: a review of remote sensing approaches. *New For.* 51, 573–596. <https://doi.org/10.1007/s11056-019-09754-5>
- Cardil, A., Vepakomma, U., Brotons, L., 2017. Assessing Pine Processionary Moth Defoliation Using Unmanned Aerial Systems. *Forests* 8, 402. <https://doi.org/10.3390/f8100402>
- Carl, C., Landgraf, D., Van der Maaten-Theunissen, M., Biber, P., Pretzsch, H., 2017. *Robinia pseudoacacia* L. Flower Analyzed by Using An Unmanned Aerial Vehicle (UAV). *Remote Sens.* 9, 1091. <https://doi.org/10.3390/rs9111091>
- Chang, N.-B., Bai, K., Chen, C.-F., 2017. Integrating multisensor satellite data merging and image reconstruction in support of machine learning for better water quality management. *J. Environ. Manage.* 201, 227–240. <https://doi.org/10.1016/j.jenvman.2017.06.045>
- Chemin, Y., Platonov, A., Ul-Hassan, M., Abdullaev, I., 2004. Using remote sensing data for water depletion assessment at administrative and irrigation-system levels: case study of the Ferghana Province of Uzbekistan. *Agric. Water Manag.* 64, 183–196. [https://doi.org/10.1016/S0378-3774\(03\)00209-9](https://doi.org/10.1016/S0378-3774(03)00209-9)
- Chen, C., Tang, S., Pan, Z., Zhan, H., Larson, M., Jönsson, L., 2007. Remotely Sensed Assessment of Water Quality Levels in the Pearl River Estuary, China. *Mar. Pollut. Bull.* 54, 1267–72. <https://doi.org/10.1016/j.marpolbul.2007.03.010>
- Chollet, F., others, 2018. Keras: The Python Deep Learning library. *Astrophys. Source Code Libr.* ascl:1806.022.
- Corti Meneses, N., Brunner, F., Baier, S., Geist, J., Schneider, T., 2018. Quantification of Extent, Density, and Status of Aquatic Reed Beds Using Point Clouds Derived from UAV–RGB Imagery. *Remote Sens.* 10, 1869. <https://doi.org/10.3390/rs10121869>
- Cunliffe, A.M., Brazier, R.E., Anderson, K., 2016. Ultra-fine grain landscape-scale quantification of dryland vegetation structure with drone-acquired structure-from-motion photogrammetry. *Remote Sens. Environ.* 183, 129–143. <https://doi.org/10.1016/j.rse.2016.05.019>
- Dandois, J.P., Ellis, E.C., 2010. Remote Sensing of Vegetation Structure Using Computer Vision. *Remote Sens.* 2, 1157–1176. <https://doi.org/10.3390/rs2041157>
- Dassenakis, M., Paraskevopoulou, V., Cartalis, C., Adaktilou, N., Katsiabani, K., 2011. Remote sensing in coastal water monitoring: Applications in the eastern Mediterranean Sea (IUPAC Technical Report). *Pure Appl. Chem.* 84, 335–375. <https://doi.org/10.1351/PAC-REP-11-01-11>
- Deng, L., Mao, Z., Li, X., Hu, Z., Duan, F., Yan, Y., 2018. UAV-based multispectral remote sensing for precision agriculture: A comparison between different cameras. *ISPRS J. Photogramm. Remote Sens.* 146, 124–136. <https://doi.org/10.1016/j.isprsjprs.2018.09.008>

## 7. References

- Directive 2006/7/EC of the European Parliament and of the Council of 15 February 2006 concerning the management of bathing water quality and repealing Directive 76/160/EEC. Official Journal of the European Union L 64, 4.3.2006, p. 37–51., 2006.
- D’Odorico, P., Besik, A., Wong, C.Y.S., Isabel, N., Ensminger, I., 2020. High-throughput drone-based remote sensing reliably tracks phenology in thousands of conifer seedlings. *New Phytol.* 226, 1667–1681. <https://doi.org/10.1111/nph.16488>
- Drusch, M., Del Bello, U., Carlier, S., Colin, O., Fernandez, V., Gascon, F., Hoersch, B., Isola, C., Laberinti, P., Martimort, P., Meygret, A., Spoto, F., Sy, O., Marchese, F., Bargellini, P., 2012. Sentinel-2: ESA’s Optical High-Resolution Mission for GMES Operational Services. *Remote Sens. Environ., The Sentinel Missions - New Opportunities for Science* 120, 25–36. <https://doi.org/10.1016/j.rse.2011.11.026>
- Dugdale, S.J., Kelleher, C.A., Malcolm, I.A., Caldwell, S., Hannah, D.M., 2019. Assessing the potential of drone-based thermal infrared imagery for quantifying river temperature heterogeneity. *Hydrol. Process.* 33, 1152–1163. <https://doi.org/10.1002/hyp.13395>
- Dworak, T., Gonzalez, C., Laaser, C., Interwies, E., 2005. The need for new monitoring tools to implement the WFD. *Environ. Sci. Policy* 8, 301–306. <https://doi.org/10.1016/j.envsci.2005.03.007>
- Easy Access Rules for Unmanned Aircraft Systems (Regulations (EU) 2019/947 and 2019/945) - Revision from September 2022. EASA. URL <https://www.easa.europa.eu/en/document-library/easy-access-rules/easy-access-rules-unmanned-aircraft-systems-regulations-eu> (accessed 2024-02-03).
- Egan, J.P., 1975. *Signal detection theory and ROC-analysis*. Academic press, New York.
- Fawcett, D., Bennie, J., Anderson, K., 2021. Monitoring spring phenology of individual tree crowns using drone-acquired NDVI data. *Remote Sens. Ecol. Conserv.* 7, 227–244. <https://doi.org/10.1002/rse2.184>
- Fernández-Guisuraga, J.M., Sanz-Ablanedo, E., Suárez-Seoane, S., Calvo, L., 2018. Using Unmanned Aerial Vehicles in Postfire Vegetation Survey Campaigns through Large and Heterogeneous Areas: Opportunities and Challenges. *Sensors* 18, 586. <https://doi.org/10.3390/s18020586>
- Fogli, S., Brancaloni, L., Lambertini, C., Gerdol, R., 2014. Mowing regime has different effects on reed stands in relation to habitat. *J. Environ. Manage.* 134, 56–62. <https://doi.org/10.1016/j.jenvman.2014.01.001>
- Franklin, S.E., 2018. Pixel- and object-based multispectral classification of forest tree species from small unmanned aerial vehicles. *J. Unmanned Veh. Syst.* 6, 195–211. <https://doi.org/10.1139/jjuvs-2017-0022>
- Gago, J., Estrany, J., Estes, L., Fernie, A.R., Alorda, B., Brotman, Y., Flexas, J., Escalona, J.M., Medrano, H., 2020. Nano and Micro Unmanned Aerial Vehicles

## 7. References

- (UAVs): A New Grand Challenge for Precision Agriculture? *Curr. Protoc. Plant Biol.* 5, e20103. <https://doi.org/10.1002/cppb.20103>
- Gago, J., Fernie, A.R., Nikoloski, Z., Tohge, T., Martorell, S., Escalona, J.M., Ribas-Carbó, M., Flexas, J., Medrano, H., 2017. Integrative field scale phenotyping for investigating metabolic components of water stress within a vineyard. *Plant Methods* 13, 90. <https://doi.org/10.1186/s13007-017-0241-z>
- Gao, B.-C., Li, R.-R., 2012. Removal of Thin Cirrus Scattering Effects for Remote Sensing of Ocean Color From Space. *IEEE Geosci. Remote Sens. Lett.* 9, 972–976. <https://doi.org/10.1109/LGRS.2012.2187876>
- GDAL/OGR contributors. (2022). GDAL - Geospatial Data Abstraction Library., 2022.
- Getzin, S., Wiegand, K., Schöning, I., 2012. Assessing biodiversity in forests using very high-resolution images and unmanned aerial vehicles. *Methods Ecol. Evol.* 3, 397–404. <https://doi.org/10.1111/j.2041-210X.2011.00158.x>
- Ghirardi, N., Bresciani, M., Free, G., Pinardi, M., Bolpagni, R., Giardino, C., 2022. Evaluation of Macrophyte Community Dynamics (2015–2020) in Southern Lake Garda (Italy) from Sentinel-2 Data. *Appl. Sci.* <https://doi.org/10.3390/app12052693>
- Giannetti, F., Puletti, N., Quatrini, V., Travaglini, D., Bottalico, F., Corona, P., Chirici, G., 2018. Integrating terrestrial and airborne laser scanning for the assessment of single-tree attributes in Mediterranean forest stands. *Eur. J. Remote Sens.* 51, 795–807. <https://doi.org/10.1080/22797254.2018.1482733>
- Gini, R., Passoni, D., Pinto, L., Sona, G., 2014. Use of Unmanned Aerial Systems for multispectral survey and tree classification: a test in a park area of northern Italy. *Eur. J. Remote Sens.* 47, 251–269. <https://doi.org/10.5721/EuJRS20144716>
- Glasgow, H.B., Burkholder, J.M., Reed, R.E., Lewitus, A.J., Kleinman, J.E., 2004. Real-time remote monitoring of water quality: a review of current applications, and advancements in sensor, telemetry, and computing technologies. *J. Exp. Mar. Biol. Ecol.*, VOLUME 300 Special Issue 300, 409–448. <https://doi.org/10.1016/j.jembe.2004.02.022>
- Gonzalez, L.F., Montes, G.A., Puig, E., Johnson, S., Mengersen, K., Gaston, K.J., 2016. Unmanned Aerial Vehicles (UAVs) and Artificial Intelligence Revolutionizing Wildlife Monitoring and Conservation. *Sensors* 16, 97. <https://doi.org/10.3390/s16010097>
- Goodman, J.A., Lee, Z., Ustin, S.L., 2008. Influence of atmospheric and sea-surface corrections on retrieval of bottom depth and reflectance using a semi-analytical model: a case study in Kaneohe Bay, Hawaii. *Appl. Opt.* 47, F1. <https://doi.org/10.1364/AO.47.0000F1>
- Harmonization of UAS techniques for agricultural and natural ecosystems monitoring (HARMONIOUS). COST. URL <https://www.cost.eu/actions/CA16219> (accessed 2024-02-03).

## 7. References

- Harris, C.R., Millman, K.J., van der Walt, S.J., Gommers, R., Virtanen, P., Cournapeau, D., Wieser, E., Taylor, J., Berg, S., Smith, N.J., Kern, R., Picus, M., Hoyer, S., van Kerkwijk, M.H., Brett, M., Haldane, A., del Río, J.F., Wiebe, M., Peterson, P., Gérard-Marchant, P., Sheppard, K., Reddy, T., Weckesser, W., Abbasi, H., Gohlke, C., Oliphant, T.E., 2020. Array programming with NumPy. *Nature* 585, 357–362. <https://doi.org/10.1038/s41586-020-2649-2>
- Hashimoto, N., Saito, Y., Maki, M., Homma, K., 2019. Simulation of Reflectance and Vegetation Indices for Unmanned Aerial Vehicle (UAV) Monitoring of Paddy Fields. *Remote Sens.* <https://doi.org/10.3390/rs11182119>
- Hedley, J.D., Harborne, A.R., Mumby, P.J., 2005. Technical note: Simple and robust removal of sun glint for mapping shallow-water benthos. *Int. J. Remote Sens.* 26, 2107–2112. <https://doi.org/10.1080/01431160500034086>
- HELCOM, 2018.
- Hommersom, A., Kratzer, S., Laanen, M., Ansko, I., Ligi, M., Bresciani, M., Giardino, C., Beltran-Abauza, J.M., Moore, G., Wernand, M.R., Peters, S.W., 2012. Intercomparison in the field between the new WISP-3 and other radiometers (TriOS Ramses, ASD FieldSpec, and TACCS). *J. Appl. Remote Sens.* 6, 063615. <https://doi.org/10.1117/1.JRS.6.063615>
- Jarmalavičius, D., Zilinskas, G., Pupienis, D., 2011. Daugiamėčiai Baltijos jūros Lietuvos paplūdimių morfodinaminiai ypatumai. *Geografija* 47. <https://doi.org/10.6001/geografija.v47i2.2111>
- Jeffrey, S.W., Humphrey, G.F., 1975. New spectrophotometric equations for determining chlorophylls a, b, c1 and c2 in higher plants, algae and natural phytoplankton. *Biochem. Physiol. Pflanz.* 167, 191–194. [https://doi.org/10.1016/S0015-3796\(17\)30778-3](https://doi.org/10.1016/S0015-3796(17)30778-3)
- Jiang, H., 2012. Research on transparency derived from remote sensing and its spatial-temporal changes in Poyang Lake. *China Rural Water Hydropower* 1, 30–33.
- Jiang, W., Ni, Y., Pang, Z., He, G., Fu, J., Lu, J., Yang, K., Long, T., Lei, T., 2020. A New Index for Identifying Water Body from Sentinel-2 Satellite Remote Sensing Imagery. *ISPRS Ann. Photogramm. Remote Sens. Spat. Inf. Sci.* V-3–2020, 33–38. <https://doi.org/10.5194/isprs-annals-V-3-2020-33-2020>
- Jiménez López, J., Mulero-Pázmány, M., 2019. Drones for Conservation in Protected Areas: Present and Future. *Drones* 3, 10. <https://doi.org/10.3390/drones3010010>
- Jones, H.G., Vaughan, R.A., 2010. *Remote Sensing of Vegetation: Principles, Techniques, and Applications*. OUP Oxford.
- Joyce, K.E., 2005. A method for mapping live coral cover using remote sensing.
- Kalvaitienė, G., Vaičiūtė, D., Bučas, M., Gyraitė, G., Kataržytė, M., 2023. Macrophytes and their wrack as a habitat for faecal indicator bacteria and *Vibrio* in coastal marine environments. *Mar. Pollut. Bull.* 194, 115325. <https://doi.org/10.1016/j.marpolbul.2023.115325>

## 7. References

- Kapur, J.N., Sahoo, P.K., Wong, A.K.C., 1985. A new method for gray-level picture thresholding using the entropy of the histogram. *Comput. Vis. Graph. Image Process.* 29, 273–285. [https://doi.org/10.1016/0734-189X\(85\)90125-2](https://doi.org/10.1016/0734-189X(85)90125-2)
- Karlsen, S.R., Anderson, H.B., Wal, R. van der, Hansen, B.B., 2018. A new NDVI measure that overcomes data sparsity in cloud-covered regions predicts annual variation in ground-based estimates of high arctic plant productivity. *Environ. Res. Lett.* 13, 025011. <https://doi.org/10.1088/1748-9326/aa9f75>
- Karstens, S., Kiesel, J., Petersen, J., Etter, K., Schneider von Deimling, J., Vafeidis, A., Gross, F., 2022. Human-Induced Hydrological Connectivity: Impacts of Footpaths on Beach Wrack Transport in a Frequently Visited Baltic Coastal Wetland. *Front. Mar. Sci.* 9. <https://doi.org/10.3389/fmars.2022.929274>
- Kašpar, V., Hederová, L., Macek, M., Müllerová, J., Prošek, J., Surový, P., Wild, J., Kopecký, M., 2021. Temperature buffering in temperate forests: Comparing microclimate models based on ground measurements with active and passive remote sensing. *Remote Sens. Environ.* 263, 112522. <https://doi.org/10.1016/j.rse.2021.112522>
- Kattenborn, T., Eichel, J., Wisser, S., Burrows, L., Fassnacht, F.E., Schmidlein, S., 2020. Convolutional Neural Networks accurately predict cover fractions of plant species and communities in Unmanned Aerial Vehicle imagery. *Remote Sens. Ecol. Conserv.* 6, 472–486. <https://doi.org/10.1002/rse2.146>
- Kattenborn, T., Lopatin, J., Förster, M., Braun, A.C., Fassnacht, F.E., 2019. UAV data as alternative to field sampling to map woody invasive species based on combined Sentinel-1 and Sentinel-2 data. *Remote Sens. Environ.* 227, 61–73. <https://doi.org/10.1016/j.rse.2019.03.025>
- Kent, R., Lindsell, J.A., Laurin, G.V., Valentini, R., Coomes, D.A., 2015. Airborne LiDAR Detects Selectively Logged Tropical Forest Even in an Advanced Stage of Recovery. *Remote Sens.* 7, 8348–8367. <https://doi.org/10.3390/rs70708348>
- Kirk, J.T.O., 2010. *Light and Photosynthesis in Aquatic Ecosystems*, 3rd ed. Cambridge University Press, Cambridge. <https://doi.org/10.1017/CBO9781139168212>
- Kislik, C., Dronova, I., Kelly, M., 2018. UAVs in Support of Algal Bloom Research: A Review of Current Applications and Future Opportunities. *Drones* 2, 35. <https://doi.org/10.3390/drones2040035>
- Knoth, C., Klein, B., Prinz, T., Kleinebecker, T., 2013. Unmanned aerial vehicles as innovative remote sensing platforms for high-resolution infrared imagery to support restoration monitoring in cut-over bogs. *Appl. Veg. Sci.* 16, 509–517. <https://doi.org/10.1111/avsc.12024>
- Kwon, Y.S., Baek, S.H., Lim, Y.K., Pyo, J., Ligaray, M., Park, Y., Cho, K.H., 2018. Monitoring Coastal Chlorophyll-a Concentrations in Coastal Areas Using Machine Learning Models. *Water* 10, 1020. <https://doi.org/10.3390/w10081020>

## 7. References

- Lambers, H., Oliveira, R.S., 2019. *Plant Physiological Ecology*. Springer International Publishing, Cham. <https://doi.org/10.1007/978-3-030-29639-1>
- Larrinaga, A.R., Brotons, L., 2019. Greenness Indices from a Low-Cost UAV Imagery as Tools for Monitoring Post-Fire Forest Recovery. *Drones* 3, 6. <https://doi.org/10.3390/drones3010006>
- Laslier, M., Hubert-Moy, L., Corpetti, T., Dufour, S., 2019. Monitoring the colonization of alluvial deposits using multitemporal UAV RGB-imagery. *Appl. Veg. Sci.* 22, 561–572. <https://doi.org/10.1111/avsc.12455>
- Lee, Z., Shang, S., Hu, C., Du, K., Weidemann, A., Hou, W., Lin, J., Lin, G., 2015. Secchi disk depth: A new theory and mechanistic model for underwater visibility. *Remote Sens. Environ.* 169, 139–149. <https://doi.org/10.1016/j.rse.2015.08.002>
- Lin, F., Gan, L., Jin, Q., You, A., Hua, L., 2022. Water Quality Measurement and Modelling Based on Deep Learning Techniques: Case Study for the Parameter of Secchi Disk. *Sensors* 22. <https://doi.org/10.3390/s22145399>
- Lin, T.-Y., Goyal, P., Girshick, R., He, K., Dollar, P., 2017. Focal Loss for Dense Object Detection. Presented at the Proceedings of the IEEE International Conference on Computer Vision, pp. 2980–2988.
- Lisein, J., Pierrot-Deseilligny, M., Bonnet, S., Lejeune, P., 2013. A Photogrammetric Workflow for the Creation of a Forest Canopy Height Model from Small Unmanned Aerial System Imagery. *Forests* 4, 922–944. <https://doi.org/10.3390/f4040922>
- Lithuanian Republic Ministry of Environment. Dėl Makrofitų tyrimų ežeruose ir tvenkiniuose metodikos patvirtinimo. įsakymo Nr. D1-934., 2013.
- Liu, T., Abd-Elrahman, A., Morton, J., Wilhelm, V.L., 2018. Comparing fully convolutional networks, random forest, support vector machine, and patch-based deep convolutional neural networks for object-based wetland mapping using images from small unmanned aircraft system. *GIScience Remote Sens.* 55, 243–264. <https://doi.org/10.1080/15481603.2018.1426091>
- Lyzenga, D.R., Malinas, N.P., Tanis, F.J., 2006. Multispectral bathymetry using a simple physically based algorithm. *IEEE Trans. Geosci. Remote Sens.* 44, 2251–2259. <https://doi.org/10.1109/TGRS.2006.872909>
- M Muslim, A., Wei Sheng, C., Che Din, M.S., Khalil, I., Hossain, M., 2019. Coral Reef Mapping of UAV: A Comparison of Sun Glint Correction Methods. *Remote Sens.* 11, 2422. <https://doi.org/10.3390/rs11202422>
- Mamaghani, B., Salvaggio, C., 2019. Multispectral Sensor Calibration and Characterization for sUAS Remote Sensing. *Sensors* 19, 4453. <https://doi.org/10.3390/s19204453>
- Mandrekar, J.N., 2010. Receiver Operating Characteristic Curve in Diagnostic Test Assessment. *J. Thorac. Oncol.* 5, 1315–1316. <https://doi.org/10.1097/JTO.0b013e3181ec173d>



## 7. References

- Martin, F.-M., Müllerová, J., Borgniet, L., Dommanget, F., Breton, V., Evette, A., 2018. Using Single- and Multi-Date UAV and Satellite Imagery to Accurately Monitor Invasive Knotweed Species. *Remote Sens.* 10, 1662. <https://doi.org/10.3390/rs10101662>
- Marusig, D., Petruzzellis, F., Tomasella, M., Napolitano, R., Altobelli, Nardini, 2020. Correlation of Field-Measured and Remotely Sensed Plant Water Status as a Tool to Monitor the Risk of Drought-Induced Forest Decline. *Forests* 11, 77. <https://doi.org/10.3390/f11010077>
- McCullough, I.M., Loftin, C.S., Sader, S.A., 2012. High-frequency remote monitoring of large lakes with MODIS 500 m imagery. *Remote Sens. Environ.* 124, 234–241. <https://doi.org/10.1016/j.rse.2012.05.018>
- Meneses, N.C., Baier, S., Reidelstürz, P., Geist, J., Schneider, T., 2018. Modelling heights of sparse aquatic reed (*Phragmites australis*) using Structure from Motion point clouds derived from Rotary- and Fixed-Wing Unmanned Aerial Vehicle (UAV) data. *Limnologica* 72, 10–21. <https://doi.org/10.1016/j.limno.2018.07.001>
- Michez, A., Piégay, H., Lisein, J., Claessens, H., Lejeune, P., 2016. Classification of riparian forest species and health condition using multi-temporal and hyperspatial imagery from unmanned aerial system. *Environ. Monit. Assess.* 188, 146. <https://doi.org/10.1007/s10661-015-4996-2>
- Michez, A., Piégay, H., Toromanoff, F., Brogna, D., Bonnet, S., Lejeune, P., Claessens, H., 2013. LiDAR derived ecological integrity indicators for riparian zones: Application to the Houille river in Southern Belgium/Northern France. *Ecol. Indic.* 34, 627–640. <https://doi.org/10.1016/j.ecolind.2013.06.024>
- Milletari, F., Navab, N., Ahmadi, S.-A., 2016. V-Net: Fully Convolutional Neural Networks for Volumetric Medical Image Segmentation, in: 2016 Fourth International Conference on 3D Vision (3DV). Presented at the 2016 Fourth International Conference on 3D Vision (3DV), pp. 565–571. <https://doi.org/10.1109/3DV.2016.79>
- Minařík, R., Langhammer, J., 2016. USE OF A MULTISPECTRAL UAV PHOTOGRAMMETRY FOR DETECTION AND TRACKING OF FOREST DISTURBANCE DYNAMICS. *Int. Arch. Photogramm. Remote Sens. Spat. Inf. Sci.* XLI-B8, 711–718. <https://doi.org/10.5194/isprs-archives-XLI-B8-711-2016>
- Mokroš, M., Výboštok, J., Merganič, J., Hollaus, M., Barton, I., Koreň, M., Tomašík, J., Čerňava, J., 2017. Early Stage Forest Windthrow Estimation Based on Unmanned Aircraft System Imagery. *Forests* 8, 306. <https://doi.org/10.3390/f8090306>
- Müller, D., Soto-Rey, I., Kramer, F., 2022. Towards a guideline for evaluation metrics in medical image segmentation. *BMC Res. Notes* 15, 210. <https://doi.org/10.1186/s13104-022-06096-y>
- Müllerová, J., 2019. UAS for Nature Conservation—Monitoring Invasive Species. *Appl. Small Unmanned Aircr. Syst. Best Pract. Case Stud.* 157.

## 7. References

- Müllerová, J., Bartaloš, T., Brůna, J., Dvořák, P., Vítková, M., 2017a. Unmanned aircraft in nature conservation: an example from plant invasions. *Int. J. Remote Sens.* 38, 2177–2198. <https://doi.org/10.1080/01431161.2016.1275059>
- Müllerová, J., Brůna, J., Bartaloš, T., Dvořák, P., Vítková, M., Pyšek, P., 2017b. Timing Is Important: Unmanned Aircraft vs. Satellite Imagery in Plant Invasion Monitoring. *Front. Plant Sci.* 8.
- Murray, C.J., Müller-Karulis, B., Carstensen, J., Conley, D.J., Gustafsson, B.G., Andersen, J.H., 2019. Past, Present and Future Eutrophication Status of the Baltic Sea. *Front. Mar. Sci.* 6.
- Näsi, R., Honkavaara, E., Blomqvist, M., Lyytikäinen-Saarenmaa, P., Hakala, T., Viljanen, N., Kantola, T., Holopainen, M., 2018. Remote sensing of bark beetle damage in urban forests at individual tree level using a novel hyperspectral camera from UAV and aircraft. *Urban For. Urban Green.*, Special feature: Strategic gardens and gardening: Inviting a widened perspective on the values of private green space 30, 72–83. <https://doi.org/10.1016/j.ufug.2018.01.010>
- Otsu, N., 1979. A Threshold Selection Method from Gray-Level Histograms 9(1), 62–66. <https://doi.org/10.1109/tsmc.1979.4310076>
- Oyama, Y., Matsushita, B., Fukushima, T., 2015. Distinguishing surface cyanobacterial blooms and aquatic macrophytes using Landsat/TM and ETM+ shortwave infrared bands. *Remote Sens. Environ.*, Special Issue: Remote Sensing of Inland Waters 157, 35–47. <https://doi.org/10.1016/j.rse.2014.04.031>
- Ozesmi, S.L., Bauer, M.E., 2002. Satellite remote sensing of wetlands. *Wetl. Ecol. Manag.* 10, 381–402. <https://doi.org/10.1023/A:1020908432489>
- Pan, Y., Flindt, M., Schneider-Kamp, P., Holmer, M., 2021. Beach wrack mapping using unmanned aerial vehicles for coastal environmental management. *Ocean Coast. Manag.* 213, 105843. <https://doi.org/10.1016/j.ocecoaman.2021.105843>
- Pande-Chhetri, R., Abd-Elrahman, A., Liu, T., Morton, J., Wilhelm, V.L., 2017. Object-based classification of wetland vegetation using very high-resolution unmanned air system imagery. *Eur. J. Remote Sens.* 50, 564–576. <https://doi.org/10.1080/22797254.2017.1373602>
- Paneque-Gálvez, J., McCall, M.K., Napoletano, B.M., Wich, S.A., Koh, L.P., 2014. Small Drones for Community-Based Forest Monitoring: An Assessment of Their Feasibility and Potential in Tropical Areas. *Forests* 5, 1481–1507. <https://doi.org/10.3390/f5061481>
- Park, J.Y., Muller-Landau, H.C., Lichstein, J.W., Rifai, S.W., Dandois, J.P., Bohlman, S.A., 2019. Quantifying Leaf Phenology of Individual Trees and Species in a Tropical Forest Using Unmanned Aerial Vehicle (UAV) Images. *Remote Sens.* 11, 1534. <https://doi.org/10.3390/rs11131534>

## 7. References

- Parsons T.R., Maita Y., Lalli C.M., 1984. A manual of chemical and biological methods for sea water analysis. *Deep Sea Res. Part Oceanogr. Res. Pap.* 31, 1523. [https://doi.org/10.1016/0198-0149\(84\)90086-4](https://doi.org/10.1016/0198-0149(84)90086-4)
- Pedregosa, F., Varoquaux, G., Gramfort, A., Michel, V., Thirion, B., Grisel, O., Blondel, M., Prettenhofer, P., Weiss, R., Dubourg, V., Vanderplas, J., Passos, A., Cournapeau, D., Brucher, M., Perrot, M., Duchesnay, É., 2011. Scikit-learn: Machine Learning in Python. *J. Mach. Learn. Res.* 12, 2825–2830.
- Pham, T.N., Ho, A.P.H., Nguyen, T.V., Nguyen, H.M., Truong, N.H., Huynh, N.D., Nguyen, T.H., Dung, L.T., 2020. Development of a Solar-Powered IoT-Based Instrument for Automatic Measurement of Water Clarity. *Sensors* 20, 2051. <https://doi.org/10.3390/s20072051>
- Poikane, S., Portielje, R., Denys, L., Elferts, D., Kelly, M., Kolada, A., Mäemets, H., Phillips, G., Søndergaard, M., Willby, N., van den Berg, M.S., 2018. Macrophyte assessment in European lakes: Diverse approaches but convergent views of ‘good’ ecological status. *Ecol. Indic.* 94, 185–197. <https://doi.org/10.1016/j.ecolind.2018.06.056>
- Pugnaire, F., Valladares, F., 1999. *Handbook of Functional Plant Ecology*. CRC Press.
- QGIS version 3.16. [WWW Document], 2022. URL <https://qgis.org/en/site/> (accessed 2023-07-20).
- Rapp, R.E., Datta, A., Irmak, S., Arkebauer, T.J., Knezevic, S.Z., 2012. Integrated Management of Common Reed (*Phragmites australis*) along the Platte River in Nebraska. *Weed Technol.* 26, 326–333. <https://doi.org/10.1614/WT-D-11-00119.1>
- Richter, R., Wang, X., Bachmann, M., Schläpfer, D., 2011. Correction of cirrus effects in Sentinel-2 type of imagery. *Int. J. Remote Sens.* 32, 2931–2941. <https://doi.org/10.1080/01431161.2010.520346>
- Ridler, T.W., Calvard, S., 1978. Picture thresholding using an iterative selection method. *IEEE Trans Syst Man Cybern* 8, 630–632.
- Ronneberger, O., Fischer, P., Brox, T., 2015. U-Net: Convolutional Networks for Biomedical Image Segmentation, in: Navab, N., Hornegger, J., Wells, W.M., Frangi, A.F. (Eds.), *Medical Image Computing and Computer-Assisted Intervention – MICCAI 2015*. Springer International Publishing, Cham, pp. 234–241. [https://doi.org/10.1007/978-3-319-24574-4\\_28](https://doi.org/10.1007/978-3-319-24574-4_28)
- Rowan, G., Kalacska, M., 2023. Remote sensing of submerged aquatic vegetation: an introduction and best practices review. <https://doi.org/10.31219/osf.io/2gpxz>
- Roy, D.P., Wulder, M.A., Loveland, T.R., Woodcock, C.E., Allen, R.G., Anderson, M.C., Helder, D., Irons, J.R., Johnson, D.M., Kennedy, R., 2014. Landsat-8: Science and product vision for terrestrial global change research. *Remote Sens. Environ.* 145, 154–172.
- Ruwaimana, M., Satyanarayana, B., Otero, V., Muslim, A.M., A, M.S., Ibrahim, S., Raymaekers, D., Koedam, N., Dahdouh-Guebas, F., 2018. The advantages of us-

## 7. References

- ing drones over space-borne imagery in the mapping of mangrove forests. *PLOS ONE* 13, e0200288. <https://doi.org/10.1371/journal.pone.0200288>
- Sagan, V., Peterson, K.T., Maimaitijiang, M., Sidike, P., Sloan, J., Greeling, B.A., Maalouf, S., Adams, C., 2020. Monitoring inland water quality using remote sensing: potential and limitations of spectral indices, bio-optical simulations, machine learning, and cloud computing. *Earth-Sci. Rev.* 205, 103187. <https://doi.org/10.1016/j.earscirev.2020.103187>
- Schindelin, J., Arganda-Carreras, I., Frise, E., Kaynig, V., Longair, M., Pietzsch, T., Preibisch, S., Rueden, C., Saalfeld, S., Schmid, B., Tinevez, J.-Y., White, D.J., Hartenstein, V., Eliceiri, K., Tomancak, P., Cardona, A., 2012. Fiji: an open-source platform for biological-image analysis. *Nat. Methods* 9, 676–682. <https://doi.org/10.1038/nmeth.2019>
- Schlacher, T.A., Schoeman, D.S., Dugan, J., Lastra, M., Jones, A., Scapini, F., McLachlan, A., 2008. Sandy beach ecosystems: key features, sampling issues, management challenges and climate change impacts. *Mar. Ecol.* 29, 70–90. <https://doi.org/10.1111/j.1439-0485.2007.00204.x>
- Schuwirth, N., 2020. Towards an integrated surface water quality assessment: Aggregation over multiple pollutants and time. *Water Res.* 186, 116330. <https://doi.org/10.1016/j.watres.2020.116330>
- Seabold, S., Perktold, J., 2010. Statsmodels: Econometric and Statistical Modeling with Python. *Proc. 9th Python Sci. Conf.* 92–96. <https://doi.org/10.25080/Majora-92bf1922-011>
- Seifert, E., Seifert, S., Vogt, H., Drew, D., van Aardt, J., Kunneke, A., Seifert, T., 2019. Influence of Drone Altitude, Image Overlap, and Optical Sensor Resolution on Multi-View Reconstruction of Forest Images. *Remote Sens.* 11, 1252. <https://doi.org/10.3390/rs11101252>
- Senf, C., Seidl, R., Hostert, P., 2017. Remote sensing of forest insect disturbances: Current state and future directions. *Int. J. Appl. Earth Obs. Geoinformation* 60, 49–60. <https://doi.org/10.1016/j.jag.2017.04.004>
- Sezgin, M., Sankur, B., 2004. Survey over image thresholding techniques and quantitative performance evaluation. *J. Electron. Imaging* 13, 146–165. <https://doi.org/10.1117/1.1631315>
- Sharifi, A., Felegari, S., 2023. Remotely sensed normalized difference red-edge index for rangeland biomass estimation. *Aircr. Eng. Aerosp. Technol.* 95, 1128–1136. <https://doi.org/10.1108/AEAT-07-2022-0199>
- Sibanda, M., Mutanga, O., Chimonyo, V.G.P., Clulow, A.D., Shoko, C., Mazvimavi, D., Dube, T., Mabhaudhi, T., 2021. Application of Drone Technologies in Surface Water Resources Monitoring and Assessment: A Systematic Review of Progress, Challenges, and Opportunities in the Global South. *Drones* 5, 84. <https://doi.org/10.3390/drones5030084>

## 7. References

- Sinkevičienė, D.Z., Matulevičiūtė, D.D., Stankevičiūtė, D.J., 2005. Makrofitų monitoringas upėse ir ežeruose 18.
- Sinkevičienė, Z., Bučas, M., Ilginė, R., Vaičiūtė, D., Kataržytė, M., Petkuvienė, J., 2017. Charophytes in the estuarine Curonian Lagoon: Have the changes in diversity, abundance and distribution occurred since the late 1940s? *Oceanol. Hydrobiol. Stud.* 46, 186–198.
- Smigaj, M., Gaulton, R., Suárez, J.C., Barr, S.L., 2019. Canopy temperature from an Unmanned Aerial Vehicle as an indicator of tree stress associated with red band needle blight severity. *For. Ecol. Manag.* 433, 699–708. <https://doi.org/10.1016/j.foreco.2018.11.032>
- Srivastava, N., Hinton, G., Krizhevsky, A., Sutskever, I., Salakhutdinov, R., 2014. Dropout: a simple way to prevent neural networks from overfitting. *J. Mach. Learn. Res.* 15, 1929–1958.
- Stephens, D.L.B., Carlson, R., Horsburgh, C.A., Hoyer, M., Bachmann, R., Canfield, D., 2015. Regional distribution of Secchi disk transparency in waters of the United States. *Lake Reserv. Manag.* 31, 55–63. <https://doi.org/10.1080/10402381.2014.1001539>
- Stock, A., 2015. Satellite mapping of Baltic Sea Secchi depth with multiple regression models. *Int. J. Appl. Earth Obs. Geoinformation* 40, 55–64. <https://doi.org/10.1016/j.jag.2015.04.002>
- Strong, J., Elliott, M., 2017. The value of remote sensing techniques in supporting effective extrapolation across multiple marine spatial scales. *Mar. Pollut. Bull.* 116. <https://doi.org/10.1016/j.marpolbul.2017.01.028>
- Swetnam, T.L., Gillan, J.K., Sankey, T.T., McClaran, M.P., Nichols, M.H., Heilman, P., McVay, J., 2018. Considerations for achieving cross-platform point cloud data fusion across different dryland ecosystem structural states. *Front. Plant Sci.* 8, 2144.
- Taddia, Y., Corbau, C., Zambello, E., Pellegrinelli, A., 2019. UAVs for Structure-From-Motion Coastal Monitoring: A Case Study to Assess the Evolution of Embryo Dunes over a Two-Year Time Frame in the Po River Delta, Italy. *Sensors* 19, 1717. <https://doi.org/10.3390/s19071717>
- Tamondong, A., Nakamura, T., Kobayashi, Y., Garcia, M., Nadaoka, K., 2020. INVESTIGATING THE EFFECTS OF RIVER DISCHARGES ON SUBMERGED AQUATIC VEGETATION USING UAV IMAGES AND GIS TECHNIQUES. *ISPRS Ann. Photogramm. Remote Sens. Spat. Inf. Sci.* V-5–2020, 93–99. <https://doi.org/10.5194/isprs-annals-V-5-2020-93-2020>
- The Habitats Directive - European Commission, 2013.
- Ting, K.M., 2017. Confusion Matrix, in: Sammut, C., Webb, G.I. (Eds.), *Encyclopedia of Machine Learning and Data Mining*. Springer US, Boston, MA, pp. 260–260. [https://doi.org/10.1007/978-1-4899-7687-1\\_50](https://doi.org/10.1007/978-1-4899-7687-1_50)

## 7. References

- Tmušić, G., Manfreda, S., Aasen, H., James, M.R., Gonçalves, G., Ben-Dor, E., Brook, A., Polinova, M., Arranz, J.J., Mészáros, J., Zhuang, R., Johansen, K., Malbeteau, Y., Lima, I.P. de, Davids, C., Herban, S., McCabe, M.F., 2020. Current Practices in UAS-based Environmental Monitoring. *Remote Sens.* 12, 1001. <https://doi.org/10.3390/rs12061001>
- Tomasello, A., Bosman, A., Signa, G., Rende, S.F., Andolina, C., Cilluffo, G., Cassetti, F.P., Mazzola, A., Calvo, S., Randazzo, G., Scarpato, A., Vizzini, S., 2022. 3D-Reconstruction of a Giant *Posidonia oceanica* Beach Wrack (Banquette): Sizing Biomass, Carbon and Nutrient Stocks by Combining Field Data With High-Resolution UAV Photogrammetry. *Front. Mar. Sci.* 9.
- Turner, W., Rondinini, C., Pettorelli, N., Mora, B., Leidner, A.K., Szantoi, Z., Buchanan, G., Dech, S., Dwyer, J., Herold, M., Koh, L.P., Leimgruber, P., Taubenboeck, H., Wegmann, M., Wikelski, M., Woodcock, C., 2015. Free and open-access satellite data are key to biodiversity conservation. *Biol. Conserv.* 182, 173–176. <https://doi.org/10.1016/j.biocon.2014.11.048>
- Villa, P., Laini, A., Bresciani, M., Bolpagni, R., 2013. A remote sensing approach to monitor the conservation status of lacustrine *Phragmites australis* beds. *Wetl. Ecol. Manag.* 21, 399–416. <https://doi.org/10.1007/s11273-013-9311-9>
- Vincevica-Gaile, Z., Sachpazidou, V., Bisters, V., Klavins, M., Anne, O., Grinfelde, I., Hanc, E., Hogland, W., Ibrahim, M.A., Jani, Y., Kriipsalu, M., Pal, D., Pehme, K.-M., Shanskiy, M., Saaremäe, E., Pilecka-Ulcugaceva, J., Celms, A., Rudovica, V., Hendroko Setyobudi, R., Wdowin, M., Zahoor, M., Aouissi, H.A., Krauklis, A.E., Zekker, I., Burlakovs, J., 2022. Applying Macroalgal Biomass as an Energy Source: Utility of the Baltic Sea Beach Wrack for Thermochemical Conversion. *Sustainability* 14, 13712. <https://doi.org/10.3390/su142113712>
- Virtanen, P., Gommers, R., Oliphant, T.E., Haberland, M., Reddy, T., Cournapeau, D., Burovski, E., Peterson, P., Weckesser, W., Bright, J., van der Walt, S.J., Brett, M., Wilson, J., Millman, K.J., Mayorov, N., Nelson, A.R.J., Jones, E., Kern, R., Larson, E., Carey, C.J., Polat, İ., Feng, Y., Moore, E.W., VanderPlas, J., Laxalde, D., Perktold, J., Cimrman, R., Henriksen, I., Quintero, E.A., Harris, C.R., Archibald, A.M., Ribeiro, A.H., Pedregosa, F., van Mulbregt, P., 2020. SciPy 1.0: fundamental algorithms for scientific computing in Python. *Nat. Methods* 17, 261–272. <https://doi.org/10.1038/s41592-019-0686-2>
- Vooban, 2018. Satellite Image Segmentation: a Workflow with U-Net. Vooban AI.
- Wallace, L., Lucieer, A., Malenovský, Z., Turner, D., Vopěnka, P., 2016. Assessment of Forest Structure Using Two UAV Techniques: A Comparison of Airborne Laser Scanning and Structure from Motion (SfM) Point Clouds. *Forests* 7, 62. <https://doi.org/10.3390/f7030062>

## 7. References

- Walt, S. van der, Schönberger, J.L., Nunez-Iglesias, J., Boulogne, F., Warner, J.D., Yager, N., Gouillart, E., Yu, T., 2014. scikit-image: image processing in Python. *PeerJ* 2, e453. <https://doi.org/10.7717/peerj.453>
- Wang, D., Xing, S., He, Y., Yu, J., Xu, Q., Li, P., 2022. Evaluation of a New Lightweight UAV-Borne Topo-Bathymetric LiDAR for Shallow Water Bathymetry and Object Detection. *Sensors* 22, 1379. <https://doi.org/10.3390/s22041379>
- Wang, H., Liu, H., Huang, N., Bi, J., Ma, X., Ma, Z., Shangguan, Z., Zhao, H., Feng, Q., Liang, T., Cao, G., Schmid, B., He, J.-S., 2021. Satellite-derived NDVI underestimates the advancement of alpine vegetation growth over the past three decades. *Ecology* 102, e03518. <https://doi.org/10.1002/ecy.3518>
- Warren, M., Simis, S., Martinez-Vicente, V., Poser, K., Bresciani, M., Alikas, K., Spyrakos, E., Giardino, C., Ansper, A., 2019. Assessment of atmospheric correction algorithms for the Sentinel-2A MultiSpectral Imager over coastal and inland waters. *Remote Sens. Environ.* 225, 267–289. <https://doi.org/10.1016/j.rse.2019.03.018>
- Westoby, M.J., Brasington, J., Glasser, N.F., Hambrey, M.J., Reynolds, J.M., 2012. ‘Structure-from-Motion’ photogrammetry: A low-cost, effective tool for geoscience applications. *Geomorphology* 179, 300–314. <https://doi.org/10.1016/j.geomorph.2012.08.021>
- White, J.C., Stepper, C., Tompalski, P., Coops, N.C., Wulder, M.A., 2015. Comparing ALS and Image-Based Point Cloud Metrics and Modelled Forest Inventory Attributes in a Complex Coastal Forest Environment. *Forests* 6, 3704–3732. <https://doi.org/10.3390/f6103704>
- Wickham, H., 2009. *ggplot2: Elegant Graphics for Data Analysis*. Springer, New York, NY. <https://doi.org/10.1007/978-0-387-98141-3>
- Windle, A.E., Silsbe, G.M., 2021. Evaluation of Unoccupied Aircraft System (UAS) Remote Sensing Reflectance Retrievals for Water Quality Monitoring in Coastal Waters. *Front. Environ. Sci.* 9.
- Woelfel, J., Hofmann, J., Müsch, M., Gilles, A., Siemen, H., Schubert, H., 2021. Beach wrack of the Baltic Sea challenges for sustainable use and management (Toolkit). <https://doi.org/10.13140/RG.2.2.10735.71840>
- Wood, S., 2023. *mgcv: Mixed GAM Computation Vehicle with Automatic Smoothness Estimation*.
- Xu, H., 2005. A study on information extraction of water body with the modified normalized difference water index (MNDWI). *J. Remote Sens.* 9, 589–595.
- Yen, J.-C., Chang, F.-J., Chang, S., 1995. A new criterion for automatic multilevel thresholding. *IEEE Trans. Image Process.* 4, 370–378. <https://doi.org/10.1109/83.366472>
- Yu, D.F., Xing, Q.G., Lou, M.J., Shi, P., 2014. Retrieval of Secchi disk depth in the Yellow Sea and East China Sea using 8-day MODIS data. *IOP Conf. Ser. Earth Environ. Sci.* 17, 012112. <https://doi.org/10.1088/1755-1315/17/1/012112>

## 7. References

- Yuan, C., Zhang, Y., Liu, Z., 2015. A survey on technologies for automatic forest fire monitoring, detection, and fighting using unmanned aerial vehicles and remote sensing techniques. *Can. J. For. Res.* 45, 783–792. <https://doi.org/10.1139/cjfr-2014-0347>
- Yuba, N., Kawamura, K., Yasuda, T., Lim, J., Yoshitoshi, R., Watanabe, N., Kurokawa, Y., Maeda, T., 2021. Discriminating *Pennisetum alopecuoides* plants in a grazed pasture from unmanned aerial vehicles using object-based image analysis and random forest classifier. *Grassl. Sci.* 67, 73–82. <https://doi.org/10.1111/grs.12288>
- Zack, G.W., Rogers, W.E., Latt, S.A., 1977. Automatic measurement of sister chromatid exchange frequency. *J. Histochem. Cytochem.* 25, 741–753. <https://doi.org/10.1177/25.7.70454>
- Zaneveld, J.R.V., Barnard, A.H., Boss, E., 2005. Theoretical derivation of the depth average of remotely sensed optical parameters. *Opt. Express* 13, 9052. <https://doi.org/10.1364/OPEX.13.009052>
- Zarco-Tejada, P.J., González-Dugo, V., Berni, J.A.J., 2012. Fluorescence, temperature and narrow-band indices acquired from a UAV platform for water stress detection using a micro-hyperspectral imager and a thermal camera. *Remote Sens. Environ., Remote Sensing of Urban Environments* 117, 322–337. <https://doi.org/10.1016/j.rse.2011.10.007>
- Zarco-Tejada, P.J., González-Dugo, V., Williams, L.E., Suárez, L., Berni, J.A.J., Goldammer, D., Fereres, E., 2013. A PRI-based water stress index combining structural and chlorophyll effects: Assessment using diurnal narrow-band airborne imagery and the CWSI thermal index. *Remote Sens. Environ.* 138, 38–50. <https://doi.org/10.1016/j.rse.2013.07.024>
- Zhang, C., Filella, I., Liu, D., Ogaya, R., Llusà, J., Asensio, D., Peñuelas, J., 2017. Photochemical Reflectance Index (PRI) for Detecting Responses of Diurnal and Seasonal Photosynthetic Activity to Experimental Drought and Warming in a Mediterranean Shrubland. *Remote Sens.* 9, 1189. <https://doi.org/10.3390/rs9111189>
- Zhang, C., Pattey, E., Liu, J., Cai, H., Shang, J., Dong, T., 2018. Retrieving Leaf and Canopy Water Content of Winter Wheat Using Vegetation Water Indices. *IEEE J. Sel. Top. Appl. Earth Obs. Remote Sens.* 11, 112–126. <https://doi.org/10.1109/JSTARS.2017.2773625>
- Zhang, J., Hu, J., Lian, J., Fan, Z., Ouyang, X., Ye, W., 2016. Seeing the forest from drones: Testing the potential of lightweight drones as a tool for long-term forest monitoring. *Biol. Conserv.* 198. <https://doi.org/10.1016/j.biocon.2016.03.027>



# 8

---

## Summary in Lithuanian

### ĮVADAS

Vandens telkiniai, įskaitant ežerus, Baltijos jūrą ir jos pakrančių regioną, susiduria su eutrofikacijos iššūkiais, kurie stebimi atsižvelgiant į tarptautines direktyvas, tokias kaip: Bendroji vandens politikos direktyva (BVPD), Jūrų strategijos pagrindų direktyva (JSPD), Buveinių direktyva ir Helsinkio konvencija. Šiomis direktyvomis siekiama užtikrinti tvarų vandens naudojimą ir jūrų ekosistemų apsaugą (Murray et al., 2019; Chemin et al., 2004; Dassenakis et al., 2011). Keli svarbiausi eutrofikacijos stebėsenos parametrai yra vandens skaidrumas, makrofitų paplitimas ir maudyklų vandens kokybė, į kurią įeina išmestų paplūdimio makrodumblių stebėjimas bei vertinimas pagal Maudyklų vandens direktyvą ir Lietuvos higienos standartus (Europos Parlamentas, 2006). Vis dėlto, tradiciniai stebėsenos metodai, pavyzdžiui, vandens skaidrumo nustatymas Secchi disku, reikalauja daug darbo, gali būti neobjektyvūs bei gali netiksliai atspindėti didesnius plotus (Jiang, 2012; Yu et al., 2014; Pham et al., 2020; Stock, 2015). Šį iššūkį pabrėžia Bendrosios vandens politikos direktyvos nustatytas reikalavimas vykdyti svarbių vandens telkinių stebėseną ir šalys, pavyzdžiui, Estija ir Švedija, kurios dėl finansinių ir praktinių apribojimų sunkiai įgyvendina šiuos tikslus (Dworak et al., 2005; Ministry of Environment, 2009; Alikas et al., 2015).

Europoje makrofitų stebėseną atliekama pasitelkiant įvairius, dažnai transektiniais metodais pagrįstus ėminių paėmimo būdus, kuriais siekiama nustatyti aprėptį

ir įvertinti ekologinę būklę, tačiau šie *in situ* matavimai reikalauja daug išteklių, yra destruktivūs, o jų atlikimo dažnumas įvairiose šalyse skiriasi (Poikane et al., 2018; Søndergaard et al., 2013; Datta et al. 2021). Pagal Buveinių direktyvą „Natura 2000“ teritorijose makrofitų buveinių stebėseną yra svarbi vertinant jų apsaugos būklę (Europos Komisija, 2013). Nors atliekant stebėseną yra renkami duomenys apie įvairias makrofitų rūšis ir vandens kokybę, į paplūdimį išmestų sąnašų – svarbaus pakrančių ekosistemų rodiklio – dabartinėje stebėsenos praktikoje vis dar mažai akcentuojama. Šie makrodumbliai yra fekalinių indikatorių bakterijų ir patogenų, keliančių pavojų sveikatai, rodiklis, todėl jų pokyčių stebėsenos protokolui reikalingas persvarstymas (Kalvaitienė ir kt., 2023 ir citatos šiame darbe).

Lietuvoje vandens skaidrumo ir makrofitų stebėseną yra neatsiejama ežerų ir pakrančių vandenų ekologinės būklės vertinimo dalis, kurios metodai yra patvirtinti Lietuvos Respublikos aplinkos ministerijos ir šiuo metu Lietuvoje kas šešerius metus ši stebėseną aprėpia apie 80 ežerų, taip pat visas gėlavandenes buveines, didesnes nei 50 ha, kaip to reikalauja Bendroji vandens politikos direktyva (Lietuvos Respublikos aplinkos ministerija, 2013; Broeck et al., 2015). Vandens skaidrumas skirstomas į penkias klases nuo „labai geros“ iki „labai blogos“, nustatant konkrečias geros ekologinės būklės ribas: ežeruose „gera“ būklė yra tuomet, kada vandens skaidrumas yra didesnis nei 1,3 m, o priekrantės vandenyse – 5,0 m. Vidaus ir tarpiniuose vandenyse taikant makrofitų vertinimo metodą imami transektiniai mėginiai, o makrofitų rūšių aprėptis vertinama pagal Brauno-Blanquet arba procentinę skalę liepos ir rugpjūčio mėnesiais. Tas pats metodas taikomas makrofitų buveinių stebėsenai pagal Buveinių direktyvą, pavyzdžiui, Kuršių mariose į raudonąją knygą įtrauktos rūšies *Nymphoides peltata* plotas yra labai svarbus jos buveinės vertinimui naudojant ortofotografines nuotraukas (Bučas ir kt., 2023). Šis metodas taip pat galėtų būti tinkamas stebėti didelio masto buveinių pokyčius (Sinkevičienė ir kt., 2017), kuriuos sudėtinga įvertinti tradiciniais metodais (transektiniais tyrimais). Be to, paplūdimio sąnašų stebėseną dažnai nenuosekliai vykdo vietinės paplūdimių institucijos, vizualiai vertindamos, ar paplūdimio sąnašų gausu ir jų daugėja, nesigilindamos į galimą poveikį aplinkai (Lietuvos Respublika, Aplinkos ministerija, 2007).

Nuotolinis stebėjimas naudojant palydovus, pavyzdžiui, daugiaspektrinį MSI (angl. MultiSpectral Instrument) jutiklį esantį Sentinel-2 palydovo platformoje, suteikia galimybę stebėti vandens kokybės pokyčius, o didelė erdvinė skiriamoji geba ir dažnas grįžimas į tą pačią vietą palengvina aplinkos stebėsenos užduotis (Drusch et al., 2012; Chen et al., 2007; Strong et al., 2017). Sentinel-2 MSI jutiklio (S2/MSI) regimosios ir artimosios infraraudonosios spektro juostos yra labai svarbios nustatant vandens kokybės rodiklius. Tyrimai, kuriuose naudojami S2/MSI vaizdai, padeda atlikti išsamius ekologinius vertinimus (Ghirardi et al., 2022). Nors nuotolinis stebėjimas, patobulintas mašininio mokymosi modeliais, pagerino aplinkos stebėseną, suteikdamas platesnę aprėptį ir ekonomiškumą, visgi šie metodai kelia iššūkių, su-

sijusių su duomenų rinkimu, apdorojimu ir sudėtingų skaičiavimo metodų poreikiu. Meteorologinės sąlygos ir saulės padėtis gali turėti įtakos duomenų tikslumui, taip pat finansinės palydovinių technologijų palaikymo išlaidos gali riboti jų naudojimą (Dugdale et al., 2019; Sibanda et al., 2021).

Nuotolinio stebėjimo srityje pradėtos taikyti bepiločių orlaivių technologijos su įrengtomis didelės skiriamosios gebos daugiaspektrinėmis kameromis, tokiomis kaip „Micasense Rededge“, kurios leidžia gauti detalesnius vaizdus (2 cm vienam pikseliui) nei tradiciniai Žemės stebėjimo palydovai. Šie bepiločiai orlaiviai fiksuoja išsamią spektrinę informaciją regimosios, artimosios infraraudonosios ir raudonosios juostos diapazonuose, taip pagerindami augmenijos ir vandens kokybės analizę (Knoth et al., 2013; Deng et al., 2018). Sujungus dronų ir palydovų duomenis galima atlikti išsamią aplinkos analizę, kuri padeda efektyviai stebėti didelius plotus ir gauti didelės skiriamosios gebos įvairių parametru duomenis (Hilton et al., 1984; Lally et al., 2019). Pasitelkiant bepiločius orlaivius suteikiama galimybė tirti vandens ekosistemas ir jų kokybę, nustatyti povandenines buveines ir įvertinti problemas, pavyzdžiui, eutrofikaciją, bei pagerinti supratimą apie augalijos sudėtingumą (Dronova et al., 2021; Zhang et al., 2016; Alvarez-Vanhard et al., 2020; Glasgow et al., 2004).

Visgi bepiločių orlaivių duomenų tikslumui įtakos turi aplinkos veiksniai, tokie kaip debesuotumas, vandens drumstumas ir saulės kampas. Visa tai apsunkina duomenų klasifikavimą ir ekosistemų analizę (Kislik et al., 2018). Nepaisant šių iššūkių, nuotolinio stebėjimo naujovės yra svarbios siekiant išsaugoti ir tvariai valdyti vandens telkinius, taip pat jos yra svarbios siekiant priimti įvairaus masto stebėsenos sprendimus ir gerinti vandens augalijos valdymą taikant specifinius analitinius metodus (Tomasello et al., 2022; Rowan & Kalacska, 2023). Nuotolinio stebėjimo srityje taikomas gilusis mokymasis yra perspektyvi priemonė siekiant nustatyti vandens taršą, automatizuoti vandens kokybės stebėseną ir tobulinti valdymo strategijas jautriose aplinkose (Sagan et al., 2020; Kwon et al., 2018; Chang et al., 2017). Vis dėlto, šioje srityje tebėra iššūkių, kadangi norint optimizuoti minėtų priemonių taikymą aplinkos apsaugoje būtina pašalinti techninius apribojimus.

### **Tyrimo tikslas ir pagrindiniai uždaviniai**

Disertacijos tikslas – išplėsti bepiločių orlaivių ir palydovų galimybes vertinant vandens ir pakrančių ekosistemų eutrofikaciją ir maudyklų vandens kokybę.

Keturi pagrindiniai šio darbo uždaviniai yra susieti su toliau nurodytais tyrimo klausimais ir hipotezėmis, kuriomis siekiama spręsti dabartinės aplinkos stebėsenos praktikos problemas:

1. Remiantis bepiločių orlaivių taikymo augalijos tyrimuose sinteze, nustatyti bendrus augalijos parametrus, pagal kuriuos formuojama darbo eiga, kuria

būtų galima vadovautis planuojant tyrimus bepiločiais orlaiviais. Iš nustatytų parametrų sukurti integruotą sistemą, skirtą kartografuoti esminius biologinės įvairovės ir ekosistemų funkcionavimo aspektus. (I publikacija)

2. Ištirti palydovinių duomenų pritaikomumą nustatant šienavimo sukeltus vandens augalijos, pavyzdžiui, nendrių sąžalynų, pokyčius ir įvertinti, kaip šie tyrimai gali prisidėti prie strateginio valdymo priemonių rengimo. (II publikacija)
3. Įvertinti bepiločių orlaivių su daugiaspektrinėmis kameromis efektyvumą nustatant Secchi gylį naudojant kvazianalitinį algoritmą vidaus vandens telkiniuose. (III publikacija)
4. Patikrinti, ar U-Net modeliams naudojamus bepiločių orlaivių daugiaspektrinių kamerų duomenis galima pritaikyti pakrančių stebėsenai, tiksliau paplūdimio sąnašų aptikimui ir stebėsenai įvairių tipų paplūdimiuose, kurių kiekvienas pasižymi unikaliomis geomorfologinėmis savybėmis. (IV publikacija)

### Darbo naujumas

Šiuo tyrimu siekiama išspręsti dabartinę nuotolinio stebėjimo duomenų, gautų pasitelkiant bepiločius orlaivius ir Žemės stebėjimo palydovus, panaudojimo vandens aplinkos stebėsenai Lietuvoje trūkumo problemą. Siūlomi metodo darbo eigos variantai galėtų būti taikomi ir kitose vietose esant panašioms aplinkos sąlygoms. Šios disertacijos naujumas yra bepiločių orlaivių galimybių pritaikymas ekologiškai ir aplinkos stebėsenai pasitelkiant tokius metodus kaip gilusis mokymasis ir automatizuota darbo eiga. Svarbus tyrimo naujumo aspektas – didelis vaizdo duomenų, surinktų iš įvairių geografinių vietovių, kiekis naudojant pažangią daugiaspektrinės kameros technologiją kartu su įprasta RGB kamera. Visa tai gerokai padidina analizės detalumą ir tikslumą. Nors atskiruose tyrimuose buvo nagrinėjamas bepiločių orlaivių taikymas aplinkotyroje, šiame darbe pateikiama įvairių sričių analizė – nuo vandens kokybės vertinimo iki augalijos pokyčių ir žemėlapių sudarymo. Vertinant kvazianalitinį algoritmą Secchi gylio nustatymui ir integruojant U-Net konvoliucinius neuroninių tinklų modelius paplūdimio sąnašų segmentavimui, šiame tyrime pristatoma paprastesnė, anksčiau šiose srityse neišbandyta ekonomiškai efektyvi metodika, gerokai sumažinanti laiką ir išteklius, reikalingus tradiciniams Secchi gylio ir paplūdimio sąnašų matavimams *in situ*. Be to, išskirtinis dėmesys pokyčiams dideliuose nendrių sąžalynų plotuose dėl šienavimo papildo žinias apie augmenijos valdymą naudojant nuotolinius tyrimus. Paskutinis komponentas – bepiločių orlaivių duomenimis paremtų ekosistemų sudėtingumo tyrimų sintezė, kuria siekiama sukurti visuotinai taikomą augalijos analizės struktūrą. Šiame darbe sujungiami įvairūs tyrimo būdai ir nustatomi

tinkamiausi metodai bei darbo eiga, kuria siekiama standartizuoti ir optimizuoti būsimus ekologinius tyrimus naudojant bepiločius orlaivius.

### Rezultatų mokslinė ir praktinė reikšmė

Šioje disertacijoje pristatomi tyrimai iliustruoja Baltijos regiono vandens ekosistemų sudėtingumą, pagerina supratimą apie paviršinio vandens kokybę inovatyviai naudojant bepiločių orlaivių ir palydovinio nuotolinio stebėjimo technologijas. Integruojant šias technologijas tyrime pateikiama naujų įžvalgų apie vandens skaidrumo ir vandens augalijos pokyčių erdvinę ir laiko dinamiką. Darbe pabrėžiamas itin svarbus didelės skiriamosios gebos duomenų vaidmuo fiksuojant subtilius mažų ir seklių vandens telkinių parametrus, kuriuos anksčiau tiksliai stebėti buvo sudėtinga.

Tyrimas išplečia mokslinę diskusiją apie nuotolinio stebėjimo metodikas ir patvirtina kvazianalitinio algoritmo (Lee et al., 2015), pritaikyto naudoti bepiločius orlaivius, veiksmingumą. Ši metodika pabrėžia algoritmo tikslumą vertinant vandens skaidrumą – svarbų parametą vandens kokybės tyrimuose.

Atsižvelgiant į ekologines problemas, susijusias su vandens augalija, tyrimas padeda geriau suprasti nendrių augimo tendencijas ir pasiskirstymo pokyčius, susijusius su antropogeninėmis intervencijomis, pavyzdžiui, šienavimu. Šiame moksliniame darbe taip pat svarbus automatinio slenksčio nustatymo algoritmų tyrimas, atskleidžiantis, kad šie algoritmai veiksmingai atskiria vandens ir pakrančių augalijos teritorijas. Nors paplūdimio sąnašų pasiskirstymas nėra tiesioginis vandens kokybės rodiklis, tyrime jo reikšmė nustatyta vertinant pakrančių ekosistemų būklę ir siūloma metodologiškai patobulinti jo stebėseną. Be to, tyrimas pagilina mokslines žinias, kadangi atskleidžia U-Net konvoliucinio neuroninio tinklo gebėjimą pagerinti dronų vaizdų klasifikavimo tikslumą. Ši išvada patvirtina vis didėjančią dirbtinio intelekto ir aplinkosaugos mokslo sinergiją, sudarančią sąlygas naudoti sudėtingesnes analitines priemones nuotolinio stebėjimo tyrimuose.

Sukurtus vandens kokybės vertinimo metodus gali naudoti aplinkosaugos atstovai ir teisės aktų kūrėjai, stebėdami vandens telkinius ir priimdami pagrįstus sprendimus, kurie padėtų sukurti veiksmingesnes ir tvaresnes valdymo strategijas. Išvados, susijusios su nendrių plotų ataugimu po šienavimo, gali būti panaudotos valdymo intervencijoms, skirtoms kontroliuoti šią augmeniją ten, kur ji laikoma invazine. Be to, įrodyta, kad bepiločių orlaivių daugiaspektrinių vaizdų taikymas matuojant vandens skaidrumą yra ekonomiškai efektyvus ir veiksmingas didelio masto vandens kokybės stebėsenos metodas, naudingas regionuose, kuriuose atlikti matavimus *in situ* yra sudėtinga arba tam reikia daug išteklių. Galiausiai, galimybė sudaryti paplūdimio sąnašų žemėlapių ir įvertinti paplūdimio sąnašų kiekį naudojant drono vaizdus ir mašininį mokymąsi gali padėti paplūdimių valdymui, potencialiai informuojant apie valymo

poreikį, mikroplastiko taršos mažinimą ir net išteklių panaudojimą, pavyzdžiui, tręšimui. Visos šios taikomosios programos gali prisidėti prie vandens ekosistemų išsaugojimo ir geresnės sveikatos.

## METODAI

### Tyrimų vietos

Tyrimai atlikti trijose skirtingose Lietuvos vandens aplinkose: Platelių ežere (makrofitų aptikimas ir šienavimo zonos vertinimas), keturiuose pajūrio paplūdimiuose: Melnragės, Karklės, Palangos ir Šventosios (paplūdimio sąnašų tyrimas), 42 ežeruose ir tvenkiniuose (Secchi gylio vertinimas naudojant bepiločių orlaivių daugiaspektrinius vaizdus). Platelių ežeras, kurio plotas yra 1200 ha, o vidutinis gylis – 10,5 m, pasirinktas dėl gerai ištirtos makrofitų bendrijos ir ežero valymo valdymo strategijos, todėl šis ežeras buvo naudinga bandomoji aplinka įvertinti makrofitų aptikimo metodus naudojant Sentinel-2 palydovines nuotraukas ir bepiločių orlaivių vaizdus. Platelių ežeras yra Žemaitijos nacionalinio parko dalis, klasifikuojamas kaip oligomezotrofinis ežeras, kurio pakrantėje netolygiai išsidėstę paprastųjų nendrių (*Phragmites australis*) sąžalynai. Tyrime daugiausia dėmesio skirta aštuonioms ežero zonoms: septynioms šienaujamos teritorijoms ir vienai nešienaujama teritorijai kaip atskaitos taškui. 42 vandens telkiniai Secchi gylio vertinimui pasirinkti atsižvelgus į jų dydį, augmenijos ir vandens komponentų įvairovę, pavyzdžiui, drumstumą, chlorofilą a ir spalvotas ištirpusias organines medžiagas, atspindinčią Lietuvos vandens telkinių aplinką. Nuo 2021 m. balandžio mėn. iki 2022 m. gegužės mėn. atlikta paplūdimio sąnašų stebėseną atrinktuose paplūdimiuose dėl jų išskirtinių savybių, pavyzdžiui, miesto artumo, laivybos, turizmo veiklos ir pakrantės geografijos, įskaitant kopas, skardžius ir klifus. Paplūdimio sąnašų sudėtį Lietuvos Baltijos jūros pakrantėje daugiausia sudaro daugiamečiai raudonieji makrodumbliai (85 %), likusią dalį – siūliniai žalieji ir rudieji makrodumbliai. Raudonųjų makrodumblių rūšys veši akmenuotame dugne, esančiame 3–16 m gylyje, siūliniai žalieji makrodumbliai aptinkami seklumoje, o rudieji makrodumbliai – didesniame gylyje ir kietesniame dugne.

### Duomenų rinkimas

Šiame skyriuje aprašomi nuotolinio stebėjimo metodai, taikyti tyrimuose, kuriuose integruoti *in situ* matavimai, bepiločių orlaivių vaizdai ir palydoviniai duomenys. Kiekviena sudedamoji dalis atlieka svarbų vaidmenį: *in situ* matavimai suteikia tiks-

liausius duomenis, bepiločiai orlaiviai suteikia didelės skiriamosios gebos erdvinę informaciją, o Žemės stebėjimo palydovai užtikrina plačią laiko ir erdvės aprėptį. Šių metodų integracija patobulina aplinkos vertinimų erdvinę ir laiko raišką bei pagerina išvadų pagrįstumą.

Bepiločių orlaivių duomenų gavimo metodų aprašymai (I publikacija) pradedami įžvalgomis, gautomis vykdant COST veiklos projektą HARMONIOUS, kurio metu daugiausia dėmesio buvo skirta bepiločių orlaivių metodų, padedančių atlikti žemės ūkio ir gamtinių ekosistemų stebėseną, suderinimui. Ekspertai nustatė bendrus bepiločiais orlaiviais atliekamų augalijos tyrimų parametrus, pabrėždami augalijos heterogeniškumo supratimo, tyrimo metodikų ir duomenų apdorojimo būdų svarbą.

Siekiant validuoti duomenis (II–IV publikacijos) ir išanalizuoti gautas ortofotografines nuotraukas, vaizdams fiksuoti buvo naudojami bepiločiai orlaiviai su didelės skiriamosios gebos kameromis. Kiekviename tyrime skyrėsi bepiločių orlaivių ir kamerų tipai, skrydžio protokolai (aukštis, vaizdų dažnis, persidengimas) ir programinė įranga, tačiau visuose tyrimuose ortofotografijoms kurti buvo naudotas algoritmas „Struktūra iš judesio“ (angl. Structure from Motion). Pjovimo poveikio (II publikacija) tyrime daugiausia dėmesio skirta nendrių sąžalynų kartografavimui naudojant DJI Phantom 4 su 20 megapikselių RGB kamera, skirta gauti detalias ortofotografines nuotraukas, kurios buvo lygintos su S2/MSI duomenimis naudojant antžeminius kontrolinius taškus tikslumui užtikrinti. III publikacijoje analizuotas erdvinis Secchi gylio pasiskirstymas ir tam naudota „DJI Inspire 2“ su „RedEdge-MX“ kamera, fiksuojančia penkias spektrines juostas 60 m aukštyje. Šiame tyrime ortofotografinių nuotraukų rezoliucija buvo apie 3 cm. Paplūdimio sąnašų tyrime (IV publikacija) stebėjimų skrydžiai atlikti kas 10 dienų atsižvelgus į optimalias sąlygas ir ES reglamentų laikymąsi. Naudojant daugiaspektrines ir RGB kameras buvo sukurtos mozaikos U-Net modeliavimui ir skaitmeniniai aukščio modeliai, apimantys įvairius paplūdimių ilgius. Šios nuotraukos vėliau susietos su Lietuvos ortofotografiniu žemėlapiu, kad būtų galima tiksliai apskaičiuoti paplūdimio sąnašų kiekius. Kameros buvo parinktos atsižvelgus į jų veiksmingumą kuriant mozaikas ir reljefo modelius.

Šiame tyrime naudoti Sentinel-2A ir Sentinel-2B (S2/MSI) palydovų duomenys, kurių erdvinę skiriamąją gebą yra 10 m, 20 m arba 60 m priklausomai nuo spektro juostos, kurių yra 12, ir apima regimosios, artimosios infraraudonosios (NIR) ir trumposios infraraudonosios (SWIR) spinduliuotės bangų ilgio diapazonus. Viena palydovo nuotrauka Platielių ežere gaunama kas tris dienas. Siekiant užtikrinti duomenų kokybę, analizuota šešiolika S2/MSI vaizdų, atrinktų taip, kad jie sutaptų su nendrių šienavimo laikotarpiu nuo liepos 20 d. iki rugsėjo 10 d., taip pat atsižvelgta į debesuotumą. Dėl neišvengiamų debesų šešėlių tam tikrose teritorijose teko parinkti alternatyvius palydovo vaizdus. Tyrime daugiausia naudoti antrojo (2A) lygio duomenys, apdoroti „Sen2Cor“ atmosferos korekcijos algoritmu, gauti iš „Copernicus Open Access Hub“ portalo.

Vandens skaidrumo (III publikacija) ir paplūdimio sąnašų (IV publikacija) aukščio matavimai atlikti kartu su bepiločiais orlaiviais. Naudojant 20 cm baltąjį Secchi diską buvo išmatuotas Secchi gylis ir kartu surinkti vandens ėminiai, kuriuose laboratorijoje buvo išmatuotos spalvotųjų ištirpusių organinių medžiagų (CDOM) ir chlorofilo *a* (Chl-*a*) koncentracijos, nustatytas drumstumas. Šis tyrimas buvo vykdomas 2021–2022 m. gegužės–rugsėjo mėn. Iš viso surinkta 43 *in situ* Secchi gylio matavimų ir bepiločių orlaivių vaizdų duomenų, kuriuose Chl-*a* koncentracija nustatyta spektrofotometriškai, CDOM išmatuota atliekant spektrofotometrinę analizę, o drumstumas kiekybiškai nustatytas naudojant drumstumo matuoklį. Nuotolinio stebėjimo atspindžio rodiklis ( $R_{rs}$ ) buvo gautas naudojant WISP-3 spektroradiometrą, kurio duomenys skirti validuoti iš bepiločio orlaivio gautus vandens atspindžius.

Atliekant paplūdimio sąnašų aukščio vertinimą kartu su bepiločių orlaivių skrydžiais buvo įvykdyta 16 lauko misijų, kurių metu paplūdimio sąnašų aukštis išmatuotas kas 10 m išilgai transektinių linijų. Šie aukščių duomenys panaudoti bepiločių orlaivių paplūdimio sąnašų aukščio vertinimo patvirtinimui.

### Vaizdų apdorojimas

Nendrių sąžalynai (II publikacija) apibrėžti rankiniu būdu iš bepiločių orlaivių ortofotografijų, o nendrių tankis vizualiai įvertintas naudojant 10 m<sup>2</sup> dydžio poligonus, atitinkančius S2/MSI pikselio dydį. Pakrantės riba apibrėžta naudojant geoportal.lt ežerų poligonų žemėlapi neįtraukiant salų, taip pat aplink pakrantę nustatyta 10 m buferinė zona, kad būtų galima atskirti medžius ir kranto augaliją nuo nendrių. Siekiant supaprastinti vaizdų apdorojimą, S2/MSI vaizdai pergrupuoti iki vienodos 10 m erdvinės skiriamosios gebos.

Tyrimo daugiausia dėmesio skirta dvinarės klasifikacijos metodų taikymui klasifikuoti indeksus ir įvertinti nendrynų plotų pokyčius. Pagrindiniai klasifikavimui naudoti indeksai buvo vandens augalijos indeksas (angl. Water Adjusted Vegetation Index, WAVI) ir normalizuotas vandens skirtumo indeksas (angl. Normalized Difference Water Index, NDWI). Klasifikavimui naudoti septyni dvinariai slenksčio nustatymo algoritmai iš „Fiji“ programinės įrangos.

Siekiant įvertinti Secchi gylį šiame tyrime (III publikacija) buvo testuotas kvazianalitinio algoritmas, sukurtas Lee ir kt. (2015). Šis pusiau analitinis metodas išsiskiria tuo, kad jam nereikalingas *in situ* kalibravimas. Tai yra reikšminga pažanga palyginus su tradiciniais empiriniais metodais. Šiame algoritme svarbiausi yra suminės absorbcijos ( $a$ ) ir grįžtamosios sklaidos koeficientai ( $b_b$ ), iš kurių išvestas difuzinio susilpnėjimo koeficientas ( $K_d$ ). Metodo tikslumas padidintas atsižvelgus į saulės zenito kampą ir parinkus vandens telkinio charakteristikoms tinkamus bangų ilgius. Pirmiam bepiločių orlaivio vaizdų apdorojimui pritaikytas saulės atspindžio koregavimas



ir maskavimas bei netinkamų vandens telkinių pašalinimas (nuotraukose matomas dugnas), po kurio galutinėje analizėje liko 39 vandens telkiniai. Vandens ir ne vandens pikseliams atskirti buvo taikomas normalizuotas vandens skirtumo indeksas, o saulės atspindžio korekcijos algoritmų tikslumas patikrintas pasitelkiant anksčiau minėto WISP-3 duomenis.

U-Net modelio treniravimui (IV publikacija) naudoti didelės skiriamosios gebos bepiločio orlaivio vaizdai buvo padalinti į 163 mažesnes dalis, iš kurių treniravimui pasirinkta 17. Modeliai buvo apmokyti naudojant šešis skirtingus duomenų derinius, į kuriuos įtraukti daugiaspektriniai, RGB, indeksų kombinacijos (NDVI, NDWI ir NDRE) bei aukščio duomenys. Duomenų kombinacijos apdorotos pasitelkus GDAL 3.4.3. Siekiant ištirti erdvinės vietos paklaidą, viename duomenų rinkinyje, apimančiame visas spektrines juostas ir aukščius, atliktas duomenų papildymas, t. y. atsitiktinis pasukimas ir apvertimas.

Norint tiksliai nustatyti paplūdimio sąnašų aukštį naudojant bepiločio orlaivio duomenis iš skaitmeninio auščių modelio buvo atimtas skaitmeninis paviršiaus modelis. Siekiant optimizuoti U-Net architektūros, pritaikytos daugiaspektriams vaizdams, mokymąsi, naudotas ankstyvas sustabdymas ir Dice (angl. Dice loss) bei centrinio nuostolio (angl. focal loss) funkcijų derinys.

U-Net modelio mokymo ženklėjimas atliktas taikant prižiūrimą mašininio mokymosi metodą ir rankinį taisymą, daugiausia dėmesio skiriant paplūdimio sąnašų atskyrimui nuo kitų objektų (potencialių sąnašų, smėlio, vandens ir kitų). Daugiaspektriniai vaizdai buvo paruošti TIFF formatu, kad juos būtų galima žymėti, o artimoji infraraudonųjų spindulių juosta padėjo atskirti makrodumblius, kuriuos sunku identifikuoti RGB vaizduose. Vaizdų segmentavimo darbo eigoje buvo naudojami paženklinėti TIFF failai ir „Python“ paketas „Smoothly-Blend-Image-Patches“, skirtas sumažinti vaizduose esančius kraštų iškraipymo efektus.

### Statistiniai metodai ir validacija

Atliekant statistinę analizę tradiciniai metodai buvo integruoti kartu su erdvinių vaizdų segmentavimu ir klasifikavimu. Daugiausia dėmesio skirta augmenijos ir vandens atskyrimui naudojant bepiločių orlaivių ortofotografines nuotraukas ir palydovinius duomenis. Nendrių sąžalynų (II publikacija) plotų klasifikacijai pasirinktas konkretus indeksas ir slenkstis, patvirtintas su 12 bepiločiais orlaiviais atliktų ortofotonuotraukų, o jų tikslumas įvertintas naudojant painiavos matricą (angl. Confusion matrix) ir plotą po kreive (angl. Area under the curve, AUC). Slenksčių nustatymo algoritmai, kurie naudojami maskuoti vandenį ir palikti augmeniją bei kurių jautrumo ir specifiškumo reikšmės buvo 0,5 arba didesnės, buvo laikomi tinkamais, o tai reiškia, kad teisingai suklasifikuota 50 % duomenų. Statistiniai testai, įskaitant t testus

(angl. t-test) ir Dunnett'o post hoc testą, buvo taikomi siekiant palyginti vidutines AUC vertes tarp skirtingų algoritmų ir augmenijos tankumų. Nendrių sąžalynų tankis apskaičiuotas naudojant Sentinel-2/MSI duomenis ir patikrintas su bepiločiais orlaiviais atliktomis ortofotografijomis pritaikius tiesinę regresiją.

Siekiant nustatyti Secchi gylio tikslumą (III publikacija) naudojant apibendrintus sudėtinius modelius (angl. Generalized Additive Models, GAM) analizuotas ryšys tarp modeliujamų ir *in situ* Secchi gylio verčių bei aplinkos veiksnių naudojant R programos statistinius ir vizualizavimo paketus. Modelio tikslumas vertintas naudojant nuokrypį, vidutinį kvadratinį nuokrypį (RMSD) ir Pearsono koreliacijos koeficientą.

Paplūdimio sąnašų modelio (IV publikacija) veikimas buvo vertinamas duomenis suskirsčius į mokymo ir rezultatų patvirtinimo rinkinius naudojant tikslumo (angl. precision), atšaukimo (angl. recall), F1 rezultato (angl. F1 score) ir intersekcijos sąjungoje (angl. Intersection over Union, IoU) metrikas.

Naudojant statistinius testus, įskaitant Dunnett'o testą ir vienpusę ANOVA, „Python“ paketus ir 0,05 reikšmingumo lygį, buvo lyginamos IoU vertės tarp skirtingų tiriamųjų paplūdimių. *In situ* išmatuoti aukščiai buvo koreliuojami su bepiločio orlaivio nustatytais aukščiais kiekybiškai vertinant vidutines kvadratinės paklaidas (angl. Root mean square error, RMSE) ir vidutinę absoliučiąją paklaidą (angl. Mean absolute error, MAE). Galiausiai prognozavimo tikslumas buvo lyginamas naudojant vidutinį absoliutų procentinį nuokrypį (angl. Mean absolute percentage error, MAPD) ir RMSD.

## REZULTATAI IR APTARIMAS

Kiekvienas iš šių tyrimų prisideda prie išsamesnio supratimo apie vandens kokybės vertinimą naudojant nuotolinius stebėjimus. I publikacijoje aprašomas bepiločių orlaivių naudojimas augmenijos stebėsenai. II tyrime stebimi vandens augalijos pokyčiai, kurie yra svarbūs vandens kokybės rodikliams. III tyrime stebimas ežerų vandens skaidrumas – pagrindinis vandens kokybės parametras. IV tyrime nuotolinis stebėjimas taikomas pakrančių zonose sudarant paplūdimio sąnašų, kurios tikėtina gali įtakoti vandens kokybę, pasiskirstymo žemėlapius. Šie darbai rodo, kad nuotolinis stebėjimas gali būti taikomas kartu su tradiciniais metodais, siekiant visapusiškai stebėti vandens kokybę vandens aplinkoje.

### **Bendrosios rekomendacijos dėl augalijos stebėsenos naudojant bepilotės skraidykles**

Šio straipsnio autoriai pateikia pagal tyrimų tikslus ir augalijos savybes pritaikytas rekomendacijas dėl bepiločių orlaivių taikymo augalijos tyrimams. Pagrindinis

pasiūlymas yra naudoti didelės spektrinės skiriamosios gebos ir pažangius vaizdų apdorojimo metodus, skirtus identifikuoti ir atskirti augalų rūšis. Vertinant ekosistemų struktūrą, rekomenduojama naudoti LiDAR ir didelės skiriamosios gebos fotogrametrinius jutiklius, kad būtų galima tiksliai įvertinti stiebų tūrį ir sudėtingumą. Tyrime pabrėžiama hiperspektrinių ir terminių vaizdų nauda vertinant augalų būklę, įskaitant fenologiją ir streso lygį. Norint nustatyti ekosistemų dinamiką rekomenduojama dažnai atlikti tyrimus naudojant bepiločius orlaivius. Šiomis gairėmis, pagrįstomis išsamia literatūros apžvalga, siekiama optimizuoti bepiločių orlaivių taikymą atliekant ekologinius vertinimus. Remiantis šiomis išvalgomis sukurta interaktyvi darbo eigos diagrama, kurią galima rasti COST Harmonious interneto svetainėje (<https://www.costharmionious.eu/characterizing-vegetation-complexity-with-uas>). Diagrama padeda pasirinkti bepiločių orlaivių atliekamų augalijos tyrimų metodus. Šie tyrimai padeda aplinkosaugos mokslininkams ir ekologams vykdyti augalijos stebėseną ir valdymą naudojant bepiločius orlaivius ir taip prisidėti prie išsamaus ekologinių parametų vertinimo įvairiose aplinkose. Atliekant augalijos stebėseną bepiločiais orlaiviais buvo išskirtos keturios būdingos savybės, kurios bus aprašytos išsamiau.

Augalijos rūšinė sudėtis, kuriai įtakos turi erdvinis ir laikinis heterogeniškumas, įvairiose biogeografinėse zonose ir biomuose skiriasi (Lambers ir Oliveira, 2019; Pugnaire ir Valladares, 1999). Bepiločių orlaivių taikymas šioje srityje įrodė, kad buveinių kartografavimas ir stebėseną išsaugojimo tikslais yra veiksminga, o šiuos metodologinius pasirinkimus lemia tikslinės rūšys arba augmenijos savybės (Müllerová, 2019). Norint atskirti rūšis, pasižyminčias minimaliais spektriniais ir struktūriniais skirtumais, reikalinga didelė duomenų skiriamoji geba ir sudėtingi algoritmai. Taip pat norint atskirti šią augaliją nuo aplinkos ar kitų augalų reikalinga formos, tekstūros ir kontekstinė informacija, kuri pagerintų identifikavimo tikslumą, kai naudojamos nebrangios RGB kameros (Franklin, 2018; Gini ir kt., 2014; Pande-Chhetri ir kt., 2017; Yuba ir kt., 2021). Atliekant sudėtingos augmenijos analizę itin svarbus detalesnės spektrinės, erdvinės ir laiko skiriamos gebos duomenų bei pažangių metodų, įskaitant objektais paremtą vaizdų analizę (angl. Object based image analysis), mašininį mokymąsi ir gilųjį mokymąsi, derinys (Kattenborn et al., 2020; Martin et al., 2018).

Ekosistemos struktūrai, kuri yra pagrindinis išteklių kintamumą lemiantis veiksnys, reikalinga išsami informacija apie lapų ir stiebų struktūrą, tarpus tarp individualių augalų ir jų erdvinį pasiskirstymą (Bagaram et al., 2018; Getzin et al., 2012; Kent et al., 2015). Dauguma bepiločių orlaivių tyrimų daugiausia dėmesio skiria miškams naudojant 3D duomenis iš įvairių jutiklių, kad būtų galima analizuoti stiebų sudėtingumą ir kiekybiškai įvertinti biomasę (Cunliffe et al., 2016; Swetnam et al., 2018; Meneses et al., 2018). LiDAR jutiklių naudojimas yra labai svarbus kuriant skaitmeninius reljefo modelius (angl. Digital terrain model, DTM) ir vertinant struktūrinius sluoksnius tankiuose augalijos plotuose (Aguilar et al., 2019; Camarreta et al., 2020; Giannetti et al., 2018; Kašpar et al., 2021). Fotogrametriniai taškų debesys yra eko-

nomiškai efektyvi alternatyva mažiau tankiai augalijai, tačiau vizualiai sudėtingoje aplinkoje išlieka nemažai iššūkių (Baltsavias et al., 2008; Dandois and Ellis, 2010; White et al., 2015; Westoby et al., 2012; Seifert et al., 2019). Duomenų šaltinių derinimas, pavyzdžiui, spektrinių savybių įtraukimas į LiDAR ir tikslus skirtingų duomenų rinkinių koordinatinių pririšimas, gali pagerinti struktūrinę analizę (Lisein et al., 2013; Wallace et al., 2016).

Bepiločiai orlaiviai, pasižymintys didele erdvine ir laikine skiriamąja geba, yra svarbūs tiriant augalų fenologiją ir reakciją į stresą. Nors daug tyrimų atliekama žemės ūkio ir miškininkystės kontekste, rūšių gausumo tyrimai yra riboti (D’Odorico et al., 2020; Zarco-Tejada et al., 2012). Norint iš anksto nustatyti spektrines savybes ir streso rodiklius, reikalingi sudėtingi jutikliai ir kompleksiniai modeliai, kurie naudojami pritaikant šiluminius vaizdus ir energijos balanso modelius (Jones ir Vaughan, 2010; Gago ir kt., 2017). Bepiločiai orlaiviai padeda išsamiai stebėti fenologinius etapus, suteikdami lankstumo laiku gauti didelės skiriamosios gebos duomenis (Carl et al., 2017; Fawcett et al., 2021).

Bepiločiai orlaiviai padeda tirti dinamiškus natūralius procesus, įskaitant vandens augalų sudėtį, ekosistemų struktūrą ir augalų būklę, pakartotinių matavimų metu taikant pokyčių aptikimo metodą (Berra et al., 2019; Fawcett et al., 2021; Park et al., 2019; Laslier et al., 2019; Michez et al., 2016). Bepiločių orlaivių lankstumas yra itin svarbus reaguojant į dramatiškus įvykius, pavyzdžiui, potvynius ar didelius vandens kokybės pokyčius, kadangi palengvina greitą duomenų rinkimą ir sumažina lauko tyrimų riziką (Novković et al., 2023). Bepiločiai orlaiviai padeda suprasti ir iš anksto aptikti vandens ekosistemų trikdžius naudojant įvairius jutiklius – nuo pažangių hiperspektrinių iki paprastų RGB kamerų, o palydovinių duomenų integracija pagerina didelės teritorijos stebėseną ir valdymą (Novković et al., 2023; Song & Park, 2020; Chabot et al., 2017).

### **Nendrių sąžalynų dinamikos analizė iš bepiločių orlaivių ir palydovų vaizdų Platelių ežere**

#### **Automatinės darbo eigos ir palydovinių vaizdų analizės veiksmingumas**

Žemės stebėjimo duomenų naudą riboja didelės skiriamosios gebos patvirtinimo duomenų trūkumas, todėl norint padidinti palydovinių stebėjimų tikslumą reikia taikyti papildomus antžeminio tikrinimo metodus (Ozesmi ir Bauer, 2002). Bepiločių orlaivių duomenų integravimas kompensuoja Žemės stebėjimo skiriamosios gebos

apribojimus, pavyzdžiui, bepiločių orlaivių duomenys, turintys didesnę skiriamąją gebą ir lankstumą, gali būti veiksminga Žemės stebėjimo palydovų nustatytų makrofitų plotų patvirtinimo priemonė, pagerinanti bendrą augalijos analizės tikslumą (Anderson ir Gaston, 2013). Nepaisant apribojimų, Žemės stebėjimo duomenys yra vertingi vykdant ilgalaikę ekologinę stebėseną vandens aplinkoje.

Vandens ir augalijos dvinarių atskyrimo slenksčių algoritmų analizė parodė, kad tam tikri algoritmai daugiau nei pusė atvejų klaidingai priskyrė vandenį augmenijai, o kiti pasižymėjo didesniu specifiškumu. Daugeliu atvejų algoritmai tiksliai atskyrė vandenį. Vis dėlto, tokie algoritmai kaip Otsu ir RenyiEntropy pasižymėjo mažu jau-trumu, todėl jie buvo pašalinti iš tolesnio nagrinėjimo sutelkiant dėmesį į penkis normalizuoto vandens skirtumo indekso algoritmus, pasižyminčius geresniais rodikliais. Yen algoritmas veiksmingiausiai atskyrė augmeniją ir vandenį, nepaisant panašių rezultatų taikant kitus algoritmus (Oyama ir kt., 2015; Bollas ir kt., 2021). Dėl pastebėtų augalijos ploto vertinimo neatitikimų tarp bepiločių orlaivių ortofotonuotraukų ir palydovinių vaizdų geresniam aptikimui rekomenduojama naudoti SWIR juostą ir modifikuotą normalizuotą vandens skirtumo indeksą (angl. NDWI). Visgi naudojant modifikuoto normalizuoto vandens skirtumo indekso duomenis atsiranda klaidingos klasifikacijos tikimybė dėl skiriamosios gebos skirtumų, palyginus su spektrais, naudojamais šiame tyrime (Xu, 2005; Jiang et al., 2020).

Šienavimo metais pastebėtas žymus augmenijos ploto sumažėjimas, o šienaujamuose plotuose šis sumažėjimas buvo didesnis nei nešienautame etaloniniame plote. Norint veiksmingai tvarkyti nendrių plotus labai svarbu nuolat šienauti. Tai įrodo 2017–2019 m. tvarkymo programos metu sumažėjęs nendrių sąžalynų plotas ir vēlesnis nendrių ataugimas 2020 m., pabrėžiantis pakartotinio šienavimo būtinybę (Ailstock et al., 2001; Asaeda et al., 2006; Derr, 2008).

### **Poveikis vandens telkinių valdymui ir nendrių sąžalynų tankio atsistatymui**

Spearman'o koreliacija parodė stiprų ir reikšmingą ryšį tarp WAVI reikšmių ir nendrių tankio, todėl WAVI yra patikimas rodiklis, leidžiantis stebėti augalijos tankį naudojant bepiločių orlaivių duomenis. Pagal WAVI vertes galima atskirti vandens ir nendrių plotus, o tai padeda valdyti augmeniją. Analizuojant augalijos tankio pokyčius skirtingais metais išryškėjo skirtingas šienavimo poveikis: tam tikrais metais pastebėti reikšmingi skirtumai, tačiau pirmaisiais šienavimo metais ir 2020 m. tikrinimo metais pokyčių nebuvo. Tyrimo metu pastebėta, kad natūralus augalijos tankis padidėja vegetacijos sezono pabaigoje. Tai įrodo šienavimo daromą įtaką nendrių augimo ciklui. Nepaisant augalijos tankio ir ploto svyravimų, rezultatai rodo, kad nendrių sąžalynai laikui bėgant atsinaujina, todėl juos reikia šienauti pakartotinai.

Nuotolinis stebėjimas papildo tradicinius stebėsenos metodus ir suteikia ekonomiškai efektyvias plataus masto stebėsenos galimybes. Šis metodas, kartu su palydoviniais ir bepiločių orlaivių duomenimis, padeda geriau valdyti ežerų ekosistemas. Taip pat šie metodai pateikia išsamią informaciją apie augaliją ir siūlo optimalų šienavimo laiką siekiant išvalyti ežerą nuo maistinių medžiagų pertekliaus.

### Vandens skaidrumo vertinimas naudojant bepiločio orlaivio vaizdus

Taikant saulės atspindžio korekcijos metodus daugiaspektriniams vaizdams gauti nevienareikšmiai rezultatai: žaliosios juostos vidutinė nuokrypio vertė buvo didžiausia, o mėlynosios juostos – mažiausia. Didžiausias multikolinearumas nustatytas tarp žaliosios ir raudonosios juostų ( $r = 0,97$ ). Tai atskleidžia sisteminius ir atsitiktinius netikslumus nustatant vandens paviršiaus parametrus. Mėlynosios juostos ryšys buvo mažiausiai stabilus dėl jautrumo sklaidai, tad tai turėjo įtakos jos signalo fiksavimui vandens aplinkoje. Palyginus korekcijos metodus Lyzenga'os metodas rodė didžiausias vidutines vertes, o Goodman'o – mažiausias, bet su didžiausia koreliacija žaliosios ir raudonosios spektrinių juostų atžvilgiu. Remiantis mažu Goodman'o RMSD, jis yra tinkamas pritaikymui, kai reikia mažo atspindžio intensyvumo nuokrypio. Įvairių tyrimų metu paaiškėjo, kad korekcijos metodų veiksmingumas skiriasi priklausomai nuo vandens kokybės rodiklių. Taikant korekciją visame vaizde, o ne tik slenksinio algoritmo atskirtose srityse, kur matomas saulės atspindžio, bendras tikslumas pranoksta metodą, kai saulės atspindžio korekcija taikoma tik tose vietose, kur jis yra ryškiausiai matomas. Goodman'o ir Hedley'io metodai buvo veiksmingiausi koreguojant saulės atspindį daugiaspektrinių bepiločių orlaivių vaizdų duomenyse. Tai patvirtina jų galimą naudą tolesniuose tyrimuose skaičiuojant vandens parametrus.

Įvertinus kvazianalitinio algoritmo (QAA) modelio, skirto apskaičiuoti Secchi gylį, rezultatus nustatyta aukšta koreliacija naudojant visus saulės atspindžio koregavimo metodus:  $r$  reikšmės svyruoja nuo 0,74 iki 0,92, o RMSD – nuo 0,65 m iki 1,05 m. Tai rodo, kad rezultatai yra priimtini. Hedley metodo RMSD buvo geriausias (0,65 m), nors  $r$  (0,91) buvo šiek tiek mažesnis palyginus su Goodman'o metodu ( $r = 0,92$ , RMSD = 1,00 m), kuris nepakankamai įvertino SG vertes. Galutiniai rezultatai parodė, kad tiek Hedley tiek Goodman'o metodai buvo efektyviausi, tačiau abu metodai turėjo savų trūkumų.

Nustatyta, kad vidutinis ežerų *in situ* Secchi gylis buvo 1,91 m, kuriuose CDOM, Chl-a koncentracijos ir drumstumas varijavo. GAM rezultatai atskleidė, kad 38 % Secchi gylio dispersijos reikšmingai lėmė šie veiksniai: CDOM kiekis ( $F = 6,808$ ,  $p < 0,05$ ) ir saulės zenito kampas ( $F = 4,84$ ,  $p = 0,02$ ), tačiau Chl-a neturėjo reikšmingos įtakos ( $F = 0,295$ ,  $p = 0,59$ ). Dideli saulės zenito kampai, pavyzdžiui, didesni nei 70 laipsnių, dėl padidėjusios šviesos sklaidos ir absorbcijos sumažino Secchi gylio mo-

delio tikslumą iki 1,5 m. Šie rezultatai pabrėžia pažangių algoritmų poreikį siekiant tiksliai prognozuoti Secchi gylį (Hashimoto et al., 2019). Stebėjimai patvirtina, kad CDOM absorbcija ultravioletiniame ir mėlyna jame spektre sumažina jutiklių aptiktus signalus, o koreliacija tarp *in situ* bei bepiločio orlaivio gauto atspindžio mėlynojoje juostoje susilpnėja (Warren et al., 2019; Mamaghani ir Salvaggio, 2019). Pažymėta, kad Goodman'o ir Hedley'io metodai buvo veiksmingi sprendžiant šias problemas. Hedley'io metodas parodė didžiausią koreliacijos koeficientą, o Goodman'o metodas pasiekė mažiausią mėlynosios juostos atspindžio RMSD, kur galutiniai atspindžiai iš daugiaspektrinės kameros artimai sutampa su *in situ* vertėmis.

### **Bepiločiu orlaiviu atliekamas paplūdimio makrodumblių sąnašų kiekybinis vertinimas**

U-Net modelis didžiausią efektyvumą parodė naudodamas iš indeksų (NDVI, NDWI, NDRE) sudarytą duomenų rinkinį, kuris pasiekė F1 balą – 0,86 ir IoU – 0,75. Rezultatas rodo, kad šis duomenų rinkinys yra tinkamas semantiniam didelės skiriamosios gebos bepiločių orlaivių vaizdų segmentavimui. Mažiausia IoU reikšmė buvo nustatyta išskiriant potencialių paplūdimio sąnašų (t.y., sąnašų esančių vandenyje) klasę visose naudotose duomenų rinkinių kombinacijose. Tai nulėmė modelių tikslumo variacijas išskiriant skirtingas klases (paplūdimio sąnašos, potencialios paplūdimio sąnašos, smėlis, vanduo, kita). Post hoc testai neparodė statistiškai reikšmingų duomenų kombinacijų tikslumo skirtumų (p reikšmės  $\geq 0,74$ ), todėl atsiranda galimybė modelius panaudoti kitose teritorijose ir kitu laiku.

Paplūdimio sąnašų segmentavimui validavimo duomenims veiksmingiausia „RGB“ kombinacija, kurios IoU buvo 0,42, o F1 balas – 0,54. „5 juostų ir aukščio“ kombinacija geriausiai veikė potencialiam paplūdimio sąnašų segmentavimui. „RGB“ kombinacija taip pat buvo geriausia atskiriant vandens ir smėlio klases, todėl galima teigti, kad bepiločiai orlaiviai yra veiksmingi stebint įvairias paplūdimių charakteristikas. Vis dėlto perkelti modelį į naujas vietas su ne tokiais homogeniškais paviršiais gali būti sudėtinga, kaip matyti Karklėje, kur aukščio duomenų įtraukimas sumažino tikslumą. Anot Taddia et al. (2019), aukščio tikslumą galima pagerinti naudojant papildomus kampu sudarytus vaizdus, dėl kurių galima tiksliau apskaičiuoti skaitmeninius aukščio modelius. Modelio veikimas su augmenteduotų duomenų kombinacija rodo, kad jį galima pritaikyti įvairiuose scenarijuose be erdvinės lokalizacijos šališkumo. Dėl vidutinio tikslumo ir mažesnių skaičiavimo reikalavimų „RGB“ kombinacija yra tinkamesnė paplūdimio sąnašų segmentavimui.

Potencialių paplūdimio sąnašų aptikimo iššūkių kyla dėl sudėtingų vandens aplinkos optinių savybių, nes vanduo keičia šviesos sugėrimą ir atspindėjimą skirtinguose gyliuose. Tai turi įtakos veiksmingai aptikti paplūdimio sąnašas automatiniu būdu.

Sprendžiant šias problemas gali prirreikti papildomų išankstinio apdoravimo etapų, kad būtų pakoreguoti nukrypimai nuotraukose dėl tokių veiksnių, kaip vandens gylis ar saulės atspindys.

Tyrimo metu kiekybiškai nustatyti paplūdimio sąnašų plotai svyravo nuo 236 m<sup>2</sup> iki 11193 m<sup>2</sup>, o pagal U-Net modelį naudojant „RGB“ duomenų kombinaciją nustatyti paplūdimio sąnašų plotai svyravo nuo 9 m<sup>2</sup> iki 3710 m<sup>2</sup>. Vidutinis rankiniu būdu nustatytas plotas buvo 1888 ± 2199 m<sup>2</sup>, palyginus su U-Net modelio apskaičiuotu 1218 ± 940 m<sup>2</sup> plotu su tiesinės dispersijos priklausomybe. „RGB“ kombinacija pasiekė didžiausią koreliacijos koeficientą ( $r = 0,87$ ) ir mažiausias paklaidas (MAE 562 ir RMSE 783).

Koreliacija tarp modelių ir *in situ* išmatuotų aukščių buvo reikšminga  $p < 0,05$  su  $r = 0,44$ , tačiau pasitelkus bepiločius orlaivius apskaičiuotas paplūdimio sąnašų aukštis, palyginus su *in situ* matavimais, buvo penkis kartus didesnis, todėl siūloma atsargiai naudoti šiuos aukščio nustatymo metodus. Ateityje tikslumą būtų galima padidinti fotografuojant ne tik kamerą nukreipus į apačią, bet ir pakreipus kampu, kad būtų galima geriau apskaičiuoti skaitmeninius aukščio modelius (Taddia et al., 2019).

Atlikus vizualinę analizę paaiškėjo, kad modelis daugumą paplūdimio sąnašų plotų klasifikavo gerai, tačiau tam tikrose srityse buvo pastebėta neatitikimų. NIR duomenys leido aiškiau atskirti paplūdimio sąnašas nuo aplinkos nei vien tik RGB duomenys. Netinkamas klasifikavimas akivaizdesnis vandens klasėse esant sudėtingoms sąlygoms, pavyzdžiui, esant banguotam vandens paviršiui ar saulės atspindžio paveiktoms ortofotonuotraukoms.

Vienos nuotraukos klasifikavimas trunka apie 5 minutes, todėl pasitelkus šį metodą paplūdimių stebėsenai galima juos greitai įvertinti, o ekonomiškai efektyvią ir veiksmingą darbo eigą galima pritaikyti įvairiems paplūdimių tipams. Ateityje mokslinius tyrimus reiktų atlikti įvairesnėmis morfologėmis sąlygomis, kad būtų galima padidinti modelio pritaikomumą ir tikslumą įtraukiant pažangius išankstinio apdoravimo metodus, pavyzdžiui, saulės atspindžio pašalinimą ir radiometrinę korekciją.

## IŠVADOS

1. Sukurta bepiločių orlaivių tyrimų sistema, parodanti, kaip įvairi duomenų skiriamoji geba, jutiklių integracija ir pažangūs analitiniai metodai padeda kartografuoti keturis nustatytus augalijos parametrus, bei pabrėžianti šių metodų veiksmingumą biologinės įvairovės išsaugojimo, ekosistemų struktūros analizės, fenologijos ir streso stebėsenos srityse. Ši sistema aplinkosaugos mokslininkams ir išteklių valdytojams suteikia išsamią metodiką, kaip panaudoti bepiločių orlaivių nuotolinį stebėjimą, kad būtų galima stebėti ir tvarkyti augmeniją įvairiose aplinkose.



## 8. Summary in Lithuanian

2. Nendrių sąžalynų pokyčiai, atsiradę dėl šienavimo, veiksmingai nustatyti naudojant Yen dvinarį slenksčio nustatymo algoritmą pagal normalizuotą vandens skirtumo indeksą, gautą iš Sentinel-2/MSI duomenų, todėl šis metodas yra patikimas stebėti ir valdyti nendrių sąžalynų dinamiką Platelių ežere. Reikšmingas aptikimo tikslumas buvo didesnis tankesniems (50 %) nendrių sąžalynų plotams, kurių dydis  $\geq 0,1$  ha.
3. Patvirtintas daugiaspektrinių bepiločių orlaivių jutiklių duomenų naudojimo su kvazianalitiniu algoritmu potencialas vertinant Secchi gylių vandens telkiniuose. Bepiločių orlaivių skrydžių metu atliktų Secchi gylio matavimų tikslumui didelę įtaką darė saulės atspindžio korekcijos metodai, iš kurių Hedley'io metodas buvo tiksliausias.
4. U-Net modelio nauda paplūdimio sąnašų segmentavimui buvo ypač veiksminga pritaikant „RGB“ duomenų kombinaciją. Modelio veikimas paplūdimiuose su skirtingomis geomorfologinėmis savybėmis (pvz. smėlėtas arba akmenuotas paplūdimys) skyrėsi, o tai rodo, kad, siekiant modelį panaudoti naujose teritorijose ir norint, kad jis veiktų tiksliau, modelį reikia sukalibruoti pridėdant naujų vaizdų. Daugiaspektrinių ir aukščio duomenų integravimas reikšmingai nepadidino tikslumo, palyginus su paprastesne „RGB“ kombinacija.

## CURRICULUM VITAE

Edvinas Tiškus was born on April 9, 1993, in Kretinga, Lithuania. He embarked on his academic journey in 2012, enrolling at Klaipėda University to pursue a bachelor's degree in Hydrology and Oceanography, which he completed in 2015. His passion for the field led him to further his studies at the same university, obtaining a master's degree in Geo-Informatics in 2018. Edvinas's academic path laid a solid foundation in geographic information science, focusing particularly on the application of GIS and remote sensing in environmental studies.

In January 2019, Edvinas began his Ph.D. at Klaipėda University, delving deeper into remote sensing and GIS, with a keen interest in their applications for environmental monitoring and analysis. During his master's and most of his Ph.D., Edvinas worked as an assistant specializing in remote sensing, a role that allowed him to apply his skills in practical settings and contribute to significant research projects.

Alongside his research, Edvinas took on the role of a lecturer in GIS and Remote Sensing at Klaipėda University from February 2018 to June 2023. His responsibilities included developing and delivering lectures, creating lesson plans, and mentoring students on their theses, showcasing his dedication to both his field and the education of future specialists.

Edvinas has been involved in several key projects, such as the TODAY project from April 2018 to April 2020, aimed at developing Earth Observation-based water quality systems, and the EOMORES project from January 2017 to November 2019, which focused on monitoring the ecological status of water bodies through Earth Observation data.

With a solid background in hydrology, oceanography, and geoinformatics, Edvinas has honed his expertise in Python, GIS, and remote sensing technologies. His work as a freelancer in the COST HARMONIOUS international project further exemplifies his capacity to innovate in the use of UAVs for environmental monitoring. Edvinas Tiškus career is marked by a commitment to enhancing the understanding and application of GIS and remote sensing in environmental science, making him a distinguished member of his academic and professional community.

**Research interests:** Remote Sensing Analysis; Geographic Information Systems (GIS) Applications; Environmental Monitoring; Water Quality Assessment; UAV Applications in Environmental Science.

---

## **Publications**

# PAPER I



Contents lists available at ScienceDirect

## Ecological Indicators

journal homepage: [www.elsevier.com/locate/ecolind](http://www.elsevier.com/locate/ecolind)

## Review



## Characterizing vegetation complexity with unmanned aerial systems (UAS) – A framework and synthesis

Jana Müllerová<sup>a,\*</sup>, Xurxo Gago<sup>b</sup>, Martynas Bučas<sup>c</sup>, Jaume Company<sup>d,e</sup>, Joan Estrany<sup>d,e</sup>,  
Josep Fortesa<sup>d,e</sup>, Salvatore Manfreda<sup>f</sup>, Adrien Michez<sup>g,h</sup>, Martin Mokroš<sup>i,j</sup>, Gernot Paulus<sup>k</sup>,  
Edvinas Tiškus<sup>c</sup>, Maria A. Tsiafouli<sup>l</sup>, Rafi Kent<sup>m</sup>

<sup>a</sup> Institute of Botany of the Czech Academy of Sciences, Prihonice, Czech Republic

<sup>b</sup> Research Group on Plant Biology under Mediterranean Conditions, Universitat de les Illes Balears (UIB), Institute of Agro-Environmental and Water Economy Research, INAGEA, Spain

<sup>c</sup> Marine Research Institute of Klaipėda University, Klaipėda, Lithuania

<sup>d</sup> Mediterranean Ecogeomorphological and Hydrological Connectivity Research Team, Department of Geography, University of the Balearic Islands, 07122 Palma, Spain

<sup>e</sup> Institute of Agro-Environmental and Water Economy Research, INAGEA, University of the Balearic Islands, 07122 Palma, Spain

<sup>f</sup> Dipartimento di Ingegneria Civile, Edile e Ambientale (DICEA), Università degli Studi di Napoli Federico II, Napoli, Italy

<sup>g</sup> Université Rennes 2 LETG (CNRS UMR 6554), CEDEX, 35043, Rennes, France

<sup>h</sup> TERRA Research and Teaching Center—Forest Is life, Gembloux Agro Bio-Tech, University of Liege, 5030 Gembloux, Belgium

<sup>i</sup> Technical University in Zvolen, Zvolen, Slovakia

<sup>j</sup> Czech University of Life Sciences Prague, Prague, Czech Republic

<sup>k</sup> Spatial Information Management, Carinthia University of Applied Sciences, Villach, Austria

<sup>l</sup> Aristotle University of Thessaloniki, School of Biology, Thessaloniki, Greece

<sup>m</sup> Independent Researcher, Bahan, Israel

## ARTICLE INFO

## Keywords:

Biodiversity  
Drones  
Heterogeneity  
Methodology  
Phenology  
Plant composition  
Plant stress  
Remote sensing  
RPAS  
Structural diversity  
UAS  
UAV

## ABSTRACT

Ecosystem complexity is among the important drivers of biodiversity and ecosystem functioning, and unmanned aerial systems (UASs) are becoming an important tool for characterizing vegetation patterns and processes. The variety of UASs applications is immense, and so are the procedures to process UASs data described in the literature. Optimizing the workflow is still a matter of discussion. Here, we present a comprehensive synthesis aiming to identify common rules that shape workflows applied in UAS-based studies facing complexity in ecosystems. Analysing the studies, we found similarities irrespective of the ecosystem, according to the character of the property addressed, such as species composition (biodiversity), ecosystem structure (stand volume/complexity), plant status (phenology and stress levels), and dynamics (disturbances and regeneration). We propose a general framework allowing to design UAS-based vegetation surveys according to its purpose and the component of ecosystem complexity addressed. We support the framework by detailed schemes as well as examples of best practices of UAS studies covering each of the vegetation properties (i.e. composition, structure, status and dynamics) and related applications. For an efficient UAS survey, the following points are crucial: knowledge of the phenomenon, choice of platform, sensor, resolution (temporal, spatial and spectral), model and classification algorithm according to the phenomenon, as well as careful interpretation of the results. The simpler the procedure, the more robust, repeatable, applicable and cost effective it is. Therefore, the proper design can minimize the efforts while maximizing the quality of the results.

## 1. Introduction

There are considerable gaps between field-based and remote sensing-based approaches as the field variables differ from those assessed by remote sensing techniques. Thanks to a very fine resolution, unmanned

aerial systems (UASs), also called unmanned aerial vehicles (UAVs), remotely piloted aerial systems (RPASs) and informally drones, can help to upscale the point or plot field measurements into the landscape scale, and potentially to larger areas bridging the gap between field surveys and satellite data (Alvarez-Vanhard et al., 2020). UASs are increasingly

\* Corresponding author.

E-mail address: [jana.mullerova@ibot.cas.cz](mailto:jana.mullerova@ibot.cas.cz) (J. Müllerová).

<https://doi.org/10.1016/j.ecolind.2021.108156>

Received 29 June 2021; Received in revised form 24 August 2021; Accepted 25 August 2021

Available online 2 September 2021

1470-160X/© 2021 The Authors.

Published by Elsevier Ltd.

This is an open access article under the CC BY-NC-ND license

<http://creativecommons.org/licenses/by-nc-nd/4.0/>

used in the last decade, becoming an important tool for characterizing different aspects/components of vegetation in many ecosystems worldwide. The tool is ideal for both research experiments and targeted operational use; e.g., in nature protection (Gonzalez et al., 2016; Jiménez López and Mulero-Pázmány, 2019; Müllerová et al., 2017a). A wide choice of aircraft types (different types of copters or fixed-wings), sensors (multispectral, hyperspectral, Light Detection and Ranging - LiDAR), procedures and algorithms are available for the acquisition as well as the processing and interpretation of data (Colomina and Molina, 2014; Fig. 1). UAS surveys can thus be customized and designed for a variety of applications (Yao et al., 2019). In order to maximize the benefits of UAS, it is crucial to choose appropriate system settings, design of the field campaign, preprocessing of the data and the algorithms (Tmusić et al., 2020). Considering the research purpose and characteristics of the studied ecosystem show to be likewise important.

Within vegetation studies, UAS tool is being used for a large variety of purposes, including mapping current vegetation state, studying processes at the level of ecosystem, community and individual, assessing and modelling the plant growth, monitoring and evaluating effects of human disturbances and natural disasters such as wildfires, torrential floods and insect outbreaks (Anderson and Gaston, 2013; Bailón-Ruiz et al., 2018; Calsamiglia et al., 2020; Estrany et al., 2019; Holman et al., 2016; Michez et al., 2016; Müllerová, 2019; Nási et al., 2018). Considering the increasing use of the tool, and the important impact the design of the study has on results, many scientists and practitioners emphasize the need for standardization to assure harmonizing the UAS data acquisition and subsequent processing with the research goal (Manfreda et al., 2018). For such standardization, a great variety of UAS-based research in the field of vegetation science needs to be synthesized into an integrated framework, including the common grounds and challenges.

Here, we present a comprehensive synthesis aiming to categorize research and identify common rules that shape workflows applied in UAS-based studies facing complexity in ecosystems. Ecosystem complexity is regarded as an important driver of biodiversity and ecosystem functioning across taxa, biomes and spatial scales (Stein et al., 2014). The variety of UAS applications in the vegetation heterogeneity assessment is immense, and so are the procedures described in the literature. Irrespective of the ecosystem, similarities can be found

according to the research aims (the ecosystem / community / individual property addressed). Vegetation properties encompass varying levels of heterogeneity in time and space, allowing classification into the following major components: (i) composition (covering a topic of biodiversity), (ii) structure (such as biomass and stand structure) and (iii) status (such as phenology stage and plant stress) (cf. Randlkofer et al., 2010). Following the concept of Essential Biodiversity Variables (EBV; Jetz et al. 2019), and remote sensing enabled EVBs (Reddy et al. 2021) these components could be translated into (i) compositional diversity (EBV groups of species populations & community composition), (ii) structural diversity (EBV group of ecosystem structure) and (iii) functional diversity (EBV groups of species traits & ecosystem function). All the components cover both static and dynamic processes, with different range and dimension of the dynamics. Still commonalities within these ecosystem components can be identified. Here, we present a synopsis as a general framework of UAS-based vegetation studies allowing us to design a UAS survey according to its purpose. We support the framework by detailed schemes of individual components, as well as examples of best practices of UAS studies covering each of the vegetation components and related applications.

## 2. General framework of UAS-based vegetation survey

The characterization of individual components within the framework of the vegetation complexity requires a specific survey design. The decision tree in Fig. 2 represents a general framework of vegetation surveys using UAS. The studies are divided according to the component of vegetation heterogeneity addressed: (1) species composition (parameters of biodiversity), (2) ecosystem structure (stand volume/complexity), (3) plant status (phenology and stress levels), and (4) dynamics (disturbances and regeneration) (see <https://www.cosh-armonious.eu/characterizing-vegetation-complexity-with-uas/> and Supplement 1 for an interactive workflow). To reach the best quality results, the design of the survey including quality of the data and selection of the processing algorithms should be driven by the purpose of research and characteristics of the ecosystem property of interest. Information on abiotic conditions (not necessarily derived from UAS surveys) are often essential for the models. Many of the processes are dynamic, so the temporal aspects related to abiotic and biotic factors



Fig. 1. Different platforms and sensors in UAS surveys; a) Lighter-Than-Air Helikite Balloon with Sony A7RII used for renaturation monitoring; b) BRAMOR ppk Fixed-Wing with Micasense Red Edge used for riparian vegetation monitoring; c) DJI Inspire 2 with zennuse x5s RGB camera, used for shallow water vegetation and beach cast monitoring (Palanga, Lithuania), and d) Leica Aibot AX 20 with multidirectional sensor prototype (5 Sony ILCE-QX1 RGB sensors for capturing NADIR and 4 oblique images). (For interpretation of the references to colour in this figure legend, the reader is referred to the web version of this article.)

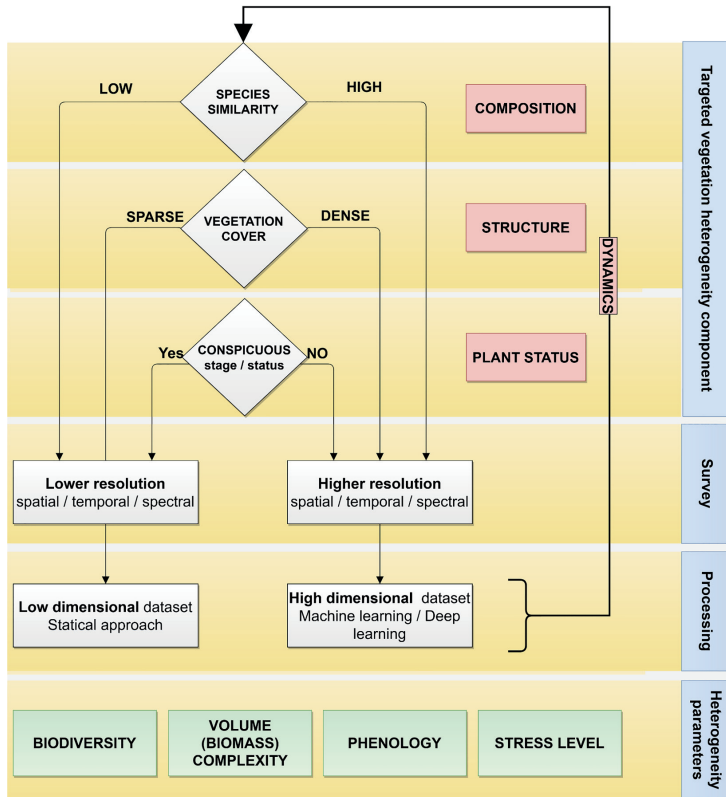


Fig. 2. Decision tree for designing the UAS-based vegetation survey according to the phenomenon/part of vegetation heterogeneity addressed. Details on each component of vegetation heterogeneity are explained in the following Figs. 3, 4 and 5, and in an interactive workflow at <https://www.costharmonious.eu/characterizing-vegetation-complexity-with-uas/> and in the Supplement 1).

need to be added to describe the changes properly. In the Fig. 2., abiotic conditions, such as geomorphology, soil properties, climatic conditions and hydrology are not included, still they all play a significant role in shaping the vegetation heterogeneity and influence the survey design (Tmusic et al., 2020).

The resolution of the UAS survey has to be adjusted depending on ecosystem characteristics, i.e. according to species and individuals' similarity and targeted heterogeneity component. The resolution, as the similarity, is hereafter considered in the following dimensions: time, space and electromagnetic spectrum. For example, when characterizing vegetation composition for the purposes of biodiversity assessment, monitoring of rare and invasive species, or understanding the processes of species coexistence and succession, it is crucial to differentiate among the species. Such differentiation will depend on the way the species occupy space through time. Furthermore, their intrinsic morphological properties will produce specific morphological and spectral signatures that can be applied for either species identification or evaluation of their status using remote sensing techniques. In case the spectral/textural characteristics of co-occurring species are similar, differentiation would require higher spectral resolution to increase their spectral separation

(Chadwick and Asner, 2016; Marvin et al., 2016). In general, the less distinct the feature is (e.g. species with a high degree of similarity to the surroundings), the more advanced sensors and the more complex methodology are required (Fig. 2). The same applies for assessing ecosystem structure, where for sparser ecosystems (e.g. sparse arid or semi-arid shrublands or tundra), photogrammetric point cloud can be sufficient, whereas for denser and more complex ecosystems such as forests, advanced LiDAR sensor becomes indispensable for most applications (Barbosa et al., 2016; Beland et al., 2019; Kent et al., 2015; Lefsky et al., 2002). The levels of conspicuousness and symptomatology of the studied phenomenon (e.g. phenological stage and/or physiological status caused by stress) influence the required level of spectral/spatial/temporal resolution (Fahlgren et al., 2015; Ghosal et al., 2018; Singh et al., 2016) and, again, the sophistication of the analytical models. In case of asymptomatic physiological status at visible range, it is very difficult to reach satisfactory results unless additional advanced hyperspectral or thermal sensors are used (Gago et al., 2017).

Insufficiently coarse resolution can decrease the accuracy, still more detail does not automatically mean better results. Whereas very high spatial resolution can be extremely beneficial for detection of small

patches or individual plants, it can tremendously increase the data complexity, processing time and data storage. Additionally, increasing spatial resolution from centimeters to millimeters can make classification extremely difficult, breaking individuals into a complex of branches and stems, green and dry leaves, individual flowers within the inflorescence, insects and soil background. Such extreme detail of UAS data also brings new challenges in the training and validation process (due to the precision limits of field Global Positioning System instruments, GPS), and proper matching of layers in case of change detection and canopy height models (Müllerová et al., 2017a). The three components of resolution, spatial, spectral and temporal, are interconnected, and certain trade-offs exist between them (Lisein et al., 2015; Michez et al., 2016). Thus, optimal resolution should be carefully chosen considering the purpose of the study as well as the target vegetation addressed.

**3. The hands-on challenge: How to assess species composition, ecosystem structure and plant status by employing UASs?**

*3.1. Species composition: Highlighting biodiversity*

Plant species composition varies along the axes of spatio-temporal heterogeneity (Lambers et al., 2008; Pugnaire and Valladares, 1999). Whereas at coarse scales it is defined by biogeographical zones and biomes, at finer scales, is determined by changes in composition as a function of abiotic conditions as well as inter-specific interactions with human management and co-occurring plant and animal species (Augustine and McNaughton, 1998; Fedele et al., 2017; Pugnaire and Valladares, 1999).

Examples where UASs have been used for specific vegetation/habitat types show that the challenges are to a certain extent case specific, depending mainly on natural characteristics. UASs were successfully applied in habitat mapping and monitoring for nature conservation purposes. Decisions on which methods and data to choose for UAS

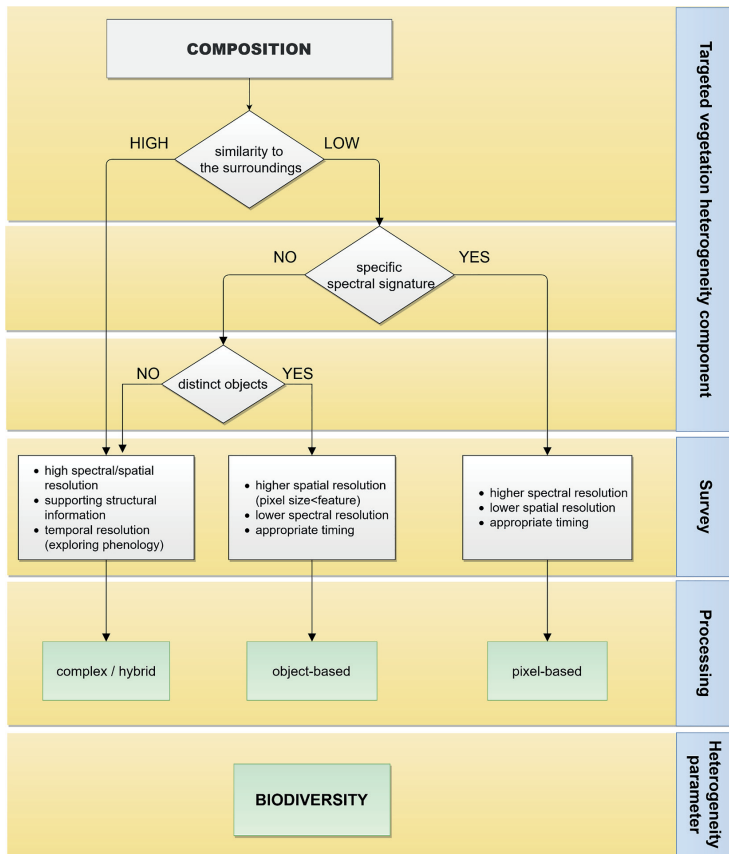


Fig. 3. Workflow for UAS-based detection of plant species composition (biodiversity, adapted from Müllerová, 2019).



assessment of plant composition shall be driven by the target species/vegetation characteristics. For species expressing low spectral and structural similarity to the co-occurring species, coarser resolution data combined with simple models would be sufficient; whereas for less distinct species, highly similar to their surroundings, a more complex approach must be applied (Müllerová, 2019). Accurate distinction between similar species is demanding in respect to the data resolution (spatial, temporal and/or spectral) and algorithms (using more complex or hybrid approaches); subtle differences in phenology or structure can help (Fig. 3).

For species that do not have a specific form (such as patchiness, and shape of individuals, inflorescences or the leaves) but are rather spectrally distinct from their surroundings, the pixel based approach might be appropriate (Müllerová et al., 2017a; Tamondong et al., 2020). Information on shape, texture and context can markedly improve precision of the species determination (Franklin, 2018; Gini et al., 2014). This is especially true for the species and/or vegetation types that have distinct shapes and/or form patches (Müllerová et al., 2017b), and for low cost digital Red-Green-Blue (RGB) cameras lacking near infrared band and with high intercorrelation of visible bands (Pande-Chhetri et al., 2017). In general, OBIA represents a powerful tool in UAS data processing that can to some extent reduce the noise and consequent “salt and pepper” effect caused by ultra high spatial resolution. However, the extreme detail leads to a large number of objects with varying spectral, morphological and proximity characteristics, which can be controlled by choosing the right spatial resolution (Yuba et al., 2021).

For complex vegetation patterns and species with a high degree of similarity, there is a need for higher spectral/spatial/temporal resolution data, multiple data sources, three-dimensional (3D) information on stand height and structure and/or advanced algorithms (e.g. Kattenborn et al., 2020; Martin et al., 2018; Michez et al., 2013). Machine and deep learning algorithms are particularly helpful to map complex vegetation, and can overcome the problem with laborious collection of training samples and ultra high spatial resolution (Liu et al., 2018).

To summarize, provided that the methodological workflow of the mission follows the species/habitat characteristics, UASs represent a powerful tool to be employed in biodiversity monitoring schemes, enabling assessment of species diversity and detection and mapping of individual species and/or habitat types. Thanks to very high spatial and temporal resolution, either repeatedly throughout the phenological season or using the optimal time window for the data acquisition, it is possible to map even the species that are difficult to distinct from the surroundings, especially in case information on 3D structure is added, several sensors combined and/or sophisticated algorithms of machine and deep learning deployed.

### 3.2. Ecosystem structure: Measuring biomass, volume and stand complexity

The structure belongs among the main drivers of resource variability. Particularly in forest environments, fine-scale information on canopy structure derived from UAS like canopy cover, gaps, vertical and horizontal structure and spatial aggregation are important since structure drives many ecological processes such as understory diversity, seed establishment, and forest regeneration, and shapes important ecosystem services (Bagaram et al., 2018; Getzin et al., 2012; Kent et al., 2015).

Examples of assessing structure can be found for various ecosystems, such as shrublands (Cunliffe et al., 2016; Swetnam et al., 2018) and riparian areas (Meneses et al., 2018), but most UAS studies regard forests. In the latter, vegetation structure is addressed to analyse the stand complexity or quantify its volume/biomass (Fig. 4). 3D information is generated by different sensors and stored as point clouds for further processing. Normalization of ground using precise Digital Terrain Model (DTM) is greatly recommended (Aguilar et al., 2019). For 3D information, both passive (optical) and active (e.g. LiDAR) sensors can be used (Camarreta et al., 2020). While 3D information describing the upper

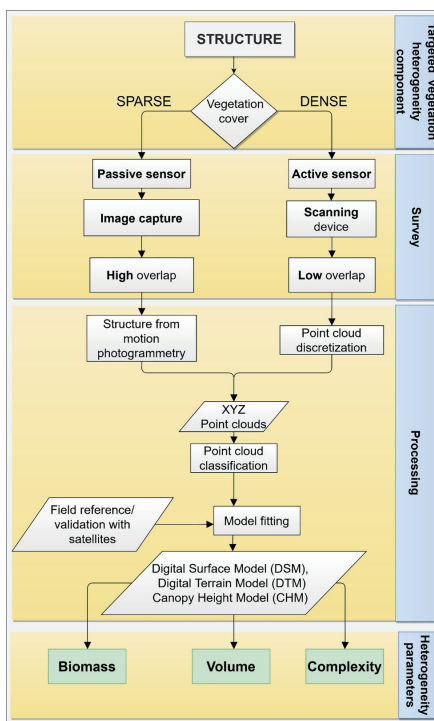


Fig. 4. Workflow for UAS-based ecosystem structure assessment.

most canopy layer can be acquired by various sensors, LiDAR sensors are necessary for the generation of DTM under the forest canopy and assessment of structural layers that is intrinsically related to the stand density and complexity.

Laser scanning provides the most accurate information on structural components including height, canopy dimensions, gaps, and biomass, and if mounted on UAS it can provide very high spatial details. However, its application is still limited due to the high costs and the fact that the sampled area is substantially smaller compared to the aerial LiDAR. In case of dense stands with complex multidimensional structure, active sensors (LiDAR) or DTM-independent approaches are an option (Gianetti et al., 2018), whereas passive sensors are not able to penetrate the canopy (especially during leaf-on season) to reach the inner structural layers and the ground (Kaspar et al., 2021). Still, for less dense and complex stands, passive optical sensors represent a low cost and simple solution to provide information on forest attributes including height, canopy dimensions, and biomass (Baltsavias et al., 2008; Dandois and Ellis, 2010; White et al., 2015). Photogrammetric point clouds are derived from overlapping imagery by using the digital imaging photogrammetry approach such as Structure from Motion (SfM) algorithm (Westoby et al., 2012), preferably with high overlap and lower flight altitudes (Seifert et al., 2019).

Still, many issues remain using passive instead of active sensors, especially related to closed or vertically complex canopy and shadows (Dandois and Ellis, 2013). Precision of results is also species specific;

while for evergreen single-stemmed tree species, photogrammetric products are comparable to LiDAR in capability to capture forest structure and estimate the biomass (especially for regularly designed forest plantations and open forests), it is less reliable for deciduous trees (especially during leaf-on period) and for canopy cover above 60 to 80% (Guerra-Hernández et al., 2017; Wallace et al., 2016). To overcome these problems, the data sources can be joined, such as adding spectral properties to LiDAR, or combining LiDAR-derived DTM and a series of photogrammetrically-derived DSMs to assess changes in the canopy (Lisein et al., 2013; Wallace et al., 2016). However, in such cases, precise co-registration is required. Alternatively, analyses of forest structure and gaps can be based solely on optical properties of UAS imagery, using the effect of darker objects (shaded gaps; Bagaram et al., 2018; Getzin et al., 2014). Nevertheless, such approach might bring even more imprecision with dense and/or highly vertically heterogeneous canopies.

As summarized in Fig. 4, from the examples proposed from different communities and environments, the choice of the sensor (active vs passive remote sensing) is particularly important for the structural assessment, and should respect the complexity of the stand to be sampled.

3.3. Plant status: phenology and plant stress

Plant status is driven by phenological stage and physiological status in response to endogenous (circadian and seasonal rhythms) and exogenous factors (abiotic stressors). High spatial and temporal resolution of

UASs provide an unprecedented detailed insight into the ecosystem's response to (a)biotic stress (D'Odorico et al., 2020). Most of the papers using UASs to assess plant stress are performed in agricultural and forestry applications focusing only on a single species at a time, while for species rich natural ecosystems, such studies are largely lacking (but see e.g. Banerjee et al., 2020; Zhang et al., 2017).

Studied phenomena can range from distinct and well defined phenomena by spectral properties that can be assessed using relatively low spatial, temporal and spectral resolution, to the less conspicuous/symptomatic phenomena, where the most sophisticated hyperspectral and thermal sensors coupled with complex modelling are needed (Fig. 5). In addition, even defining specific factors affecting the particular plant physiological status might be difficult due to the fact that the plant response to different types of stress is often indistinctive (Jones and Vaughan, 2010).

For example, UASs thermal imagery and the related leaf energy balance model estimations can be used to detect (a)biotic stress early since stomata are highly reactive to any stress, from abiotic stress such as drought (Gago et al., 2017) and herbivory attacks (Smigaj et al., 2019). In addition, stomata closure promotes general increase in canopy temperature that can be used as a physiological stress indicator (Smigaj et al., 2019). Very high spatial resolution of UAS data opens the opportunity to assess drought stress at individual level.

As for phenological stage, UASs provide both very high spatial detail and possibility of right timing of the data acquisition to capture a particular phenomenon, e.g. flowering (Carl et al. 2017; Müllerová

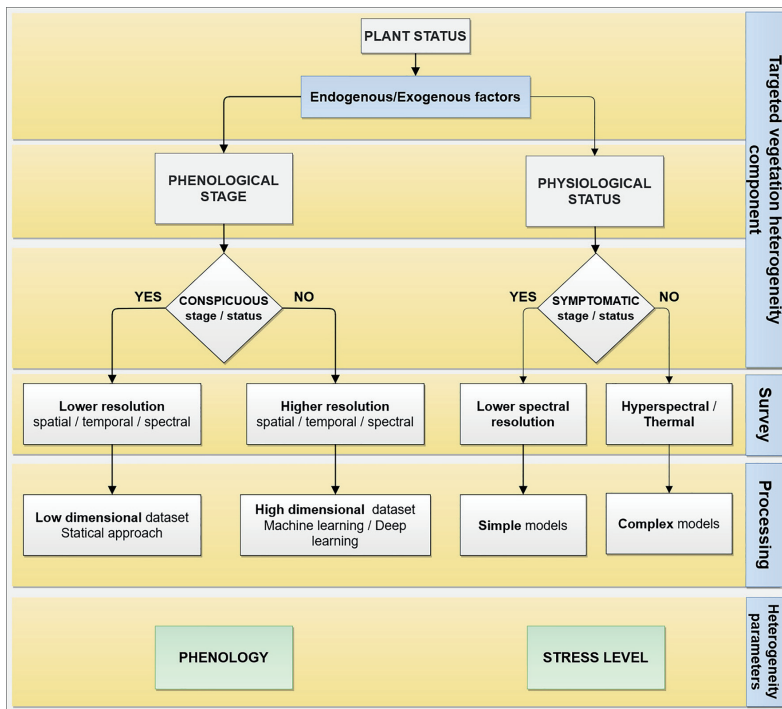


Fig. 5. Workflow for UAS-based assessment of plant status.

et al., 2017b; de Sá et al. 2018). Unlike the satellite data, UAS surveys allow data acquisition on demand and enable to zoom on individual plants within the stand, and therefore to study variation within plant populations and/or trace the very first or last individuals of particular phenophase (Fawcett et al., 2020). Improvements of sensor resolution and/or ability of UAS to fly very close to the canopies obtaining sub-cm resolution (such as for nano and micro-UASs) are still not widely employed even though the spatial information they provide is tremendous. For instance, ultra high spatial resolution enables the detection of flowering individuals without the need for higher spectral resolution sensors, opening a new opportunity to use micro-UASs to characterize ecosystem dynamics (Gago et al., 2020).

#### 3.4. Ecosystem dynamics: Disturbances and regeneration

Many natural processes are dynamic, addressing plant composition, ecosystem structure or plant status from a temporal perspective. Whereas data collection itself follows the workflows suggested in previous sections depending on the type of ecosystem/phenomenon and heterogeneity addressed, a change detection approach is adopted for repeated UAS measurements to study the changes in time. Still, we have to bear in mind that for different components of heterogeneity (composition, structure and status), the dynamics can show different ranges and dimensions that must be reflected by the survey design.

To assess dynamic processes, such as phenological development or stress response, the temporal dimension is indispensable. Operational satellite data are the most commonly used for this purpose, however due to lower spatial resolution they are suitable mostly at global and landscape scales and for large homogeneous stands (Berra et al., 2019), and their temporal coverage is limited by their revisiting frequency. On the contrary, UAS can provide very high spatial and temporal resolution (revisiting time), and flexible, frequent and “ad hoc” data acquisition. Thus, UASs allow to explore the phenological cycle in unprecedented detail, e.g. individual-level phenological patterns and intraspecific variation (Fawcett et al., 2020; Park et al., 2019). Because of unprecedented fine scales, UAS are also very appropriate for dynamic ecosystems such as riparian areas and river ecosystems (Laslier et al., 2019; Michez et al., 2016).

In case of dramatic events, absence of data is common. Here, flexibility provided by UAS brings immediate revenues, since the surveys need to be conducted as soon as possible after the disturbance to support the decision-making and prevent further damage. Flights can be conducted immediately, eliminating the risk of injury linked to field surveys, such as in case of forest fires and windthrow (Mokroš et al., 2017; Yuan et al., 2015). UASs was also shown to assist in monitoring post-fire regeneration (Fernández-Guisuraga et al., 2018; Larrinaga and Brotons, 2019).

Insect disturbances in forests act at varying spatial and temporal scales, and understanding local dynamics as well as early detection of infestation onsets, which can be both facilitated by UAS, are very important (Senf et al., 2017). A variety of approaches and sensors were applied in UAS analyses of forest infestation dynamics; not only sophisticated hyperspectral sensors (Näsi et al., 2018) but also simpler sensors, such as multispectral or even low cost consumer grade cameras (Cardil et al., 2017; Minařík and Langhammer, 2016). UAS can also serve to study natural regeneration of forest after the outbreak (Röder et al., 2018). UAS assessment allows more cost-effective monitoring compared to the field surveys, and enables to acquire data at very high frequency providing observation data about the gradual spectral change after the attack. It can therefore be used to estimate the impacts of forest defoliation in spatial and temporal terms, for better assessing outbreak spread patterns and providing guidance in forest management programs. For possible extension of monitoring over larger areas, integration of UAS and satellite data is to be considered.

#### 4. Research gaps and future perspectives

Exploring the capabilities of different statistical, spatial, temporal and textural settings, UAS represent a huge potential for assisted vegetation assessment. There is no doubt that recent technical advances significantly increase capabilities and accessibility of both platforms and sensors. One such example is the geometrical precision of UAS orthomosaics. Geometric distortions, particularly significant in forest or other complex environments (see Ludwig et al., 2020), can to a large extent deteriorate reproducibility, complicate the assessment of dynamic processes and decrease the power of change detection in general. Even though the number and design of ground control points are still an open debate in the scientific community (Padró et al., 2019), recent advances in affordable miniaturized GPS and on board UAS (such as Real-time kinematic - RTK) push the boundaries towards automation and increased geometric accuracy without (or with severely limited amount of) field work.

In addition, technological progress is opening brand new opportunities, such as extraction of meaningful information through standardized procedures without a need to be a specialist in the remote sensing field, mechanistic models and/or on-the-fly incorporation of ground and plant measurements to calibrate the remote sensing models, different flight modes (flying closer to the target, longer flights covering larger area, penetrating the forest canopy to assess the forest herb layer, Hyypää et al. 2020; Ryddel et al., 2020), autonomous/real-time sensing (improving temporal resolution to assess plant stress, detection of non forested and eroded areas in tropical rainforest, Cruz et al. 2016), or targetless workflows to capture accurate reflectance values (Schneider-Zapp et al., 2019).

However, even though technological advances are expected to overcome many limits of current technologies and methodologies, some constraints will certainly remain, such as UAS regulations and restrictions. Recent harmonization of UAS regulations within the EU will definitely foster collaborative efforts and promote competitive development in the field.

#### 5. Concluding remarks

UAS offer products and applications never imagined just a decade ago. However, optimizing the workflow is still a matter of discussion. In our review, we summarized and generalized the procedures of UAS-based vegetation research. Aiming to provide a framework for optimal workflow to characterize vegetation complexity with UAS, we divided it by the major components of vegetation complexity: biodiversity, structure and status, covering also the dynamic processes. We propose a general framework and detailed decision trees for each component including examples, and synthesize that any UAS survey must be built respecting the following steps: (i) get familiar with the phenomenon to be studied; (ii) choose suitable UAS and appropriate temporal, spatial and spectral resolution; (iii) select either simple or more sophisticated processing, classification algorithms and models depending on the complexity of the studied phenomenon; and (iv) carefully interpret the results considering the weaknesses and limits of UASs methods. During the process one must bear in mind that the simpler the procedure, the more robust, repeatable, applicable and cost effective it is; proper design minimizes the efforts and maximizes the best results, and appropriate temporal, spatial and spectral resolution are essential key-points. The experimental design must thus be adapted to the studied phenomenon and not the other way around. Still, even if UAS technology is capable and widely available, a combination of profound ecological background (Goddard et al., 2021) and robust knowledge on the limits of UAS technology are indispensable to avoid misinterpretation of the findings.

#### Declaration of Competing Interest

The authors declare that they have no known competing financial

interests or personal relationships that could have appeared to influence the work reported in this paper.

#### Acknowledgements

This research was supported by the COST Action CA16219 “HARMONIOUS - Harmonization of UAS techniques for agricultural and natural ecosystems monitoring”. JM was supported by RVO 67985939 (Czech Academy of Sciences) and LTC18007 (Ministry of Education, Youth and Sport, CR). XG, JE, JF and JC were supported by the research project CGL2017-88200-R “Functional hydrological and sediment connectivity at Mediterranean catchments: global change scenarios – MEDHyCON2” funded by the Spanish Ministry of Science, Innovation and Universities, the Spanish Agency of Research (AEI) and the European Regional Development Funds (ERDF). JF has a postdoctoral contract funded by the Ministry of Innovation, Research and Tourism of the Autonomous Government of the Balearic Islands (FPI/2048/2017). JC is in receipt of a Young Qualified Program Grant funded by the Employment Service of the Balearic Islands and European Social Fund (SJ-QSP 48/19). MM was supported by Grant No. CZ.02.1.01/0.0/0.0/16 019/000803 (OP RDE) and by the Slovak Research and Development Agency through Grant No. APVV-18-0305.

#### Author Contribution

JM conceived and co-ordinated the writing, RK and XG supported formulation of the framework and the paper outline, and all authors took an active part in writing the paper.

#### Appendix A. Supplementary data

Supplementary data to this article can be found online at <https://doi.org/10.1016/j.ecolind.2021.108156>.

#### References

Aguilar, F.J., Rivas, J.R., Nemmaoui, A., Peñalver, A., Aguilar, M.A., 2019. UAV-based digital terrain model generation under leaf-off conditions to support teak plantations inventories in tropical dry forests. A case of the coastal region of Ecuador. *Sensors* 19 (8), 1934.

Alvarez-Vanhard, E., Houet, T., Mony, C., Lecoq, L., Corpetti, T., 2020. Can UAVs fill the gap between in situ surveys and satellites for habitat mapping? *Remote Sens. Environ.* 243, 111780.

Anderson, K., Gaston, K.J., 2013. Lightweight unmanned aerial vehicles will revolutionize spatial ecology. *Front. Ecol. Environ.* 11 (3), 138–146.

Augustine, D.J., McNaughton, S.J., 1998. Ungulate effects on the functional species composition of plant communities: herbivore selectivity and plant tolerance. *J. Wildl. Manag.* 62 (4), 1165–1183.

Bagaram, M., Giuliarelli, D., Chirici, G., Giannetti, F., Barbati, A., 2018. UAV remote sensing for biodiversity monitoring: are forest canopy gaps good covariates? *Remote Sensing* 10 (9), 1397.

Ballon-Ruiz, R., Lacroix, S., Bit-Monnot, A., 2018. Planning to monitor wildfires with a fleet of UASs. In: 2018 IEEE/RSJ International Conference on Intelligent Robots and Systems (IROS). IEEE, pp. 4729–4734.

Baltsavias, E., Gruen, A., Eisenbeiss, H., Zhang, L., Water, L.T., 2008. High-quality image matching and automated generation of 3D tree models. *Int. J. Remote Sens.* 29 (5), 1243–1259.

Banerjee, B.P., Raval, S., Cullen, P.J., 2020. UAS-hyperspectral imaging of spectrally complex environments. *Int. J. Remote Sens.* 41 (11), 4136–4159.

Barbosa, J.M., Asner, G.P., Martin, R.E., Baldeck, C.A., Hughes, F., Johnson, T., 2016. Determining subcanopy Psidium cattleianum invasion in Hawaiian forests using imaging spectroscopy. *Remote Sensing* 8 (1), 33.

Beland, M., Parker, G., Sparrow, B., Harding, D., Chasmer, L., Phinn, S., Antonarakis, A., Strahler, A., 2019. On promoting the use of lidar systems in forest ecosystem research. *For. Ecol. Manag.* 450, 117484.

Berra, E.F., Gallton, R., Barr, S., 2019. Assessing spring phenology of a temperate woodland: A multiscale comparison of ground, unmanned aerial vehicle and Landsat satellite observations. *Remote Sens. Environ.* 223, 229–242.

Calsamiglia, A., Gago, J., Garcia-Comendador, J., Bernat, J.F., Calvo-Cases, A., Estrany, J., 2020. Evaluating functional connectivity in a small agricultural catchment under contrasting flood events by using UAS. *Earth Surf. Proc. Land.* 45 (4), 800–815.

Camarretta, N., Harrison, P.A., Bailey, T., Potts, B., Lucier, A., Davidson, N., Hunt, M., 2020. Monitoring forest structure to guide adaptive management of forest restoration: a review of remote sensing approaches. *New Forest.* 51 (4), 573–596.

Cardil, A., Vepakomma, U., Brotons, L., 2017. Assessing pine processionary moth defoliation using unmanned aerial systems. *Forests* 8 (10), 402.

Carl, C., Landgraf, D., der Maaten-Theunissen, V., Biber, P., Pretzsch, H., 2017. Robinia pseudoacacia L. flower analyzed by using an unmanned aerial vehicle (UAV). *Remote Sensing* 9 (11), 1091.

Chadwick, K.D., Asner, G.P., 2016. Organismic-scale remote sensing of canopy foliar traits in lowland tropical forests. *Remote Sensing* 8 (2), 87.

Colomina, I., Molina, P., 2014. Unmanned aerial systems for photogrammetry and remote sensing: A review. *ISPRS J. Photogramm. Remote Sens.* 92, 79–97.

Cruz, H.O., Eckert, M., Meneses, J.M., Martínez, J.F., 2016. Precise real-time detection of nonforested areas with UAVs. *IEEE Trans. Geosci. Remote Sens.* 55 (2), 632–644.

Cunliffe, A.M., Brazier, R.E., Anderson, K., 2016. Ultra-fine grain landscape-scale quantification of dryland vegetation structure with drone-acquired structure-from-motion photogrammetry. *Remote Sens. Environ.* 183, 129–143.

Dandois, J.P., Ellis, E.C., 2010. Remote sensing of vegetation structure using computer vision. *Remote Sensing* 2, 1157–1176.

Dandois, J.P., Ellis, E.C., 2013. High spatial resolution three-dimensional mapping of vegetation spectral dynamics using computer vision. *Remote Sens. Environ.* 136, 259–276.

D’Odorico, P., Besik, A., Wong, C.Y., Isabel, N., Ensminger, I., 2020. High-throughput drone-based remote sensing reliably tracks phenology in thousands of conifer seedlings. *New Phytol.* 226 (6), 1667–1681.

Estrany, J., Ruiz, M., Calsamiglia, A., Carrifujó, M., García-Comendador, J., Nadal, M., Fortes, J., López-Tarazon, J.A., Hipólito, M., Gago, J., 2019. Sediment connectivity linked to vegetation using UASs: High-resolution imagery for ecosystem management. *Sci. Total Environ.* 671, 1192–1205.

Fahlgren, N., Gehan, M.A., Baxter, I., 2015. Lights, camera, action: high-throughput plant phenotyping is ready for a close-up. *Curr. Opin. Plant Biol.* 24, 93–99.

Fawcett, D., Bennie, J., Anderson, K., 2020. Monitoring spring phenology of individual tree crowns using drone-acquired NDVI data. *Remote Sens. Ecol. Conserv.* 7 (2), 227–244.

Fedele, G., Locatelli, B., Djoudi, H., 2017. Mechanisms mediating the contribution of ecosystem services to human well-being and resilience. *Ecosyst. Serv.* 28, 43–54.

Fernández-Guisuraga, J.M., Sanz-Abianedo, E., Suárez-Seoane, S., Calvo, L., 2018. Using unmanned aerial vehicles in positive vegetation survey campaigns through large and heterogeneous areas: Opportunities and Challenges. *Sensors* 18 (2), 586.

Franklin, S.E., 2018. Pixel- and object-based multispectral classification of forest tree species from small unmanned aerial vehicles. *J. Unmanned Vehicle Systems* 6 (4), 195–211.

Gago, J., Estrany, J., Estes, L., Fernie, A.R., Alorda, B., Brotman, Y., Flexas, J., Escalona, J.M., Medrano, H., 2020. Nano and Micro Unmanned Aerial Vehicles (UAVs): A New Grand Challenge for Precision Agriculture? *Current Protocols in Plant Biology* 5 (1), e20103.

Gago, J., Fernie, A.R., Nikoloski, Z., Tohge, T., Martorell, S., Escalona, J.M., Ribas-Carbó, M., Flexas, J., Medrano, H., 2017. Integrative field scale phenotyping for investigating metabolic components of water stress within a vineyard. *Plant Methods* 13 (1), 1–14.

Getzin, S., Nuske, R.S., Wiegand, K., 2014. Using unmanned aerial vehicles (UAV) to quantify spatial gap patterns in forests. *Remote Sensing* 6 (8), 6988–7004.

Getzin, S., Wiegand, K., Schöning, L., 2012. Assessing biodiversity in forests using very high-resolution images and unmanned aerial vehicles. *Methods Ecol. Evol.* 3 (2), 397–404.

Ghosal, S., Blystone, D., Singh, A.K., Ganapathysubramanian, B., Singh, A., Sarkar, S., 2018. An explainable deep machine vision framework for plant stress phenotyping. *Proc. Natl. Acad. Sci.* 115 (18), 4613–4618.

Giannetti, F., Puletti, N., Quattrini, V., Travaglini, D., Bottalico, F., Corona, P., Chirici, G., 2018. Integrating terrestrial and airborne laser scanning for the assessment of single-tree attributes in Mediterranean forest stands. *Eur. J. Remote Sens.* 51 (1), 795–807.

Gini, R., Passoni, D., Pinto, L., Soná, G., 2014. Use of unmanned aerial systems for multispectral survey and tree classification: A test in a park area of northern Italy. *Eur. J. Remote Sens.* 47 (1), 251–269.

Goddard, M.A., Davies, Z.G., Guenat, S., Ferguson, M.J., Fisher, J.C., Akanni, A., Dallimer, M., 2021. A global horizon scan of the future impacts of robotics and autonomous systems on urban ecosystems. *Nat. Ecol. Evol.* 5, 219–230.

Gonzalez, L.F., Montes, G.A., Puig, E., Johnson, S., Mengersen, K., Gaston, K.J., 2016. Unmanned aerial vehicles (UASs) and artificial intelligence revolutionizing wildlife monitoring and conservation. *Sensors* 16 (1), 97.

Guerra-Hernández, J., González-Ferreiro, E., Monleón, V.J., Fajás, S.P., Tomé, M., Díaz-Varela, R.A., 2017. Use of multi-temporal UAS-derived imagery for estimating individual tree growth in Pinus pinea stands. *Forests* 8 (8), 300.

Holman, F.H., Riche, A.B., Michalski, A., Castle, M., Wooster, M.J., Hawkesford, M.J., 2016. High throughput field phenotyping of wheat plant height and growth rate in field plot trials using UAS based remote sensing. *Remote Sens.* 8 (12), 1031.

Hyypää, E., Hyypää, J., Hakala, T., Kukko, A., Wulder, M.A., White, J.C., Kaartinen, H., 2020. Under-canopy UAV laser scanning for accurate forest field measurements. *ISPRS J. Photogramm. Remote Sens.* 164, 41–60.

Jetz, W., McGeoch, M.A., Guralnick, R., Ferrier, S., Beck, J., Costello, M.J., Turak, E., 2019. Essential biodiversity variables for mapping and monitoring species populations. *Nat. Ecol. Evol.* 3 (4), 539–551.

Jiménez López, J., Mulero-Pázmány, M., 2019. Drones for conservation in protected areas: present and future. *Drones* 3 (1), 10.

Jones, H.G., Vaughan, R.A., 2010. *Remote Sensing of Vegetation: Principles, Techniques, and Applications*. Oxford University Press.

Kaspar, V., Hederová, L., Macek, M., Müllerová, J., Prošek, J., Surový, P., Wild, J., Kopecký, M., 2021. Temperature buffering in temperate forests: comparing

- microclimate models based on ground measurements with active and passive remote sensing. *Remote Sens. Environ.* 263, 112522.
- Kattenborn, T., Eichel, J., Wisler, S., Burrows, L., Fassnacht, F.E., Schmidlein, S., 2020. Convolutional Neural Networks accurately predict cover fractions of plant species and communities in Unmanned Aerial Vehicle imagery. *Remote Sens. Ecol. Conserv.* 6 (4), 472–486.
- Kent, R., Lindsell, J.A., Laurin, G.V., Valentini, R., Coomes, D.A., 2015. Airborne LiDAR detects selectively logged tropical forest even in an advanced stage of recovery. *Remote Sensing* 7 (7), 8348–8367.
- Lammers, H., Chapin III, F.S., Pons, T.L., 2008. *Plant Physiological Ecology*. Springer Science Business Media.
- Larrinaga, A.R., Brotons, L., 2019. Greenness indices from a low-cost UAV imagery as tools for monitoring post-fire forest recovery. *Drones* 3 (1), 6.
- Laslier, M., Hubert-Moy, L., Corpetti, T., Dufour, S., 2019. Monitoring the colonization of alluvial deposits using multitemporal UAV RGB-imagery. *Appl. Veg. Sci.* 22, 561–572.
- Lefsky, M.A., Cohen, W.B., Parker, G.G., Harding, D.J., 2002. Lidar remote sensing for ecosystem studies: Lidar, an emerging remote sensing technology that directly measures the three-dimensional distribution of plant canopies, can accurately estimate vegetation structural attributes and should be of particular interest to forest, landscape, and global ecologists. *Bioscience* 52 (1), 19–30.
- Lisein, J., Michez, A., Claessens, H., Lejeune, P., 2015. Discrimination of deciduous tree species from time series of unmanned aerial system imagery. *PLoS ONE* 10 (11), e014006.
- Lisein, J., Pierrot-Deseilligny, M., Bonnet, S., Lejeune, P., 2013. A photogrammetric workflow for the creation of a forest canopy height model from small unmanned aerial system imagery. *Forests* 4, 922–944.
- Liu, T., Abd-Elrahman, A., Morton, J., Wilhelm, V.L., 2018. Comparing fully convolutional networks, random forest, support vector machine, and patch-based deep convolutional neural networks for object-based wetland mapping using images from small unmanned aircraft system. *GIScience Remote Sensing* 55 (2), 243–264.
- Ludwig, M., Runge, C.M., Friess, N., Koch, T.L., Richter, S., Seyfried, S., Wraase, L., Lobo, A., Sebastián, M.-T., Reudenbach, C., Naus, T., 2020. Quality Assessment of Photogrammetric Methods—A Workflow for Reproducible UAS Orthomosaics. *Remote Sensing* 12 (22), 3831.
- Manfreda, S., McCabe, M.F., Miller, P.E., Lucas, R., Pajuelo Madrigal, V., Mallinis, G., Toth, B., 2018. On the use of unmanned aerial systems for environmental monitoring. *Remote Sensing* 10 (4), 641.
- Martin, F.M., Müllerová, J., Borgniet, L., Dommanget, F., Breton, V., Evette, A., 2018. Using single-and multi-date UAV and satellite imagery to accurately monitor invasive knotweed species. *Remote Sensing* 10 (10), 1662.
- Marvin, D.C., Koh, L.P., Lynam, A.J., Wich, S., Davies, A.B., Krishnamurthy, R., Stokes, E., Starkey, R., Asner, G.P., 2016. Integrating technologies for scalable ecology and conservation. *Global Ecol. Conserv.* 7, 262–275.
- Meneses, N.C., Baier, S., Reidelstürz, P., Geist, J., Schneider, T., 2018. Modelling heights of sparse aquatic reed (*Phragmites australis*) using Structure from Motion point clouds derived from Rotary- and Fixed-Wing Unmanned Aerial Vehicle (UAV) data. *Limnologia* 72, 10–21.
- Michez, A., Piégay, H., Lisein, J., Claessens, H., Lejeune, P., 2016. Classification of riparian forest species and health condition using multi-temporal and hyperspatial imagery from unmanned aerial system. *Environ. Monit. Assess.* 188 (3), 146.
- Michez, A., Piégay, H., Toromanoff, F., Brogna, D., Bonnet, S., Lejeune, P., Claessens, H., 2013. LiDAR derived ecological integrity indicators for riparian zones: Application to the Houille river in Southern Belgium/Northern France. *Ecol. Ind.* 34, 627–640.
- Minarik, R., Langhammer, J., 2016. Use of a Multispectral UAV Photogrammetry for Detection and Tracking of Forest Disturbance Dynamics. *International Archives of the Photogrammetry, Remote Sensing Spatial Information Sciences*, p. 41.
- Mokros, M., Vybostok, J., Merganic, J., Hollaus, M., Barton, I., Koren, M., Tomastik, J., Cernava, J., 2017. Early Stage Forest Windthrow Estimation Based on Unmanned Aircraft System Imagery. *Forests* 8, 306.
- Müllerová, J., 2019. UAS for Nature Conservation-Monitoring Invasive Species. In: Sharma, J.B. (Ed.), *Applications of Small Unmanned Aircraft Systems: Best Practices and Case Studies*. CRC Press, pp. 157–178.
- Müllerová, J., Bartalós, T., Bruna, J., Dvorák, P., Vitková, M., 2017a. Unmanned aircraft in nature conservation: an example from plant invasions. *Int. J. Remote Sens.* 38, 2177–2198.
- Müllerová, J., Bruna, J., Bartalós, T., Dvorák, P., Vitková, M., Pyšek, P., 2017b. Timing Is Important: Unmanned Aircraft vs. Satellite Imagery in Plant Invasion Monitoring. *Front. Plant Sci.* 8, 1–13.
- Näsi, R., Honkavaara, E., Blomqvist, M., Lyytikäinen-Saarenmaa, P., Hakala, T., Viljanen, N., Kantola, T., Holopainen, M., 2018. Remote sensing of bark beetle damage in urban forests at individual tree level using a novel hyperspectral camera from UAV and aircraft. *Urban Forestry Urban Green.* 30, 72–83.
- Padró, J.C., Muñoz, F.J., Planas, J., Pons, X., 2019. Comparison of four UAS georeferencing methods for environmental monitoring purposes focusing on the combined use with airborne and satellite remote sensing platforms. *Int. J. Appl. Earth Obs. Geoinf.* 75, 130–140.
- Pande-Chhetri, R., Abd-Elrahman, A., Liu, T., Morton, J., Wilhelm, V.L., 2017. Object-based classification of wetland vegetation using very high-resolution unmanned aerial system imagery. *Eur. J. Remote Sens.* 50 (1), 564–576.
- Park, J.Y., Muller-Landau, H.C., Lichtenstein, J.W., Rifai, S.W., Dandois, J.P., Bohlman, S.A., 2019. Quantifying leaf phenology of individual trees and species in a tropical forest using unmanned aerial vehicle (UAS) images. *Remote Sens.* 11 (13), 1534.
- Pugnaire, F., Valladares, F. (Eds.), 1999. *Handbook of functional Plant Ecology*. CRC Press.
- Randlkofer, B., Obermaier, E., Hilker, M., Meiners, T., 2010. Vegetation complexity—The influence of plant species diversity and plant structures on plant chemical complexity and arthropods. *Basic Appl. Ecol.* 11, 383–395.
- Reddy, C.S., Kurian, A., Srivastava, G., Singhal, J., Varghese, A.O., Padalia, H., Rao, P.V. N., 2021. Remote sensing enabled essential biodiversity variables for biodiversity assessment and monitoring: technological advancement and potentials. *Biodivers. Conserv.* 30, 1–14.
- Röder, M., Latifi, H., Hill, S., Wild, J., Svoboda, M., Bruna, J., Macek, M., Nováková, M. H., Gülch, E., Heurich, M., 2018. Application of optical unmanned aerial vehicle-based imagery for the inventory of natural regeneration and standing deadwood in post-disturbed spruce forests. *Int. J. Remote Sens.* 39, 5288–5309.
- Rydehl, J., Tuulidahl, M., Blöck, E., Axelsson, L., Köhler, P., 2020. Autonomous UAV-based forest mapping below the canopy. In: 2020 IEEE/ION Position, Location and Navigation Symposium (PLANS). IEEE, pp. 112–117.
- de Sá, N.C., Castro, P., Carvalho, S., Marchante, E., López-Núñez, F.A., Marchante, H., 2018. Mapping the flowering of an invasive plant using unmanned aerial vehicles: is there potential for biocontrol monitoring? *Front. Plant Sci.* 9, 293.
- Schneider-Zapp, K., Cubero-Castan, M., Shi, D., Strelcha, C., 2019. A new method to determine multi-angular reflectance factor from lightweight multispectral cameras with sky sensor in a target-less workflow applicable to UAS. *Remote Sens. Environ.* 229, 60–68.
- Seifert, E., Seifert, S., Vogt, H., Drew, D., Van Aardt, J., Kunneke, A., Seifert, T., 2019. Influence of drone altitude, image overlap, and optical sensor resolution on multi-view reconstruction of forest images. *Remote Sensing* 11 (10), 1252.
- Senf, C., Seidl, R., Hostert, P., 2017. Remote sensing of forest insect disturbances: Current state and future directions. *Int. J. Appl. Earth Obs. Geoinf.* 60, 49–60.
- Singh, A., Ganapathysubramanian, B., Singh, A.K., Sarkar, S., 2016. Machine learning for high-throughput stress phenotyping in plants. *Trends Plant Sci.* 21 (2), 110–124.
- Smigaj, M., Gaulton, R., Suarez, J.C., Barr, S.L., 2019. Canopy temperature from an Unmanned Aerial Vehicle as an indicator of tree stress associated with red band needle blight severity. *For. Ecol. Manage.* 433, 699–708.
- Stein, A., Gerstner, K., Krefl, H., 2014. Environmental heterogeneity as a universal driver of species richness across taxa, biomes and spatial scales. *Ecol. Lett.* 17 (7), 866–880.
- Swetnam, T.L., Gillan, J.K., Sankey, T.T., McClaran, M.P., Nichols, M.H., Heilman, P., McVay, J., 2018. Considerations for achieving cross-platform point cloud data fusion across different dryland ecosystem structural states. *Front. Plant Sci.* 8, 2144.
- Tamondong, A., Nakamura, T., Kobayashi, Y., Garcia, M., Nadooka, K., 2020. Investigating the effects of river discharges on submerged aquatic vegetation using UAV images and GIS techniques. *ISPRS Ann. Photogrammetry. Remote Sens. Spatial Inform. Sci.* 5, 93–99.
- Tmusić, G., Manfreda, S., Aasen, H., James, M.R., Gonçalves, G., Ben-Dor, E., Zhuang, R., 2020. Current practices in UAS-based environmental monitoring. *Remote Sensing* 12 (6), 1001.
- Wallace, L., Lucieer, A., Malenovsky, Z., Turner, D., Vopěnka, P., 2016. Assessment of forest structure using two UAV techniques: A comparison of airborne laser scanning and structure from motion (SfM) point clouds. *Forests* 7, 62.
- Westoby, M.J., Brasington, J., Glasser, N.F., Hambrey, M.J., Reynolds, J.M., 2012. ‘Structure-from-Motion’ photogrammetry: A low-cost, effective tool for geoscientific applications. *Geomorphology* 179, 300–314.
- White, J., Stepper, C., Tompalski, P., Coops, N., Walzer, M., 2015. Comparing ALS and image-based point cloud metrics and modelled forest inventory attributes in a complex coastal forest environment. *Forests* 6 (10), 3704–3732.
- Yao, H., Qin, R., Chen, X., 2019. Unmanned aerial vehicle for remote sensing applications—A review. *Remote Sensing* 11 (12), 1443.
- Yuan, C., Zhang, Y., Liu, Z., 2015. A survey on technologies for automatic forest fire monitoring, detection, and fighting using unmanned aerial vehicles and remote sensing techniques. *Can. J. For. Res.* 45 (7), 783–792.
- Yuba, N., Kawamura, K., Yasuda, T., Lim, J., Yoshitoshi, R., Watanabe, N., Kurokawa, Y., Maeda, T., 2021. Discriminating *Pennisetum alopecuroides* plants in a grazed pasture from unmanned aerial vehicles using object-based image analysis and random forest classifier. *Grassland Sci.* 67 (1), 73–82.
- Zhang, C., Filella, I., Liu, D., Ogawa, R., Llusà, J., Asensio, D., Peñuelas, J., 2017. Photochemical reflectance index (PRI) for detecting responses of diurnal and seasonal photosynthetic activity to experimental drought and warming in a mediterranean shrubland. *Remote Sens.* 9 (11), 1189.

## **PAPER II**



## European Journal of Remote Sensing


ISSN: (Print) (Online) Journal homepage: <https://www.tandfonline.com/loi/tejr20>


### Evaluation of common reed (*Phragmites australis*) bed changes in the context of management using earth observation and automatic threshold

Edvinas Tiškus, Diana Vaičiūtė, Martynas Bučas & Jonas Gintauskas

To cite this article: Edvinas Tiškus, Diana Vaičiūtė, Martynas Bučas & Jonas Gintauskas (2023) Evaluation of common reed (*Phragmites australis*) bed changes in the context of management using earth observation and automatic threshold, European Journal of Remote Sensing, 56:1, 100-114, DOI: [10.1080/22797254.2022.2161070](https://doi.org/10.1080/22797254.2022.2161070)

To link to this article: <https://doi.org/10.1080/22797254.2022.2161070>

 © 2023 The Author(s). Published by Informa UK Limited, trading as Taylor & Francis Group.

 Published online: 05 Jan 2023.

 Submit your article to this journal [↗](#)

 Article views: 44

 View related articles [↗](#)

 View Crossmark data [↗](#)

Full Terms & Conditions of access and use can be found at  
<https://www.tandfonline.com/action/journalInformation?journalCode=tejr20>

## Evaluation of common reed (*Phragmites australis*) bed changes in the context of management using earth observation and automatic threshold

Edvinas Tiškus , Diana Vaičiūtė, Martynas Bučas and Jonas Gintauskas

Marine Research Institute, Klaipėda University, Klaipėda, Lithuania

### ABSTRACT

There is no easy in situ way to monitor large waterbodies for their aquatic vegetation change, especially during mowing works. The objective of this study is to choose the best automatic workflow that would estimate a change in the reed bed area and density over time. This workflow will assess the mowing effect on reeds over 3 years in the Plateliai Lake (Lithuania). Sentinel-2/MSI images were used to derive reed beds using water adjusted vegetation index (WAVI) and normalised difference water index (NDWI). The indices were classified using seven different binary thresholding algorithms. Results were validated with orthophotos gathered from unmanned aerial vehicle surveys in mowed regions and one reference area. Analysis demonstrated that using the NDWI together with the Yen thresholding algorithm generated the best accuracy results, with the highest accuracy resulting with high vegetation areas where the area under the curve values were  $0.85 \pm 0.17$ . The changes in estimated density did not show a significant correlation between mowed and reference areas and years. The results indicate that Sentinel-2/MSI is a feasible tool for the evaluation of reed bed change. On this basis, it is recommended to implement it as an additional monitoring tool that covers larger areas than in situ monitoring.

### ARTICLE HISTORY

Received 19 August 2022  
Revised 11 November 2022  
Accepted 16 December 2022

### KEYWORDS

Mowing; reed beds;  
vegetation indices; water  
indices; Sentinel-2/MSI;  
unmanned aerial vehicle

### Introduction

One of the most common invasive species in inland waterbodies is considered a common reed (*Phragmites australis*), which is an easily grown plant that thrives in deep moisture-retentive soils (Duke, 1983). Due to its ability to acclimatise, a common reed has spread all over Europe, Northern America, Asia and Australia, as well as other parts of the world (Eller et al., 2017). Reed expansion is generally considered undesirable in nature reserves because areas dominated by common reeds generally have lower plant species richness than the initial marsh or fen vegetation. Commonly, the mowing of reeds is performed in wetlands for animal species requiring an open vegetation structure (Güsewell et al., 2000). Moreover, the mowing of reeds also removes nutrients from the water and keeps a waterbody attractive to tourists. Management programs have proven that common reeds can be controlled, and in most cases, natural vegetation will return; however, it is also important to note that some areas have been so heavily manipulated and degraded that it may be impossible to eliminate common reeds from them. There is no doubt that physical removal of reeds is useful in the short term but long-term effects of mowing are still unclear (e.g. how intensive mowing should be performed and what optimal height of mowing reeds), and recommendations to restore reed-invaded fen meadows by mowing in

the summer are based on circumstantial evidence and still need experimental testing (Güsewell et al., 1998).

Monitoring provides the data needed to decide if control measures are necessary to control invasive macrophyte populations. When a control program is begun, it is important to monitor targeted macrophyte populations so that the program's effectiveness can be determined and, if possible, leave untreated control areas that could be monitored as well for comparison. Relying only on in situ measurements can be time-consuming, hard to cover large areas and do frequent measurements, as well it is often difficult to get aquatic vegetation samples as accessibility to them is hard (Silva et al., 2008; Vis et al., 2003). It is imperative to continue monitoring even if a control program succeeds initially because common reeds may reinvade and the sooner new patches of infestation of an earlier stage are detected, the easier and cheaper they can be suppressed, also control techniques may need to be applied several times or, perhaps, regularly (Datta et al., 2021). Reed change due to mowing disturbances and herbicides has been thoroughly studied by Derr (2008) and it was found that reeds do not fully recover from the first year of mowing and reed regrowth rate the next year after mowing could be reduced by approximately 55% if no herbicide is applied; nevertheless, it was done in a small area of 4.5 m<sup>2</sup> as well in controlled containers. Monitoring effects of reed

**CONTACT** Edvinas Tiškus  [edvinas.tiskus@jmtc.ku.lt](mailto:edvinas.tiskus@jmtc.ku.lt)  Marine Research Institute, Klaipėda University, Klaipėda, Lithuania

© 2023 The Author(s). Published by Informa UK Limited, trading as Taylor & Francis Group.  
This is an Open Access article distributed under the terms of the Creative Commons Attribution License (<http://creativecommons.org/licenses/by/4.0/>), which permits unrestricted use, distribution, and reproduction in any medium, provided the original work is properly cited.



mowing could be improved by using more efficient methods such as remote sensing data (Bresciani et al., 2011).

Earth Observation-based (EO) products can potentially support public authorities in managing inland waters, e.g. for controlling invasive aquatic plants by giving spatial information useful to evaluate the invasion dynamics (Pinardi et al., 2018). Some studies were already performed for common reed detection using EO data. Detection of macrophytes in these studies was done by calculating vegetation indices that also allowed the assessment of the health of vegetation as well as complexity (Villa et al., 2013). Most of the studies use Landsat 7 ETM+ or Landsat 8 OLI data that has a long timeframe starting from 1984 with spectral (six spectral bands in the visible and near-infrared regions) and temporal (revisiting time of 16 days) resolution, which allow vegetation change monitoring. Even though Landsat 7/8 has a sufficient spatial resolution (up to 30 m), Sentinel-2 MSI surpassed it with up to 10 m resolution and is more useful for monitoring smaller changes in vegetation (Qin et al., 2021). The simplest normalised vegetation index (NDVI) algorithm was used for reed detection in several studies (Bresciani et al., 2009; and references therein). In Lake Garda (Italy), NDVI demonstrated 91% of accuracy in reed bed spatial coverage detection (Villa et al., 2013). Relying only on NDVI can generate misleading classification, as some features in water, e.g. cyanobacteria surface accumulations, have similar reflectance as macrophytes. In past decades, more sophisticated algorithms such as Water Adjusted Vegetation Index (WAVI) and Normalised Difference Aquatic Vegetation Index (NDAVI) were developed that are adjusted to the water environment (Villa et al., 2013, 2014, May), and together with higher Sentinel-2 resolution, these algorithms improve vegetation monitoring accuracy. Experiments that were done in Lake Garda and Mantua Lake system (Italy) showed that NDAVI and WAVI demonstrated high sensitivities, comparable and often slightly higher than the other indices (NDVI, leaf area index, soil adjusted vegetation index), in particular over aquatic vegetation (Villa et al., 2014, May). Despite the high detection accuracy of vegetation indices, it is a challenge to delineate transitional zones such as between water and floating-leaved or emerged macrophytes (helophytes) and between helophytes and land vegetation, therefore, using normalised difference water index (NDWI) can improve delineation between canopy and water as shown by some studies (Gao, 1996; McFeeters, 2013; Szabó et al., 2016).

Interest in the mapping of wetland environments and the classification of their resources using EO is a growing topic as spectral signatures may vary substantially in different wetlands, and they are hard to access for detailed in situ analysis (Amani et al., 2018; Bhatnagar et al., 2020). The studies on calculating Above Ground Biomass (AGB) in wetlands from EO

images acquired efficient results such as an accuracy of  $R^2 = 0.59$  and  $RMSE = 194 \text{ g m}^{-2}$  with UAV-derived reed heights and ratio vegetation index in the Nan Da Gang Wetland Reserve (Lu et al., 2022). A higher AGB accuracy ( $R^2 = 0.65$  and  $RMSE = 168 \text{ g m}^{-2}$ ) was achieved by combining the LiDAR and hyperspectral images in the Zhangye National Wetland Park (Luo et al., 2017). Although this parameter is useful for wetland management (including the effectiveness of reed mowing), extensive in situ measurements together with laboratory analysis should be done first to calibrate the reed height estimates derived from UAV or LiDAR, as non-local models should be used with caution (Bojórquez et al., 2020).

Efficient and automatic segmentation of vegetation indices is an important step for evaluating the mowing effect. For single-band images, thresholding is the most common pre-processing step and the simplest form of thresholding is binary, where foreground and background are separated. The goal of using an automatic threshold is to reduce the need for in situ measurements that can be costly and time-consuming. The most commonly used thresholding algorithm for remote sensing images is Otsu (Otsu, 1979), which was used for vegetation detection (Srinivas et al., 2019), coastal aquaculture area (Lu Yewei and Lu Yewei, 2015), shoreline mapping (Sunder et al., 2017), etc. Despite the apparent easiness of the thresholding process, it is a complex procedure given the vast array of circumstances and environments that are unique to each image (Carabias, 2012).

The objective of this study was to determine the best approach for the evaluation of reed bed area changes due to mowing using remote sensing methods and automatic thresholding algorithms. This was done by testing water and aquatic vegetation indices by masking open water. We also assessed, if and how the determined approach accuracy of detecting reed beds depends on their density. Based on this method, we hypothesised that the mowing effect from EO data should be more apparent in larger than 0.1 ha reed bed areas since such area almost corresponds to the area of Sentinel-2/MSI 10 m<sup>2</sup> pixel size with a buffer of one pixel in all directions.

## Materials and methods

### Study area

Plateliai Lake (area 1.200 ha, average depth 10.5 m, maximum depth of 49.1 m) is an oligo-mesotrophic lake ( $2.4 \pm 1.8 \mu\text{g chlorophyll-a l}^{-1}$  in the period 2001–2010) that belongs to the Žemaitija National Park, located in the western part of Lithuania (Figure 1(a)). Vegetated areas by common reeds are not spread evenly throughout the lake, and more reed beds are in the eastern part (Sinkevičienė et al., 2005). From 2017 to 2019, the Žemaitija National Park directory implemented mowing of reed beds in the littoral zone of the lake in 7 areas

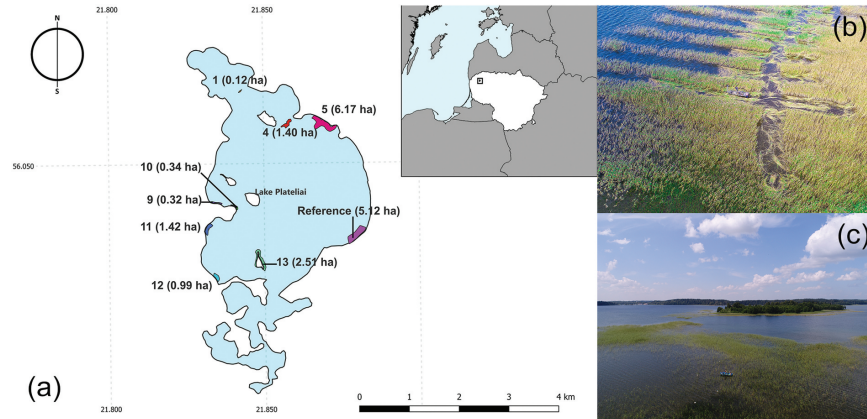


**Figure 1.** (a) Plateliai Lake with areas of interest (AOIs) indicated by numbers (where mowing of reed beds was performed), “reference” (where mowing of reed beds was not performed) and their size (in ha), (b) UAV image (acquired on the 10<sup>th</sup> July 2018) of AOI 5, where reed beds were mowed every second line and mowing process, (c) example of reed bed (AOI 4) before mowing.

(Figure 1(a)). In total, eight AOIs (area of interest) were selected for further analysis. Seven AOIs correspond to the areas where the mowing of reed beds was performed, and one AOI was selected as a reference, where the mowing was not performed (Figure 1(a)). The first seven AOIs were numbered after the technical specification document of reed mowing (Technical specification of Plateliai Lake reed mowing, 2017). All areas combined cover 18 ha, 1.5% of the whole lake area. A common reed dominated in selected AOIs, while lakeshore bulrush (*Schoenoplectus lacustris*) formed small stands only in a few AOIs. Therefore, all macrophyte species within the reeds were considered as part of the reed bed in this study.

The exact date of each year’s mowing is not known, but it was always performed between 20 July and 10 September. The mechanical cutting method was applied from a boat in deeper areas (Figure 1(b)) and using a scythe in shallower areas. In depths  $\geq 0.5$  m, reeds were cut by leaving 30 cm stems from the bottom, and in shallow areas ( $< 0.5$  m depth), they were cut to the bottom. In most of the areas, reeds were entirely mowed, except for one AOI that is relatively the largest (AOI 5), where the mowing was performed in stripes of 5 m width by leaving a part of the reed beds to enhance biodiversity conditions and habitats for local bird and fish species (Figure 1(b)).

The study covered the period from 2016 to 2020. The mowing of reeds was performed in 2017, 2018 and 2019, while 2016 and 2020 are considered the reference years since mowing was not performed.

#### UAV data for validation

UAV images were acquired in several AOIs (Table 2, AOI: 1, 4, 5, 10, 11, reference) to compose orthophotos and validate the mapped reed beds that were derived from satellite data (see Sect 2.4). The images were acquired using a DJI Phantom 4 multi-rotor UAV that has a 1” CMOS 20-megapixel RGB camera with an 84° field of view. Flight missions were planned before flight using the DroneDeploy app with the following parameters: flight height of 40 m; 75% front and side overlap between images; flight angle facing towards or away from the sun to minimize a sun glint effect (Joyce et al., 2019); coverage polygon larger than mapped AOI. With these parameters, UAV aerial images had a ground spatial resolution of 2 cm per pixel.

Four ground control points (GCPs), made from plastic, were used to georeference orthophotos and get more accurate results. GCPs were measured with a Leica 1200 smart GPS rover that uses the Global navigation satellite system. Image mosaicking was performed using the OpenDroneMap (*OpenDroneMap*, 2020) software that implements structure from motion to build orthophotos, digital elevation models and 3D models of the area. Homogenous water surface lacks tie-points (distinct pixels matching in two pictures taken next to each other), therefore only areas with emerged macrophytes were mosaicked.

After composing orthophotos, 12 of them out of 16 were selected (with clouds and water waves not influencing the final result) for validation with classified rasters derived from satellite images. Reed beds were manually delineated from the orthophotos using QGIS

version 3.16 (QGIS.org, 2022, 2022). The density of reeds was evaluated visually by dividing orthophotos into 10 m<sup>2</sup> polygons equal to Sentinel-2 pixel size. Polygons without vegetation were classified as water (0% vegetation, n = 540), while polygons with reeds were classified into three density classes: low density (25% vegetation, n = 687), medium density (50%, n = 461) and high density (100%, n = 360).

### Satellite data

The Multispectral Instrument (MSI) on board Sentinel-2A and Sentinel-2B data were used. Sentinel-2/MSI has a spatial resolution of 10 m (4 bands), 20 m (6 bands) and 60 m (2 bands) and a spectral resolution ranging from 440 nm to 2202 nm in 12 bands. Over Plateliai Lake Sentinel-2/MSI revisit time is every 3 days.

Most Sentinel-2/MSI products were already processed to Level-2A data and are available for download in the Copernicus Open Access Hub (<https://scihub.copernicus.eu/>). The atmospherically corrected (Level-2A) images before September 2017 were not available for download, therefore Sen2Cor processor was used for the atmospheric correction of Top-Of-Atmosphere (TOA) Level-1C images. All Sentinel-2/MSI images were resampled to a final spatial resolution of 10 m. In total, 16 Sentinel-2/MSI images were used (Table 1), considering the date closest to the beginning and end of the mowing period (i.e. between the 20 of July and the 10 of September). Most of the images were cloud-free, except for AOI 5, where the

image closest to the mowing of reeds (6 September 2020) contained cloud shadows; therefore, the image acquired on the 1 September 2020 was used instead, in AOI 5. In addition, the 19 June 2016 image had a cloud shadow on half of AOI 13, but since there were no cloudless images during this time, the image was used excluding AOI 13 from the analysis.

### Calculation of the area and density covered by reeds using sentinel-2/MSI data

The effect of reed mowing in Plateliai Lake was tested using two parameters: changes in the area covered by a common reed and changes in its density within AOIs. The evaluation was performed in five major steps indicated in the workflow (Figure 2).

Step 1: Masking the land. The Sentinel-2 image from mid-spring was used for masking the land (Table 1). The image acquired in mid-spring represents the period when aquatic vegetation had not yet started growing. The normalized difference vegetation index (NDVI) was utilized (Rouse & Haas, 1973) since it is most commonly used for land vegetation mapping and is also suitable for aquatic plants (Powell et al., 2014; Sakuno & Kunii, 2013). This algorithm uses a red spectral band, where radiation is mostly absorbed by vegetation, and Near Infrared (NIR) band, which appears relatively bright on vegetation. In the case of Sentinel-2/MSI, NDVI (Eq. 1) was calculated using Band 8 (NIR) and Band 4 (Red). The NDVI raster was classified with an Otsu binary

**Table 1.** Dates of sentinel 2 image acquisition with corresponding dates of validation from the UAV images and AOI and mowing status of reed beds (see Sect 2.2).

Sentinel-2 MSI	UAV dates and AOI	Mowing status
10 May 2016	-	Land masking
19 Jun 2016	-	Before mowing
28 Aug 2016	-	Before mowing
05 May 2017	-	Land masking
14 Jul 2017	-	Before mowing
31 Aug 2017	-	After mowing
10 May 2018	-	Land masking
17 Jul 2018	2018 Jul 10 (AOI:5, reference); 18(AOI:4,5); 19(AOI:1, 10, 11)	Before mowing
20 Sep 2018	-	After mowing
23 Apr 2019	-	Land masking
12 Jul 2019	-	Before mowing
26 Aug 2019	2019 Aug 12(AOI: 10, 11, reference); 20(AOI:5, 9)	After mowing
20 Apr 2020	-	Land masking
18 Jul 2020	-	No mowing
01 Sep 2020	-	No mowing
06 Sep 2020	-	No mowing

**Table 2.** Performance of reed bed classification using seven thresholding algorithms for WAVI (top) and NDWI (bottom).

Parameter	Otsu	RenyiEntropy	Yen	Triangle	Iso	Li	Mean
AUC all	0.67 ± 0.12	0.72 ± 0.14	0.70 ± 0.13	0.64 ± 0.19	0.59 ± 0.12	0.59 ± 0.13	0.65 ± 0.19
Sensitivity all	0.34 ± 0.23	0.45 ± 0.28	0.40 ± 0.25	0.95 ± 0.07	0.74 ± 0.35	0.77 ± 0.31	0.95 ± 0.07
Specificity all	1.00 ± 0.00	0.99 ± 0.02	0.99 ± 0.02	0.33 ± 0.43	0.45 ± 0.50	0.41 ± 0.51	0.34 ± 0.43
AUC all	0.71 ± 0.14	0.70 ± 0.14	0.76 ± 0.12	0.75 ± 0.17	0.74 ± 0.17	0.73 ± 0.17	0.64 ± 0.16
Sensitivity all	0.42 ± 0.27	0.54 ± 0.29	0.53 ± 0.23	0.86 ± 0.19	0.83 ± 0.14	0.84 ± 0.13	0.70 ± 0.26
Specificity all	0.99 ± 0.02	0.97 ± 0.06	0.98 ± 0.06	0.43 ± 0.47	0.63 ± 0.42	0.65 ± 0.42	0.69 ± 0.44

Performance was measured by mean (±standard deviation) area under the curve (AUC), sensitivity and specificity.

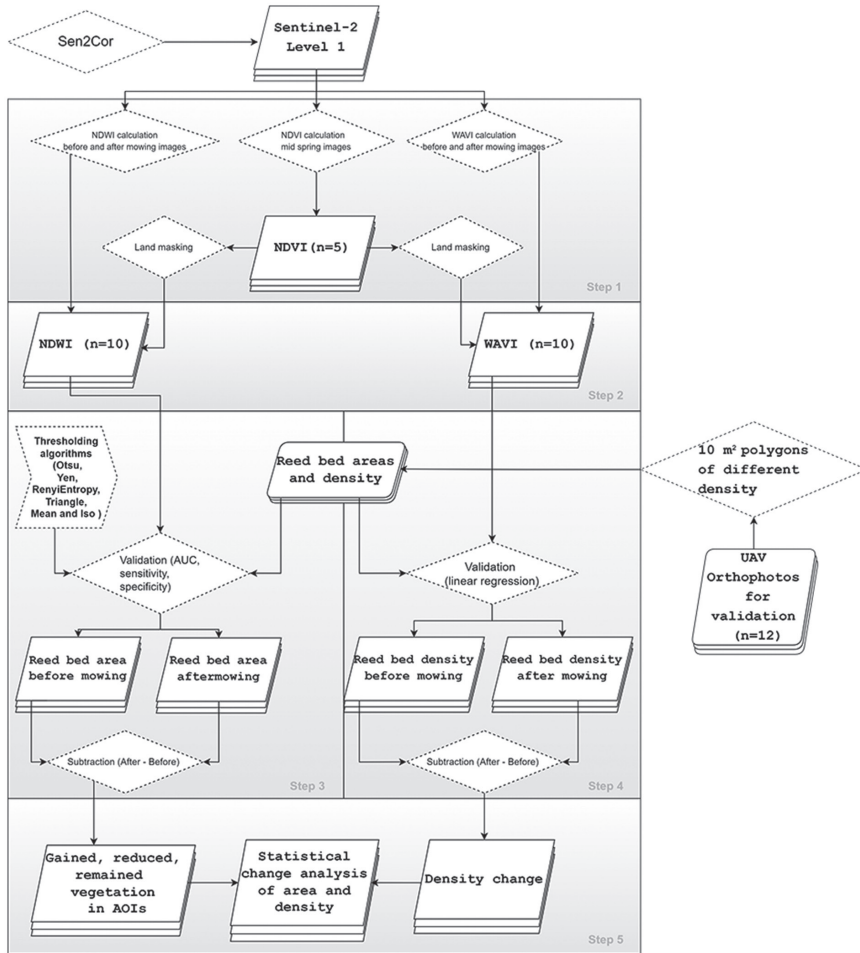


Figure 2. Workflow of remote-sensing data processing, validation and analysis. Step 1- masking land; step 2 - masking water; step 3 - validation of reed bed areas and density with UAV data; step 4 - extracting data in considered AOIs; step 5 - assessment of the changes in the area covered by common reed and their density.

algorithm (Otsu, 1979) and the class representing the land was masked for further analysis.

$$NDVI = \frac{R_{rs}NIR - R_{rs}Red}{R_{rs}NIR + R_{rs}Red} \quad (1)$$

where  $R_{rs}Red$  is remote sensing reflectance in a red satellite band and  $R_{rs}NIR$  is remote sensing reflectance in the NIR satellite band.

Step 2: masking water. The most complicated task is to find the optimal threshold (Carabias, 2012) that accurately masks water and leaves only aquatic vegetation. For this, two indices were tested, which demonstrated the highest potential in particular

over aquatic vegetation (Villa et al., 2014, May): Normalised Difference Water Index (NDWI) and Water Adjusted Vegetation Index (WAVI). NDWI (Eq. 2) utilizes remote sensing reflectance in the green and NIR spectral regions that were corresponded by Band 3 and Band 8 in the case of Sentinel-2/MSI data (McFeeters, 2013), and WAVI (Eq. 3) utilizes remote sensing reflectance in the blue and NIR spectral regions that are corresponded by Band 2 and Band 8 in case of Sentinel-2/MSI data:

$$NDWI = \frac{R_{rs}Green - R_{rs}NIR}{R_{rs}Green + R_{rs}NIR} \quad (2)$$

$$WAVI = \frac{R_{rs}NIR - R_{rs}Blue}{R_{rs}NIR + R_{rs}Blue + L} \quad (3)$$

where  $R_{rs}Green$  is remote sensing reflectance in a green satellite band,  $R_{rs}Blue$  is remote sensing reflectance in a blue satellite band, and  $R_{rs}NIR$  is remote sensing reflectance in the NIR satellite band.  $L$  is the WAVI background correction factor.

For the WAVI background correction factor  $L$ , a single value of 0.5 was used, which is the best option in the case where no a priori data about vegetation density is available, as suggested by Huete (1988), and confirmed by other studies (Qi et al., 1994; Rondeaux et al., 1996).

NDWI and WAVI indices were selected considering the band spatial resolution in Sentinel-2/MSI images, as both of them use bands (blue, green and NIR) that have 10 m spatial resolution. NDAVI was not used as it uses the same bands as WAVI, which is better adjusted for the water environment (Guanhua Zhou et al., 2018).

Both indices (WAVI and NDWI) were automatically classified into water and reeds using seven binary thresholding algorithms, selected out of 16 available in Fiji software (Schindelin et al., 2012), after visually inspecting two images (17 July 2018 and 26 August 2019 used for validation with UAV orthophotos) with calculated indices, using function `try all`. Seven thresholding algorithms were left for further analysis: Otsu (1979), Yen et al. (1995), RenyiEntropy (Kapur et al., 1985), Triangle (Zack et al., 1977), Mean and Iso (T. W. Ridler and S. Calvard, 1978). The simplest example of these algorithms would be the mean thresholding (Eq. 4) where the threshold is calculated by the mean of two peak values of an image histogram.

$$t = \frac{g_{peak1} + g_{peak2}}{2} \quad (4)$$

where  $t$  is the threshold value,  $g_{peak1}$  is the first maximum value in a histogram, and  $g_{peak2}$  is the second maximum value in a histogram. Sezgin and Sankur (2004) described 40 thresholding techniques under unified notation and grouped these thresholding algorithms according to information they are exploiting from an image histogram: shape, measurement space clustering, entropy, object attributes, spatial correlation and local grey-level surface. According to this classification, Otsu, Mean and Iso are defined as clustering thresholding algorithms, Yen and RenyiEntropy as entropy thresholding algorithms and Triangle as a geometric thresholding algorithm.

Step 3: validation of reed bed areas with UAV data. Two satellite images were used for validation: 17 July 2018 and 26 August 2019. The most suitable index with a threshold was selected after validation with 12 UAV orthophotos. Polygons of 10 m<sup>2</sup> from

orthophotos were classified as vegetation or water and compared to overlapping pixels of reed beds derived from satellite data (step 2). The accuracy of satellite-derived reed beds was assessed by the means of a confusion matrix (Ting, 2017), where the true positive and negative values indicated the number of matches between, respectively, presence and absence of reed beds derived from the UAV and satellite data (i.e. observed and predicted reed beds). From the confusion matrix, the Area Under the Curve (AUC; Egan, 1975) together with sensitivity and specificity was calculated to determine the most accurate approach for reed bed area mapping using satellite imagery. Sensitivity shows how accurately the true (vegetation) class was predicted, and specificity shows how well the false class (water) was predicted, whereas the AUC estimate covers both aspects. The thresholding algorithm was considered suitable, if the value for sensitivity and specificity was equal to or higher than the arbitrary value of 0.5, meaning correct classification was achieved for 50% of the data. After rejecting unsuitable thresholding algorithms, the post-hoc Bonferroni test was used on AUC values to test which method, using indices (WAVI or NDWI) together with the thresholding algorithm, performed the best at masking water and leaving aquatic vegetation.

To find whether at a certain density thresholding algorithm becomes unreliable, the confusion matrix of the best performing Sentinel-2/MSI index with thresholding algorithm was tested again (using the same accuracy metrics) considering each vegetation density (low, medium, high) derived from the UAV orthophotos. To reduce the likelihood of type one error, the multiple comparisons Dunnett's post hoc test was used to compare the mean AUC of the treatment group (each vegetation density) to a control group (AUC value of 0.5), representing poor discrimination between classes (Mandrekar, 2010).

Step 4: validation of reed bed density with UAV data. The estimated density values of reed beds in AOIs were retrieved from Sentinel-2/MSI data using WAVI (Villa et al., 2014, May). The performance of WAVI was validated with the density visually determined from UAV orthophoto and classified polygons (see Sect 2.2). From WAVI values, averaged over each class of vegetation in percentages and including water class, linear regression was derived and linear regression function was used to convert WAVI values to estimated density values.

Step 5: assessment of the impact of reed mowing. The effect of reed bed mowing was evaluated in each AOI, comparing satellite-derived and classified (with the most accurate index and threshold algorithm) areas covered by reeds before and after mowing during the corresponding year (2016–2020). The differences in areas were classified according to three aspects: lost area (reed bed areas decreased), remaining area (reed bed areas have not changed) and gained area (reed bed

areas increased). The analysis was performed using a zonal statistic in QGIS version 3.16 (QGIS.org, 2022, 2022). Results are presented in hectares as well as in percentages relative to each AOI size, considering it to be 100% (Figure 1). To find whether mowing occurred in an AOI, an arbitrary threshold of 0.1 ha vegetated area (equal to one Sentinel-2/MSI pixel (10 m<sup>2</sup>) together with a buffer of surrounding pixels combined) was considered significant.

## Results

### Validation of water and vegetation indices for reed bed area determination

Results from confusion matrices comparing vegetation areas (reed beds) calculated from WAVI and NDWI indices in each AOI to vegetation areas derived from UAV orthophoto (see Table 1. UAV data) showed that five thresholding algorithms (Triangle, Iso, Li, Mean for WAVI and Triangle for NDWI) incorrectly identified water as a vegetated area in more than 50% (specificity lower than 0.5) of the cases (Table 2). The rest of the thresholding algorithms showed a larger than 0.5 specificity rate (correct distinction of water for more than 50% of data), while the sensitivity (correct distinction of macrophytes for more than 50% of data) of the four thresholding algorithms (Otsu, RenyiEntropy, Yen for WAVI and Otsu for NDWI) were lower than 0.5. Therefore, previously mentioned thresholding algorithms were removed from further analysis, and only five thresholding algorithms for the NDWI index (RenyiEntropy, Yen, Iso, Li and Mean) were compared.

The Yen thresholding algorithm for the NDWI index had the highest mean AUC (Table 2); however, using the Dunnett post hoc test it was not statistically

different ( $p > 0.05$ ) compared to the other thresholding algorithms. The mean specificity obtained by the Iso, Li and Mean was 30% lower than the one determined by the RenyiEntropy and Yen, which resulted in many false-positive values in one of the validation images (Figure 3). Consequently, the RenyiEntropy and Yen thresholding algorithms were selected and compared with each other. The mean AUC and specificity of RenyiEntropy were slightly lower than the Yen thresholding algorithm, therefore the Yen thresholding algorithm was selected as the final method for classification between vegetated area and water.

The Dunnett post hoc test showed greater values for high ( $df(43) = 5.78$ ,  $p < 0.05$ ) and medium ( $df(43) = 4.30$ ,  $p < 0.05$ ) vegetation density AUC, compared to the AUC value of 0.5 that indicates no discrimination between classes (Mandrekar, 2010). No significant difference ( $df(43) = 2.12$ ,  $p = 0.1$ ) was found when comparing the same AUC value of 0.5 to the AUC of low-density vegetation. The mean specificity for all densities was similar and was higher than 0.97 (see Figure 4). For high and medium vegetation density, the mean sensitivity values were higher than 0.5 and therefore reliable; whereas, for low vegetation density, the sensitivity was  $< 0.5$ .

### The changes in vegetated area induced by reed mowing

The changes in estimated reed bed area in all AOIs during the whole period of study were diverse; nevertheless, significant changes in the vegetated area derived from the satellite images acquired before and after mowing were evident (Figure 5(a)). The reed bed area in the reference AOI did not significantly change

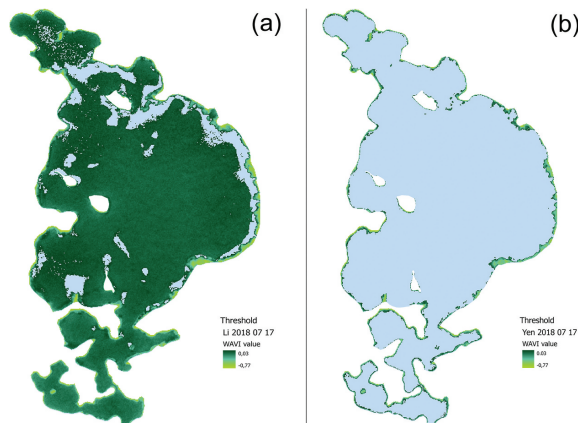


Figure 3. NDWI index (derived from Sentinel-2 image acquired on 17 July 2018) with Li threshold showing overestimation of reed beds in the open lake part (a), and with Yen thresholding showing the distribution of reed beds with no overestimation (b).

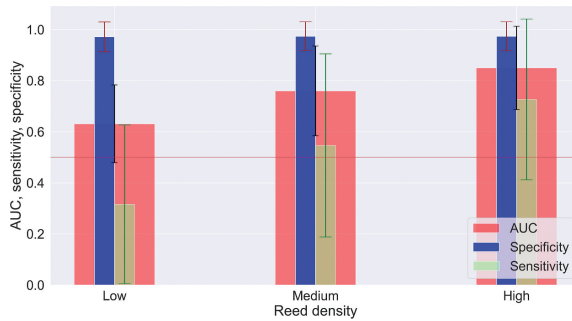


Figure 4. Mean area under the curve (AUC), sensitivity and specificity using Yen thresholding for NDWI, considering different densities of vegetation derived from the UAV data.

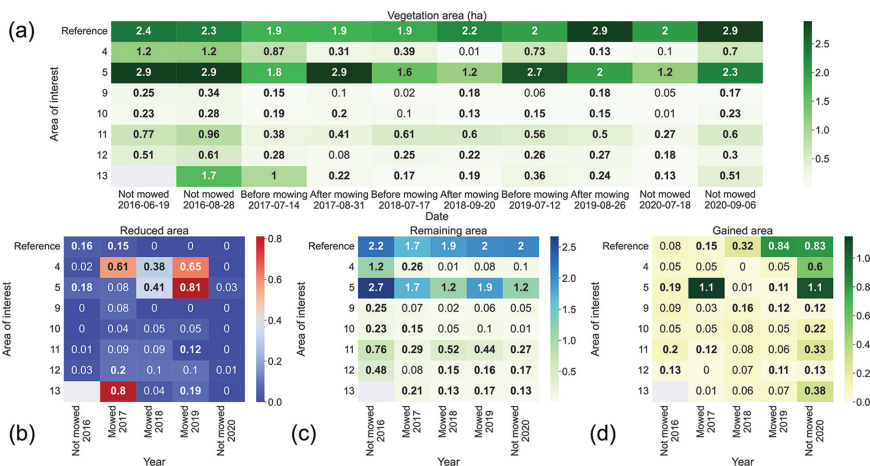


Figure 5. Estimated reed bed areas (ha) in 8 AOIs derived from sentinel-2/MSI images after removal of water pixels determined by the Yen thresholding algorithm for NDWI (a). The estimated reed bed areas (ha) that were reduced (b), remained (c) and gained (d) during the study years. Scale is different for each parameter to highlight specific cases of change. Significant (> 0.1 ha) vegetation area or change is highlighted in bold.

in 2016 and 2017; however, the vegetated area significantly increased (>0.32 ha) in later years, i.e. 2018, 2019 and 2020.

Similar patterns as in the reference AOI were observed in AOI 9 where the reed bed area increased significantly in the same years. The most evident decrease in the vegetation area was observed in AOI 4 during the years, when the mowing was performed, while the increase in the vegetated area was observed in the reference years (2016 and 2020). The vegetated area decreased in AOI 5 by a significant amount in 2018 (0.40 ha) and 2019 (0.70 ha); however, it increased significantly (1.07 ha) in the first year of mowing 2017. The largest one-time loss throughout the study was in AOI 13, where the vegetated area was reduced by half of its area (0.79 ha) in the first year of

mowing and remained relatively small through the rest of the years. In 2020, when the mowing was not performed, the vegetated area recovered in all AOIs.

The reduction of reed bed areas in the reference AOI was observed in two investigated years, in 2016 it decreased by 3.1% of the total area of AOI, and in 2017 by 2.9% (Figure 5(b)). In 2017, the loss of reed bed area is relatively low in comparison with the reduced vegetation area in other AOIs (on average  $19.9 \pm 14.8\%$ ). The remaining vegetation area was relatively stable over the studied period in the reference AOI with an average of  $38.7 \pm 3.9\%$  of the total area of AOI (Figure 5(c)). A gradual increase of the gained vegetation area in the reference AOI was determined starting from the first study year, when it was 0.08 ha (1.6% of the total area), to 2019, when gained vegetated area

comprised 0.84 ha, i.e. 16.3% of the total area, and 2020 with 0.83 ha of gained vegetated area, i.e. 16.1% of the total area (Figure 5(d)).

In AOI 4, the most evident reduction of the vegetated area was observed in 2017, 2018 and 2019, i.e. the investigated years, when the mowing of reed beds was performed (Figure 5(b)). The reduced area accounted for 0.61 ha (43.5% of the total AOI area), in 2018 it was 0.38 (27.1% of the total AOI area), while in 2019 the reduced vegetated area was 46.4% of the total AOI area. The remaining vegetation in AOI 4 was the largest in 2016 at 1.2 ha (85.6% of the total AOI area) as well as significant areas remained in 2017 at 0.26 ha (18.5% of the total AOI area).

In AOI 5, the reduced vegetation area followed a similar pattern as in the reference AOI in the first reference year of 2016 reducing by 0.18 ha and in the first mowing year of 2017 reducing by 0.08 ha (2.9% and 1.3%, respectively). In the following two mowing years of 2018 and 2019, reduced vegetation areas were highest in AOI 5 of 0.41 ha (6.6%) and 0.81 ha (13.1%), respectively. As this AOI is one of the largest, the remaining vegetation was significant in all years, with the lowest being in 2018 and 2020 at 1.2 ha (19.2% of the total AOI area) and the largest in 2016 at 2.7 ha (31.0%). Gained vegetation area was significant during most of the study years except for 2018 when gained vegetation area was only 0.01 ha (0.2%).

In AOI 9, reduced vegetation area was low with the only change being in 2017 of 0.08 ha (24.7% of the total AOI area). The remaining vegetation area was only significant in 2016 with 0.25 ha (77.1%). Gained vegetation area for most mowed AOIs was not different from reference AOI ( $p > 0.5$ ) except for AOI 9 with  $32.1 \pm 14.9\%$ , which was significantly different ( $df(5) = 3.9$ ,  $p < 0.01$ ) from reference AOI that averaged  $8.6 \pm 7.1\%$ . In AOI 9 gained vegetation was significant with 0.16 ha (49.3% of the total AOI area) in 2016 and 0.12 ha (37.0%) in 2019 and 2020.

AOI 10 reduced vegetation area only in mowing years; however, this reduced area was not significant, with 0.04 ha (11.7%) in 2017 and 0.05 ha (14.6%) in 2018 and 2019. The remaining vegetation area was significant in 2016 and 2017 with 0.23 ha (67.3%) and 0.15 ha (43.9%), respectively. Gained vegetation area was only significant in 2020 with 0.22 ha (64.4% of the total AOI area).

A significant reduction of vegetation area in AOI 11 was observed in 2019 of 0.12 ha (8.4% of the total AOI area). The remaining vegetation area was significant in all years ranging from 0.27 ha (18.9%) in 2017 to 0.76 ha (53.2%) in 2016, but comparing the mean remaining vegetation area in AOI 11 ( $31.9 \pm 13.2\%$ ) to reference AOI that also had significant remaining vegetation in all years, it did not significantly ( $df(5)$

$= -2.78$ ,  $p = 0.025$ ) differ from the mean ( $38.7 \pm 3.9\%$ ) in the reference AOI.

AOI 12 reduced in vegetation area significantly in 2017 with 0.2 ha (20.1% of the total AOI area). This AOI had a significant remaining area in most of the years except for 2017 when it was 0.08 ha (8.0%). AOI 12 gained significant vegetation area in reference years with 0.13 ha (13.0%) in 2016 and the same amount in 2020 in 2019 with 0.11 ha (11.0%).

AOI 13 had one of the biggest reduced vegetation areas during a single year of 0.8 ha (31.7%) in 2017, and also in 2019 this AOI reduced a significant vegetation area by 0.19 ha (7.5%). The remaining area variation in AOI 13 was small  $6.3 \pm 3.1\%$  compared to its area, but the data is missing in 2016 when the highest remaining vegetation was in all other mowed AOIs. Gained vegetation area was observed in 2020 of 0.38 ha (15.0%).

In the reference years, average reduced vegetation area was significantly ( $df(35) = -6.3$ ,  $p < 0.01$ ) lower ( $0.8 \pm 1.1\%$ ) than in years when mowing was performed ( $14.7 \pm 13.0\%$ ). In the same years, the remaining vegetation was higher ( $35.5 \pm 28.6\%$ ) than in mowing years ( $18.3 \pm 11.6\%$ ) with a significant difference ( $df(35) = 3.46$ ,  $p < 0.01$ ). The average gained vegetation area of all AOIs were highly influenced by vegetation gained in 2020 (the year after mowing was completed) where the average of all AOIs was significantly ( $df(21) = -5.2$ ,  $p < 0.01$ ) higher  $30.4 \pm 18.8\%$  ( $0.69 \pm 0.74$  ha) compared to 2017 of  $7.2 \pm 6.8\%$ , 2018 of  $11.8 \pm 16.9\%$  and 2019  $10.7 \pm 12.5\%$ .

### Temporal changes in reed density

The averaged WAVI values were highly correlated with the emergent vegetation density ( $r = 0.99$ ,  $p < 0.05$ ) derived from the UAV data. As WAVI could be considered as a proxy for reed density, the derived linear regression function (Figure 6) was used to convert WAVI values to relative coverage of reeds. According to the linear regression function, the values below 0.04 were considered as water (0% vegetation) and any value over 0.22 was considered as fully covered by reeds (100% vegetation).

Comparing individual AOI vegetation density values to the reference AOI, AOI 13 corresponded almost to a similar density in 2017 and was lower in 2018 (Figure 7). None of the mowed AOIs had an average estimated vegetation densities as high as the reference AOI  $84.6 \pm 30.1\%$  ( $p < .05$ ) except for AOI 5 where the difference was not significantly different ( $p > .05$ ) and the estimated vegetation density average was  $72.7 \pm 24.6\%$ . The second-largest reed density was in AOI 11 with  $54.8 \pm 19.4\%$ . The lowest estimated vegetation density was in AOI 9 of  $23.0 \pm 18.7\%$ , this AOI is also the smallest in size.



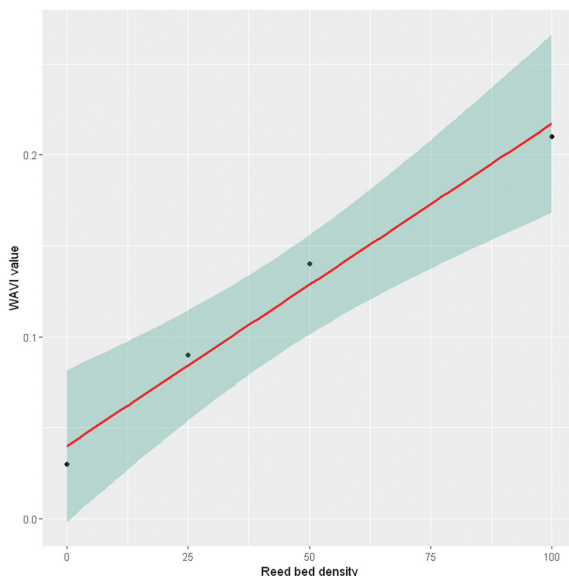


Figure 6. The relationship between the reed bed density (0%, 25%, 50%, 100%) estimated from the UAV images and averaged WAVI values. The regression line is provided with 95% confidence intervals.

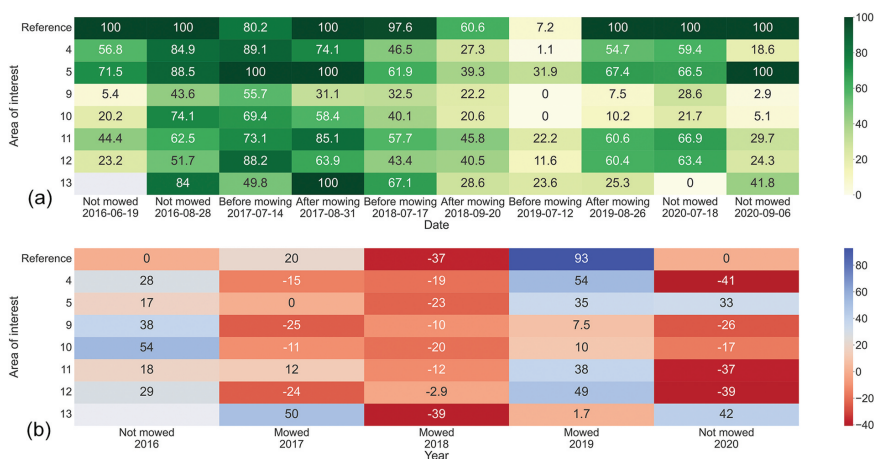


Figure 7. The reed density values in percentages of 8 AOIs (a) estimated from WAVI values retrieved from sentinel-2/MSI images that represent the period before and after mowing of the investigated years. Density differences in each year before and after reed growth season (b).

Nonetheless, comparing before and after mowing estimated vegetation densities, a significant difference in average change (Figure 7(b)) was found in years 2016 with vegetation density being higher by  $36.2 \pm 19.2\%$ , lower in 2018 by  $-17.9 \pm 11.3\%$  and higher again in 2019 by  $28.0 \pm 21.1\%$ ; however, significant (df

(7) = 0.43,  $p > 0.05$ ) change was not found in the first mowing year with an average of  $-1.8 \pm 26.4\%$  lower in the vegetation density, and the reference year 2020 lower on average by  $-12.0 \pm 35.1\%$  (df(7) = 0.2,  $p > 0.05$ ).

Even though the lower vegetation densities were in 2018 when the smallest vegetation areas were

determined (Figure 5(a)), no relationship ( $r = .05$ ,  $p > .05$ ) was observed between the change in the vegetated area (Figure 5) and estimated vegetation densities (Figure 7(a)), and as well no relationship ( $r = .05$ ,  $p > .05$ ) was found comparing only AOIs where the significant loss or gain in the vegetation area occurred (Figure 5 bolded values).

## Discussion

### *The remote sensing of the vegetated area by reeds: methodological considerations*

The workflow in this study is based on the concept that remote sensing can evaluate areas of reeds in the whole lake, as it is fairly simple to delineate between water and dense vegetation as well as mask the land from the water environment. Methods of masking all pixels automatically that were not related to aquatic vegetation, were chosen as this approach does not require any prior measurements, whereas most other similar studies (Bresciani et al., 2009; Powell et al., 2014; Villa et al., 2013) relied on in situ data for thresholding.

In general, remote sensing for vegetation area evaluation showed a good correlation between UAV-derived vegetation and dense vegetation detected from a satellite. Nonetheless, one satellite image (17 of July 2019) that was used for validation with UAV images had a low intra-class variance due to a cloud haze (Figure 3(b)) that was not corrected by Sen2Cor atmospheric correction (Gao & Li, 2012; Richter et al., 2011). This could have an influence on the final results of this image classification by some algorithms (Triangle, Iso, Mean, and Li) and also on density values that do not match area results (area decreased but density increased). For this reason, it is important to thoroughly inspect images before using them for classification or testing other atmospheric correction algorithms that are available for Sentinel-2, e.g. iCOR (De Keukelaere et al., 2018), ATCOR (Schläpfer & Richter, 2014), ACOLITE (Martins et al., 2017). In this image, the water area appeared more similar to vegetated areas, and the unvegetated shallow bottom was classified as the background, which shows that binary thresholding should be chosen carefully and might not be the best option for classifying areas in some cases; therefore, more sophisticated algorithms such as clustering or artificial neural network-based segmentation could be tested that might improve results (Singh et al., 2020; Zheng & Chen, 2021).

Overall, results from the study demonstrated that the mowing effect can be detected from the EO data, especially in mowed AOIs larger than 0.1 ha, where the reduced area was significantly different from the reference AOI, and also the reduced vegetation area was significantly higher in the mowing years.

Vegetated areas derived from the satellite images were slightly underestimated compared to the areas delineated by UAV orthophotos. These small differences might be due to high spatial resolution differences between orthophotos 2 cm/pixel and Sentinel-2/MSI 10 m/pixel (Bollas et al., 2021). Another reason for the underestimation was that low-density vegetation was included in a total estimation of vegetation area, which did not reach a reliable AUC threshold as low-density vegetation had lower index values, making overall discrimination between water and aquatic vegetation poorer. For better water vegetation detection, it is suggested to implement a short-wave infrared (SWIR) band that has significantly different reflections comparing aquatic vegetation and cyanobacteria (Oyama et al., 2015). Modified normalized difference water index (MNDWI) implements SWIR band to water index calculations and is claimed to reach better results than NDWI (Xu, 2005) as well as Sentinel-2 Water Index (SWI) that showed higher classification accuracy than NDWI (Jiang et al., 2020). Even though these indices showed good potential to distinguish between water and vegetation, the SWIR band has to be resampled from 20 to 10 m resolution to match other bands in indices, and looking at smaller scales, as in this study, can lead to misclassifications.

The reed beds with a density of  $\geq 50\%$  were proven to be classified more accurately (50–85%) than reed beds with a density of 25% (31% accuracy). Therefore, the tested approach of reed bed delineation in this study is only suggested to use for the densest reed beds, which may lead to an underestimation of 15%. The highest estimated vegetation density was in AOI 5 and the reference AOI throughout the study period. The reason for this might be that this is the only AOI (5th) where different cutting methods were applied; nonetheless, this area still gives a signal to satellite images and pixels were counted as vegetated areas. In general, a higher estimated vegetation density (WAVI higher by 0.02 on average) was detected after mowing at the end of the vegetation season since the reeds reach their physiological maturity at the end of August (Villa et al., 2013).

### *Practical use of the results in waterbody management*

A method using Yen thresholding on the NDWI index applied to Sentinel-2 images showed good results in the separation of water from reed beds, therefore it is recommended to use as a tool for evaluating area change during mowing works in waterbodies. Although the accuracy for determining the density is not sufficient, especially when it comes to medium- and low-density classes, having reference AOIs with 100% density allows for a robust way to assess the

effect of mowing, follow the recovery, and plan mowing works accordingly.

The management program of 2017–2019 showed a significant reduction of reed bed areas compared to reference years, meaning successful nutrient removal from the lake environment. The gained vegetation area was significantly higher in the year after mowing ended; suggesting that the reed bed areas will recover over time and mowing will have to be repeated after a few years.

In 2018 and 2019, the reduced vegetated area was still higher compared to the reference years but lower than in the first year (2017) of mowing. This could be explained by the fact that vegetation still had not fully recovered from the first year of mowing, and as suggested by Derr (2008), the reed regrowth rate the next year after mowing could be reduced by approximately 55% if no herbicide is applied. The recovery of reed beds after mowing works implies that it has to be performed continuously (Ailstock et al., 2001; Asaeda et al., 2006; Derr, 2008).

Macrophyte monitoring is commonly performed every 3 years (e.g. EPA Ireland and EPA Illinois) along several transects, where macrophyte relative abundance is estimated in situ. The tested method in this study allows monitoring of reed bed hotspots in the whole lake area and not just mowed AOIs; therefore, remote sensing techniques can provide a synoptic, more frequent in time view over a wide range of ecosystems and are very cost-effective in monitoring changes. Frequent satellite image data allow choosing the correct time of mowing as it is crucial to get information on the timescale for all reed stands since different lakes require optimal conditions for mowing depending on the end goal of lake management whether it would be to reduce reed aboveground biomass or remove nutrients from the lake (Fogli et al., 2014).

This approach could be used for the long-term (retrospective) analysis of aquatic vegetation dynamics, by adding, for example, the Landsat satellite series. The retrospective analysis could allow the indication of the areas in a lake that continuously had higher vegetation areas and densities, and where new mowing areas could be selected for better management of the lake environment. However, before using other satellite datasets, testing of the workflow presented in the study should be done first, as they might have different spectral, spatial and radiometric resolutions than Sentinel-2.

It is common to use in situ observations as validation data for satellite images (Lawley et al., 2016), although popularity grows on using UAV data for validation, which is relatively accurate and covers a relatively larger area (Kattenborn et al., 2019). UAV flights could be conducted by mowing personnel or lake manager, while the use of a structure from

motion allows the high accuracy of above ground biomass (Meneses et al., 2018).

## Conclusion

After analysis, the presented method using Yen binary thresholding on NDWI index calculated from Sentinel-2/MSI images is proposed, as it had the best performance. The conclusion is as follows: (1) Suggested method is suitable for medium and dense reed beds; (2) A larger reduction in reed bed areas was detected during the period of mowing; (3) Results showed a strong correlation between WAVI and visually evaluated reed densities; (4) No correlation was detected between estimated vegetation densities and vegetation area changes in mowing period.

It is hard to monitor vegetation just from satellite images alone because many variables can skew the results. Our workflow is recommended to use this method as an additional one to in situ measurement. It is relatively quick and covers large areas to evaluate the effectiveness of reed and other emergent macrophytes mowing in waterbodies.

By using the developed approach, it would be possible to evaluate the mowing effect also without prior knowledge of when and where the mowing was performed. In such cases, a longer period, e.g. covering the entire vegetation season or evaluation of several years, should be considered. Time series of relatively frequent satellite images, combining data originating from different optical sensors, or synergistic use of optical and active microwave remote sensing data (Anderson et al., 2021), would also be an advantage. However, a primary understanding of vegetation temporal dynamics, phenology and relation with environmental conditions, like air temperature and precipitation, is highly important. This additional information and sufficient time series of satellite images would allow the detection of intra-seasonal changes in coverage or density, less related to a natural environmental impact, but with a mowing performed.

In addition, UAVs could also be used for the robust estimation of the above-ground biomass of reeds after the calibration with additional reed height data collected in the field (Lu et al., 2022). Several studies have already proved that the estimation of biomass from reed beds could also be performed using satellite images (Jabłońska et al., 2021; Luo et al., 2017). In this way, this information would support the estimation of how much nutrients could be removed by mowing, how much biomass can be further used for bioenergy heating or as a green construction material (Sluis et al., 2013), and therefore significantly contribute to the management objectives.

## Disclosure statement

No potential conflict of interest was reported by the authors.

## ORCID

Edvinas Tiškus  <http://orcid.org/0000-0002-6293-2140>

## References

- Ailstock, M.S., Norman, C.M., & Bushmann, P.J. (2001). Common reed phragmites australis: Control and effects upon biodiversity in freshwater nontidal wetlands. *Restoration Ecology*, 9(1), 49–59. <https://doi.org/10.1046/j.1526-100x.2001.009001049.x>
- Amani, M., Salehi, B., Mahdavi, S., & Brisco, B. (2018). Spectral analysis of wetlands using multi-source optical satellite imagery. *Isprs Journal of Photogrammetry and Remote Sensing*, 114, 119–136. <https://doi.org/10.1016/j.isprsjprs.2018.07.005>
- Anderson, C. J., Heins, D., Pelletier, K. C., Bohnen, J. L., & Knight, J. F. Mapping invasive phragmites australis using unoccupied aircraft system imagery, canopy height models, and synthetic aperture radar. (2021). *Remote Sensing*, 13(16), 3303. Article 16. <https://doi.org/10.3390/rs13163303>
- Asaeda, T., Rajapakse, L., Manatunge, J., & Sahara, N. (2006). The effect of summer harvesting of phragmites australis on growth characteristics and rhizome resource storage. *Hydrobiologia*, 553(1), 327–335. <https://doi.org/10.1007/s10750-005-1157-6>
- Bhatnagar, S., Gill, L., Regan, S., Naughton, O., Johnston, P., Waldren, S., & Ghosh, B. (2020). Mapping vegetation communities inside wetlands using sentinel-2 imagery in Ireland. *International Journal of Applied Earth Observation and Geoinformation*, 88, 102083. <https://doi.org/10.1016/j.jag.2020.102083>
- Bojórquez, A., Martínez-Yrizar, A., Búrquez, A., Jaramillo, V. J., Mora, F., Balvanera, P., & Álvarez-Yépez, J. C. (2020). Improving the accuracy of above-ground biomass estimations in secondary tropical dry forests. *Forest Ecology and Management*, 474, 118384. <https://doi.org/10.1016/j.foreco.2020.118384>
- Bollas, N., Kokinou, E., & Polychronos, V. (2021). Comparison of sentinel-2 and UAV multispectral data for use in precision agriculture: An application from Northern Greece. *Drones*, 5(2), 35. <https://doi.org/10.3390/drones5020035>
- Bresciani, M., Sotgia, C., Fila, G. L., Musanti, M., & Bolpagni, R. (2011). Assessing common reed bed health and management strategies in Lake Garda (Italy) by means of leaf area index measurements. *Italian Journal of Remote Sensing*, 43(2), 9–22. <https://doi.org/10.5721/ItJRS20114321>
- Bresciani, M., Stroppiana, D., Fila, G., Montagna, M., & Giardino, C. (2009). Monitoring reed vegetation in environmentally sensitive areas in Italy. *Italian Journal of Remote Sensing*, 41(2), 125–137. <https://doi.org/10.5721/ItJRS20094129>
- Carabias, D.M. (2012). *Analysis of image thresholding methods for their application to augmented reality environments*. Universidad Complutense De Madrid.
- Datta, A., Maharaj, S., Prabhu, G. N., Bhowmik, D., Marino, A., Akbari, V., Rupavatharam, S., Sujeetha, J. A. R., Anantrao, G. G., Poduvattil, V. K., Kumar, S., & Kleczkowski, A. (2021). Monitoring the spread of water hyacinth (*Pontederia crassipes*): Challenges and future developments. *Frontiers in Ecology and Evolution*, 9, 1–8. <https://doi.org/10.3389/fevo.2021.631338>
- De Keukelaere, L., Sterckx, S., Adriaenssens, S., Knaeps, E., Reusen, I., Giardino, C., Bresciani, M., Hunter, P., Neil, C., Van der Zande, D., & Vaiciute, D. (2018). Atmospheric correction of Landsat-8/OLI and sentinel-2/MSI data using iCOR algorithm: Validation for coastal and inland waters. *European Journal of Remote Sensing*, 51(1), 525–542. <https://doi.org/10.1080/22797254.2018.1457937>
- Derr, J. F. (2008). Common reed (*Phragmites australis*) response to mowing and herbicide application. *Invasive Plant Science and Management*, 1(1), 12–16. <https://doi.org/10.1614/IPSM-07-001.1>
- Duke, J. A. (1983). *Handbook of energy crops*. Centre for New Crops and Plant Products, Purdue University.
- Egan, J. P. (1975). *Signal detection theory and ROC-analysis*. Academic press.
- Eller, F., Skálová, H., Caplan, J. S., Bhattarai, G. P., Burger, M. K., Cronin, J. T., Guo, W. -Y., Guo, X., Hazelton, E. L. G., Kettenring, K. M., Lambertini, C., McCormick, M. K., Meyerson, L. A., Mozdzer, T. J., Pyšek, P., Sorrell, B. K., Whigham, D. F., & Brix, H. (2017). Cosmopolitan species as models for ecophysiological responses to global change: The common reed *Phragmites australis*. *Frontiers in plant science*, 8, 1833. <https://doi.org/10.3389/fpls.2017.01833>
- Fogli, S., Brancaloni, L., Lambertini, C., & Gerdol, R. (2014). Mowing regime has different effects on reed stands in relation to habitat. *Journal of Environmental Management*, 134, 56–62. <https://doi.org/10.1016/j.jenvman.2014.01.001>
- Gao, B. (1996). NDWI—A normalized difference water index for remote sensing of vegetation liquid water from space. *Remote Sensing of Environment*, 58(3), 257–266. [https://doi.org/10.1016/S0034-4257\(96\)00067-3](https://doi.org/10.1016/S0034-4257(96)00067-3)
- Gao, B. -C., & Li, R. -R. (2012). Removal of thin cirrus scattering effects for remote sensing of ocean color from space. *IEEE Geoscience and Remote Sensing Letters*, 9(5), 972–976. <https://doi.org/10.1109/LGRS.2012.2187876>
- Güsewell, S., Buttler, A., & Klötzli, F. (1998). Short-term and long-term effects of mowing on the vegetation of two calcareous fens. *Journal of Vegetation Science*, 9(6), 861–872. <https://doi.org/10.2307/3237051>
- Güsewell, S., Le Nédic, C., & Buttler, A. (2000). Dynamics of common reed (*Phragmites australis* trin.) in Swiss fens with different management. *Wetlands Ecology and Management*, 8(6), 375–389. <https://doi.org/10.1023/a:1026553700571>
- Huete, A. R. (1988). A soil-adjusted vegetation index (SAVI). *Remote Sensing of Environment*, 25(3), 295–309. [https://doi.org/10.1016/0034-4257\(88\)90106-X](https://doi.org/10.1016/0034-4257(88)90106-X)
- Jabłońska, E., Winkowska, M., Wiśniewska, M., Geurts, J., Zak, D., & Kotowski, W. (2021). Impact of vegetation harvesting on nutrient removal and plant biomass quality in wetland buffer zones. *Hydrobiologia*, 848(14), 3273–3289. <https://doi.org/10.1007/s10750-020-04256-4>
- Jiang, W., Ni, Y., Pang, Z., He, G., Fu, J., Lu, J., Yang, K., Long, T., & Lei, T. (2020). A new index for identifying water body from sentinel-2 satellite remote sensing imagery. *ISPRS Annals of the Photogrammetry, Remote Sensing and Spatial Information Sciences*, V-3-2020, 33–38. <https://doi.org/10.5194/isprs-annals-V-3-2020-33-2020>
- Joyce, K. E., Duce, S., Leahy, S. M., Leon, J., & Maier, S. W. (2019). Principles and practice of acquiring drone-based image data in marine environments. *Marine & Freshwater Research*, 70(7), 952. <https://doi.org/10.1071/MF17380>

- Kapur J, Sahoo P and Wong A. (1985). A new method for gray-level picture thresholding using the entropy of the histogram. *Computer Vision, Graphics, and Image Processing*, 29(3), 273–285. [10.1016/0734-189X\(85\)90125-2](https://doi.org/10.1016/0734-189X(85)90125-2)
- Kattenborn, T., Lopatin, J., Förster, M., Braun, A. C., & Fassnacht, F. E. (2019). UAV data as alternative to field sampling to map woody invasive species based on combined sentinel-1 and sentinel-2 data. *Remote Sensing of Environment*, 227, 61–73. <https://doi.org/10.1016/j.rse.2019.03.025>
- Lawley, V., Lewis, M., Clarke, K., & Ostendorf, B. (2016). Site-based and remote sensing methods for monitoring indicators of vegetation condition: An Australian review. *Ecological indicators*, 60, 1273–1283. <https://doi.org/10.1016/j.ecolind.2015.03.021>
- Lu, L., Luo, J., Xin, Y., Duan, H., Sun, Z., Qiu, Y., & Xiao, Q. (2022). How can UAV contribute in satellite-based phragmites australis aboveground biomass estimating? *International Journal of Applied Earth Observation and Geoinformation*, 114, 103024. <https://doi.org/10.1016/j.jag.2022.103024>
- Luo, S., Wang, C., Xi, X., Pan, F., Qian, M., Peng, D., Nie, S., Qin, H., & Lin, Y. (2017). Retrieving aboveground biomass of wetland phragmites australis (common reed) using a combination of airborne discrete-return LiDAR and hyperspectral data. *International Journal of Applied Earth Observation and Geoinformation*, 58, 107–117. <https://doi.org/10.1016/j.jag.2017.01.016>
- Lu Yewei, L. Q. (2015). A method of coastal aquaculture area automatic extraction with high spatial resolution images. *Remote Sensing Technology and Application*, 30(3), 486–494. <https://doi.org/10.11873/j.issn.1004-0323.2015.3.0486>
- Mandrekar, J. N. (2010). Receiver operating characteristic curve in diagnostic test assessment. *Journal of Thoracic Oncology*, 5(9), 1315–1316. <https://doi.org/10.1097/JTO.0b013e3181ec173d>
- Martins, V. S., Barbosa, C. C. F., De Carvalho, L. A. S., Jorge, D. S. F., Lobo, F. D. L., & Novo, E. M. L. D. M. Assessment of atmospheric correction methods for sentinel-2 MSI images applied to Amazon floodplain lakes. (2017). *Remote Sensing*, 9(4), 322. Article 4. <https://doi.org/10.3390/rs9040322>
- McFeeters, S. K. (2013). Using the normalized difference water index (NDWI) within a geographic information system to detect swimming pools for mosquito abatement: A practical approach. *Remote Sensing*, 5(7), 3544–3561. <https://doi.org/10.3390/rs5073544>
- Meneses, N. C., Baier, S., Reidelstürz, P., Geist, J., & Schneider, T. (2018). Modelling heights of sparse aquatic reed (*Phragmites australis*) using structure from motion point clouds derived from rotary- and fixed-wing unmanned aerial vehicle (UAV) data. *Limnologia*, 72, 10–21. <https://doi.org/10.1016/j.limno.2018.07.001>
- OpenDroneMap. (2020). Authors ODM - a command line toolkit to generate maps, point clouds, 3D models and DEMs from drone, balloon or kite images. OpenDroneMap/ODM GitHub Page 2020; <https://github.com/OpenDroneMap/ODM>
- Otsu, N. (1979). A threshold selection method from gray-level histograms. *IEEE Transactions on Systems, Man, and Cybernetics*, 9(1), 62–66. <https://doi.org/10.1109/tsmc.1979.4310076>
- Oyama, Y., Matsushita, B., & Fukushima, T. (2015). Distinguishing surface cyanobacterial blooms and aquatic macrophytes using Landsat/TM and ETM+ shortwave infrared bands. *Remote Sensing of Environment*, 157, 35–47. <https://doi.org/10.1016/j.rse.2014.04.031>
- Picture Thresholding Using an Iterative Selection Method. *IEEE Trans. Syst., Man, Cybern.*, 8(8), 630–632. [10.1109/TSMC.1978.4310039](https://doi.org/10.1109/TSMC.1978.4310039)
- Pinardi, M., Bresciani, M., Villa, P., Cazzaniga, I., Laini, A., Tóth, V., Fadel, A., Austoni, M., Lami, A., & Giardino, C. (2018). Spatial and temporal dynamics of primary producers in shallow lakes as seen from space: Intra-annual observations from sentinel-2A. *Limnologia*, 72, 32–43. <https://doi.org/10.1016/j.limno.2018.08.002>
- Powell, S. J., Jakeman, A., & Croke, B. (2014). Can NDVI response indicate the effective flood extent in macrophyte dominated floodplain wetlands? *Ecological indicators*, 45, 486–493. <https://doi.org/10.1016/j.ecolind.2014.05.009>
- QGIS.org. 2022. <https://www.qgis.org/en/site/>
- Qi, J., Chehbouni, A., Huete, A. R., Kerr, Y. H., & Sorooshian, S. (1994). A modified soil adjusted vegetation index. *Remote Sensing of Environment*, 48(2), 119–126. [https://doi.org/10.1016/0034-4257\(94\)90134-1](https://doi.org/10.1016/0034-4257(94)90134-1)
- Qin, Q., Xu, D., Hou, L., Shen, B., & Xin, X. (2021). Comparing vegetation indices from sentinel-2 and Landsat 8 under different vegetation gradients based on a controlled grazing experiment. *Ecological indicators*, 133, 108363. <https://doi.org/10.1016/j.ecolind.2021.108363>
- Richter, R., Wang, X., Bachmann, M., & Schläpfer, D. (2011). Correction of cirrus effects in sentinel-2 type of imagery. *International Journal of Remote Sensing*, 32(10), 2931–2941. <https://doi.org/10.1080/01431161.2010.520346>
- Rondeaux, G., Steven, M., & Baret, F. (1996). Optimization of soil-adjusted vegetation indices. *Remote Sensing of Environment*, 55(2), 95–107. [https://doi.org/10.1016/0034-4257\(95\)00186-7](https://doi.org/10.1016/0034-4257(95)00186-7)
- Rouse, W., & Haas, R. H. (1973). *Monitoring vegetation systems in the great plains with ERTS*. Third Earth Resources Technology Satellite-1 Symposium, Goddard Space Flight Center at Washington, DC. 1, 309–317.
- Sakuno, Y., & Kunii, H. (2013). Estimation of growth area of aquatic macrophytes expanding spontaneously in Lake Shinji using ASTER data. *International Journal of Geosciences*, 4(06), 1–5. <https://doi.org/10.4236/ijg.2013.46A1001>
- Schindelin, J., Arganda-Carreras, I., Frise, E., Kaynig, V., Longair, M., Pietzsch, T., Preibisch, S., Rueden, C., Saalfeld, S., Schmid, B., Tinevez, J. -Y., White, D. J., Hartenstein, V., Eliceiri, K., Tomancak, P., & Cardona, A. (2012). Fiji: An open-source platform for biological-image analysis. *Nature Methods*, 9(7), 676–682. <https://doi.org/10.1038/nmeth.2019>
- Schläpfer, D., & Richter, R. (2014). Evaluation of brefor BRDF effects correction for HYSPEX, CASI, and APEX imaging spectroscopy data. *2014 6th Workshop on Hyperspectral Image and Signal Processing: Evolution in Remote Sensing (WHISPERS)*, 1–4. <https://doi.org/10.1109/WHISPERS.2014.8077488>
- Sezgin, M., & Sankur, B. (2004). Survey over image thresholding techniques and quantitative performance evaluation. *Journal of Electronic Imaging*, 13(1), 146–165. <https://doi.org/10.1117/1.1631315>
- Silva, T. S. F., Costa, M. P. F., Melack, J. M., & Novo, E. M. L. M. (2008). Remote sensing of aquatic vegetation: Theory and applications. *Environmental Monitoring and Assessment*, 140(1), 131–145. <https://doi.org/10.1007/s10661-007-9855-3>

- Singh, G., Reynolds, C., Byrne, M., & Rosman, B. (2020). A remote sensing method to monitor water, aquatic vegetation, and invasive water hyacinth at national extents. *Remote Sensing*, 12(24), 4021. <https://doi.org/10.3390/rs12244021>
- Sinkevičienė, D. Z., Matulevičiūtė, D. D., & Stankevičiūtė, D. J. (2005). *Report on macrophyte monitoring in rivers and lakes*.
- Sluis, T. V. D., Poppens, R. P., Kraisivitnii, P., Rii, O., Lesschen, J. P., Galytska, M., & Elbersen, H. W. (2013). *Reed harvesting from wetlands for bioenergy: Technical aspects, sustainability and economic viability of reed harvesting in Ukraine (No. 2460)*. Alterra, Wageningen-UR. <https://library.wur.nl/WebQuery/wurpubs/444612>
- Srinivas, C., Prasad, M., & Sirisha, M. (2019). Remote sensing image segmentation using OTSU algorithm. *International Journal of Computer Applications*, 178(12), 46–50, 0975 – 8887.
- Sunder, S., Ramsankaran, R., & Ramakrishnan, B. (2017). Inter-comparison of remote sensing sensing-based shoreline mapping techniques at different coastal stretches of India. *Environmental Monitoring and Assessment*, 189(6), 290. <https://doi.org/10.1007/s10661-017-5996-1>
- Szabó, S., Gácsi, Z., & Balázs, B. (2016). Specific features of NDVI, NDWI and MNDWI as reflected in land cover categories. *Landscape & Environment*, 10(3–4), 194–202. <https://doi.org/10.21120/LE/10/3-4/13>
- Technical specification of Plateliai Lake reed mowing*. (2017).
- Ting, K. M. (2017). Confusion Matrix. In C. Sammut & G. I. Webb (Eds.), *Encyclopedia of machine learning and data mining* (p. 260). Springer US. [https://doi.org/10.1007/978-1-4899-7687-1\\_50](https://doi.org/10.1007/978-1-4899-7687-1_50)
- Villa, P., Bresciani, M., Pinardi, M., & Bolpagni, R. (2014, May). Multitemporal assessment of macrophytes using aquatic vegetation indices. SENTINEL-2 for Science, Rome. <https://doi.org/10.13140/2.1.3856.3525>
- Villa, P., Laini, A., Bresciani, M., & Bolpagni, R. (2013). A remote sensing approach to monitor the conservation status of lacustrine phragmites australis beds. *Wetlands Ecology and Management*, 21(6), 399–416. <https://doi.org/10.1007/s11273-013-9311-9>
- Vis, C., Hudon, C., & Carignan, R. (2003). An evaluation of approaches used to determine the distribution and biomass of emergent and submerged aquatic macrophytes over large spatial scales. *Aquatic Botany*, 77(3), 187–201. [https://doi.org/10.1016/S0304-3770\(03\)00105-0](https://doi.org/10.1016/S0304-3770(03)00105-0)
- Xu, H. (2005). A study on information extraction of water body with the modified normalized difference water index (MNDWI). *Journal of Remote Sensing*, 9(5), 589–595.
- Yen J C, Chang F J, Chang S. (1995). A new criterion for automatic multilevel thresholding. *IEEE Trans Image Process*, 4(3), 370–8. [10.1109/83.366472](https://doi.org/10.1109/83.366472)
- Zack G W, Rogers W E and Latt S A. (1977). Automatic measurement of sister chromatid exchange frequency. *J Histochem Cytochem.*, 25(7), 741–753. [10.1177/25.7.70454](https://doi.org/10.1177/25.7.70454)
- Zheng, X., & Chen, T. (2021). High spatial resolution remote sensing image segmentation based on the multi-classification model and the binary classification model. *Neural Computing & Applications*. <https://doi.org/10.1007/s00521-020-05561-8>
- Zhou, G., Ma, Z., Sathyendranath, S., Platt, T., Jiang, C., & Sun, K. (2018). Canopy reflectance modeling of aquatic vegetation for algorithm development: Global sensitivity analysis. *Remote Sensing*, 10(6), 837. <https://doi.org/10.3390/rs10060837>

## **PAPER III**



Article

# An Evaluation of Sun-Glint Correction Methods for UAV-Derived Secchi Depth Estimations in Inland Water Bodies

Edvinas Tiškus , Martynas Bučas , Diana Vaičiūtė, Jonas Gintauskas and Irma Babrauskienė

Marine Research Institute, Klaipeda University, 92294 Klaipeda, Lithuania; martynas.bucas@ku.lt (M.B.); diana.vaiciute@ku.lt (D.V.); jonas.gintauskas@ku.lt (J.G.); irma.babr@gmail.com (I.B.)

\* Correspondence: edvinas.tiskus@ku.lt

**Abstract:** This study investigates the application of unoccupied aerial vehicles (UAVs) equipped with a Micasense RedEdge-MX multispectral camera for the estimation of Secchi depth (SD) in inland water bodies. The research analyzed and compared five sun-glint correction methodologies—Hedley, Goodman, Lyzenga, Joyce, and threshold-removed glint—to model the SD values derived from UAV multispectral imagery, highlighting the role of reflectance accuracy and algorithmic precision in SD modeling. While Goodman’s method showed a higher correlation (0.92) with in situ SD measurements, Hedley’s method exhibited the smallest average deviation (0.65 m), suggesting its potential in water resource management, environmental monitoring, and ecological modeling. The study also underscored the quasi-analytical algorithm (QAA) potential in estimating SD due to its flexibility to process data from various sensors without requiring in situ measurements, offering scalability for large-scale water quality surveys. The accuracy of SD measures calculated using QAA was related to variability in water constituents of colored dissolved organic matter and the solar zenith angle. A practical workflow for SD acquisition using UAVs and multispectral data is proposed for monitoring inland water bodies.

**Keywords:** UAVs; Secchi depth; multispectral imagery; sun glint; quasi-analytical algorithm; remote sensing



Citation: Tiškus, E.; Bučas, M.;

Vaičiūtė, D.; Gintauskas, J.;

Babrauskienė, I. An Evaluation of

Sun-Glint Correction Methods for

UAV-Derived Secchi Depth

Estimations in Inland Water Bodies.

*Drones* **2023**, *7*, 546. <https://doi.org/10.3390/drones7090546>

Academic Editors: Jingzhe Wang,

Yangyi Wu, Yinghui Zhang, Ivan

Lizaga and Zipeng Zhang

Received: 21 July 2023

Revised: 19 August 2023

Accepted: 21 August 2023

Published: 23 August 2023



Copyright: © 2023 by the authors.

Licensee MDPI, Basel, Switzerland.

This article is an open access article

distributed under the terms and

conditions of the Creative Commons

Attribution (CC BY) license (<https://creativecommons.org/licenses/by/4.0/>).

## 1. Introduction

Secchi depth (SD), an essential measure of water transparency in aquatic ecosystems, provides a critical indication of water quality and ecological health [1–3]. In Europe, SD is important for following the water quality rules set by the European Water Framework Directive (WFD), which mandates member states to uphold ecological standards [4]. SD thus helps identify impairments affecting water quality and aids in devising and executing management plans to protect water bodies [5].

The Secchi disk is the main tool used for obtaining SD measurements, particularly in vast and complex aquatic ecosystems [6–8]. However, traditional methods—visual observations using a white Secchi disk—can be labor-intensive, time-consuming, and potentially influenced by observer bias [9,10]. They also typically offer point-level measurements, which may not reflect water transparency over larger areas [11,12].

The limitations of traditional methods have spurred interest in remote sensing techniques for estimating SD in complex aquatic ecosystems. Techniques ranging from satellite data to unoccupied aerial vehicles (UAVs) equipped with light detection and ranging (LiDAR) systems and hyperspectral imagery have been explored for accuracy [13]. These techniques promise cost-effective and efficient high-resolution spatial data on water transparency over large areas, with multispectral imagery from UAVs emerging as a promising alternative [14].

UAVs can provide higher-resolution images than satellites, allowing for more precise measurements of water bodies, including small and shallow ponds [15,16], which are



often not well captured by satellite imagery [16,17]. Furthermore, UAVs can be flown at a specific time and location, which is particularly important for SD measurements, as the measurement of water transparency can be influenced by various environmental factors, such as partial cloud cover, water turbidity, and the angle of the sun [18,19]. Although weather conditions influence the ability of UAV flight (with Inspire 2 UAV if winds exceed around 10 m/s), UAVs can collect data during fully cloudy conditions, where optical satellite data are heavily affected by clouds. Additionally, they can be equipped with diverse sensors for capturing multispectral or hyperspectral images, thus providing valuable data on water quality and ecology [14,20]. Furthermore, UAVs can serve as ground truth to validate satellite data [21,22], thereby enhancing accuracy for the monitored area, e.g., one tile coverage of Sentinel-2 can reach from 100,000 ha, while UAVs cannot cover relatively large areas. Moreover, UAV technology presents a strategic advantage in regions where conventional methodologies struggle due to logistical complications.

SD is primarily influenced by three optical components: Chl-a, colored dissolved organic matter (CDOM), and total suspended matter (TSM) [23,24]. Different wavelengths of light penetrate water bodies to different extents. For instance, blue light can penetrate deeper into clear waters than green or red light. Conversely, in more turbid waters, red and near-infrared (NIR) light is absorbed more rapidly and scatters quickly, leading to a diminished signal at the surface. Hence, the spectral signatures captured by remote sensors are significantly influenced by the composition and clarity of the water body.

Various algorithms exist to calculate water parameters from multispectral data, including mechanistic models [25], artificial neural networks [26], and regression algorithms [27]. Each offers unique advantages and applicability, depending on the specific characteristics of the data and the aquatic ecosystem under study. For instance, a study by Chusnah and Chu [28] demonstrated the application of machine learning in estimating Chl-a concentrations, which are commonly used as indicators for assessing the trophic level of lakes and the state of water quality. The study utilized machine learning to implement a band ratio algorithm and generate Chl-a maps from Sentinel-2 and Sentinel-3 satellite images. However, mechanistic models, relying on physical laws and principles to simulate light attenuation and scattering processes in water, often provide the most reliable and accurate predictions, particularly when dealing with smaller datasets, which would not be sufficient for machine learning models [29].

Lee et al. [30] provided a foundational understanding of the optical properties influencing SD, which significantly contributed to the development of the quasi-analytical algorithm (QAA) for more accurate and reliable water clarity estimations. The QAA, a commonly used mechanistic model for SD, has been utilized in various water bodies [29,31,32]. It has been applied to MODIS and MERIS satellite data, where it reduced the root-mean-square error (RMSE) of SD estimation from 1.5 m to 1.0 m. Furthermore, the QAA has been used to account for the residual error in reflectance data from MODIS satellite data, demonstrating its potential for remote sensing in monitoring and managing water resources [33]. The algorithm showed excellent results ( $R^2 = 0.96$ , MAPD = 0.18) when validated with independent measurements covering oceanic, coastal, and lake waters [34]. However, previous studies have not delved into the potential benefits of utilizing multispectral cameras onboard UAVs in combination with the QAA algorithm. The integration of these cameras with UAVs offers potential improvements in spatial resolution and data availability, bridging the gap between in situ and satellite remote sensing measurements [18].

It is important to accurately account for reflected light from the water surface—more specifically, the sun-glint effect—as it can lead to inaccuracies in further processing of water quality algorithms [18,35,36]. The simplest way of avoiding sun glint is careful UAV flight time and direction planning; however, since the water surface is often uneven, it is hard to reduce sun glint completely [37]. There are several methods of reducing the sun-glint effect in multispectral UAV images during postprocessing, for example, M Muslim et al. [36] tested four methods proposed by Lyzenga et al. [38], Joyce [39], Hedley et al. [40], and Goodman et al. [41] and applied them to either the whole image or just the glinted area.

Other studies used the methods of Hochberg et al. [42], removing glinted pixels as NIR threshold or using HydroLight simulations [18]. The application of these methods should align with the specific requirements of the study. For instance, if the primary objective entails bottom mapping, the method proposed by Lyzenga offers superior results, as demonstrated in M Muslim's et al. [36] study. On the other hand, if the analysis is focused on assessing surface water quality parameters, the Hedley method emerged as the preferred choice by Windle and Silsbe [18]. Thus, the selection of sun-glint correction techniques requires careful consideration of the objectives, ensuring the most effective and accurate outcomes in different scenarios.

By yielding accurate, timely, and spatially inclusive data on water transparency, UAVs equip decision-makers with invaluable resources, necessitating immediate intervention or remediation measures. This is particularly evident when we consider the capabilities of UAVs for mapping vast areas. A single UAV flight, which takes approximately 25 min, can effectively map an area as large as 25 ha.

This research aimed to evaluate the effectiveness of QAA for the determination of SD using multispectral cameras onboard UAVs. It was performed by testing QAA on image datasets preprocessed using five different methods of sun-glint correction. Additionally, the study examined how water constituents and solar zenith angle affected the discrepancy between actual and modeled SD values. We hypothesize that the radiometric accuracy of a calibrated UAS sensor should meet the required accuracy of 5%, expected with ocean color remote sensing, when compared to in situ measures of Hooker et al. [43] and application of sun-glint correction methods will improve usability in SD modeling, by deviation of RMSD of the same 5% from in situ measures, which would still provide practical results for water quality assessment.

## 2. Materials and Methods

The study was performed in 43 water bodies in Lithuania (Figure 1), represented by high variability and proportion of optically active in-water components—turbidity, Chl-a and CDOM (Supplementary Table S1)—thus bolstering the robustness and generalizability of the findings. The research was conducted from May 2021 to May 2023.

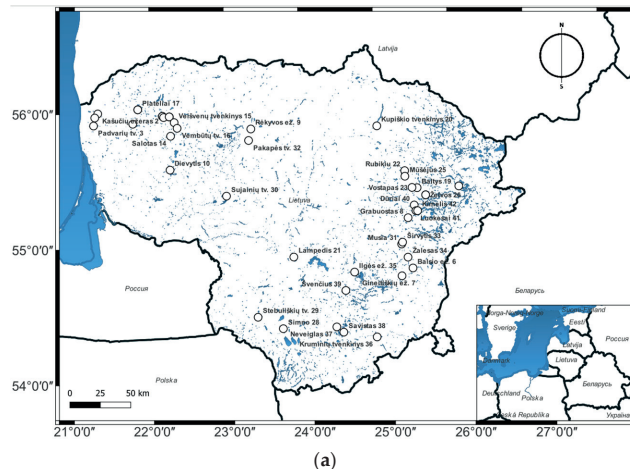
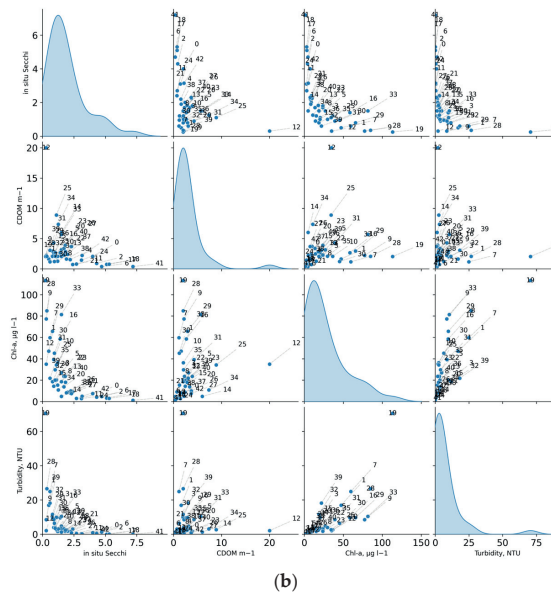


Figure 1. Cont.



**Figure 1.** (a) Study area with indicated study sites. (b) Pair plot between in situ parameters, measured in the areas of interest. The diagonal plots show kernel density estimations for each parameter, offering a smoothed representation of the distribution of data values. ID numbers in pair plots represent the lake number after the name in the map with  $n = 43$ .

### 2.1. UAV Data Collection and Calibration

An Inspire 2 UAV equipped with a RedEdge-MX camera was used to facilitate the acquisition of data [44]. The camera features five bands: blue ( $475 \text{ nm} \pm 16 \text{ nm}$ ), green ( $560 \text{ nm} \pm 13 \text{ nm}$ ), red ( $668 \text{ nm} \pm 8 \text{ nm}$ ), red edge ( $717 \text{ nm} \pm 6 \text{ nm}$ ), and NIR ( $842 \text{ nm} \pm 28 \text{ nm}$ ). To ensure optimal image capture, the UAV was flown at a height of 60 m to optimize the balance between spatial resolution and the area covered in each image, allowing for both relatively high-resolution imagery (from 3 to 4 cm/pixel) and a reasonable area coverage per flight (around 40–50 m<sup>2</sup>), with the camera programmed to capture images every three seconds. This frequency was necessitated by the inability to view the live feed and capture images in desired areas from the Micasense RedEdge-MX camera at a distance. The maximum distance between the SD measurement site, where GPS coordinates were recorded, and the image GPS coordinates were approximately 40 m, while the minimum distance was 0 when the measurement was above the boat. For the majority of water bodies, a single measurement site was selected in alignment with the methods of the Environmental Protection Agency of Lithuania. However, for a few larger water bodies, two sampling points were obtained for a more comprehensive understanding. The operation of the UAV was coordinated by two individuals: one controlling the UAV from the shore and the other onboard a boat, both communicating via phone during the Secchi disk measurements. The onboard operator also concurrently measured other water quality parameters outlined in Section 2.2.

For image calibration, the original Micasense RedEdge calibration panel was used. In accordance with Micasense's guidelines, a calibration panel image was captured at the shore before and after each flight, ensuring no shadows were cast on the reference panel or drone [44]. Three images were taken each time for assurance. Furthermore, the

Downwelling Light Sensor (DLS2) provides real-time, continuous measurements of the ambient light conditions during the flight, ensuring that the images captured are properly calibrated regardless of changes in the lighting environment.

### 2.2. In Situ Data

Concurrently with the UAV image capturing, in situ SD measurements were performed using a 30 cm white Secchi disk, a widely accepted method for assessing water transparency in lakes, rivers, and oceans [45].

The parameters of CDOM—the light-absorbing component of dissolved organic matter, Chl-a (an indicator of phytoplankton biomass), and turbidity (a measure of the cloudiness or haziness of water)—were measured alongside SD to assess their potential influence on water transparency. Parameters were only measured in areas where SD was lower than the depth of the specific point being assessed.

Water samples for Chl-a measurements were filtered through glass fiber GF/F filters with a nominal pore size of 0.7  $\mu\text{m}$  and extracted into 90% acetone. Photosynthetic pigments were measured spectrophotometrically and estimated according to the trichromatic method [46,47]. CDOM was measured spectrophotometrically after filtration through 0.22  $\mu\text{m}$  membrane filters. The CDOM absorption coefficient at 440 nm was derived according to Kirk [48]. A Shimadzu UV-2600 spectrophotometer was used for the analysis of Chl-a and CDOM. Turbidity was measured with a portable turbidity meter (Eutech Instruments TN-100, Landsmeer, The Netherlands) in the Nephelometric Turbidity Unit (NTU). The instrument has a light-emitting diode in the near-infrared range (Hach Lange at 860 nm and Eutech Instruments at 850 nm), and the detector measures the scatter at a 90° angle. This method is based on International Organization for Standardization (ISO) 7027.

In situ remote sensing reflectance  $R_{rs}$  was acquired to validate wavelengths from UAV observations of water surface reflectance.  $R_{rs}$  was measured in the spectral range of 400–800 nm by simultaneous measurements of downwelling irradiance, upwelling radiance, and downwelling radiance, performed with a WISP-3 spectroradiometer [49].  $R_{rs}$  was calculated according to Equation (1):

$$R_{rs} = \frac{L_u - \rho L_d}{E_d} \quad (1)$$

where  $L_u$  is the upwelling radiance,  $L_d$  the downwelling radiance,  $E_d$  the downwelling irradiance, and  $\rho$  a water surface reflectance factor equal to 0.028.

Central wavelengths of the Rededge MX camera were used (475 nm, 560 nm, 668 nm, 717 nm, 842 nm). NIR data were excluded from comparison with in situ reflectance, which was not measured at 842 nm; however, NIR was still used for the sun-glint correction step Section 2.4.

### 2.3. Preprocessing the UAV Data

The collected UAV images underwent preprocessing of correcting atmospheric effects and standardizing the format suitable for analysis (Figure 2). The conversion of raw images to radiance involves several corrective steps to eliminate biases and errors, accounting for dark-pixel offset, vignette effect, as well as aligning images due to distances between sensors, which could potentially affect the accuracy and reliability of the data. These steps were achieved using the Micasense Python (version 3.7, Python Software Foundation, 2018) workflow, mainly the function `raw_image_to_radiance`, as described in the Micasense Github repository for users [44].



would not be affected (Figure 3a). One water body (Kruminių Reservoir) was surveyed at late in the day, when the zenith angle was approximately 80 degrees, resulting in shadows covering half the area; however, the unshaded area was able to be used for the analyses (Figure 3b), removing the shadowed area using binary thresholding. In total, 39 water bodies were left for statistical analysis after discarding unsuitable ones.

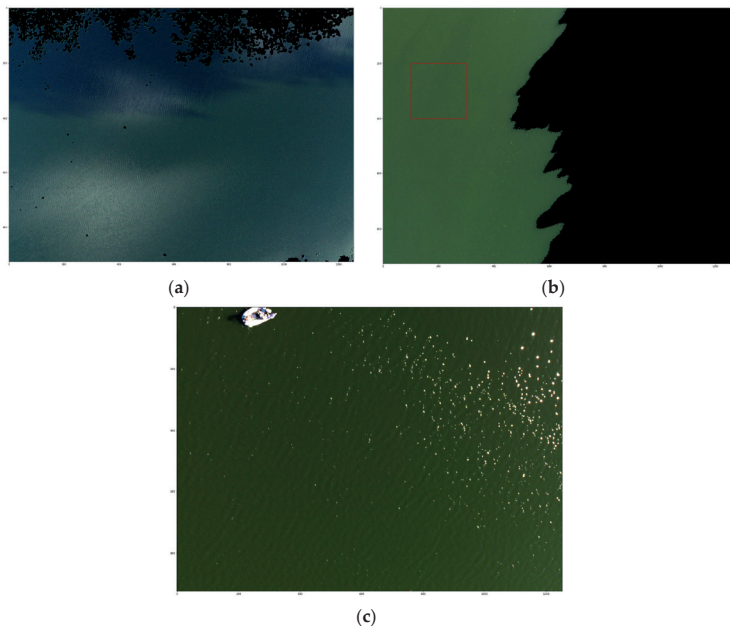


**Figure 3.** (a) RGB of an image affected by shadows, bottom reflectance and floating macrophytes after thresholding (Grabuostas Lake), (b) RGB of contaminated image (Kruminių Reservoir) with shadow and shore, but where values can still be used by selecting an area (red square) that was good, (c) RGB example of a relatively good image (Musia Lake) before removing sun glint and boat.

To ensure accurate SD measurements, objects (boats, coast, macrophytes) and shadows potentially affecting the measurements' accuracy were removed. Firstly, the normalized difference water index (NDWI) was calculated to distinguish between water and non-water pixels (3). This index was then classified into binary parts using Yen thresholding [53,54], where non-water pixels were masked as NaN values. Yen method was used also on just the NIR band to classify areas where pixels were affected by sun glint and masked as NaN in one of the sun-glint removal tests. This sun-glint removal method was later called the threshold-removed glint method.

$$NDWI = \frac{RrsGreen - RrsNir}{RrsGreen + RrsNir} \quad (3)$$

In 11 images, water waves caused a substantial amount of sun glint (Figure 4a), despite images being captured early in the morning around 10 a.m. GMT+3, when the sun reflection from calm water should not have reached the lens. Therefore, the sun-glint correction was performed using the algorithms developed by Hedley et al. [40], Goodman et al. [41], Lyzenga et al. [38], and Joyce [39], which assume that the water surface reflectance is a

linear combination of water reflectance and sun-glint reflectance. The models were fitted using a set of training data consisting of image pixels where sun glint was absent, calculated from an area with 10% lowest value NIR pixels [18]. The model was then used to predict water reflectance for sun-glint-affected pixels, reducing reflectance values according to Equations (4)–(7).

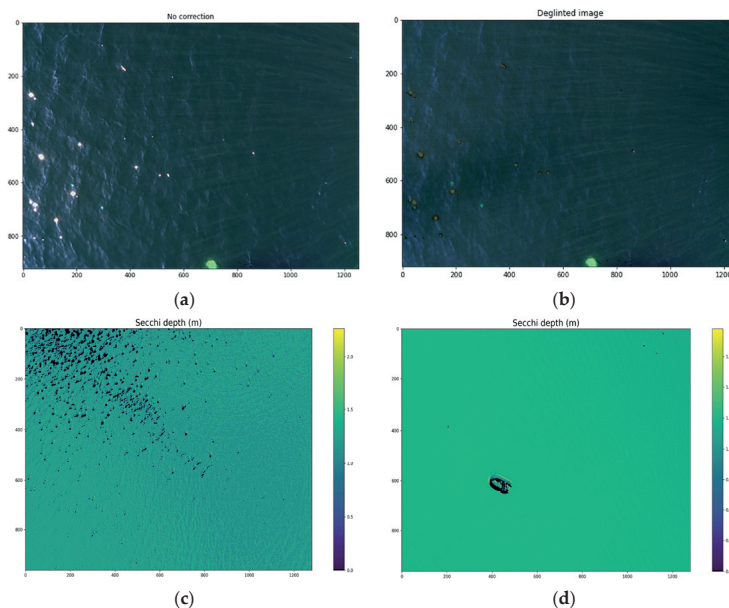


**Figure 4.** (a) RGB image before the sun-glint correction. (b) Deglinted RGB image using Hedley’s method. (c) Threshold-removed sun-glint area from NDWI image, recalculated to SD; black areas represent removed values. (d) The boat removed from NDWI using Yen’s threshold and recalculated to SD; black areas represent removed values.

The Hedley method (4) calculates the remote sensing reflectance ( $R_{rs}$ ) for each pixel in each band. The method first finds the minimum NIR value and then calculates the slope for each band using linear regression. The Lyzenga and Joyce methods ((5) and (6)) are similar to the Hedley method, but use the mean and mode, respectively, of the lowest 10% of NIR values instead of the minimum NIR value. The Goodman method (7) calculates the  $R_{rs}$  for each pixel in each band using a constant A (0.000019) and a factor B (0.1) that is multiplied by the difference between the red and NIR bands:

$$\text{Hedley } R_{rs\lambda} = \lambda + bi_{\lambda} \times (NIR - NIR_{min}) \tag{4}$$

$$\text{Lyzenga } R_{rs\lambda} = \lambda + bij_{\lambda} \times (NIR - NIR_{mean}) \tag{5}$$

$$\text{Joyce } R_{rs\lambda} = \lambda + bi_{\lambda} \times (NIR - NIR_{mode}) \tag{6}$$

$$\text{Goodman } R_{rs\lambda} = \lambda - NIR + \delta, \text{ where } \delta = A + B \times (Red_{\lambda} - NIR_{\lambda}) \tag{7}$$

where  $\lambda$  is the band of interest (blue, green, red, red edge, NIR),  $b_{i\lambda}$  is the slope of the band,  $b_{ij\lambda}$  is equal to covariance between  $\lambda$  and NIR divided by variance in NIR, and  $NIR_{min}$ ,  $NIR_{mode}$ , and  $NIR_{mean}$  are the minimum, mode, and mean NIR values, respectively. For Goodman's method,  $\delta$  is a constant offset across all wavelengths where A and B are constants ( $A = 0.000019$  and  $B = 0.1$ ). Additionally, removing only sun-glint-affected areas (determined by the binary thresholding Yen algorithm) was compared as an alternative approach to sun-glint correction methods (Figure 4c).

The images of four water bodies (Vembutų, Stebuliškių, Pakapės, and Krūminių reservoirs) were also affected by either shore or cloud-glint artefacts. However, most of these artefacts were successfully removed using binary thresholding, except for one image (Figure 3b) where the area had to be manually chosen because the thresholding method was unable to accurately separate the unwanted areas.

### 2.5. Secchi Depth Model

The quasi-analytical algorithm (QAA) proposed by Lee et al. [30] provides a robust framework for monitoring SD (8), particularly in scenarios where in situ measurements may be unavailable. Compared to the empirical approach, this semianalytical method offers a significant advantage: it does not necessitate the recalibration of the retrieval algorithm with in situ data [31]. This enhances its utility in diverse settings. As such, it was considered more suitable for monitoring SD in various water bodies.

Lee et al. [30] introduced a mechanistic model that accounts for the effects of light attenuation, scattering, and reflection in the water column, as well as the properties of the Secchi disk itself, in determining the SD. The parameters that determine SD in this algorithm are the total absorption coefficient ' $a$ ' and the total backscattering coefficient ' $bb$ '. From these parameters, the diffuse attenuation coefficient  $K_d$  was calculated, which is the main variable in the SD formula, besides the  $R_{rs}$  band:

$$K_T - K_d = \frac{1.04 * (1 + 5.4u)^{0.5}}{1 / \left(1 - \frac{\sin(\theta)^2}{RI^2}\right)^{0.5}} \quad (8)$$

$$SD = \frac{1}{k_t - k_d * \min K_d} \ln \left( \frac{0.14 - \min R_{rs}}{0.013} \right) \quad (9)$$

where  $\min K_d$  is the minimum value of  $K_d$  chosen from  $K_d$  calculated with blue, green and red bands and  $\min R_{rs}$  is the above-surface remote sensing reflectance of the band that had the lowest  $K_d$  value.  $K_T - K_d$  is the upwelling radiance diffuse attenuation coefficient and was used instead of a constant value of 1.5 as suggested by Jiang et al. [31], where  $\theta$  is the solar zenith angle,  $RI$  is the refractive index value of water equal to 1.33 and  $u$  denotes the ratio of backscattering coefficient to the sum of absorption and backscattering coefficient.

The sun zenith angle was computed from in situ measurements using the time and location of the observation. This information was then used to calculate the solar position using the Python library pytz [55]. This approach provided a reliable means of determining the solar zenith angle, which is an important parameter in applications related to SD acquisition from  $R_{rs}$ .

Selecting the appropriate reference wavelength is of major importance for the final SD value [34]. The green band (560 nm) was used as a reference if the red band  $R_{rs}$  (668 nm) was  $< 0.0015 \text{ sr}^{-1}$ . Otherwise, the red band (668 nm) was used, with accordingly modified calculations of other parameters, as suggested by Lee et al [30].

SD was calculated using the QAA method for images of 6 types: corrected after Hedley, Lyzenga, Joyce and Goodman sun-glint algorithms, threshold-removed images and images with no correction.



### 2.6. Validation and Interpretation of Results

All of the final modeled SD values and reflectance images were averaged to ensure that images could be compared with in situ data. Pearson correlation coefficients were calculated to assess multicollinearity between the reflectance values of different wavelengths. The final reflectances obtained after applying various correction methods and no correction (Sections 2.3 and 2.4) were validated with in situ reflectances (WISP-3). The accuracy of these methods was evaluated by bias (9), while the root-mean-square deviation (RMSD) was used as an indicator of the QAA model's precision (10), and the Pearson's correlation coefficient ( $r$ ) described the relationship strength between the model's output and the real data values.

$$\text{Bias} = \frac{1}{N} \sum_{i=1}^N (X_{\text{estimated},i} - X_{\text{measured},i}) \quad (10)$$

$$\text{RMSD} = \sqrt{\frac{\sum_{i=1}^N (X_{\text{estimated},i} - X_{\text{measured},i})^2}{N}} \quad (11)$$

The same accuracy and precision measures were applied to modeled SD values. Generalized additive models (GAMs) were employed [56] to investigate the relationships between the difference in modeled and in situ SD (the response variable) and a set of independent variables: CDOM, Chl-a, turbidity, and solar zenith. The GAMs were chosen due to their flexibility in modeling nonlinear relationships and their ability to handle interactions between predictors. The GAMs were utilized using R programming language with the `mgcv` [57] library for statistical parameters and `ggplot2` [58] library for visualization. Before analysis, the cross-correlation (based on the Pearson correlation coefficient) between the independent variables was determined. The correlation was relatively high ( $r = 0.76$ ) between Chl-a and turbidity; therefore, turbidity was not included in the GAMs. Before the interpretation of the GAM results, the residuals were visually inspected with diagnostic plots for normality and equal variance against the fitted values.  $F$  and  $p$  values were obtained to assess the relative importance and significance of the independent variables ( $p < 0.05$  was considered a statistically significant relationship). The fit of the model was evaluated using the explained deviance. A response plot was graphically represented to visualize the relationship between an explanatory variable and the response. As there were multiple predictors, each one was plotted separately with a smooth curve and the confidence interval of the effect.

To visualize the SD results, a subset of images with calculated SD values were exported as TIFF and mosaiced according to image metadata GPS coordinates in QGIS version 3.16 [59]. The result was then visualized on top of the RGB mosaic that was mosaiced using OpenDroneMap [60] photogrammetry software.

## 3. Results

### 3.1. Band Validation after Sun-Glint Correction

Across all correction methods and the in situ data, the green band (560 nm) consistently showed the peak mean value, while the blue band (475 nm) indicated the valley or lowest mean value. The general shape of the data appears to peak at the green band, with decreasing values on either side at the blue and red bands (668 nm), and a slight increase at the red edge band (717 nm). This pattern was consistent across all the correction methods and the in situ data, indicating the robustness of this spectral feature in the multispectral UAV image data. In terms of multicollinearity, the green and red exhibited the strongest correlation of 0.97, closely followed by correlations between the green and red edge at 0.96 and the red and red edge at 0.95. The blue band also exhibited strong multicollinearity with the other bands: 0.97 with green, 0.94 with red and 0.91 with red edge.

The highest mean values across all bands were observed with the Lyzenga correction method, while the lowest was observed with the Goodman correction method (Figure 5). The in situ values were generally lower than the corrected values, except for the Goodman correction method.

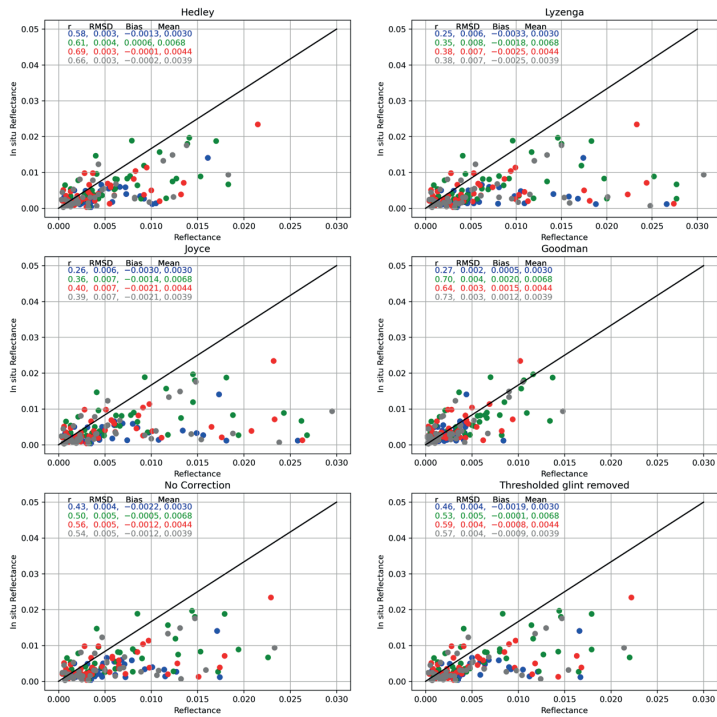


**Figure 5.** Spectral scatterplots demonstrating the agreement between in situ measured and sun-glint-corrected (or not corrected) reflectances in the UAV images. Statistics ( $r$ , RMSD, bias) and points are color-coded accordingly, except for the red edge, which is gray. A diagonal black line marks perfect agreement (1:1).

Removing the two outlier points, one from green and one from the red edge band, decreases  $r$  values and the  $r$  mean becomes similar to the red bands. However, it also decreases RMSD and bias for these bands, thus not decreasing the accuracy of the data.

The validation results provided robust evidence regarding the performance of the correction methods and the reliability of the final reflectance values. The correlation for all methods (Figure 6) had the same trend, where it was the lowest for the blue band ( $r = 0.38 \pm 0.12$ ) as well as for the red band ( $r = 0.56 \pm 0.14$ ), but higher for the green band ( $r = 0.75 \pm 0.11$ ) and red edge band ( $r = 0.80 \pm 0.10$ ). However, RMSD was relatively low for the blue band (RMSD =  $0.0043 \pm 0.0016$ ) and red (RMSD =  $0.0048 \pm 0.0018$ ) bands and slightly higher for the green (RMSD =  $0.0060 \pm 0.0013$ ) and red edge (RMSD =  $0.0053 \pm 0.0014$ ) bands. Bias for most methods followed a similar trend of larger underestimation for the blue band and green bands, then slight overestimation for the red band with Goodman, Hedley and threshold-removed glint methods, but still undervaluation for other methods, and slightly lower undervaluation for the red edge band. Goodman’s method was exceptional to these trends, as green, red and red edge bands were overestimated.

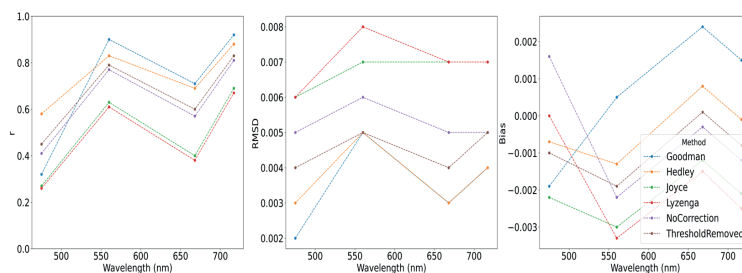


**Figure 6.** Mean  $r$ , RMSD and bias between corrected reflectances with each method and in situ measured reflectances across all available wavelengths. RMSD and bias are presented in reflectance values.

Overall, Goodman's algorithm showed the highest correlation for the green and red edge bands, with  $r$  values of 0.90 and 0.92, respectively. However, it had low  $r$  values for the blue and red bands, with 0.32 and 0.71, respectively. The RMSD values for Goodman were relatively low across all bands, ranging from 0.002 to 0.005. Similarly, the Hedley algorithm consistently performed well across all bands, with  $r$  values ranging from 0.58 to 0.88. The RMSD values were similar to those of Goodman, ranging from 0.003 to 0.005.

The Joyce and Lyzenga algorithms showed matching performances, with lower  $r$  values and higher RMSD and bias values compared to Goodman and Hedley. The  $r$  values ranged from 0.27 to 0.69 for Joyce and from 0.26 to 0.67 for Lyzenga. The RMSD values ranged from 0.006 to 0.007 for both algorithms.

The control group with no correction applied showed moderate  $r$  values, ranging from 0.41 to 0.81. The RMSD values were similar to those of Goodman and Hedley, ranging from 0.005 to 0.006.

### 3.2. Validation of QAA SD Model

The performance of the QAA model's (Figure 7) ability to predict SD when compared with in situ measurements showed a relatively high correlation across all methods, with  $r$  ranging from 0.74 (threshold-removed glint) to 0.92 (Hedley glint correction). RMSD (from 0.65 to 1.05 m) and bias (from  $-0.78$  to 0.58 m) showed acceptable results for all methods as well.

Comparing methods between themselves, the accuracy of all parameters had similar trends as accuracy for band comparison with in situ measurements (Section 2.1), where the SD values were overestimated for the smaller SD values and underestimated for the larger ones, except for Goodman's method, where most of the SD values were overestimated.

Hedley's sun-glint-corrected images achieved the best results according to the RMSD measures (0.65 m), while  $r$  was just slightly smaller (0.91) than with Goodman's method (0.92), which achieved the best results based on the  $r$  value of 0.92. However, the RMSD value for Goodman's method was relatively high (1.00 m) compared to the values of other methods. This method overestimated most of the values for both small and large SD values.

The Joyce and Lyzenga methods showed similar results between themselves with  $r$  values of 0.87 and 0.85, respectively. The RMSD values for Joyce and Lyzenga were 0.79 and 0.86 m, respectively, and biases showed underestimation.

The worst-performing method was when only sun-glint-affected pixels were removed and all other pixels were left unchanged ( $r = 0.75$ , RMSD = 1.05 m, bias = 0.13 m). The control group with no correction showed slightly better results:  $r$  value of 0.89, RMSD value of 0.74 m and underestimation according to bias.

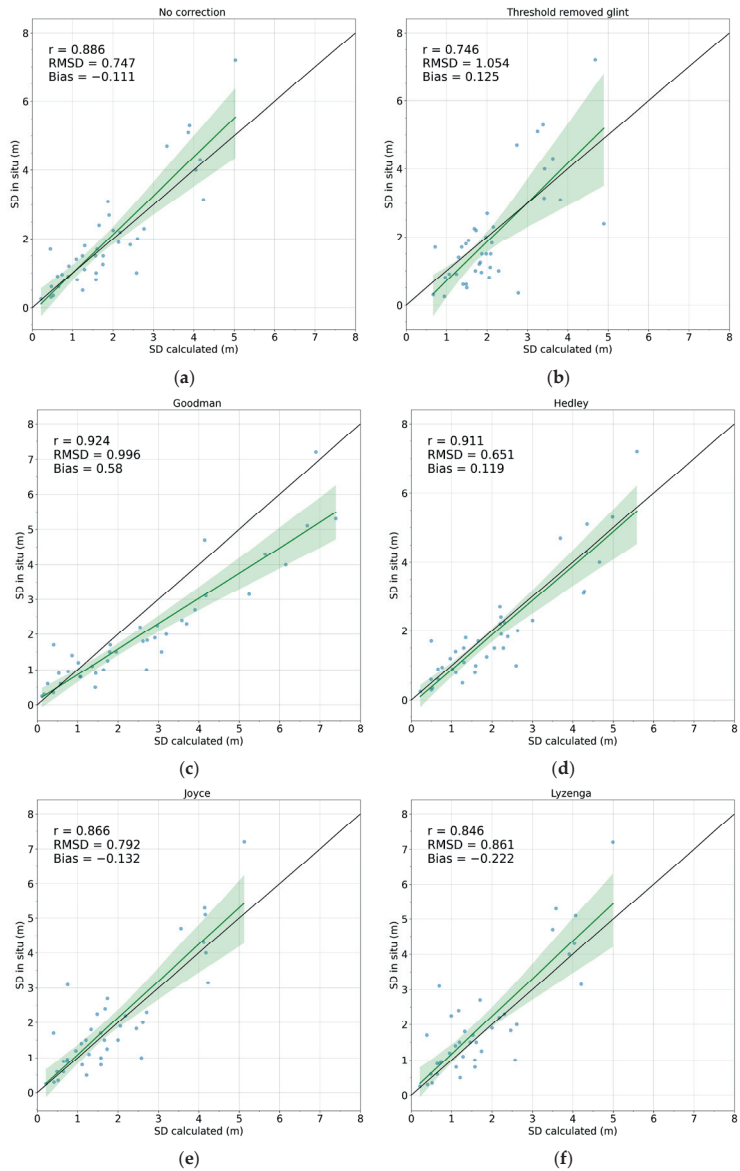


**Figure 7.** Scatterplots with linear regression line and 95% degrees of freedom (green) of modeled and in situ SD. Best-fit line (1:1) (black) for each image dataset, using different preprocessing methods: (a) no correction, (b) threshold-removed glint, (c) Goodman, (d) Hedley, (e) Joyce, (f) Lyzenga ( $n = 39$ ).

### 3.3. Relation with Water Constituents

The average in situ SD of the lakes was  $1.91 \pm 1.53$  m ( $\pm$ standard deviation), ranging from a minimum of 0.25 to a maximum of 7.2 m. The mean CDOM was  $2.95 \pm 3.2$   $\text{m}^{-1}$  (min–max: 0.37–20.01  $\text{m}^{-1}$ ), the mean Chl-a concentration  $26.59 \pm 26.48$  (1.13–113.23) and the mean turbidity  $6.76 \pm 11.8$  NTU (0.00–70.62 NTU).

The environmental factors in GAMs significantly explained (38.3%) the variance in the difference in SD measurements. The interaction term of the sun zenith angle and CDOM was significant ( $F = 6.808$ ,  $p$ -value  $< 0.05$ ), suggesting that these factors together affect the accuracy of SD retrieval (Figure 8). The most important and statistically significant factor was CDOM ( $F = 10.47$ ,  $p < 0.05$ ), followed by the solar zenith ( $F = 4.84$ ,  $p = 0.02$ ). Chl-a values did not have a significant effect on the GAM model ( $F = 0.295$ ,  $p = 0.59$ ).

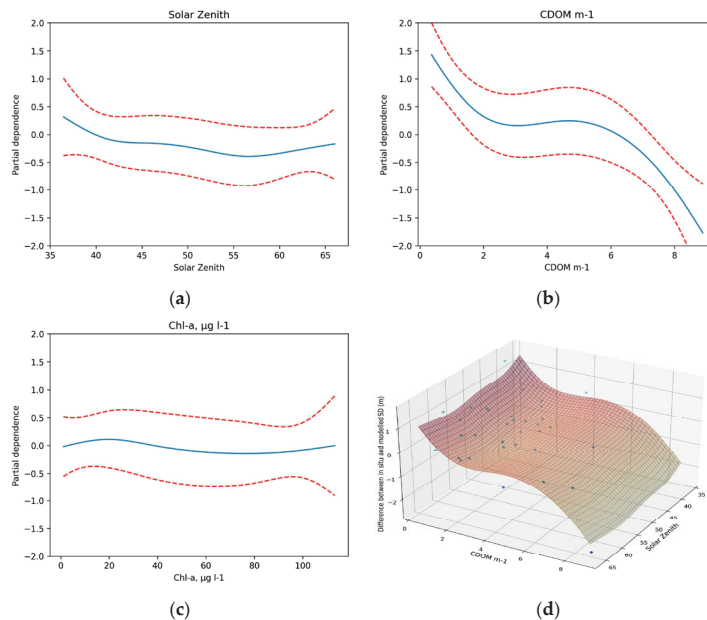


**Figure 8.** GAMs fitted smooth lines (blue lines) between the difference in SD (modeled vs. in situ) and graphs for each independent environmental factor: (a) solar zenith (b) CDOM (c) Chl-a and (d) interaction plot of solar zenith angle, CDOM and predicted difference plane between in situ and modeled SD (m). The red dashed lines show a 95% confidence interval for fitted lines.

In the residual plots of the model a random scatter of points was observed (Figure 9), with no discernible pattern or trend. This scatter indicates that the residuals have a constant variance, which suggests homoscedasticity. The absence of any systematic structure or pattern in the residuals reinforces the notion that nonlinear relationships assumed by our model are an adequate representation of this dataset. Additionally, we did not identify any significant outliers that could unduly influence our model's predictions.

The modeled SD values were overestimated (to over 1.3 m) when CDOM values were  $< 7.5$   $\text{m}^{-1}$ , while underestimated (over 1 m) when CDOM was  $> 7.5$  (although underestimation did not significantly change when CDOM  $> 12$ ). For the solar zenith, the SD values were overestimated (over 0.7 m) at the lower solar zenith angles ( $< 45$  degrees), and then a relatively low effect (within  $\pm 0.5$  m) was between 45 and 75 degrees of the solar zenith

angle and the underestimation sharply increased to over 1.5 m when the solar zenith angle was >75 degrees.

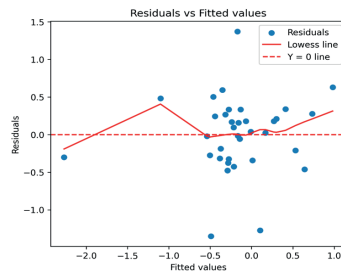


**Figure 9.** A scatterplot of residuals and fitted values with the red line presenting the best fit and dashed red line representing the  $Y = 0$  line.

## 4. Discussion

### 4.1. Advancements in SD Measurements

This research focused on evaluating the effectiveness of the QAA for determining SD using a multispectral camera onboard UAVs. This novel approach expands the current understanding of measuring SD by introducing the potential use of UAVs, balancing the broad coverage provided by remote sensing methods with the high accuracy characteristic of in situ measurements, thereby serving as a more comprehensive alternative to traditional methods.

The experimental results did not uniformly support our hypothesis that the application of sun-glint correction methods would enhance the utility of multispectral images in SD modeling by reducing the RMSD by about 5% and reducing the bias by a similar amount. The precision observed across all bands appears to correspond with the spectral band reflectance intensity, where bands demonstrating relatively lower reflectance intensity (e.g., blue band) typically displayed a lower compliance between the reflectance measured from the UAV and the in situ reflectance measurements and the reverse held true for bands with relatively higher reflectance intensity. Environmental factors such as weak water surface signal and roughness of the water surface can introduce systematic and random errors, respectively, into water surface detection [13]. The correlation with the blue was identified as the least robust (Figure 7), which can be ascribed to increased vulnerability to scattering, a trait inherent to these bands in the water environment [61].

Among the tested glint correction methods, the Hedley and Goodman methods emerged as the most effective across all bands, with Hedley demonstrating the lowest RMSD across all bands. For instance, a study conducted by M Muslim et al. [36] employed a similar methodology to our study, testing multiple sun-glint correction methods. Their findings indicated that the Lyzenga method yielded the most accurate results. However, it is important to note that the primary objective of their research was to map coral reefs, and in most of the study area, the bottom was visible, which may have influenced their results. In contrast, Windle and Silsbe [18] found that the Hedley method provided the highest correlation coefficient ( $r$ ) and the lowest RMSD, corresponding closely with the results of our study.

The key distinction between the three glint correction methods (excluding the Goodman method) lies in the slope or covariance index of NIR band values. In the case of the Hedley method, the slope was the largest, as it takes the minimum value of the band as the starting point, as opposed to the mode (Joyce method) or the mean (Lyzenga method) [38–40]. This suggests that the images used in our study required a larger numeric correction due to the lowest initial reflectance values.

The results showed that the Goodman's method reflectance intensity values tend to be significantly different from other methods for the blue, red and red edge bands. This method, which was ranked as the second-best-performing in our study, adopted a different approach, using constant values to correct for the sun-glint effect [41]. This approach led to overall better  $r$  values between in situ and the green, red, and red edge bands onboard the UAV. However, the performance of the blue band was significantly lower than when using the Hedley method. Despite this, the Goodman method demonstrated the lowest RMSD values and small overestimation bias, underscoring its effectiveness in applications where low reflectance intensity deviation from in situ radiometer is required.

The results also indicated that applying glint correction to the entire image rather than just the binary thresholded area can yield better results in terms of the overall accuracy of the reflectance values. This observation implies that the method of applying glint correction solely to the binary thresholded area might not be the most effective strategy, as it may overlook potential glint effects present beyond this area. Additional sun-glint correction research should be considered in the future for better generalization of reflectance correction [62].

The overall agreement between the in situ SD measurements and the modeled SD values might be connected to their handling of in-water constituents such as colored dissolved organic matter (CDOM) and solar zenith angles, which significantly influenced the accuracy of the models. CDOM was found to predominantly influence the discrepancies between in situ measurements and modeled SD. Given that CDOM primarily absorbs light in the ultraviolet (UV) and blue regions of the spectrum, resulting in a relatively low acquired signal by sensor [63], this agrees with our observation that the blue band demonstrated one of the weakest correlations between in situ and UAV-derived reflectance measurements [64]. It is plausible that Goodman's and Hedley's methods more effectively managed this factor, where Hedley's had the highest  $r$  and Goodman's had the lowest RMSD for blue band reflectance, resulting in a closer match with in situ values. Another potential interference is bottom reflection, particularly in clear waters, where the difference between the SD and the actual water depth is minimal. While the SD was consistently less than the water body depth in our study, situations where this difference is minimal could lead to bottom influences on the measurements.

Similarly, high solar zenith angles above  $70^\circ$  impacted the accuracy of modeled SD, leading to underestimations by up to 1.5 m. This is likely due to increased scattering and absorption of light at higher zenith angles, resulting in less light reaching the water's surface and thus larger differences between modeled and in situ SD values [65]. This reinforces the need for sophisticated algorithms that can accurately model these complex environmental factors in SD predictions.

#### 4.2. Practical Applications

Accurate SD determination in large areas is particularly important given the increasing demand for high-resolution data on water transparency for applications including water resource management, environmental monitoring, and ecological modeling [66]. Measures of SD can reduce the need for boat measurements in lakes, also allowing for data collection at a higher frequency, surpassing traditional monthly monitoring intervals that may be inadequate for dynamic water bodies with recurring algal blooms, which in some cases can be inaccessible due to terrain or vegetation around the lake [67]. UAVs could also be used in shallow coastal waters (<1.5 m), where a research vessel usually cannot access them, e.g., in the Curonian Lagoon [68].

The optimal fit model using Hedley sun-glint correction on the whole image was used to construct a mosaic from 45 individual images (Figure 10) of Kašučiu Lake on 20 September 2021. All of the pixels were left unmasked to show how shadows affect the final results, and therefore this aspect should be taken into consideration while planning the acquisitions.

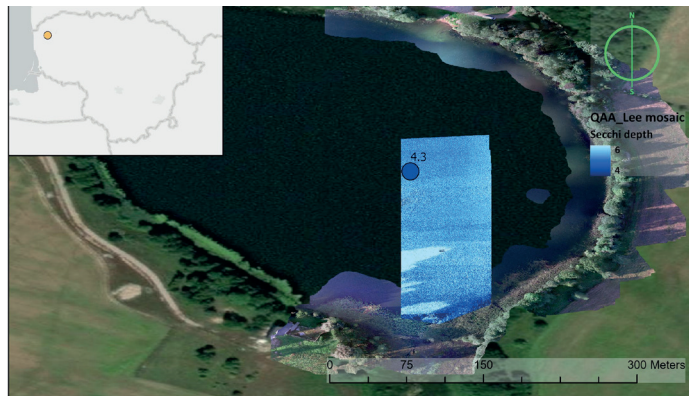


**Figure 10.** An SD transect of 45 mosaiced images in Kašučių Lake 20 September 2021. The dot with color represents in situ SD of 4.3 m.

This example shows the efficacy of the QAA best-fit model in transforming discrete data into a coherent, large-scale representation of SD. The SD varied from 4 to 6 m, where the highest values were determined in the areas covered by tree shadows. Elsewhere, SD values were more homogeneous (4.0 to 4.8 m), but some noise was still apparent in the orthomosaic (snow-like effect), as SD values are calculated for each pixel. For this reason, the mean value of the whole image was compared to in situ measurements in the area, instead of selecting a small square or point in the images, which would have resulted in lower accuracies.

This method has potential applications in shaping policies and regulations related to water bodies. With the methods provided in this paper, processing workflow for one 5 ha lake should not take longer than 20 min. Moreover, this process can be fully automated, requiring only the supervision of the final results. To put this into context, Lithuania has around 6000 lakes, and about 340 of them are larger than 5 ha [69], which would be suitable for monitoring using a Sentinel-2 satellite, assuming that the shape is not elongated. The rest of the smaller lakes could be monitored by applying methodology from this study and potentially could improve the accuracy and coverage of current national monitoring conducted by the Environmental Protection Agency, which currently covers around 80 lakes every 6 years in Lithuania.

#### 4.3. Future Research and Potential Limitations

The QAA model possesses the flexibility to process remote sensing data sourced from an array of sensors, including but not limited to MODIS, MERIS, OLCI, MSI and GOCI. By integrating a more diverse set of global in situ measurements corresponding to various water types, it is conceivable to further refine the precision and effectiveness of the QAA model.

While the research results demonstrate potential, it is essential to emphasize that the investigation was conducted across a broad range of unique aquatic environments and included measurements captured under variable sun zenith angles. Consequently, for future work, there is potential to modify the existing QAA used for SD estimations to better account for CDOM and sun zenith angle, which in this study have been shown to be critical parameters. This modification could improve our understanding and predictions in the context of diverse and changeable aquatic conditions. Several limitations need to be addressed in future research. One of the main limitations is the assumption of linearity in the Hedley method. This method requires at least one dark pixel unaffected by glint [40] to



be visible in the image, and if the whole image is affected by glint, this deglinting method will provide incorrect data. Understanding these limitations aids in contextualizing the results and fosters the development of more refined glint correction methodologies in the future. This is also relevant for a partial cloud glint when clouds are reflected from the water surface in some, but not all areas of the image, for the analysis of multispectral drone imagery [40,70]. Most methodological studies on water surface mapping using UAVs suggest careful planning of flight time, preferably during conditions of clear skies and low sun glint [37]; however, this restricts one of the main advantages of UAVs—obtaining data on demand—especially if there is a need to visit several inland water bodies on the same day.

Many studies underscore the importance of choosing the appropriate quasi-analytical algorithm (QAA) for different optical water types [13,29,34]. The optical properties of coastal and inland waters, which are primarily influenced by the concentrations of suspended particulate matter, phytoplankton, and dissolved organic material, exhibit spatial and temporal variability, leading to diverse optical water types [71,72]. Applying a universal algorithm in these optically complex waters often results in significant uncertainties [71,72]. This insight highlights the importance of optical water classification to enhance retrieval accuracy, as indicated by numerous studies that developed class-specific algorithms for bio-optical parameters and achieved improvements by applying optical classification in the retrieval of these parameters [72–75]. In our study, relatively high concentrations of CDOM significantly affected the optical properties of the water, thereby introducing uncertainties in the results. One possible approach to improve the accuracy of the QAA is to calibrate the algorithm for the CDOM-dominated water bodies.

In addition to the aforementioned limitations, another significant challenge to consider is the interference of high-vegetation pixels in the analysis of multispectral drone imagery [76]. Vegetation and their shadows, especially when in close proximity to water bodies, can skew the reflectance measurements and thus influence the accuracy of Secchi depth estimates. Consequently, implementing strategies to exclude these pixels during image analysis can enhance the reliability of the measurements.

The applicability of water parameters extends beyond SD, allowing for the calculation of additional parameters. Prior research has demonstrated the feasibility of employing multispectral UAVs for turbidity [77–79], Chl-a [77,79–81], CDOM [79], TSS [80,82], cyanobacteria [80] and macrophytes [16,53,83]. Given the inherent scalability of the UAV-based methodology, it stands as a promising tool for extensive SD assessments and water quality surveys, thereby facilitating large-scale studies focused on water transparency. This advancement brings us a step closer to exploiting the full potential of UAV-based remote sensing for assessing and monitoring aquatic environments.

## 5. Conclusions

This study revealed that the accuracy of SD measurements is profoundly influenced by sun-glint correction methods employed in UAV flights. There was a consistent agreement across all methods and the in situ radiometric data, particularly for the green band, emphasizing the robustness of multispectral UAV image data. Among the tested methods, Hedley's method demonstrated superior accuracy (RMSD = 0.65 m) and precision, thereby significantly contributing to the accuracy of the UAV-derived SD data.

Moreover, findings underscored the significant role of environmental factors, particularly the CDOM and solar zenith angle, causing inaccuracies in SD measurements: a solar zenith angle  $> 70^\circ$  resulted in an underestimation of up to 1.5 m in modeled SD, while CDOM  $> 12 \text{ m}^{-1}$  caused similar underestimations. Our research, therefore, supports the use of UAVs equipped with multispectral cameras as a viable method for SD determination in inland water bodies with SD of up to 7 m and lower than  $12 \text{ m}^{-1}$  CDOM. The results point towards an approach capable of reaching a correlation as high as 0.91 and reducing the RMSD by up to 12.85% (Hedley's method), thereby enhancing the versatility and reliability of SD measurements.

**Supplementary Materials:** The following supporting information can be downloaded at <https://www.mdpi.com/article/10.3390/drones7090546/s1>. Table S1. Summary of investigated lakes and reservoirs in Lithuania. Descriptive statistics of in situ-measured SD, chlorophyll-a, CDOM and turbidity.

**Author Contributions:** E.T.: conceptualization, methodology, software, validation, formal analysis, investigation, resources, data curation, writing—original draft, writing—review and editing, visualization, supervision; M.B.: conceptualization, methodology, validation, investigation, resources, data curation, writing—review and editing, supervision; D.V.: conceptualization, validation, investigation, resources, data curation, writing—review and editing, supervision; J.G.: conceptualization, validation, investigation, resources, writing—review and editing; I.B.: resources, data curation, funding acquisition. All authors have read and agreed to the published version of the manuscript.

**Funding:** This research was supported by a doctorate scholarship program in Ecology and Environmental Sciences at Klaipėda University, Lithuania. The field campaigns were cofunded by the Environmental Protection Agency contract “Assessment of the water condition and its more efficient management of the remote monitoring data collection, processing, use and storage system, to ensure accurate results (NUOTOLIS)” (grant 28T-2021-64/SUT-21P-20).

**Data Availability Statement:** The data presented in this study are available on request from the corresponding author.

**Conflicts of Interest:** The authors declare no conflict of interest.

## References

1. Cloern, J.E.; Abreu, P.C.; Carstensen, J.; Chauvaud, L.; Elmgren, R.; Grall, J.; Greening, H.; Johansson, J.O.R.; Kahru, M.; Sherwood, E.T.; et al. Human Activities and Climate Variability Drive Fast-Paced Change across the World’s Estuarine–Coastal Ecosystems. *Glob. Chang. Biol.* **2016**, *22*, 513–529. [[CrossRef](#)] [[PubMed](#)]
2. MacKay, M.D.; Neale, P.J.; Arp, C.D.; De Senerpont Domis, L.N.; Fang, X.; Gal, G.; Jöhnk, K.D.; Kirillin, G.; Lenters, J.D.; Litchman, E.; et al. Modeling Lakes and Reservoirs in the Climate System. *Limnol. Oceanogr.* **2009**, *54*, 2315–2329. [[CrossRef](#)]
3. Paerl, H.W. Nuisance Phytoplankton Blooms in Coastal, Estuarine, and Inland Waters1. *Limnol. Oceanogr.* **1988**, *33*, 823–843. [[CrossRef](#)]
4. European Parliament, Council of the European Union. *Directive 2000/60/EC of the European Parliament and of the Council of 23 October 2000 Establishing a Framework for Community Action in the Field of Water Policy*; European Environment Agency: Luxembourg, 2000.
5. Aas, E.; Høkedal, J.; Sørensen, K. Secchi Depth in the Oslofjord–Skagerrak Area: Theory, Experiments and Relationships to Other Quantities. *Ocean Sci.* **2014**, *10*, 177–199. [[CrossRef](#)]
6. Ibelings, B.W.; Portielje, R.; Lammens, E.H.R.R.; Noordhuis, R.; Van Den Berg, M.S.; Joosse, W.; Meijer, M.L. Resilience of Alternative Stable States during the Recovery of Shallow Lakes from Eutrophication: Lake Veluwe as a Case Study. *Ecosystems* **2007**, *10*, 4–16. [[CrossRef](#)]
7. Schultze-Lam, S.; Schultze-Lam, S.; Beveridge, T.J.; Des Marais, D.J. Whiting Events: Biogenic Origin Due to the Photosynthetic Activity of Cyanobacterial Picoplankton. *Limnol. Oceanogr.* **1997**, *42*, 133–141. [[CrossRef](#)]
8. Spyros, E.; O’Donnell, R.; Hunter, P.D.; Miller, C.; Scott, M.; Simis, S.G.H.; Neil, C.; Barbosa, C.C.F.; Binding, C.E.; Bradt, S.; et al. Optical Types of Inland and Coastal Waters. *Limnol. Oceanogr.* **2018**, *63*, 846–870. [[CrossRef](#)]
9. Jiang, H. Research on Transparency Derived from Remote Sensing and Its Spatial-Temporal Changes in Poyang Lake. *China Rural. Water Hydropower* **2012**, *1*, 30–33.
10. Yu, D.F.; Xing, Q.G.; Lou, M.J.; Shi, P. Retrieval of Secchi Disk Depth in the Yellow Sea and East China Sea Using 8-Day MODIS Data. *IOP Conf. Ser. Earth Environ. Sci.* **2014**, *17*, 012112. [[CrossRef](#)]
11. Pham, T.N.; Ho, A.P.H.; Nguyen, T.V.; Nguyen, H.M.; Truong, N.H.; Huynh, N.D.; Nguyen, T.H.; Dung, L.T. Development of a Solar-Powered IoT-Based Instrument for Automatic Measurement of Water Clarity. *Sensors* **2020**, *20*, 2051. [[CrossRef](#)]
12. Stock, A. Satellite Mapping of Baltic Sea Secchi Depth with Multiple Regression Models. *Int. J. Appl. Earth Obs. Geoinf.* **2015**, *40*, 55–64. [[CrossRef](#)]
13. Wang, D.; Xing, S.; He, Y.; Yu, J.; Xu, Q.; Li, P. Evaluation of a New Lightweight UAV-Borne Topo-Bathymetric LiDAR for Shallow Water Bathymetry and Object Detection. *Sensors* **2022**, *22*, 1379. [[CrossRef](#)] [[PubMed](#)]
14. Manfreda, S.; McCabe, M.F.; Miller, P.E.; Lucas, R.; Pajuelo Madrigal, V.; Mallinis, G.; Ben Dor, E.; Helman, D.; Estes, L.; Cirraolo, G.; et al. On the Use of Unmanned Aerial Systems for Environmental Monitoring. *Remote Sens.* **2018**, *10*, 641. [[CrossRef](#)]
15. Flynn, K.; Chapra, S. Remote Sensing of Submerged Aquatic Vegetation in a Shallow Non-Turbid River Using an Unmanned Aerial Vehicle. *Remote Sens.* **2014**, *6*, 12815–12836. [[CrossRef](#)]
16. Müllerová, J.; Gago, X.; Bučas, M.; Company, J.; Estrany, J.; Fortesa, J.; Manfreda, S.; Michez, A.; Mokroš, M.; Paulus, G.; et al. Characterizing Vegetation Complexity with Unmanned Aerial Systems (UAS)—A Framework and Synthesis. *Ecol. Indic.* **2021**, *131*, 108156. [[CrossRef](#)]

17. Yang, S.; Wang, J.; Wang, P.; Gong, T.; Liu, H. Low Altitude Unmanned Aerial Vehicles (UAVs) and Satellite Remote Sensing Are Used to Calculated River Discharge Attenuation Coefficients of Ungauged Catchments in Arid Desert. *Water* **2019**, *11*, 2633. [[CrossRef](#)]
18. Windle, A.E.; Silsbe, G.M. Evaluation of Unoccupied Aircraft System (UAS) Remote Sensing Reflectance Retrievals for Water Quality Monitoring in Coastal Waters. *Front. Environ. Sci.* **2021**, *9*, 674247. [[CrossRef](#)]
19. Yunlin, Z. Distribution, Seasonal Variation and Correlation Analysis of the Transparency in Taihu Lake. *Trans. Oceanol. Limnol.* **2003**, *96*, 36–39.
20. Rahman, A.; Maulud, K.N.A.; Mohd, F.; Jaafar, O.; Tahar, K.N. Volumetric Calculation Using Low Cost Unmanned Aerial Vehicle (UAV) Approach. *IOP Conf. Ser. Mater. Sci. Eng.* **2017**, *270*, 012032. [[CrossRef](#)]
21. Otsu, K.; Pla, M.; Vayreda, J.; Brotóns, L. Calibrating the Severity of Forest Defoliation by Pine Processionary Moth with Landsat and UAV Imagery. *Sensors* **2018**, *18*, 3278. [[CrossRef](#)]
22. Zhang, H.; Sun, Y.; Chang, L.-D.; Qin, Y.; Chen, J.; Qin, Y.; Du, J.; Yi, S.; Wang, Y. Estimation of Grassland Canopy Height and Aboveground Biomass at the Quadrat Scale Using Unmanned Aerial Vehicle. *Remote Sens.* **2018**, *10*, 851. [[CrossRef](#)]
23. Castagna, A.; Amadei Martínez, L.; Bogorad, M.; Daveloose, I.; Dasseville, R.; Dierssen, H.M.; Beck, M.; Mortelmans, J.; Lavigne, H.; Dogliotti, A.; et al. Optical and Biogeochemical Properties of Belgian Inland and Coastal Waters. *Earth Syst. Sci. Data* **2022**, *14*, 2697–2719. [[CrossRef](#)]
24. Garaba, S.P.; Friedrichs, A.; Voß, D.; Zielinski, O. Classifying Natural Waters with the Forel-Ule Colour Index System: Results, Applications, Correlations and Crowdsourcing. *Int. J. Environ. Res. Public Health* **2015**, *12*, 16096–16109. [[CrossRef](#)] [[PubMed](#)]
25. Giardino, C.; Bresciani, M.; Stroppiana, D.; Oggioni, A.; Morabito, G. Optical Remote Sensing of Lakes: An Overview on Lake Maggiore. *J. Limnol.* **2013**, *73*, 201–214. [[CrossRef](#)]
26. Anuar, N.N.M.; Fauzi, N.F.; Halim, H.; Khairudin, N.I.; Bakhtiar, N.S.A.; Shafii, N.H.B. Implementation of Long-Short Term Memory Neural Network (LSTM) for Predicting the Water Quality Parameters in Sungai Selangor. *J. Comput. Res. Innov.* **2021**, *6*, 40–49. [[CrossRef](#)]
27. Coskun, H.G.; Tanik, A.; Alganci, U.; Cigizoglu, H.K. Determination of Environmental Quality of a Drinking Water Reservoir by Remote Sensing, GIS and Regression Analysis. *Water Air Soil Pollut.* **2008**, *194*, 275–285. [[CrossRef](#)]
28. Chusnah, W.N.; Chu, H.-J. Estimating Chlorophyll-a Concentrations in Tropical Reservoirs from Band-Ratio Machine Learning Models. *Remote Sens. Appl. Soc. Environ.* **2022**, *25*, 100678. [[CrossRef](#)]
29. Zhang, Y.; Zhang, Y.; Shi, K.; Zhou, Y.; Li, N. Remote Sensing Estimation of Water Clarity for Various Lakes in China. *Water Res.* **2021**, *192*, 116844. [[CrossRef](#)]
30. Lee, Z.; Shang, S.; Hu, C.; Du, K.; Weidemann, A.; Hou, W.; Lin, J.; Lin, G. Secchi Disk Depth: A New Theory and Mechanistic Model for Underwater Visibility. *Remote Sens. Environ.* **2015**, *169*, 139–149. [[CrossRef](#)]
31. Jiang, D.; Matsushita, B.; Setiawan, F.; Vundo, A. An Improved Algorithm for Estimating the Secchi Disk Depth from Remote Sensing Data Based on the New Underwater Visibility Theory. *ISPRS J. Photogramm. Remote Sens.* **2019**, *152*, 13–23. [[CrossRef](#)]
32. Wei, L.; Wang, Z.; Huang, C.; Zhang, Y.; Wang, Z.; Xia, H.; Cao, L. Transparency Estimation of Narrow Rivers by UAV-Borne Hyperspectral Remote Sensing Imagery. *IEEE Access* **2020**, *8*, 168137–168153. [[CrossRef](#)]
33. Chen, J.; Han, Q.; Chen, Y.; Li, Y. A Secchi Depth Algorithm Considering the Residual Error in Satellite Remote Sensing Reflectance Data. *Remote Sens.* **2019**, *11*, 1948. [[CrossRef](#)]
34. Qing, S.; Cui, T.; Lai, Q.; Bao, Y.; Diao, R.; Yue, Y.; Hao, Y. Improving Remote Sensing Retrieval of Water Clarity in Complex Coastal and Inland Waters with Modified Absorption Estimation and Optical Water Classification Using Sentinel-2 MSI. *Int. J. Appl. Earth Obs. Geoinf.* **2021**, *102*, 102377. [[CrossRef](#)]
35. De Keukelaere, L.; Moelans, R.; Knaeps, E.; Sterckx, S.; Reusen, I.; De Munck, D.; Simis, S.G.H.; Constantinescu, A.M.; Scricciu, A.; Katsouras, G.; et al. Airborne Drones for Water Quality Mapping in Inland, Transitional and Coastal Waters—MapEO Water Data Processing and Validation. *Remote Sens.* **2023**, *15*, 1345. [[CrossRef](#)]
36. Muslim, A.M.; Wei Sheng, C.; Che Din, M.S.; Khalil, I.; Hossain, M. Coral Reef Mapping of UAV: A Comparison of Sun Glint Correction Methods. *Remote Sens.* **2019**, *11*, 2422. [[CrossRef](#)]
37. Joyce, K.E.; Duce, S.; Leahy, S.M.; Leon, J.; Maier, S.W. Principles and Practice of Acquiring Drone-Based Image Data in Marine Environments. *Mar. Freshw. Res.* **2019**, *70*, 952. [[CrossRef](#)]
38. Lyzenga, D.R.; Malinas, N.P.; Tanis, F.J. Multispectral Bathymetry Using a Simple Physically Based Algorithm. *IEEE Trans. Geosci. Remote Sens.* **2006**, *44*, 2251–2259. [[CrossRef](#)]
39. Joyce, K.E. A Method for Mapping Live Coral Cover Using Remote Sensing. Ph.D. Thesis, The University of Queensland, Brisbane, QLD, Australia, 2005.
40. Hedley, J.D.; Harborne, A.R.; Mummy, P.J. Technical Note: Simple and Robust Removal of Sun Glint for Mapping Shallow-water Benthos. *Int. J. Remote Sens.* **2005**, *26*, 2107–2112. [[CrossRef](#)]
41. Goodman, J.A.; Lee, Z.; Ustin, S.L. Influence of Atmospheric and Sea-Surface Corrections on Retrieval of Bottom Depth and Reflectance Using a Semi-Analytical Model: A Case Study in Kaneohe Bay, Hawaii. *Appl. Opt.* **2008**, *47*, F1. [[CrossRef](#)]
42. Hochberg, E.J.; Andréfouët, S.; Tyler, M.R. Sea Surface Correction of High Spatial Resolution Ikonos Images to Improve Bottom Mapping in Near-Shore Environments. *IEEE Trans. Geosci. Remote Sens.* **2003**, *41*, 1724–1729. [[CrossRef](#)]
43. Hooker, S.B.; Firestone, E.R.; McClain, C.R.; Esaias, W.E.; Barnes, W.; Guenther, B.; Endres, D.; Mitchell, B.G.; Barnes, R. *SeaWiFS Calibration and Validation Plan, Volume 3*; NASA: Washington, DC, USA, 1992.

44. User Guide for MicaSense Sensors. Available online: <https://support.micasense.com/hc/en-us/articles/360039671254-User-Guide-for-MicaSense-Sensors> (accessed on 13 March 2023).
45. Preisendorfer, R.W. Secchi Disk Science: Visual Optics of Natural Waters1. *Limnol. Oceanogr.* **1986**, *31*, 909–926. [[CrossRef](#)]
46. Jeffrey, S.W.; Humphrey, G.F. New Spectrophotometric Equations for Determining Chlorophylls a, b, C1 and C2 in Higher Plants, Algae and Natural Phytoplankton. *Biochem. Physiol. Pflanz.* **1975**, *167*, 191–194. [[CrossRef](#)]
47. Parsons, T.R.; Maita, Y.; Lalli, C.M. A Manual of Chemical and Biological Methods for Sea Water Analysis. *Deep Sea Res. Part A Oceanogr. Res. Pap.* **1984**, *31*, 1523. [[CrossRef](#)]
48. Kirk, J. Light and Photosynthesis in Aquatic Systems. In *Light and Photosynthesis in Aquatic Ecosystems*, 3rd ed.; Cambridge University Press: Cambridge, UK, 2010; Volume VI, pp. 1–651. [[CrossRef](#)]
49. Hommersom, A.; Kratzer, S.; Laanen, M.; Ansko, I.; Ligi, M.; Bresciani, M.; Giardino, C.; Beltran-Abauza, J.M.; Moore, G.; Wernand, M.R.; et al. Intercomparison in the Field between the New WISP-3 and Other Radiometers (TriOS Ramses, ASD FieldSpec, and TACCS). *JARS* **2012**, *6*, 063615. [[CrossRef](#)]
50. Mobley, C. Estimation of the Remote-Sensing Reflectance from Above-Surface Measurements. *Appl. Opt.* **2000**, *38*, 7442–7455. [[CrossRef](#)] [[PubMed](#)]
51. Qiu, R.; Wang, S.; Shi, J.; Shen, W.; Zhang, W.; Zhang, F.; Li, J. Sentinel-2 MSI Observations of Water Clarity in Inland Waters across Hainan Island and Implications for SDG 6.3.2 Evaluation. *Remote Sens.* **2023**, *15*, 1600. [[CrossRef](#)]
52. Wang, D.; Ma, R.; Xue, K.; Loiselle, S.A. The Assessment of Landsat-8 OLI Atmospheric Correction Algorithms for Inland Waters. *Remote Sens.* **2019**, *11*, 169. [[CrossRef](#)]
53. Tiškus, E.; Vaičiūtė, D.; Bučas, M.; Gintauskas, J. Evaluation of Common Reed (*Phragmites Australis*) Bed Changes in the Context of Management Using Earth Observation and Automatic Threshold. *Eur. J. Remote Sens.* **2023**, *56*, 2161070. [[CrossRef](#)]
54. Yen, J.-C.; Chang, F.-J.; Chang, S. A New Criterion for Automatic Multilevel Thresholding. *IEEE Trans. Image Process.* **1995**, *4*, 370–378. [[CrossRef](#)]
55. Bishop Pytz Python Historical Timezone Library and Database. Available online: <https://github.com/stub42/pytz> (accessed on 3 April 2023).
56. Wood, S.N. Fast Stable Restricted Maximum Likelihood and Marginal Likelihood Estimation of Semiparametric Generalized Linear Models. *J. R. Stat. Soc. Ser. B Stat. Methodol.* **2011**, *73*, 3–36. [[CrossRef](#)]
57. Wood, S.N. *Generalized Additive Models: An Introduction with R*; CRC Press: Boca Raton, FL, USA, 2017. [[CrossRef](#)]
58. Wickham, H. *Ggplot2: Elegant Graphics for Data Analysis*; Springer: New York, NY, USA, 2009; ISBN 978-0-387-98140-6.
59. QGIS Version 3.16. Available online: <https://qgis.org/en/site/> (accessed on 20 July 2023).
60. Drone Mapping Software. Available online: <https://www.opendronemap.org/> (accessed on 20 July 2023).
61. Zaneveld, J.R.V.; Barnard, A.H.; Boss, E. Theoretical Derivation of the Depth Average of Remotely Sensed Optical Parameters. *Opt. Express* **2005**, *13*, 9052. [[CrossRef](#)] [[PubMed](#)]
62. Overstreet, B.; Legleiter, C. Removing Sun Glint from Optical Remote Sensing Images of Shallow Rivers: Removing Sun Glint from River Imagery. *Earth Surf. Process. Landf.* **2016**, *42*, 318–333. [[CrossRef](#)]
63. Warren, M.; Simis, S.; Martinez-Vicente, V.; Poser, K.; Bresciani, M.; Alikas, K.; Spyarakos, E.; Giardino, C.; Ansper, A. Assessment of Atmospheric Correction Algorithms for the Sentinel-2A MultiSpectral Imager over Coastal and Inland Waters. *Remote Sens. Environ.* **2019**, *225*, 267–289. [[CrossRef](#)]
64. Mamaghani, B.; Salvaggio, C. Multispectral Sensor Calibration and Characterization for SUAS Remote Sensing. *Sensors* **2019**, *19*, 4453. [[CrossRef](#)] [[PubMed](#)]
65. Hashimoto, N.; Saito, Y.; Maki, M.; Homma, K. Simulation of Reflectance and Vegetation Indices for Unmanned Aerial Vehicle (UAV) Monitoring of Paddy Fields. *Remote Sens.* **2019**, *11*, 2119. [[CrossRef](#)]
66. Soullignac, F.; Vinçon-Leite, B.; Lemaire, B.J.; Scarati Martins, J.R.; Bonhomme, C.; Dubois, P.; Mezemate, Y.; Tchiguirinskaia, I.; Schertzer, D.; Tassin, B. Performance Assessment of a 3D Hydrodynamic Model Using High Temporal Resolution Measurements in a Shallow Urban Lake. *Environ. Model. Assess.* **2017**, *22*, 309–322. [[CrossRef](#)]
67. Alikas, K.; Kratzer, S. Improved Retrieval of Secchi Depth for Optically-Complex Waters Using Remote Sensing Data. *Ecol. Indic.* **2017**, *77*, 218–227. [[CrossRef](#)]
68. Tyrimų laivas „Vėjūnas“. Aplinkos Apsaugos Agentūra. Available online: <https://www.gamta.lt/apie-agentura/tyrimu-laivas-vejunas/45> (accessed on 20 July 2023).
69. Vaitekūnas, S.; Valančienė, E. *Lietuvos Geografija (Geography of Lithuania)*; Alma Litera: Vilnius, Lithuania, 2004.
70. Partama, I.G.Y.; Kanno, A.; Ueda, M.; Akamatsu, Y.; Inui, R.; Sekine, M.; Yamamoto, K.; Imai, T.; Higuchi, T. Removal of Water-Surface Reflection Effects with a Temporal Minimum Filter for UAV-Based Shallow-Water Photogrammetry. *Earth Surf. Process. Landf.* **2018**, *43*, 2673–2682. [[CrossRef](#)]
71. Le, C.; Li, Y.; Zha, Y.; Sun, D.; Huang, C.; Zhang, H. Remote Estimation of Chlorophyll a in Optically Complex Waters Based on Optical Classification. *Remote Sens. Environ.* **2011**, *115*, 725–737. [[CrossRef](#)]
72. Cui, T.W.; Zhang, J.; Wang, K.; Wei, J.W.; Mu, B.; Ma, Y.; Zhu, J.H.; Liu, R.J.; Chen, X.Y. Remote Sensing of Chlorophyll a Concentration in Turbid Coastal Waters Based on a Global Optical Water Classification System. *ISPRS J. Photogramm. Remote Sens.* **2020**, *163*, 187–201. [[CrossRef](#)]
73. Jackson, T.; Sathyendranath, S.; Mélin, F. An Improved Optical Classification Scheme for the Ocean Colour Essential Climate Variable and Its Applications. *Remote Sens. Environ.* **2017**, *203*, 152–161. [[CrossRef](#)]

74. Yu, X.; Lee, Z.; Shen, F.; Wang, M.; Wei, J.; Jiang, L.; Shang, Z. An Empirical Algorithm to Seamlessly Retrieve the Concentration of Suspended Particulate Matter from Water Color across Ocean to Turbid River Mouths. *Remote Sens. Environ.* **2019**, *235*, 111491. [[CrossRef](#)]
75. Zhang, F.; Li, J.; Shen, Q.; Zhang, B.; Tian, L.; Ye, H.; Wang, S.; Lu, Z. A Soft-Classification-Based Chlorophyll-a Estimation Method Using MERIS Data in the Highly Turbid and Eutrophic Taihu Lake. *Int. J. Appl. Earth Obs. Geoinf.* **2019**, *74*, 138–149. [[CrossRef](#)]
76. Doña, C.; Morant, D.; Picazo, A.; Rochera, C.; Sánchez, J.M.; Camacho, A. Estimation of Water Coverage in Permanent and Temporary Shallow Lakes and Wetlands by Combining Remote Sensing Techniques and Genetic Programming: Application to the Mediterranean Basin of the Iberian Peninsula. *Remote Sens.* **2021**, *13*, 652. [[CrossRef](#)]
77. McEliece, R.; Hinz, S.; Guarini, J.-M.; Coston-Guarini, J. Evaluation of Nearshore and Offshore Water Quality Assessment Using UAV Multispectral Imagery. *Remote Sens.* **2020**, *12*, 2258. [[CrossRef](#)]
78. Su, T.-C. A Study of a Matching Pixel by Pixel (MPP) Algorithm to Establish an Empirical Model of Water Quality Mapping, as Based on Unmanned Aerial Vehicle (UAV) Images. *Int. J. Appl. Earth Obs. Geoinf.* **2017**, *58*, 213–224. [[CrossRef](#)]
79. Zeng, C.; Richardson, M.; King, D.J. The Impacts of Environmental Variables on Water Reflectance Measured Using a Lightweight Unmanned Aerial Vehicle (UAV)-Based Spectrometer System. *ISPRS J. Photogramm. Remote Sens.* **2017**, *130*, 217–230. [[CrossRef](#)]
80. Becker, R.H.; Sayers, M.; Dehm, D.; Shuchman, R.; Quintero, K.; Bosse, K.; Sawtell, R. Unmanned Aerial System Based Spectroradiometer for Monitoring Harmful Algal Blooms: A New Paradigm in Water Quality Monitoring. *J. Great Lakes Res.* **2019**, *45*, 444–453. [[CrossRef](#)]
81. Choo, Y.; Kang, G.; Kim, D.; Lee, S. A Study on the Evaluation of Water-Bloom Using Image Processing. *Environ. Sci. Pollut. Res.* **2018**, *25*, 36775–36780. [[CrossRef](#)]
82. Olivetti, D.; Roig, H.; Martinez, J.-M.; Borges, H.; Ferreira, A.; Casari, R.; Salles, L.; Malta, E. Low-Cost Unmanned Aerial Multispectral Imagery for Siltation Monitoring in Reservoirs. *Remote Sens.* **2020**, *12*, 1855. [[CrossRef](#)]
83. Doughty, C.L.; Ambrose, R.; Okin, G.; Cavanaugh, K. Characterizing Spatial Variability in Coastal Wetland Biomass across Multiple Scales Using UAV and Satellite Imagery. *Remote Sens. Ecol. Conserv.* **2021**, *7*, 411–429. [[CrossRef](#)]

**Disclaimer/Publisher's Note:** The statements, opinions and data contained in all publications are solely those of the individual author(s) and contributor(s) and not of MDPI and/or the editor(s). MDPI and/or the editor(s) disclaim responsibility for any injury to people or property resulting from any ideas, methods, instructions or products referred to in the content.

# PAPER IV

Article

# U-Net Performance for Beach Wrack Segmentation: Effects of UAV Camera Bands, Height Measurements, and Spectral Indices

Edvinas Tiškus \*, Martynas Bučas, Jonas Gintauskas, Marija Kataržytė and Diana Vaičiūtė

Marine Research Institute, Klaipėda University, 92294 Klaipėda, Lithuania; martynas.bucas@ku.lt (M.B.); jonas.gintauskas@ku.lt (J.G.); marija.katarzyte@ku.lt (M.K.); diana.vaiciute@ku.lt (D.V.)

\* Correspondence: edvinas.tiskus@ku.lt

**Abstract:** This study delves into the application of the U-Net convolutional neural network (CNN) model for beach wrack (BW) segmentation and monitoring in coastal environments using multi-spectral imagery. Through the utilization of different input configurations, namely, “RGB”, “RGB and height”, “5 bands”, “5 bands and height”, and “Band ratio indices”, this research provides insights into the optimal dataset combination for the U-Net model. The results indicate promising performance with the “RGB” combination, achieving a moderate Intersection over Union (IoU) of 0.42 for BW and an overall accuracy of IoU = 0.59. However, challenges arise in the segmentation of potential BW, primarily attributed to the dynamics of light in aquatic environments. Factors such as sun glint, wave patterns, and turbidity also influenced model accuracy. Contrary to the hypothesis, integrating all spectral bands did not enhance the model’s efficacy, and adding height data acquired from UAVs decreased model precision in both RGB and multispectral scenarios. This study reaffirms the potential of U-Net CNNs for BW detection, emphasizing the suitability of the suggested method for deployment in diverse beach geomorphology, requiring no high-end computing resources, and thereby facilitating more accessible applications in coastal monitoring and management.

**Keywords:** drone; photogrammetry; deep learning; multispectral camera; data combinations

**Citation:** Tiškus, E.; Bučas, M.; Gintauskas, J.; Kataržytė, M.; Vaičiūtė, D. U-Net Performance for Beach Wrack Segmentation: Effects of UAV Camera Bands, Height Measurements, and Spectral Indices. *Drones* **2023**, *7*, x. <https://doi.org/10.3390/xxxxx>

Academic Editor(s): Name

Received: 22 October 2023

Revised: 7 November 2023

Accepted: date

Published: date



**Copyright:** © 2023 by the authors. Submitted for possible open access publication under the terms and conditions of the Creative Commons Attribution (CC BY) license (<https://creativecommons.org/licenses/by/4.0/>).

## 1. Introduction

Beach wrack (BW), also known as shore algal deposits or marine debris, is an important component of coastal ecosystems that can provide various ecological, economic, and social benefits [1]. BW is often used as a habitat for a variety of organisms, such as birds and invertebrates, and can serve as a source of food and shelter for these organisms, as well as a source of nutrients for plants [2]. In addition, BW can play a role in protecting the shoreline from erosion and storm waves [3]. It also has economic value, as it can be used as a source of organic matter for soil enhancement and fertilization, and in some cases, can be converted into biogas, a renewable energy source [4]. BW also has cultural and recreational value, as it is often used in traditional practices such as amber collecting and can attract tourists to coastal areas [5]. However, the degradation of BW and the accompanying unpleasant odors may disrupt recreational activities and pose health risks due to the habitation of fecal bacteria, which may thrive in such environments [6].

A complex interplay of meteorological conditions influences the deposition of BW, particularly wave action and storm events. Hydrodynamic measurements have indicated that BW is mostly formed during high sea level and wave events [7]. Furthermore, the morphological evolution of foredunes, which can impact wrack deposition, is driven by wave energy [8]. Storms not only induce deposition but also cause erosion, affecting the equilibrium of beach gradients [9]. These factors collectively contribute to the marine-

terrestrial transfer of BW, with significant ecological implications for nearshore environments.

For the monitoring of BW, it is important to understand BW dynamics and the factors that influence its distribution and abundance [10]. However, the detection of BW can be challenging due to its variability in distribution and abundance, its accessibility, particularly in remote or difficult-to-reach areas, and the limitations of traditional methods for mapping it [11,12]. The traditional methods for monitoring BW have been described as labor-intensive and reliant on manual field surveys. A study by Suursaar et al. [7] indicates that BW sampling can be considered a tool for describing the species composition of macrovegetation in near-coastal sea areas. This method involves the physical collection and analysis of BW samples, and while effective, it is subject to human error. Although variable in their applicability, empirical models offer another avenue for monitoring [13]. An integrated framework combining multiple techniques is advocated for comprehensive and effective management [14].

Advanced remote sensing methodologies such as aerial photography, satellite imaging, and light detection and ranging (LiDAR) show potential in identifying BW [15]. Widely recognized spectral indices such as the normalized difference vegetation index (NDVI) and the normalized difference red edge index (NDRE) are pivotal in this domain, exploiting the reflectance attributes inherent to diverse vegetation classes [16]. Furthermore, object-oriented image analysis constitutes another robust strategy to delineate and spatially represent beach zones within the remotely sensed data [17].

According to Yao et al. [18], in many instances, unmanned aerial vehicle (UAV) results outperformed satellite-based techniques. A study by Pan et al. [15] demonstrated that RGB aerial imagery captured with UAVs could be segmented with up to 75% accuracy using machine learning algorithms such as K-nearest neighbor, support vector machine, and random forests. A subsequent study by the same authors employed a camera trap for the continuous monitoring of detached macrophytes deposited along shorelines, offering an efficient and pragmatic method for tracking ecological dynamics [19]. Concurrently, Karstens et al. [20] utilized supervised machine learning methods to map and segment images acquired with UAVs to predict the locations of BW accumulation. Despite these advancements, the studies mentioned limitations, particularly in the number of images utilized for both segmentation and validation, and an imbalanced sample size of classes. While these methods showed promise in terms of their transferability to other areas, they still require additional real-world applications for comprehensive evaluation.

The efficacy of convolutional neural networks (CNNs) in segmenting remote sensing data is contingent on multiple variables, such as the nature and volume of image data. Several limitations to mapping BW should be considered when interpreting the segmentation results. One limitation is the availability and quality of the remote sensing data, which may affect the accuracy and resolution of the BW segmentation. Equally significant is the choice of the CNN model and the accompanying image processing techniques; these parameters directly impact the reliability and accuracy of the results. While the CNN model and image processing techniques are central to achieving high accuracy, the object-specific and environmental variables cannot be overlooked, as they may significantly affect the results' applicability across different locations and times; therefore, a careful selection and optimization of data composition for training and ongoing monitoring are essential for achieving reliable and generalizable outcomes [21]. Research by Lu et al. [22] demonstrated that multispectral images, particularly those with five bands (blue, green, red, red edge, and NIR), yielded accuracy levels comparable to hyperspectral images for vegetation mapping. Concurrently, a study by Wang et al. [23] enhanced landslide detection efficiency by integrating NDVI and near-infrared spectroscopy features, thereby augmenting four-band pre- and post-landslide images to create nine-band composite images.

In the field of remote sensing, digital surface models (DSMs) have shown their utility in complex terrain mapping and analysis, specifically in the context of BW identification and monitoring. For example, Tomasello et al. [24] examined the utility of UAVs for both



the volume estimation and segmentation of BW through machine learning techniques, and endorsed this approach for future monitoring initiatives. Moreover, this height information can be integrated with multispectral imagery captured by UAVs to increase the feature set for the CNN models, thereby enhancing segmentation accuracy for BW mapping.

This study aims to evaluate the U-net model’s performance when using six distinct combinations of spectral and height data, to assess the BW area using multispectral imagery from UAV. Additionally, the study aims to compare the performance of this model across different areas of interest (AOIs), by proving the transferability of the model. This research utilizes an extensive dataset, comprising over 150 multispectral 5000-pixel square image tiles. We tested whether the U-Net model’s performance in distinguishing BW will not significantly differ across AOIs, thereby demonstrating the model’s transferability. We hypothesize that incorporating all available data (multispectral and height) would improve the U-Net model’s performance for BW area detection. Also, we tested if the inclusion of height data would have a measurable impact on the final results, contributing to a more comprehensive representation (i.e., volume) of the BW. This study will contribute towards creating a workflow that would not require high-end computing power for CNNs and can facilitate fast, accurate BW estimation without the need for many on-site visits.

**2. Materials and Methods**

*2.1. Study Area*

The study area is located on the exposed coast of the southeastern Baltic Sea (Figure 1). This region is subject to a wind fetch exceeding 200 km, and experiences average wave heights of ~2 m. However, during extreme storm events, wave heights can reach up to 6 m [25]. Four areas of interest (AOIs) were selected along the Lithuanian coastline for monitoring over a year from December 2020 to January 2022. These AOIs represent the four most visited and easily accessible beaches on the continental part of Lithuania. Distinct features, including the proximity to urban areas, the presence of shipping and tourism, dunes, and other coastal features, characterize each of these AOIs (Table 1).



**Figure 1.** Area of interest (AOI) map and images from each one of the four areas, starting from top left and going to bottom right: Melnrage, Karkle, Palanga, Sventoji.

**Table 1.** Description of AOIs according to different attributes.

Attribute	Melnrage	Karkle	Palanga	Sventoji
Proximity to urban area	Close to the port city	Far from urban areas	Close to resort city	Close to resort city
Beach cleaning	No	No	Frequently	Frequently
Coastal features	Sand dunes	Sand dunes, boulders, and clay cliffs	Sand dunes	Sand dunes

Reefs (hard substrate overgrown by macroalgae)	Breakwater	Natural reefs	Natural reefs, groyne, and scaffoldings of pier	Scaffoldings of pier
Beach width by Jarmalavičius et al. [26]	±45 m	±11 m	±76 m	±107 m

Specifically, Melnrage is located in an area intensively used for shipping and is also close to Klaipėda—the largest city in the western Lithuanian region. Karkle beach is distinguished by the presence of boulders, favorable for the growth of algae, and is far from urban areas, surrounded by many trees; it is the narrowest of the four researched beaches with around 11 m in width [26]. Palanga beach, a popular tourist destination during the summer season, is often cleaned by the municipality, removing larger litter from the sand as well as BW. Sventoji, featuring a fishery port and a popular tourist destination, has the widest sandy beach of all AOIs, measuring around 107 m. All studied beaches have sand dunes, with Karkle beach also featuring clay cliffs. The total length of the beaches in the study area was approximately 39 km, with all coasts exposed to the Baltic Sea.

The BW on the Lithuanian Baltic coast is primarily composed (85% of the total relative BW biomass) of perennial red algae (mainly *Furcellaria lumbricalis* and *Vertebrata fucoides*) while filamentous green algae (mainly *Cladophora glomerata*, *C. rupestris*) and brown algae (mainly *Fucus vesiculosus* and *Sphacelaria arctica*), respectively, comprise 14% and 1% of the total relative BW biomass [27]. Red algae species dominate on stony bottoms within depths of 3–16 m, while filamentous green algae densely cover stones in shallower depths (<6 m). Filamentous brown algae such as *Sphacelaria arctica* usually cover hard substrate in deeper parts (>9 m), while overgrowths of *Pylaiella/Ectocarpus* sp. can be found on natural and artificial hard substrates (boulders, piers, scaffoldings) at depths of 1–5 m [28]. Stands of *Fucus vesiculosus* have not been recorded on the hard bottom habitats along the south-eastern Baltic Sea coast, suggesting its transport from other more sheltered coastal areas.

## 2.2. UAV-Based Remote Sensing of BW

A DJI Inspire 2 multirotor UAV equipped with a MicaSense RedEdge-MX multispectral (MicaSense Inc., Seattle, WA, USA) camera was used to acquire the images. The RedEdge-MX camera has 5 bands: Blue (475 nm ± 16 nm), Green (560 nm ± 13 nm), Red (668 nm ± 8 nm), Red edge (717 nm ± 6 nm), and Near-infrared (842 nm ± 28 nm), with 1.2 MP each, and a 47.2° horizontal and 34.4° vertical field of view (micasense.com accessed on 30 October 2023). The RedEdge-MX, with its higher sensitivity (compared to conventional RGB cameras) due to 16-bit image capture, was used for U-Net models. The RedEdge-MX also has additional bands and a global shutter that reduces the risk of blurred images. In addition to multispectral mosaics, RGB mosaics were acquired solely for BW heights, using Zenmuse X5S (DJI, Shenzhen, Guangdong, China) camera (see Section 2.4).

Flights were conducted approximately every 10 days at locations where BW was present and under suitable weather conditions to ensure the quality of the data collected: wind gust speeds of less than 10 m/s, no precipitation, and temperatures above 0 °C (lower temperatures could shorten flight times due to battery performance limitations). If these conditions were not met, the nearest suitable day was chosen for the flight. A flight time was typically scheduled just after sunrise (between 6 am and 10 am local time) to reduce sun glint effects on the water and to minimize the presence of people on the beach, as flights must comply with European regulations prohibiting flying over crowds. The PIX4Dcapture app was used to plan the flights, with a flight height of 60 m. An additional buffer transect was also added to the flight plan to reduce distortions in the center of the final mosaics.

The multispectral camera images had a ground sampling distance (GSD) of ~3.5 cm per pixel, while RGB camera images had a GSD of approximately 1.5 cm per pixel. The mosaics ranged from 0.20 to 1.70 km of beach length, depending on the size of the BW. For U-Net training, 29 multispectral images were mosaiced and partitioned into 163 tiles (Figure 2) of size 5000 × 5000. Out of 75 total flight missions, multispectral images consisted of 7 in Melnrage, 4 in Karkle, 3 in Palanga, and 15 in Sventoji, while the rest were RGB images (see Section 2.4).

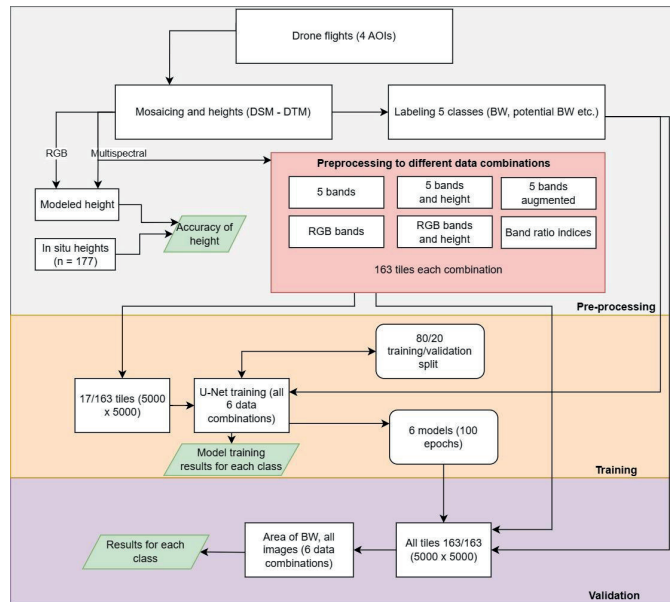


**Figure 2.** Processing workflow for UAV images. Arrows represent image processing from one stage to another. Green squares represent the finished results. Processing workflow for UAV images, including the data augmentation step employing rotations, flips, and other transformations to mitigate spatial location bias and enhance model robustness (see Section 2.3.2).

The PIX4Dmapper 4.6.4 software was used to process the UAV images both from Zenmuse X5S and RedEdge-MX. This software was chosen for its ability to create high-quality image mosaics and generate digital surface models (DSMs) and digital terrain models (DTMs), which are used for calculating the height of BW (see Section 2.4). The mosaics were georeferenced to a Lithuanian orthophoto map with a 0.5 m spatial resolution using QGIS georeferencing tools. At least three ground control points were chosen each time during the georeferencing process, selecting known objects that do not change location, ideally situated in the corners of the final UAV orthophoto.

### 2.3. Machine Learning Methods

#### 2.3.1. Labeling

The multispectral images were mosaiced into three band image files for visual labeling, using the green, blue, and near-infrared bands. The final product of the labeling process is a TIFF file with each pixel assigned to one of five classes: 0 for BW, 1 for potential beach wrack (that is still underwater), 2 for water, 3 for sand, and 4 for other objects (such as buildings, bushes, trees, wooden paths, etc.). It is worth noting that the image background, with a value of Nan, had a large number of pixels in all images, and these were labeled as “other”. The labeled images were then opened in ImageJ and exported as TIFF files. Classes were masked by experts, with the main goal of marking the areas of BW accumulations. In some cases, the labeling was done roughly, where BW was spread out in many pieces at a small scale (Figure 3).

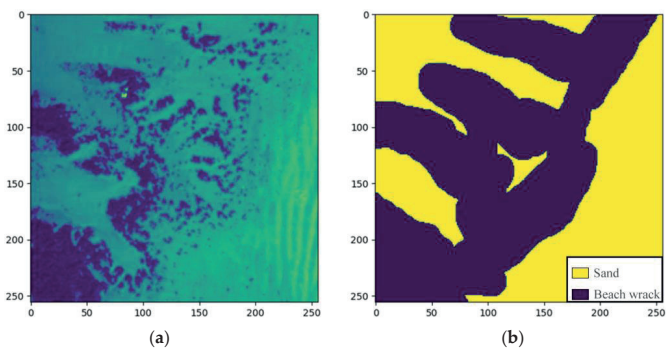


**Figure 3.** Example of manual labeling and its rough mask of BW in some areas at a pixel level, where (a) is a single red band with color pallet and (b) are the labeled areas of the same image. X and y coordinates show the locations of pixels ( $256 \times 256$ ) equal to around  $8 \text{ m}^2$ .

The accurate labeling of the mosaic tiles allows the U-Net CNN model to distinguish BW from other classes in the scene, such as sand, water, or other objects. It provides data against which the model’s predictions are evaluated, enabling the assessment of its effectiveness in BW identification and quantification. Labeling was performed on orthomosaic tiles with a maximum size of 5000 by 5000 using the “Labkit” [29] plugin in ImageJ FIJI. This plugin uses traditional supervised machine learning to assist with labeling using given samples, which were manually reviewed, and any incorrect labels were corrected by an expert. The near-infrared band was particularly useful in distinguishing between small rocks and BW, which can be challenging to differentiate in RGB images, as BW consists of algae that have chlorophyll-a, which is more reflective in the near-infrared band spectrum.

#### 2.3.2. Data Pre-Processing

The model training was performed on a computer equipped with 32 GB RAM, an Intel Core i7 8th gen (Intel Corporation, Santa Clara, CA, USA) CPU, and an NVIDIA GTX 1070 (NVIDIA Corporation, Santa Clara, CA, USA) GPU (8GB vRAM). To accommodate the memory constraints inherent to deep learning approaches, high-resolution tiles were partitioned into smaller  $256 \times 256$  pixel segments. These reduced dimensions were sufficient to maintain the visibility of the objects relevant to the study’s context.

Out of 163 tiles generated from the partitioning, 17 were selected by expert judgment for inclusion in the model training set (Table 2). The selection aimed to include at least one

tile from each date and AOI, to ensure a comprehensive representation of all segmentation classes.

**Table 2.** The partitioning of training data for the U-Net CNN model. Images corresponding to each AOI and date. Check marks (✓) indicate tile of AOI and data and multiple check marks (✓✓) show that multiple tiles were used from the same date and AOI.

Date/AOI	Melnrage	Karkle	Palanga	Sventoji
25 August 2021	✓			✓✓
8 September 2021				✓
15 September 2021	✓		✓	
17 September 2021		✓✓		✓
22 September 2021	✓			✓
29 September 2021				✓
1 October 2021				✓
26 October 2021		✓		✓
4 March 2022	✓			
22 March 2022				✓

For basic image manipulation (merging, selecting bands, augmentation processes, etc.), Python with GDAL 3.4.3 [30] library was used. Six different combinations from multispectral data were used to train the final models to assess the impact of different data types on the model’s performance. The combinations included the use of RGB bands, RGB and heights, 5 bands, 5 bands and height, augmented, and the band ratio indices merged into one TIFF, and will each be detailed later in this section to explain their combination process.

The indices included the normalized vegetation index (NDVI) (1), the normalized difference water index (NDWI) (2), and the normalized difference red edge index (NDRE) (3):

$$NDVI = \frac{NIR-Red}{NIR+Red} \tag{1}$$

$$NDWI = \frac{Green-NIR}{Green+NIR} \tag{2}$$

$$NDRE = \frac{NIR-Red\ edge}{NIR+Red\ edge} \tag{3}$$

where each remote sensing reflectance (Rrs) band is represented by a band name.

The choice of NDVI, NDWI, and NDRE over other indices was based on their specific spectral sensitivities relevant to BW identification. NDVI leverages red and NIR spectral bands, which are well established in vegetation studies, offer robust data on plant health [31,32], and are directly relevant to BW mapping, as it mostly consists of macroalgae. NDWI, which computes reflectance from the green and NIR spectral regions, helps distinguish water and land areas, and is useful in detecting potential underwater BW. NDWI is important in delineating water features and is crucial for identifying submerged or partially submerged vegetation [33,34]. However, NDWI may be impacted by shadows and surface roughness, necessitating its use alongside other indices. Lastly, the NDRE index helps to measure the amount of chlorophyll-a in the plants, and it can also be used for biomass estimation [35], which is also related to BW and the amount of it.

Data augmentation was undertaken as an exploratory measure to investigate potential spatial location bias related to class pixel locations within the dataset, rather than as a strategy for genuine model improvement. It was implemented solely on a single dataset that incorporated all spectral bands and the heights (see Section 2.4). Data augmentation was implemented by manipulating images through specific transformations: random rotations of images at defined angles (0°, 90°, 180°, and 270°), and horizontal and vertical

flips, each with an equal probability of 50%. This methodological approach ensures a diverse dataset, enhancing the robustness of the subsequent analyses.

### 2.3.3. U-Net Semantic Segmentation

The U-Net architecture, introduced by Ronneberger et al. [36], was selected for this study due to its precision in localization and its ability to effectively handle smaller datasets for complex image segmentation tasks. The distinguishing attribute of CNNs lies in their capacity to master spatial feature hierarchies, effected through the use of convolutional strata that scrutinize the input image, consequently deploying filters to abstract features across various scales. In this paper, a similar architecture (Figure 4) was used to the one described in the original U-Net paper, with the addition of extra layers for the multi-spectral images and a reduced input image size. Also, padding and a dropout of 20% was used, which is a regularization technique that involves randomly dropping a certain percentage of the neurons in the model during training, which helps to prevent the model from becoming too complex and overfitting the training data [37].

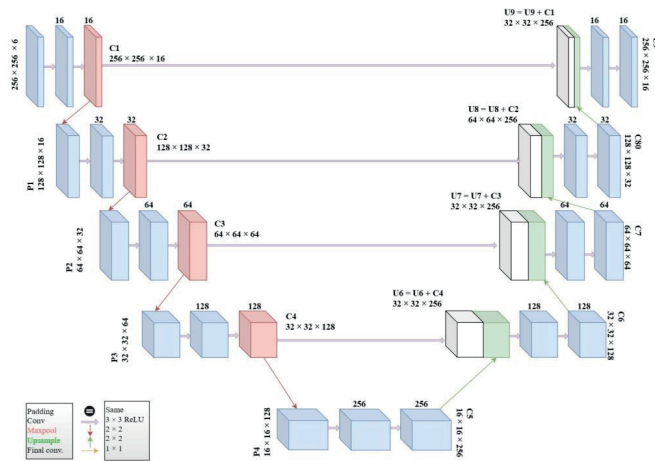
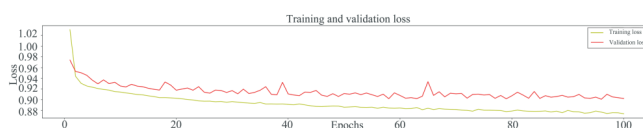


Figure 4. U-Net architecture (modified from Ronneberger et al. [36]).

The training itself was conducted in Python 3.9 using Keras version 2.3.1 [38] for model construction, with custom operations implemented in TensorFlow 2.1.0 [39]. The U-Net model was trained using a batch size of 16 patches (i.e., in each iteration of an epoch, 16 images were processed together), as it was the maximum limit for the computing power used in this study. The training was set to run for 100 epochs, but an early stopping mechanism was implemented to prevent overfitting. The training was halted if the model's performance did not improve after 6 consecutive epochs. This approach ensured that the model was not overtrained on the data, which could lead to a poor generalization of the testing data. The training models showed that all datasets around the first 20 epochs' results improved the most (Figure 5) for validation and training loss. After the 20th epoch, training and validation loss still decreased, but at a slower pace, while validation loss did not improve near epoch 40.



**Figure 5.** Example of loss for training and validation over 100 epochs. The dataset used for this training was all 5 bands and height.

The workflow for image segmentation began by assigning labeled TIFFs to the final pre-processed images. All classes were given equal weight, and the loss function was defined as the combination of dice loss and focal loss. The dice loss measure [40] quantifies the overlap between classes on a scale from 0 to 1, with higher values indicating better performance. The focal loss [41] helps to address the issue of unbalanced class distributions by decreasing the contribution of well-trained pixels and focusing on poorly trained ones.

To eliminate the edge effect when patching images, the Smoothly-Blend-Image-Patches [42] package was used, which employs a U-Net for image segmentation and blends predicted patches smoothly through 2D interpolation between overlapping patches.

#### 2.4. BW Heights

In addition to multispectral mosaics, 16 RGB mosaics were acquired for assessment of BW heights in Melnrage, 11 in Karkle, 6 in Palanga, and 13 in Sventoji using the Zenmuse X5S RGB camera that has an RGB lens with 20.8 MP and a 72° field of view (dji.com accessed on 30 October 2023).

To validate the UAV-derived height of BW deposits, a total of 16 in situ sampling missions were carried out concurrently with UAV flights (Table 3). The height of BW deposits was initially assessed using a plastic ruler at the study site. To ensure accuracy, the ruler was placed gently on the deposits to prevent penetration into the underlying sand, and was aligned vertically to measure at around every 10 m of BW, in a transect line of three points: the start of the BW (near the water), middle point selected by expert judgement, and the end of the BW (furthest from the water). They comprised a total of 177 points within each site, covering areas of BW deposits and reference areas without BW.

**Table 3.** In situ sampling of BW on the coast and in the water at four study sites from December 2020 to January 2022. Bolded dates indicated when the RGB camera was used and not bolded when the multispectral camera was used. The number of height measurements per sampling is provided in brackets.

Melnrage	Karkle	Palanga	Sventoji
<b>2021.04.20 (3)</b>	<b>220.12.05 (1)</b>	<b>2020.12.05 (2)</b>	<b>2020.12.05 (4)</b>
<b>2021.06.02 (20)</b>	<b>2021.07.27 (3)</b>	<b>2021.07.29 (3)</b>	<b>2021.07.07 (10)</b>
<b>2021.06.18 (11)</b>	2021.09.17 (23)		2021.08.27 (3)
<b>2021.08.10 (8)</b>			2021.09.17 (58)
2021.09.16 (25)			
2022.01.24 (3)			

The estimation of the BW height from the UAV images involved subtracting the DSM from the DTM using GDAL.

#### 2.5. Performance Metrics

To validate the model's performance during training, the data were randomly split into two sets, 80% for training and 20% for validation, according to common practice to avoid overfitting and test the model's ability to generalize. This split ensured that the

model was trained on a large enough dataset to learn the necessary features, while also having a separate set of data to test its performance [43]. A separate validation set, consisting of all tiles, was used to assess the model's ability to generalize to new data and ensure that it was not overfitting to the training data.

Several metrics were employed to assess the model's performance: precision, recall, F1 score, and Intersection over Union (IoU). Precision quantifies the proportion of correctly predicted positive values to the total predicted positives, while recall measures the fraction of correctly predicted positive values to the total actual positive values. The F1 score harmoniously combines precision and recall, providing a balanced performance metric [44]. The IoU, also known as the Jaccard index, offers a comprehensive assessment of the model's performance, going beyond pixel accuracy to measure the similarity between the predicted and ground truth labels [45]. In general, models trained on specific datasets will have a higher IoU than models trained to be more general, but the latter will have a wider range of applicability [46]. The effectiveness of the selected models was evaluated on testing data by comparing the IoU metric. The IoU was also compared for each AOI and each class. No single IoU threshold fits all use cases; however, it is common practice to use a threshold of 0.5 for accurate segmentation [47]. Therefore, IoU values above 0.7 were considered as high, from 0.5 to 0.7 as moderate, and below 0.5 as low.

In addition, the IoU between labeled and segmented BW for tiles in the whole mosaic BW areas were calculated and compared with each other as well. Furthermore, for the comparison of IoU between AOIs, the normality and homogeneity of variance assumptions were tested, using the Shapiro–Wilk and Levene's tests, respectively. Given the violations of normality and homogeneity of variance assumptions, the Dunn's test post hoc pairwise comparisons of IoU between the AOIs was utilized. The p-values were adjusted using the Bonferroni correction to control for multiple comparisons. The comparison between averages was performed with a one-way ANOVA test. All statistical analyses were performed using numpy [48], scipy [49], statsmodels [50], and sklearn [51] Python packages, at a significance level of 0.05.

In situ measured heights and heights calculated from UAV were assessed for correspondence using Pearson's correlation coefficient ( $r$ ). The precision of these measurements was further quantified by the root mean square error (RMSE) and mean absolute error (MAE). This was also tested for separate AOIs.

### 3. Results

#### 3.1. Performance of Various Input Training Data

In training the U-Net model's performance across various data combinations, the "band ratio indices" combination consistently showcased the best results (Table 4), especially for the segmentation of BW. With this combination, the model achieved an F1 score of 0.86 and an IoU of 0.75 for BW. Notably, the "5 bands" combination also delivered good results, particularly for potential BW, with an F1 score of 0.57 and an IoU of 0.40. However, when examining the potential BW class, all combinations presented relatively lower IoU scores. The "augmented data" combination displayed the least promising outcomes across the metrics.



**Table 4.** IoU, precision, recall, and F1 scores for different classes resulting from a convolutional neural network U-Net model’s training set, on various data combinations. The columns in the table represent different datasets, while the rows contain the performance scores for each class. These results were obtained after 100 epochs of training. Best performing values for average, BW, and potential BW are marked with the \* symbol.

Dataset Type	5 Bands and Height	5 Bands	RGB	RGB and Height	Augmented Data	Band Ratio Indices
IoU avg.	0.67	0.71 *	0.69	0.69	0.66	0.67
Beach wrack	0.72	0.73	0.71	0.66	0.67	0.75 *
Potential beach wrack	0.35	0.4	0.35	0.38	0.3	0.39 *
Water	0.68	0.73	0.69	0.73	0.7	0.65
Sand	0.75	0.81	0.76	0.78	0.74	0.71
Other	0.86	0.89	0.93	0.92	0.88	0.86
F1 score avg.	0.87	0.9 *	0.88	0.89	0.87	0.86
Beach wrack	0.83	0.84	0.83	0.79	0.8	0.86 *
Potential beach wrack	0.52	0.57 *	0.51	0.55	0.46	0.56
Water	0.81	0.85	0.82	0.84	0.83	0.79
Sand	0.86	0.89	0.86	0.88	0.85	0.83
Other	0.94	0.96	0.97	0.97	0.96	0.94
Precision avg.	0.88	0.90 *	0.89	0.9*	0.88	0.87
Beach wrack	0.76	0.87	0.87	0.89*	0.83	0.79
Potential beach wrack	0.51	0.54	0.5	0.48	0.37	0.8 *
Water	0.77	0.83	0.79	0.82	0.79	0.77
Sand	0.87	0.89	0.88	0.91	0.89	0.79
Other	0.99	0.98	0.98	0.97	0.98	0.98
Recall avg.	0.87	0.89 *	0.88	0.89 *	0.87	0.86
Beach wrack	0.93	0.81	0.79	0.72	0.77	0.94 *
Potential beach wrack	0.53	0.6	0.53	0.66*	0.58	0.43
Water	0.86	0.87	0.86	0.86	0.87	0.8
Sand	0.85	0.9	0.84	0.85	0.82	0.88
Other	0.9	0.95	0.97	0.97	0.93	0.91

The post hoc test revealed that none of the pairwise comparisons were statistically significant ( $p \geq 0.74$ ), suggesting that different data combinations did not significantly impact the IoU scores.

The “5 bands” combination yielded the best results for the sand and water classes, achieving the highest F1 scores and IoU values among the combinations. In contrast, the “RGB” combination was the most effective for the other class, showcasing exemplary F1 scores and IoU values. The precision and recall rates for each of these optimal combinations were also notably high, confirming the findings.

### 3.2. Validation of Trained U-Net Model for Testing Data

In the segmentation of BW, the combination that used “RGB” bands yielded the best performance with an IoU of 0.42 (Figure 6) and further demonstrated an F1 score of 0.54. Following closely, the combination utilizing “augmented data” had an IoU of 0.41, supported by an F1 score of 0.55. The “5 bands and height” combination also showcased notable performance with an IoU of 0.39 and an F1 score of 0.54. Conversely to training data, for validation the “band ratio indices” combination yielded the lowest IoU of 0.37 for BW classification, alongside an F1 score of 0.50.

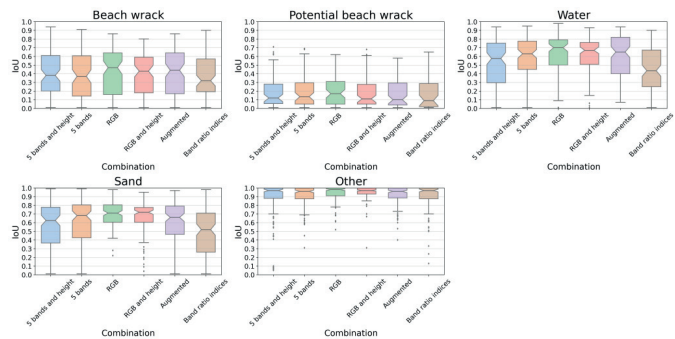


**Figure 6.** The boxplots present the IoU scores for the six different data combinations applied during the U-Net (CNN) model validation. The plots show the distribution of IoU scores for each segmentation class: BW, potential BW, water, sand, and other. The central line inside each box represents the median, while the edges of the box indicate the 25th and 75th percentiles. Outliers may be represented by individual points.

The “5 bands and height” combination emerged as the most effective for potential BW segmentation, recording an IoU of 0.20 and 0.38 for the F1 score. The “RGB” and “5 bands” combinations followed closely, with an IoU of 0.20. While the “RGB” combination achieved an F1 score of 0.46, the “5 bands” combination had an F1 score of 0.38. The “augmented data” combination exhibited the least efficacy in segmenting potential BW, with the lowest IoU of 0.16 and accompanying F1 score of 0.34.

Regarding the additional classes, in the water class, the “RGB” combination emerged superior with an IoU of 0.64 and an F1 score of 0.76. In contrast, the “band ratio indices” combination exhibited the lowest performance, securing an IoU of 0.45 and an F1 score of 0.58. In the sand class, the “RGB” combination outperformed the rest with an IoU of 0.70 and 0.82 for the F1 score, while the “band ratio indices” combination trailed with an IoU of 0.48, alongside an F1 score of 0.61. For the class of other, the “RGB and height” combination achieved the highest IoU of 0.95, supported by an F1 score of 0.97, whereas the “5 bands and height” combination had the lowest IoU of 0.87, with an F1 score of 0.91.

For the overall average performance of all combinations, there was no significant difference between them ( $f = 0.10$ ,  $p > 0.05$ ). The “5 bands” combination achieved an F1 score and IoU of 0.88 and 0.54, respectively. When height was incorporated, the “5 bands and height” combination demonstrated a slight dip in performance, with average metrics for the F1 score at 0.85 and an IoU of 0.51. The “augmented data” combination showcased metrics closely resembling the “5 bands” combination, with 0.88 for F1 score and 0.54 for IoU. A noticeable decrease in average performance was observed with the “band ratio indices” combination, yielding 0.84 and 0.47 for the F1 score and IoU, respectively. The “RGB” combination recorded the highest average metrics among all combinations: F1 score of 0.92 and IoU of 0.58. Lastly, the “RGB and height” combination mirrored the “RGB” combination in precision and recall, but displayed a slightly lower average F1 score and IoU of 0.92 and 0.57, respectively.

Comparing the segmentation results of BW between AOIs, Dunn’s post hoc tests for IoU showed significant differences between Karkle and the rest of the AOIs ( $p < 0.05$ ), while no significant differences ( $p > 0.05$ ) were observed between Melnrage, Palanga, and Svetoji (Figure 7).

Specifically, in Svetoji, the “5 bands and height” combination yielded the highest IoU at  $0.48 \pm 0.26$ , while in Palanga, the “RGB and height” combination was most effective with an IoU of  $0.46 \pm 0.22$ . For the class of potential BW, the “RGB and height” combination

in Karkle registered an IoU of  $(0.29 \pm 0.22)$ , and in Melnrage, the “RGB” combination yielded  $(0.26 \pm 0.19)$ .

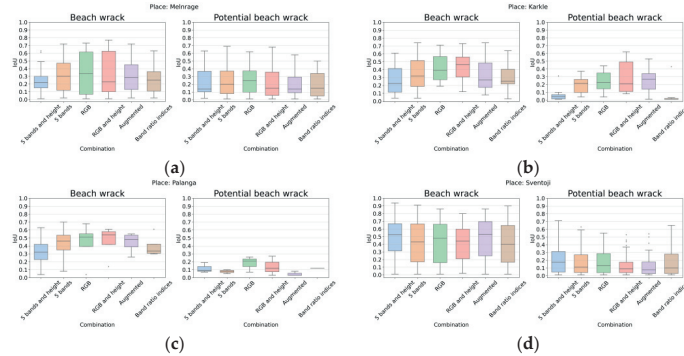


**Figure 7.** Boxplots for each AOI separately where (a) is Melnrage, (b) Karkle, (c) Palanga, and (d) Sventoji. Each boxplot represents the results for all data combinations, and notches show a confidence interval around the median.

For the water class, the “RGB” combination in Melnrage produced an IoU of  $(0.63 \pm 0.23)$ , followed by the “RGB and height” combination in Karkle with  $(0.50 \pm 0.19)$ . In the sand class, the “RGB and height” combination in Karkle led with an IoU of  $(0.65 \pm 0.25)$ , closely followed by the “RGB” combination in Melnrage, having an IoU of  $0.68 \pm 0.15$ . Lastly, for the other class, the “RGB and height” combination in Karkle achieved the highest IoU at  $(0.93 \pm 0.06)$ , while Melnrage scored  $(0.94 \pm 0.09)$  using the “RGB” combination.

3.3. Heights and Areas of BW

The labeled areas of BW were from approximately  $235.55 \text{ m}^2$  to  $11193.33 \text{ m}^2$ , while the area of BW derived from the U-Net model using the “RGB” combination exhibited a wider range, from  $8.83 \text{ m}^2$  to  $3710.01 \text{ m}^2$  (Figure 8). While the relationship was generally linear between the labeled BW areas and areas retrieved using the U-Net model with the “RGB” combination, there was a relatively large average with standard deviation, namely, a labeled area of  $1887.94 \pm 2198.93 \text{ m}^2$ , corresponding to the area of  $1217.80 \pm 939.90 \text{ m}^2$  derived from the U-Net model using the “RGB” combination.

Palanga had the best agreement comparing labeled to RGB areas, with an average of  $39.09 \pm 39.43 \text{ m}^2$ . For Karkle, all areas were overestimated with an average of  $-572.05 \pm 427.17 \text{ m}^2$ . As for Sventoji, it had the largest average,  $3005.83 \pm 2603.98 \text{ m}^2$  of BW area, and the differences were also the largest,  $1295.03 \pm 2118.10 \text{ m}^2$ . In Melnrage, most of the values were underestimated except for one on 8 September 2021, and the average overestimation was  $315.66 \pm 238.01 \text{ m}^2$ .

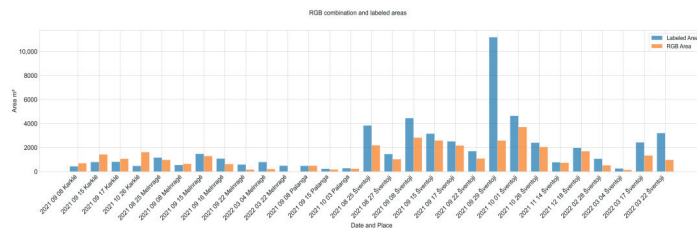


**Figure 8.** The areas of BW coverage in the investigated AOIs retrieved from UAV after the application of the U-Net model with the “RGB” combination and labeled BW areas.

While comparing labeled to segmented areas of BW, the “RGB” combination exhibited the highest correlation coefficient ( $r = 0.87$ ) among all tested approaches for agreement with the area, followed closely by the “RGB and heights” combination with an  $r$  of 0.86. Additionally, both these models had the lowest MAE and RMSE values, 562.27 and 783.59 for “RGB”, and 658.28 and 897.08 for “RGB and height”, respectively.

Other data combinations (Table 5) had lower correlation coefficients ranging from 0.46 for “5 bands” to 0.73 for “augmented data” combinations. The MAE and RMSE were also worst for “5 bands” at 825.54 and 1377.34, respectively, and for the “augmented data” combination, that was the next best combination after “RGB” and “RGB and height”, with a MAE of 575.91 and an RMSE of 902.87.

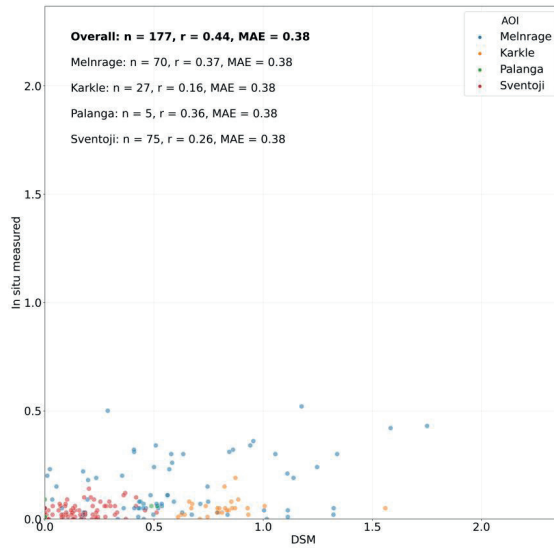
**Table 5.** Statistics between labeled and segmented areas of BW. Pearson’s correlation coefficient— $r$ , MAE—mean absolute error, RMSE—root mean square error.

Data Combinations	$r$	MAE	RMSE
5 bands and height area	0.48	807.99	1512.91
Augmented data area	0.73	575.91	902.87
Band ratio indices area	0.68	648.42	1097.48
5 bands area	0.46	825.54	1377.34
RGB area	0.87	562.27	783.59
RGB and height area	0.86	658.28	897.08

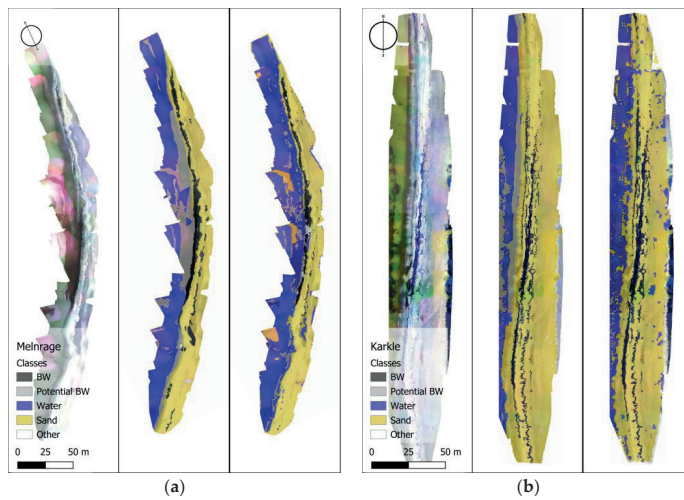
The average calculated height of BW ( $0.46 \pm 0.40$  m) from UAV overestimated the in situ measured height by five-fold ( $0.09 \pm 0.11$  m) from a sample size of 177 (Figure 9). The maximum BW height calculated was 2.37 m, while the maximum in situ measurement was only 0.52 m, with a standard deviation of calculated height—0.03 and in situ—0.01 m. The correlation between modeled and in situ heights was 0.44 ( $p < 0.05$ ).

From the example of the visual representation of all AOIs (Figure 10), it is evident that the model’s performance is adequate in accurately classifying the majority of the BW. In these examples, Melnrage is overestimated by 455.10 m<sup>2</sup>, Karkle underestimated by 251.59 m<sup>2</sup>, Palanga overestimated by 56.75 m<sup>2</sup>, and Sventoji overestimated by 934.70 m<sup>2</sup>.

This precision captures the expected locations and distribution patterns of all classes, confirming the model’s robustness. Specific regions, such as Palanga and Melnrage, present minor challenges, with a few discrepancies in detecting the potential BW. However, these instances are more the exception than the norm. The sand and water classes have the best visual results with few minor variations. Similarly, the class of other is also excellent, with just a few objects, mainly in Palanga, misclassified as sand.



**Figure 9.** Agreement between in situ height and mosaic-calculated height. Different colors represent different AOI. r—Pearson’s correlation coefficient, MAE—mean absolute error.



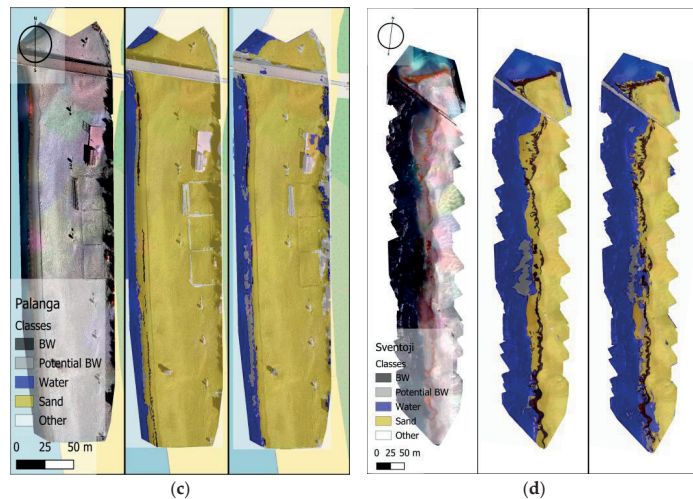


**Figure 10.** Examples of BW spatial distribution in each AOI after UAV image processing with the U-Net model using the “RGB” combination. RGB (left), labeled BW (middle), and modeled BW (right) maps are provided for (a) 16 September 2021 in Melnrage, (b) 17 September 2021 in Karkle, (c) 15 September 2021 in Palanga, and (d) 1 October 2021 in Sventoji. The colors of BW in Sventoji and Karkle are different because they are combinations of green, blue, and NIR bands, making them easier to distinguish visually. The different colors near and above the water are noise (see 4.2).

#### 4. Discussion

##### 4.1. Assessment of U-Net Model Performance in BW Segmentation

The U-Net CNN model exhibited commendable results in BW segmentation, particularly when utilizing the “RGB” combination. The segmentation accuracy not only allowed the delineation of BW but also enabled the estimation of its total area across the selected AOIs, ranging from 8.83 m<sup>2</sup> to 3710.01 m<sup>2</sup>. This capability to accurately segment and subsequently estimate the BW area reaffirms the efficiency of U-Net models in semantic segmentation tasks, especially for high-resolution remote sensing images [52].

To the best of the authors’ knowledge, only two studies [15,20] were carried out in the context of UAV monitoring of BW. Both of them performed object-based image analysis (OBIA) and achieved relatively high accuracy (producer accuracy > 80%) in classification. In contrast, our research primarily employed the IoU metric, which is suggested as a superior method, especially when combined with other measures like the F1 score. It is also more reliable as it takes into account the whole area rather than a random sample of points or polygons [53], achieving more reliable ML model performance evaluation. However, the labeling process is time-consuming to achieve metrics that include an entire image, especially for large datasets, as in this study (29 mosaiced orthophotos), but after the first training, the U-Net model can be run on new images and instead of labeling all images, the results can just be adjusted as labels for the new round of training, this way reducing the labeling time and overtime, and improving the model’s accuracy and generalizability. While recognizing that the absence of producer accuracy calculations precludes a direct statistical comparison with the referenced OBIA studies, it is suggested that future research should incorporate producer accuracy or equivalent measures to enable such direct comparisons.

Some of the images captured during sunrise featured substantial shadow coverage on the beach due to the westward orientation of the AOIs. Such shadows may influence the CNN model's segmentation precision; however, investigating shadow impacts would entail a controlled experimental design that would distract from the study's core objectives. Future research should factor sun position in to minimize shadow occurrence during UAV imagery collection for BW segmentation. External elements like cloud cover and sun angle significantly impact UAV imagery quality [54]. Moreover, accurately pinpointing the waterline in UAV imagery remains a persistent challenge due to the sea surface's ever-changing nature, as noted by Long et al. [55] and Brouwer et al. [56].

The training duration can be extensive, especially with large datasets and intricate models. In our scenario, with 17 tiles measuring  $5000 \times 5000$  each and more than four encoder layers, the "5 bands and height" took roughly 4 h for 100 epochs. Nonetheless, predicting an individual image tile only takes about 5 min, which is important for management tasks that need to estimate quickly whether the amount of BW should be removed. The processing time is also essential, especially as monitoring scales increase. One way to improve it could be the employment of architectures that merge an anchor-free detector with a region-based CNN, which has demonstrated superior precision and faster inference speeds, which is advantageous for smaller datasets [57].

#### 4.2. Model Transferability

In general, the IoU values for BW were consistently moderate using all combinations, suggesting that the model's generalizability and transferability in time are possible, considering that the dataset encompassed images captured during varied seasons and under diverse weather conditions, and ensuring a comprehensive representation, contrary to previously mentioned studies. Such results resonate with the broader understanding that UAVs are potent tools for monitoring diverse beach aspects, from mixed sand and gravel to litter [58,59].

The transferability to unseen AOIs could be complicated, as good results were achieved for three AOIs (Sventoji, Melnrage, and Palanga) with relatively homogenous surfaces, characterized by sedimentological uniformity with minimally varying geomorphic attributes and objects, ensuring a predictable substrate across the examined terrain. Differently from other AOIs, surface conditions were heterogenous in Karkle, which could explain in the low performance of combinations that included heights (BW IoU = 0.37) compared to other data combinations (BW IoU from 0.39 to 0.56), suggesting that heights acquired using the methods in this study should be used carefully. Additionally, the diminished IoU results after incorporating height in both RGB and multispectral data indicate potential errors in the derived heights, or that an overload of layers might be confounding the model; this aligns with the observations of Pichon et al. [60] and Gruszczyński et al. [61]. The accuracy of height could be improved by taking images with oblique angles in addition to nadir, increasing the information available for DSM calculations using structures from motion algorithms [62].

Additionally, the "augmented data" combination did not exhibit a significant divergence from the "5 bands and height" combination. This observation suggests that the model does not exhibit a bias towards the spatial localization of objects within the image. Consequently, this reinforces the notion of the model's transferability across varied scenarios where objects and areas may be positioned differently within the AOI, indicating the model's adaptability in handling them effectively.

#### 4.3. Data Combination Influence on the Results

The model's effectiveness varies with different data combinations and classes. Notably, the "5 bands" combination had decent results for the potential BW segmentation, achieving an F1 score of 0.57 and an IoU of 0.40. However, this was inconsistent across the classes of sand, water, and other. The performance inconsistencies across data

combinations, such as the superior results of the “RGB” in the BW class but not universally, signal the need for future exploration. While the IoU results for BW were anticipated to be the best with the “5 bands and height” combination due to its comprehensive data, the outcomes were the opposite (IoU = 0.38), and the “RGB” combination IoU was 0.42; however, the difference between combinations was not significant. This suggests that for the segmentation of chosen classes, simpler sensors (such as RGB cameras) could be employed as the accuracy is not worse than with multispectral ones, and the training and prediction time for fewer bands is also shorter. This finding contradicts other studies that found that for multispectral combinations, segmentation accuracy is improved [63].

In this study, equal weights were used for different bands; however, a potential need for different weight distributions in the initial U-Net model for various bands and classes could improve the results of multispectral combination, as hinted by Amiri et al. [64] and Matuszewski et al. [65]. Therefore, the “RGB” combination’s surprising efficacy further stresses the need for model adjustments, such as the depth and complexity of CNN models. Rao et al. [66] noted that deeper models can achieve higher detection accuracies but demand more parameters and longer training and inference times.

Data pre-processing and augmentation are equally impactful on CNN performance. As pointed out by Rodrigues et al. [67], CNNs generally fare better with non-pre-processed images when trained from scratch. Thus, the pre-processing and augmentation approach for various combinations could be responsible for the disparities observed across different classes. Moreover, selecting activation functions and optimization methods can also lead to differentiated results. For example, S. Dubey et al. [68] observed that the difGrad optimizer excels when training CNNs with varied activation functions.

To find the relative importance of each spectral band in the U-Net model, it is suggested to perform a feature ablation analysis, where bands are individually omitted to observe the effect on segmentation accuracy [69]. Additionally, feature permutation importance could be employed, shuffling band values to quantify their impact on model performance [70]. Furthermore, Grad-CAM could provide insight into which bands most influence the predictions of model through gradient-based importance mapping [71]. These methodologies could enable a precise understanding of each band’s role in the model’s functionality. In this study, these techniques were not employed, but it would be beneficial for future work to test these techniques to optimize the model’s spectral band selection.

Exploring the U-Net model’s synergy with other technologies or data sources could be beneficial. Thomazella et al. [72] documented the efficacy of drone imagery merged with CNNs for environmental monitoring. Given the promising results of the “RGB” and “RGB and height” combinations, integrating them with resources like satellite images could create a more comprehensive system for coastal environment monitoring.

#### 4.4. Class Influence on the Results

The model’s challenges become particularly discernible in its capacity to detect potential BW. The complexities in detecting this class are largely due to the inherent complexities of aquatic environments and underwater light behavior. A primary challenge stems from how water impacts light absorption and reflection [73], with optical complexities in water bodies rendering some remote sensing algorithms less effective. Light shifting at varying water depths can modify the spectral characteristics of reflected light, affecting the model’s capability to accurately segment potential BW. Furthermore, the sun’s glint can overshadow the upwelled water-leaving radiance during elevated solar angles. As Gagliardini et al. [74] noted, this leads to noise in the image information. Overstreet and Legleiter [75] further demonstrated that sun glint might induce over-corrections in shallow areas of water in the imagery, producing unreliable data. Factors such as wave activity and sea surface roughness add complexity to the water’s optical properties, affecting the quality of remote sensing reflectance, as described by Zhang et al. [76]. Improving



the segmentation of potential BW could be achieved by adding further pre-processing steps that would correct for water depth [77] and the sun glint effect [78,79].

The limitation of potential BW detection in shallow coastal waters holds significant implications. The deposition of potential BW, especially in vast amounts under intense heat, requires its prompt removal to uphold the beach's ecological equilibrium, smell, and visual appeal. Overlooked potential BW might lead to significant underestimations of BW deposition on beaches, thereby affecting beach management.

This study recommends prioritizing the use of "RGB" data configurations for U-Net CNN applications in BW segmentation due to their moderate accuracy and lower computational demand. It is recommended to re-evaluate the inclusion of height data from UAVs, as it did not significantly improve and sometimes even reduced model precision. Beach managers should consider these findings to optimize BW monitoring workflows, ensuring that methods remain cost-effective and suitable for various beach types without the need for high-end computing resources. This approach will help in scaling up coastal monitoring efforts while maintaining efficiency and accuracy.

While this study has laid important groundwork in applying U-Net CNN models for BW segmentation using UAV imagery combinations, there remain areas for enhancement. Future studies could benefit from incorporating a wider range of environmental conditions and beach morphologies to strengthen the model's generalizability. Moreover, integrating advanced data pre-processing techniques to reduce the effects of variable water reflectance could further refine segmentation accuracy. Additionally, employing a systematic approach to evaluate the impact of individual spectral bands on the model's performance could provide deeper insights into the model's interpretability and guide more efficient feature selection.

## 5. Conclusions

The U-Net model showed promising results using a model trained only on the "RGB" combination for validation data, where the accuracy of BW segmentation was moderate (IoU = 0.42 and F1 score = 0.54), while a relatively better accuracy (F1 score = 0.92 and IoU = 0.59) was achieved for the overall model (the segmentation of all classes). The achieved segmentation accuracy enabled a consistent estimation of BW across the studied AOLs, and BW was found to be in a range of 8.83 m<sup>2</sup> to 3710.01 m<sup>2</sup>. However, the model underperformed in the segmentation of potential BW, influenced by the inherent challenges presented by variable water reflectance, which might be modulated by factors such as wave patterns, turbidity, transparency, depth, and sun glint. The empirical evidence confirmed a notable degree of transferability in the deployment of the U-Net model across other locations with similar geomorphology of beaches (e.g., sandy or pebble beaches) to those utilized in the training data.

Contrary to the initial hypothesis, incorporating all spectral bands did not improve the model's performance across all classes. Interestingly, the inclusion of height data, acquired from UAV DSM that were only acquired using nadir-facing images, should be re-considered as the heights will not have accurate information.

Finally, this study underscores the utilization of U-Net CNNs for BW detection, demonstrating that effective model training and analysis can be conducted without the reliance on high-end computing resources, thereby allowing for more accessible and scalable applications in BW monitoring and management.

**Author Contributions:** E.T.: conceptualization, methodology, software, validation, formal analysis, investigation, resources, data curation, writing—original draft, writing—review and editing, visualization, supervision; M.B.: conceptualization, methodology, validation, investigation, resources, data curation, writing—review and editing, supervision; D.V.: conceptualization, validation, investigation, resources, data curation, writing—review and editing, supervision; J.G.: conceptualization, validation, investigation, resources, writing—review and editing; M.K.: resources, funding

acquisition, writing—review and editing, supervision. All authors have read and agreed to the published version of the manuscript.

**Funding:** This research was supported by the Doctorate scholarship program in Ecology and Environmental Sciences at Klaipėda University, Lithuania. The field campaigns were co-funded by the Interreg LAT\_LIT Programme, co-financed by the European Regional Development Fund (LLI-525 ESMIC).

**Data Availability Statement:** The data presented in this study are available on request from the corresponding author.

**Acknowledgments:** Authors kindly acknowledge Arūnas Balčiūnas, Greta Gyraitė, Greta Kalvaitienė, and Viktorija Sabaliauskaitė for their support in performing the field work/campaigns.

**Conflicts of Interest:** The authors declare no conflicts of interest.

## References

1. Robbe, E.; Woelfel, J.; Balčiūnas, A.; Schernewski, G. An Impact Assessment of Beach Wrack and Litter on Beach Ecosystem Services to Support Coastal Management at the Baltic Sea. *Environ. Manag.* **2021**, *68*, 835–859. <https://doi.org/10.1007/s00267-021-01533-3>.
2. Orr, M.; Zimmer, M.; Jelinski, D.E.; Mews, M. Wrack Deposition on Different Beach Types: Spatial and Temporal Variation in the Pattern of Subsidy. *Ecology* **2005**, *86*, 1496–1507. <https://doi.org/10.1890/04-1486>.
3. Gibson, R.; Atkinson, R.; Gordon, J.; Editors, T.; In, F.; Airolidi, L.; Beck, M. Loss, Status and Trends for Coastal Marine Habitats of Europe. *Annu. Rev.* **2007**, *45*, 345–405. <https://doi.org/10.1201/9781420050943.ch7>.
4. Rudovica, V.; Rotter, A.; Gaudêncio, S.P.; Novoveská, L.; Akgül, F.; Akslen-Hoel, L.K.; Alexandrino, D.A.; Anne, O.; Arbidans, L.; Atanassova, M. Valorization of Marine Waste: Use of Industrial by-Products and Beach Wrack towards the Production of High Added-Value Products. *Front. Mar. Sci.* **2021**, *8*, 723333.
5. McLachlan, A.; Defeo, O. *The Ecology of Sandy Shores*; Academic Press: Cambridge, MA, USA, 2017; ISBN 978-0-12-809698-7.
6. Kalvaitienė, G.; Vaičiūtė, D.; Bučas, M.; Gyraitė, G.; Kataržytė, M. Macrophytes and Their Wrack as a Habitat for Faecal Indicator Bacteria and *Vibrio* in Coastal Marine Environments. *Mar. Pollut. Bull.* **2023**, *194*, 115325. <https://doi.org/10.1016/j.marpolbul.2023.115325>.
7. Suursaar, Ü.; Torn, K.; Martin, G.; Herkül, K.; Kullas, T. Formation and Species Composition of Stormcast Beach Wrack in the Gulf of Riga, Baltic Sea. *Oceanologia* **2014**, *56*, 673–695. <https://doi.org/10.5697/oc.56-4.673>.
8. Moulton, M.A.B.; Hesp, P.A.; Miot da Silva, G.; Keane, R.; Fernandez, G.B. Surfzone-Beach-Dune Interactions along a Variable Low Wave Energy Dissipative Beach. *Mar. Geol.* **2021**, *435*, 106438. <https://doi.org/10.1016/j.margeo.2021.106438>.
9. Gómez-Pazo, A.; Pérez-Alberti, A.; Trenhaile, A. Recording Inter-Annual Changes on a Boulder Beach in Galicia, NW Spain Using an Unmanned Aerial Vehicle. *Earth Surf. Process. Landf.* **2019**, *44*, 1004–1014. <https://doi.org/10.1002/esp.4549>.
10. Schlacher, T.A.; Schoeman, D.S.; Dugan, J.; Lastra, M.; Jones, A.; Scapini, F.; McLachlan, A. Sandy Beach Ecosystems: Key Features, Sampling Issues, Management Challenges and Climate Change Impacts. *Mar. Ecol.* **2008**, *29*, 70–90. <https://doi.org/10.1111/j.1439-0485.2007.00204.x>.
11. Bussotti, S.; Guidetti, P.; Rossi, F. *Posidonia Oceanica* Wrack Beds as a Fish Habitat in the Surf Zone. *Estuar. Coast. Shelf Sci.* **2022**, *272*, 107882. <https://doi.org/10.1016/j.ecss.2022.107882>.
12. Woelfel, J.; Hofmann, J.; Müsch, M.; Gilles, A.; Siemen, H.; Schubert, H. *Beach Wrack of the Baltic Sea Challenges for Sustainable Use and Management (Toolkit)*; Report of the Interreg Project CONTRA. 2021, 49 pp.
13. Nevers, M.B.; Whitman, R.L. Efficacy of Monitoring and Empirical Predictive Modeling at Improving Public Health Protection at Chicago Beaches. *Water Res.* **2011**, *45*, 1659–1668. <https://doi.org/10.1016/j.watres.2010.12.010>.
14. Schernewski, G.; Balciunas, A.; Gräwe, D.; Gräwe, U.; Klesse, K.; Schulz, M.; Wesnigk, S.; Fleet, D.; Haseler, M.; Möllman, N.; et al. Beach Macro-Litter Monitoring on Southern Baltic Beaches: Results, Experiences and Recommendations. *J. Coast. Conserv.* **2018**, *22*, 5–25. <https://doi.org/10.1007/s11852-016-0489-x>.
15. Pan, Y.; Flindt, M.; Schneider-Kamp, P.; Holmer, M. Beach Wrack Mapping Using Unmanned Aerial Vehicles for Coastal Environmental Management. *Ocean Coast. Manag.* **2021**, *213*, 105843. <https://doi.org/10.1016/j.ocecoaman.2021.105843>.
16. Mishra, S.; Mishra, D.R. Normalized Difference Chlorophyll Index: A Novel Model for Remote Estimation of Chlorophyll-a Concentration in Turbid Productive Waters. *Remote Sens. Environ.* **2012**, *117*, 394–406. <https://doi.org/10.1016/j.rse.2011.10.016>.
17. Hantson, W.; Kooistra, L.; Slim, P.A. Mapping Invasive Woody Species in Coastal Dunes in the Netherlands: A Remote Sensing Approach Using LIDAR and High-Resolution Aerial Photographs. *Appl. Veg. Sci.* **2012**, *15*, 536–547. <https://doi.org/10.1111/j.1654-109X.2012.01194.x>.
18. Yao, H.; Qin, R.; Chen, X. Unmanned Aerial Vehicle for Remote Sensing Applications—A Review. *Remote Sens.* **2019**, *11*, 1443. <https://doi.org/10.3390/rs11121443>.
19. Pan, Y.; Ayoub, N.; Schneider-Kamp, P.; Flindt, M.; Holmer, M. Beach Wrack Dynamics Using a Camera Trap as the Real-Time Monitoring Tool. *Front. Mar. Sci.* **2022**, *9*, 813516. <https://doi.org/10.3389/fmars.2022.813516>.

20. Karstens, S.; Kiesel, J.; Petersen, J.; Etter, K.; Schneider von Deimling, J.; Vafeidis, A.; Gross, F. Human-Induced Hydrological Connectivity: Impacts of Footpaths on Beach Wrack Transport in a Frequently Visited Baltic Coastal Wetland. *Front. Mar. Sci.* **2022**, *9*, 929274. <https://doi.org/10.3389/fmars.2022.929274>.
21. Pan, X.; Zhao, J.; Xu, J. An Object-Based and Heterogeneous Segment Filter Convolutional Neural Network for High-Resolution Remote Sensing Image Classification. *Int. J. Remote Sens.* **2019**, *40*, 5892–5916. <https://doi.org/10.1080/01431161.2019.1584687>.
22. Lu, B.; He, Y.; Dao, P. Comparing the Performance of Multispectral and Hyperspectral Images for Estimating Vegetation Properties. *IEEE J. Sel. Top. Appl. Earth Obs. Remote Sens.* **2019**, *12*, 1784–1797. <https://doi.org/10.1109/JSTARS.2019.2910558>.
23. Wang, Y.; Wang, X.; Jian, J. Remote Sensing Landslide Recognition Based on Convolutional Neural Network. *Math. Probl. Eng.* **2019**, *2019*, e8389368. <https://doi.org/10.1155/2019/8389368>.
24. Tomasello, A.; Bosman, A.; Signa, G.; Rende, S.F.; Andolina, C.; Cilluffo, G.; Cassetti, F.P.; Mazzola, A.; Calvo, S.; Randazzo, G.; et al. 3D-Reconstruction of a Giant Posidonia Oceanica Beach Wrack (Banquette): Sizing Biomass, Carbon and Nutrient Stocks by Combining Field Data With High-Resolution UAV Photogrammetry. *Front. Mar. Sci.* **2022**, *9*, 903138.
25. Kelpšaitė-Rimkienė, L.; Dailidienė, I. Influence of Wind Wave Climate Change on Coastal Processes in the Eastern Baltic Sea. *J. Coast. Res.* **2011**, 220–224.
26. Jarmalavičius, D.; Zilinskas, G.; Pupienis, D. Daugiamėčiai Baltijos Jūros Lietuvos Paplūdimių Morfodinaminiai Ypatumai. *Geografija* **2011**, *47*, 98–106. <https://doi.org/10.6001/geografija.v47i2.2111>.
27. Kalvaitienė, G.; Bučas, M.; Vaičiūtė, D.; Balčiūnas, A.; Gyraitė, G.; Kataržytė, M. Impact of Beach Wrack on Microorganisms Associated with Faecal Pollution at the Baltic Sea Beaches. *SSRN* **2023**. <https://doi.org/10.2139/ssrn.4604299>.
28. Bučas, M.; Daunys, D.; Olenin, S. Recent Distribution and Stock Assessment of the Red Alga *Furcellaria Lumberalis* on an Exposed Baltic Sea Coast: Combined Use of Field Survey and Modelling Methods. *Oceanologia* **2009**, *51*, 341–359.
29. Arzt, M.; Deschamps, J.; Schmied, C.; Pietzsch, T.; Schmidt, D.; Tomancak, P.; Haase, R.; Jug, F. LABKIT: Labeling and Segmentation Toolkit for Big Image Data. *Front. Comput. Sci.* **2022**, *4*, 777728.
30. GDAL/OGR Contributors. GDAL—Geospatial Data Abstraction Library. 2022. Available online: [Gdal.Org](https://gdal.org/) (accessed on 18 September 2023).
31. Karlsen, S.R.; Anderson, H.B.; van der Wal, R.; Hansen, B.B. A New NDVI Measure That Overcomes Data Sparsity in Cloud-Covered Regions Predicts Annual Variation in Ground-Based Estimates of High Arctic Plant Productivity. *Environ. Res. Lett.* **2018**, *13*, 025011. <https://doi.org/10.1088/1748-9326/aa9f75>.
32. Wang, H.; Liu, H.; Huang, N.; Bi, J.; Ma, X.; Ma, Z.; Shanguan, Z.; Zhao, H.; Feng, Q.; Liang, T.; et al. Satellite-Derived NDVI Underestimates the Advancement of Alpine Vegetation Growth over the Past Three Decades. *Ecology* **2021**, *102*, e03518. <https://doi.org/10.1002/ecy.3518>.
33. Marusig, D.; Petruzzellis, F.; Tomasella, M.; Napolitano, R.; Altobelli, A.; Nardini, A. Correlation of Field-Measured and Remotely Sensed Plant Water Status as a Tool to Monitor the Risk of Drought-Induced Forest Decline. *Forests* **2020**, *11*, 77. <https://doi.org/10.3390/f11010077>.
34. Zhang, C.; Pattey, E.; Liu, J.; Cai, H.; Shang, J.; Dong, T. Retrieving Leaf and Canopy Water Content of Winter Wheat Using Vegetation Water Indices. *IEEE J. Sel. Top. Appl. Earth Obs. Remote Sens.* **2018**, *11*, 112–126. <https://doi.org/10.1109/JSTARS.2017.2773625>.
35. Sharifi, A.; Felegari, S. Remotely Sensed Normalized Difference Red-Edge Index for Rangeland Biomass Estimation. *Aircr. Eng. Aerosp. Technol.* **2023**, *95*, 1128–1136. <https://doi.org/10.1108/AEAT-07-2022-0199>.
36. Ronneberger, O.; Fischer, P.; Brox, T. U-Net: Convolutional Networks for Biomedical Image Segmentation. In Proceedings of the Medical Image Computing and Computer-Assisted Intervention—MICCAI 2015, Munich, Germany, 5–9 October 2015; Navab, N., Hornegger, J., Wells, W.M., Frangi, A.F., Eds.; Springer International Publishing: Cham, Switzerland, 2015; pp. 234–241.
37. Srivastava, N.; Hinton, G.; Krizhevsky, A.; Sutskever, I.; Salakhutdinov, R. Dropout: A Simple Way to Prevent Neural Networks from Overfitting. *J. Mach. Learn. Res.* **2014**, *15*, 1929–1958.
38. Chollet, F. Keras. 2015. Available online: <https://github.com/fchollet/keras> (accessed on 30 October 2023).
39. Abadi, M.; Agarwal, A.; Barham, P.; Brevdo, E.; Chen, Z.; Citro, C.; Corrado, G.S.; Davis, A.; Dean, J.; Devin, M.; et al. TensorFlow: Large-Scale Machine Learning on Heterogeneous Distributed Systems. *arXiv* **2016**, arXiv:1603.04467.
40. Milletari, F.; Navab, N.; Ahmadi, S.-A. V-Net: Fully Convolutional Neural Networks for Volumetric Medical Image Segmentation. In Proceedings of the 2016 Fourth International Conference on 3D Vision (3DV), Stanford, CA, USA, 25–28 October 2016; pp. 565–571.
41. Lin, T.-Y.; Goyal, P.; Girshick, R.; He, K.; Dollar, P. Focal Loss for Dense Object Detection. *IEEE Transactions on Pattern Analysis and Machine Intelligence* **2020**, *42*, 318–327. doi:10.1109/TPAMI.2018.2858826.
42. Vooban / Smoothly-Blend-Image-Patches. Available online: <https://github.com/Vooban/Smoothly-Blend-Image-Patches>. (accessed on 30 October 2023).
43. Kohavi, R. A Study of Cross-Validation and Bootstrap for Accuracy Estimation and Model Selection. In Proceedings of the Proceedings of the 14th International Joint Conference on Artificial Intelligence, Montreal, QC, Canada, 20–25 August 1995.
44. Kumar, S.; Jain, A.; Agarwal, A.; Rani, S.; Ghimire, A. Object-Based Image Retrieval Using the U-Net-Based Neural Network. *Comput. Intell. Neurosci.* **2021**, *2021*, 1–14. <https://doi.org/10.1155/2021/4395646>.

45. Kim, J.H.; Lee, H.; Hong, S.J.; Kim, S.; Park, J.; Hwang, J.Y.; Choi, J.P. Objects Segmentation From High-Resolution Aerial Images Using U-Net With Pyramid Pooling Layers. *IEEE Geosci. Remote Sens. Lett.* **2019**, *16*, 115–119. <https://doi.org/10.1109/LGRS.2018.2868880>.
46. Taravat, A.; Wagner, M.P.; Bonifacio, R.; Petit, D. Advanced Fully Convolutional Networks for Agricultural Field Boundary Detection. *Remote Sens.* **2021**, *13*, 722. <https://doi.org/10.3390/rs13040722>.
47. Rezatofighi, H.; Tsai, N.; Gwak, J.; Sadeghian, A.; Reid, I.; Savarese, S. Generalized Intersection Over Union: A Metric and a Loss for Bounding Box Regression. In Proceedings of the 2019 IEEE/CVF Conference on Computer Vision and Pattern Recognition (CVPR), Long Beach, CA, USA, 15–20 June 2019; pp. 658–666.
48. Harris, C.R.; Millman, K.J.; van der Walt, S.J.; Gommers, R.; Virtanen, P.; Cournapeau, D.; Wieser, E.; Taylor, J.; Berg, S.; Smith, N.J.; et al. Array Programming with NumPy. *Nature* **2020**, *585*, 357–362. <https://doi.org/10.1038/s41586-020-2649-2>.
49. Virtanen, P.; Gommers, R.; Oliphant, T.E.; Haberland, M.; Reddy, T.; Cournapeau, D.; Burovski, E.; Peterson, P.; Weckesser, W.; Bright, J.; et al. SciPy 1.0: Fundamental Algorithms for Scientific Computing in Python. *Nat. Methods* **2020**, *17*, 261–272. <https://doi.org/10.1038/s41592-019-0686-2>.
50. Seabold, S.; Perktold, J. Statsmodels: Econometric and Statistical Modeling with Python. In Proceedings of the 9th Python in Science Conference, Austin, TX, USA, 28 June–2 July 2010; pp. 92–96. <https://doi.org/10.25080/Majora-92bf1922-011>.
51. Pedregosa, F.; Varoquaux, G.; Gramfort, A.; Michel, V.; Thirion, B.; Grisel, O.; Blondel, M.; Prettenhofer, P.; Weiss, R.; Dubourg, V.; et al. Scikit-Learn: Machine Learning in Python. *J. Mach. Learn. Res.* **2011**, *12*, 2825–2830.
52. Su, Z.; Li, W.; Ma, Z.; Gao, R. An Improved U-Net Method for the Semantic Segmentation of Remote Sensing Images. *Appl. Intell.* **2022**, *52*, 3276–3288. <https://doi.org/10.1007/s10489-021-02542-9>.
53. Müller, D.; Soto-Rey, I.; Kramer, F. Towards a Guideline for Evaluation Metrics in Medical Image Segmentation. *BMC Res. Notes* **2022**, *15*, 210. <https://doi.org/10.1186/s13104-022-06096-y>.
54. Anita, S.M.; Arend, K.; Mayer, C.; Simonson, M.; Mackey, S. Different Colours of Shadows: Classification of UAV Images. *Int. J. Remote Sens.* **2017**, *38*, 8–10.
55. Long, N.; Millesamps, B.; Guillot, B.; Pouget, F.; Bertin, X. Monitoring the Topography of a Dynamic Tidal Inlet Using UAV Imagery. *Remote Sens.* **2016**, *8*, 387. <https://doi.org/10.3390/rs8050387>.
56. Brouwer, R.; De Schipper, M.; Rynne, P.; Graham, F.; Reniers, A.; Macmahon, J. Surfzone Monitoring Using Rotary Wing Unmanned Aerial Vehicles. *J. Atmos. Ocean. Technol.* **2015**, *32*, 855–863. <https://doi.org/10.1175/JTECH-D-14-00122.1>.
57. Zhang, L.; Li, Y.; Chen, H.; Wu, W.; Chen, K.; Wang, S. Anchor-Free YOLOv3 for Mass Detection in Mammogram. *Expert Syst. Appl.* **2022**, *191*, 116273. <https://doi.org/10.1016/j.eswa.2021.116273>.
58. Bao, Z.; Sodango, T.; Shifaw, E.; Li, X.; Sha, J. Monitoring of Beach Litter by Automatic Interpretation of Unmanned Aerial Vehicle Images Using the Segmentation Threshold Method. *Mar. Pollut. Bull.* **2018**, *137*, 388–398. <https://doi.org/10.1016/j.marpolbul.2018.08.009>.
59. Lu, C.-H. Applying UAV and photogrammetry to monitor the morphological changes along the beach in Penghu Islands. *ISPRS Int. Arch. Photogramm. Remote Sens. Spat. Inf. Sci.* **2016**, *XLI-B8*, 1153–1156. <https://doi.org/10.5194/isprs-archives-XLI-B8-1153-2016>.
60. Pichon, L.; Ducanhez, A.; Fonta, H.; Tisseyre, B. Quality of Digital Elevation Models Obtained from Unmanned Aerial Vehicles for Precision Viticulture. *OENO One* **2016**, *50*, 3. <https://doi.org/10.20870/oeno-one.2016.50.3.1177>.
61. Gruszczynski, W.; Puniach, E.; Cwiakała, P.; Matwij, W. Application of Convolutional Neural Networks for Low Vegetation Filtering from Data Acquired by UAVs. *ISPRS J. Photogramm. Remote Sens.* **2019**, *158*, 1–10. <https://doi.org/10.1016/j.isprsjprs.2019.09.014>.
62. Taddia, Y.; Corbau, C.; Zambello, E.; Pellegrinelli, A. UAVs for Structure-From-Motion Coastal Monitoring: A Case Study to Assess the Evolution of Embryo Dunes over a Two-Year Time Frame in the Po River Delta, Italy. *Sensors* **2019**, *19*, 1717. <https://doi.org/10.3390/s19071717>.
63. Tao, C.; Meng, Y.; Li, J.; Yang, B.; Hu, F.; Li, Y.; Cui, C.; Zhang, W. MSNet: Multispectral Semantic Segmentation Network for Remote Sensing Images. *GISci. Remote Sens.* **2022**, *59*, 1177–1198. <https://doi.org/10.1080/15481603.2022.2101728>.
64. Amiri, M.; Brooks, R.; Rivaz, H. Fine-Tuning U-Net for Ultrasound Image Segmentation: Different Layers, Different Outcomes. *IEEE Trans. Ultrason. Ferroelectr. Freq. Control* **2020**, *67*, 2510–2518. <https://doi.org/10.1109/TUFFC.2020.3015081>.
65. Matuszewski, D.J.; Sintorn, I.-M. Reducing the U-Net Size for Practical Scenarios: Virus Recognition in Electron Microscopy Images. *Comput. Methods Progr. Biomed.* **2019**, *178*, 31–39. <https://doi.org/10.1016/j.cmpb.2019.05.026>.
66. Rao, A.; Nguyen, T.; Palaniswami, M.; Ngo, T. Vision-Based Automated Crack Detection Using Convolutional Neural Networks for Condition Assessment of Infrastructure. *Struct. Health Monit.* **2020**, *20*, 1–19. <https://doi.org/10.1177/1475921720965445>.
67. Rodrigues, L.F.; Naldi, M.C.; Mari, J.F. Comparing Convolutional Neural Networks and Preprocessing Techniques for HEp-2 Cell Classification in Immunofluorescence Images. *Comput. Biol. Med.* **2020**, *116*, 103542. <https://doi.org/10.1016/j.compbiomed.2019.103542>.
68. Dubey, S.R.; Chakraborty, S.; Roy, S.K.; Mukherjee, S.; Singh, S.K.; Chaudhuri, B.B. diffGrad: An Optimization Method for Convolutional Neural Networks. *IEEE Trans. Neural Netw. Learn. Syst.* **2019**, *31*, 4500–4511. <https://doi.org/10.1109/TNNLS.2019.2955777>.
69. Zeiler, M.D.; Fergus, R. Visualizing and Understanding Convolutional Networks. In Proceedings of the Computer Vision – ECCV 2014. Springer International Publishing: Cham, **2014**; pp. 818–833.

70. Altmann, A.; Toloşi, L.; Sander, O.; Lengauer, T. Permutation Importance: A Corrected Feature Importance Measure. *Bioinformatics* **2010**, *26*, 1340–1347. <https://doi.org/10.1093/bioinformatics/btq134>.
71. Selvaraju, R.R.; Cogswell, M.; Das, A.; Vedantam, R.; Parikh, D.; Batra, D. Grad-CAM: Visual Explanations from Deep Networks via Gradient-Based Localization. In Proceedings of the 2017 IEEE International Conference on Computer Vision (ICCV), Venice, Italy, 22–29 October 2017; pp. 618–626.
72. Thomazella, R.; Castanho, J.E.; Dotto, F.R.L.; Júnior, O.P.R.; Rosa, G.H.; Marana, A.N.; Papa, J.P. Environmental Monitoring Using Drone Images and Convolutional Neural Networks. In Proceedings of the IGARSS 2018—2018 IEEE International Geoscience and Remote Sensing Symposium, Valencia, Spain, 22–227 July 2018; pp. 8941–8944.
73. Xue, K.; Zhang, Y.; Duan, H.; Ma, R. Variability of Light Absorption Properties in Optically Complex Inland Waters of Lake Chaohu, China. *J. Great Lakes Res.* **2017**, *43*, 17–31. <https://doi.org/10.1016/j.jglr.2016.10.006>.
74. Gagliardini, D.A.; Colón, P.C. A Comparative Assessment on the Use of SAR and High-Resolution Optical Images in Ocean Dynamics Studies. *Int. J. Remote Sens.* **2004**, *25*, 1271–1275. <https://doi.org/10.1080/01431160310001592166>.
75. Overstreet, B.T.; Legleiter, C.J. Removing Sun Glint from Optical Remote Sensing Images of Shallow Rivers. *Earth Surf. Process. Landf.* **2017**, *42*, 318–333. <https://doi.org/10.1002/esp.4063>.
76. Zhang, H.; Yang, K.; Lou, X.; Li, Y.; Zheng, G.; Wang, J.; Wang, X.; Ren, L.; Li, D.; Shi, A. Observation of Sea Surface Roughness at a Pixel Scale Using Multi-Angle Sun Glitter Images Acquired by the ASTER Sensor. *Remote Sens. Environ.* **2018**, *208*, 97–108. <https://doi.org/10.1016/j.rse.2018.02.004>.
77. Nomura, K.; Sugimura, D.; Hamamoto, T. Underwater Image Color Correction Using Exposure-Bracketing Imaging. *IEEE Signal Process. Lett.* **2018**, *25*, 893–897. <https://doi.org/10.1109/LSP.2018.2831630>.
78. Tiškus, E.; Bučas, M.; Vaičiūtė, D.; Gintauskas, J.; Babrauskienė, I. An Evaluation of Sun-Glint Correction Methods for UAV-Derived Secchi Depth Estimations in Inland Water Bodies. *Drones* **2023**, *7*, 546. <https://doi.org/10.3390/drones7090546>.
79. Windle, A.E.; Silsbe, G.M. Evaluation of Unoccupied Aircraft System (UAS) Remote Sensing Reflectance Retrievals for Water Quality Monitoring in Coastal Waters. *Front. Environ. Sci.* **2021**, *9*, 674247.

**Disclaimer/Publisher's Note:** The statements, opinions and data contained in all publications are solely those of the individual author(s) and contributor(s) and not of MDPI and/or the editor(s). MDPI and/or the editor(s) disclaim responsibility for any injury to people or property resulting from any ideas, methods, instructions or products referred to in the content.

Klaipėdos universiteto leidykla

Edvinas Tiškus

ADVANCEMENTS IN ECOLOGICAL MONITORING THROUGH UNMANNED AERIAL  
VEHICLE AND SATELLITE DATA: STUDIES IN WATER CLARITY, COASTAL MANAGE-  
MENT, AND VEGETATION DYNAMICS

*Doctoral dissertation*

EKOLOGINĖS STEBĖSENOS TOBULINIMAS NAUDOJANT BEPILOČIŲ ORLAIVIŲ IR  
PALYDOVŲ DUOMENIS: VANDENS SKAIDRUMO, PAKRANČIŲ VALDYMO IR AUG-  
MENIJOS KAITOS TYRIMAI

*Daktaro disertacija*

Klaipėda, 2024

SL 1335. 2024 04 29. Apimtis 14,34 sąl. sp. l. Tiražas 20 egz.

Klaipėdos universiteto leidykla, Herkaus Manto g. 84, 92294 Klaipėda

Tel. (8 46) 398 891, el. paštas: leidykla@ku.lt, interneto adresas: <http://www.ku.lt/leidykla/>

Spausdino UAB „Druka“, Mainų g. 5, 94101 Klaipėda



